Efficient Numerical Simulation of Aerothermoelastic Hypersonic Vehicles

by

Ryan J. Klock

A dissertation submitted in partial fulfillment
of the requirements for the degree of
Doctor of Philosophy
(Aerospace Engineering)
in the University of Michigan
2017

Doctoral Committee:

Professor Carlos E. S. Cesnik, Chair
Professor Iain D. Boyd
Professor Bogdan I. Epureanu
Doctor Crystal L. Pasiliao, Air Force Research Laboratory
Associate Professor Veera Sundararaghavan

Ryan J. Klock

rjklock@umich.edu

ORCID iD: 0000-0001-6647-7387

For my family.

Acknowledgements

This dissertation is the product of a community, just as I am. Without the support, encouragement, and challenge offered by my community, nothing presented here would have been possible. To Ronald, Vickie, and Aaron Klock, your unending love and enthusiasm has helped me during the most trying times of my academic career. Even when the task seemed insurmountable, a reminder that the sun will come up tomorrow was often just enough to see me through.

To my advisor and mentor, Professor Carlos Cesnik, the opportunities you have created will shape the remainder of my life. Thank you providing consistent and enduring wisdom during my development as a student, researcher, and person. You never failed to inspire me toward improving on my talents and to guide me toward new skills to add to my repertoire.

To the entire Active Aeroelasticity and Structures Research Laboratory of Jessica Jones, Christopher Lupp, Renato Medeiros, Zi Yang Pang, Patricia Teixeira, Hui Zhang, and especially Ryan Kitson, your companionship and conversations has made these last few years an enjoyable and memorable experience. The good times we had outside of the lab were just as critical to the completion of this dissertation as the times inside.

To the dissertation committee of Prof. Iain Boyd, Prof. Bogdan Epureanu, Dr. Crystal Pasiliao, and Associate Prof. Veera Sundararaghavan, thank you for your consideration, time, and feedback during the drafting of this dissertation. Your collective expertise has ensured that the work presented here is both comprehensive and of the highest quality.

Finally, this work would not have been possible without the support of the Air Force Research Laboratory (AFRL) Air Vehicles Directorate under grant number FA 8650-07-2-3744 with Michael Bolender as technical monitor, the AFRL Munitions Directorate under grant number FA 8651-13-2-0007 with Crystal Pasiliao as technical monitor, and the University of Michigan Rackham Merit Fellowship Program.

Table of Contents

List of Figures

List of Tables

List of Symbols

A	=	snapshot matrix, state space matrix
A_d	=	diffuser area ratio
A_e	=	exit area
A_n	=	nozzle area ratio
a	=	speed of sound
B	=	vectorized sample, input matrix
$\overline{B}$	=	vectorized sample matrix
b	=	kriging input
C	=	full order damping matrix, correlation matrix
C_D	=	coefficient of drag
C_L	=	coefficient of lift
c	=	generalized damping matrix, thermal mode amplitude vector
c_f	=	coefficient of skin friction
c_h	=	coefficient of heat transfer
c_P	=	coefficient of pressure
c_p	=	constant pressure specific heat capacity

$\overline{c}$ = thermal mode amplitude polynomial matrix

D = drag

d = Ritz mode amplitude vector

d_{const} = constant permutation input matrix

d_{linear} = linear permutation input matrix

d_{quad} = quadratic permutation input matrix

$\tilde{d}$ = unsampled input matrix

E = Young's modulus

F = full order load vector

F^{A} = aerodynamic loads

F^{G} = gravitational loads

F^{P} = propulsive loads

f = generalized load vector, arbitrary function

f_{st} = stoichiometric fuel ratio

G = rigidity modulus

g = arbitrary function, gravitational acceleration

H_{f} = lower heating value

h = enthalpy

I = identity matrix

I_{x} = x-axis rotational inertia

I_{y} = y-axis rotational inertia

I_{yy} = y-axis second moment of area

I_{z} = z-axis rotational inertia

I_{zz} = z-axis second moment of area

J = area torsional constant

K = full order stiffness matrix

k = generalize stiffness matrix, defined coefficient

L = Lewis number, lift

L_{aft} = aft-body length

L_{fore} = forebody length

M = full order mass matrix

M_{W} = molecular weight

M_{∞} = freestream Mach number

m = generalized mass matrix

$\dot{m}_{a}$ = fuel mass inflow rate

N = number of samples

n = total number of indices

$O(\ )$ = order of function

o = thermodynamic coefficient

Pr = Prandtl number

p = pressure, x-axis rotation rate

q = area specific heat flux, y-axis rotation rate

R = specific gas constant

Re = Reynolds number

R_{krig} = kriging regression function

R_{mb} = main body state residual

R_{ls} = least-squares regression matrix

R_{svd} = singular value decomposition regression matrix

R_u = universal gas constant

r = radius, z-axis rotation rate

r_{disp} = displacement residual

r_f = recovery factor

r_{trim} = trim solution cost

S = Sutherland's constant

S = sample matrix

$\tilde{S}$ = unsampled matrix

St = Stanton number

s = eigenvector matrix

T = temperature

T_{rot} = interface transformation matrix

t = time

tol = residual or error tolerance

U = left singular vectors matrix

u	=	x-axis velocity
V	=	right singular vectors matrix
v	=	y-axis velocity, Poisson's ratio
w	=	z-axis velocity
X	=	training sample set, sub-function
x	=	degree of freedom vector, sample input, x-axis displacement scalar
y	=	sample output, y-axis displacement scalar
$\hat{y}$	=	kriging prediction
Z	=	kriging correlation function
z	=	z-axis displacement scalar
α	=	angle of attack
α_T	=	coefficient of thermal expansion
β	=	wave angle, flight path angle
γ	=	ratio of specific heats
δ	=	control surface deflection angle
Δ	=	substantive difference
ε	=	radiative emissivity
ε_{rel}	=	relative energy
ε_{xk}	=	perturbation of the k^{th} state
ζ	=	eigenvector
η	=	elastic mode amplitude vector
η_c	=	combustor efficiency

Θ	=	characteristic temperature
θ	=	flow angle, pitch Euler angle
λ	=	eigenvalue matrix
μ	=	dynamic viscosity
μ_{aft}	=	aft-body mass per unit length
μ_{fore}	=	forebody mass per unit length
ν	=	Prandtl-Meyer function
π	=	ratio of the circumference to diameter of a circle
ρ	=	density
Σ	=	indexed sum function, singular values matrix
σ	=	Stefan-Boltzmann constant
Φ	=	basis matrix, fuel equivalence ratio
ϕ	=	mode shape, roll Euler angle
Ψ	=	truncated basis matrix
ψ	=	yaw Euler angle
ω	=	frequency
ω_x	=	rotation rate about inertial *x*-axis
ω_y	=	rotation rate about inertial *y*-axis
ω_z	=	rotation rate about inertial *z*-axis

Subscripts

AE	=	aeroelastic value

AT	=	aerothermal value
CFD	=	computational fluid dynamics
D	=	dissociation value
e	=	reference state value
G	=	geometric value
HT	=	heat transfer value
i	=	vector or matrix row number
j	=	vector of matrix column number
k	=	mode index
m	=	number of modes
$\max$	=	maximum value
$\min$	=	minimum value
n	=	normal, time level
POD	=	proper orthogonal decomposition
$perf$	=	calorically perfect value
r	=	recovery, restrained
rr	=	restrained
ru	=	restrained-unrestrained coupled
ref	=	reference value
SEP	=	shock, expansion, and piston theory
u	=	unsteady, unrestrained
ur	=	unrestrained-restrained coupled
uu	=	unrestrained

w	=	wall value
0	=	stagnation value
∞	=	freestream condition

Superscripts

A	=	aerodynamic load
C	=	constrained
E	=	elastic
H	=	thermal load
(n)	=	time level
r	=	number of retained modes
T	=	matrix transpose
W	=	wing frame value
W/B	=	wing to body frame transformed value
-1	=	inverse
*	=	Eckert reference value

Abstract

Efficient Numerical Simulation of Aerothermoelastic Hypersonic Vehicles

by

Ryan J. Klock

Chair: Carlos E. S. Cesnik

Hypersonic vehicles operate in a high-energy flight environment characterized by high dynamic pressures, high thermal loads, and non-equilibrium flow dynamics. This environment induces strong fluid, thermal, and structural dynamics interactions that are unique to this flight regime. If these vehicles are to be effectively designed and controlled, then a robust and intuitive understanding of each of these disciplines must be developed not only in isolation, but also when coupled. Limitations on scaling and the availability of adequate test facilities mean that physical investigation is infeasible. Ever growing computational power offers the ability to perform elaborate numerical simulations, but also has its own limitations. The state of the art in numerical simulation is either to create ever more high-fidelity physics models that do not couple well and require too much processing power to consider more than a few seconds of flight, or to use low-fidelity analytical models that can be tightly coupled and processed quickly, but do not represent realistic systems due to their simplifying assumptions. Reduced-order models offer a middle

ground by distilling the dominant trends of high-fidelity training solutions into a form that can be quickly processed and more tightly coupled.

This thesis presents a variably coupled, variable-fidelity, aerothermoelastic framework for the simulation and analysis of high-speed vehicle systems using analytical, reduced-order, and surrogate modeling techniques. Full launch-to-landing flights of complete vehicles are considered and used to define flight envelopes with aeroelastic, aerothermal, and thermoelastic limits, tune in-the-loop flight controllers, and inform future design considerations. A partitioned approach to vehicle simulation is considered in which regions dominated by particular combinations of processes are made separate from the overall solution and simulated by a specialized set of models to improve overall processing speed and overall solution fidelity. A number of enhancements to this framework are made through

1. the implementation of a publish-subscribe code architecture for rapid prototyping of physics and process models.
2. the implementation of a selection of linearization and model identification methods including high-order pseudo-time forward difference, complex-step, and direct identification from ordinary differential equation inspection.
3. improvements to the aeroheating and thermal models with non-equilibrium gas dynamics and generalized temperature dependent material thermal properties.

A variety of model reduction and surrogate model techniques are applied to a representative hypersonic vehicle on a terminal trajectory to enable complete aerothermoelastic flight simulations. Multiple terminal trajectories of various starting altitudes and Mach numbers are optimized to maximize final kinetic energy of the vehicle upon reaching the surface. Surrogate

models are compared to represent the variation of material thermal properties with temperature. A new method is developed and shown to be both accurate and computationally efficient.

While the numerically efficient simulation of high-speed vehicles is developed within the presented framework, the goal of real time simulation is hampered by the necessity of multiple nested convergence loops. An alternative all-in-one surrogate model method is developed based on singular-value decomposition and regression that is near real time.

Finally, the aeroelastic stability of pressurized cylindrical shells is investigated in the context of a maneuvering axisymmetric high-speed vehicle. Moderate internal pressurization is numerically shown to decrease stability, as showed experimentally in the literature, yet not well reproduced analytically. Insights are drawn from time simulation results and used to inform approaches for future vehicle model development.

CHAPTER I

Introduction and Literature Review

This chapter outlines the problem of aerothermoelastic simulation of hypersonic vehicles (HSVs) and begins with an overview of the history of hypersonic flight. The dominant physical processes encountered in the hypersonic regime are then introduced along with their coupling mechanisms. Literature relevant to the processes and couplings investigated in this dissertation are noted, including research into supersonic and hypersonic aerodynamics, aeroheating, structural thermodynamics, aerothermoelasticity, and hypersonic flight dynamics. The University of Michigan High Speed Vehicle (UM/HSV) simulation framework is then introduced along with its development over the last decade. A review of the reduced-order and surrogate modeling techniques that underpin its operation is given. Finally, a list of the main objectives of this dissertation is provided.

1.1 Introduction

Hypersonic flight is loosely defined as flight above the speed of Mach 5,[1] although there is no clear threshold at which hypersonic principles become important. When a vehicle travels supersonically, shock waves form as a means for the surrounding air to react to the vehicle's presence and move aside. If leading edges of the vehicle are sufficiently sharp, then these shock waves can approach and attach to the surface of the vehicle as oblique shock waves that slant away

from the vehicle surface in the direction of the prevailing flow, similar to as shown in Figure 1.1. As the Mach number of the vehicle is increased, the shocks lie closer to the surface of the vehicle and create a region of intense pressure and temperature. The pressures and temperatures are sufficient to cause the air to chemically react due to molecular dissociation, recombination, and even ionization.[2] The exact Mach number at which the heat or reactivity of the air becomes a design consideration for the vehicle is the Mach number at which the vehicle is said to be hypersonic.

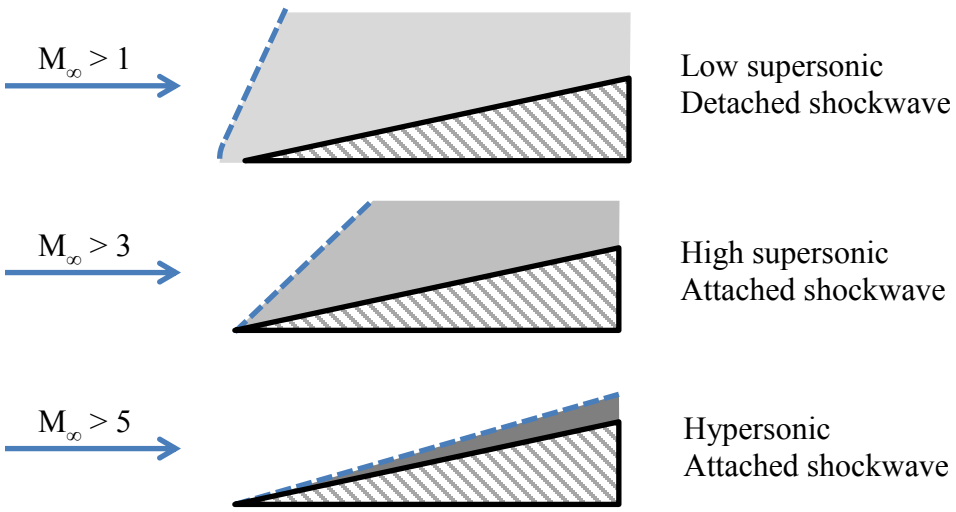

Figure 1.1: Supersonic flow regimes

HSVs are often lifting bodies due to the high dynamic pressure present at high speeds and the need to mitigate the buildup of heat within the vehicle structure. It is this buildup of heat that distinguishes hypersonic aerothermoelastic design from classical aeroelastic design by influencing the elastic behavior of the structure and modifying the flow properties surrounding the vehicle. Time traces of a representative hypersonic terminal trajectory[3] are shown in Figure 1.2 which highlight the extreme velocities, pressure loads, and flow temperatures present in this regime.

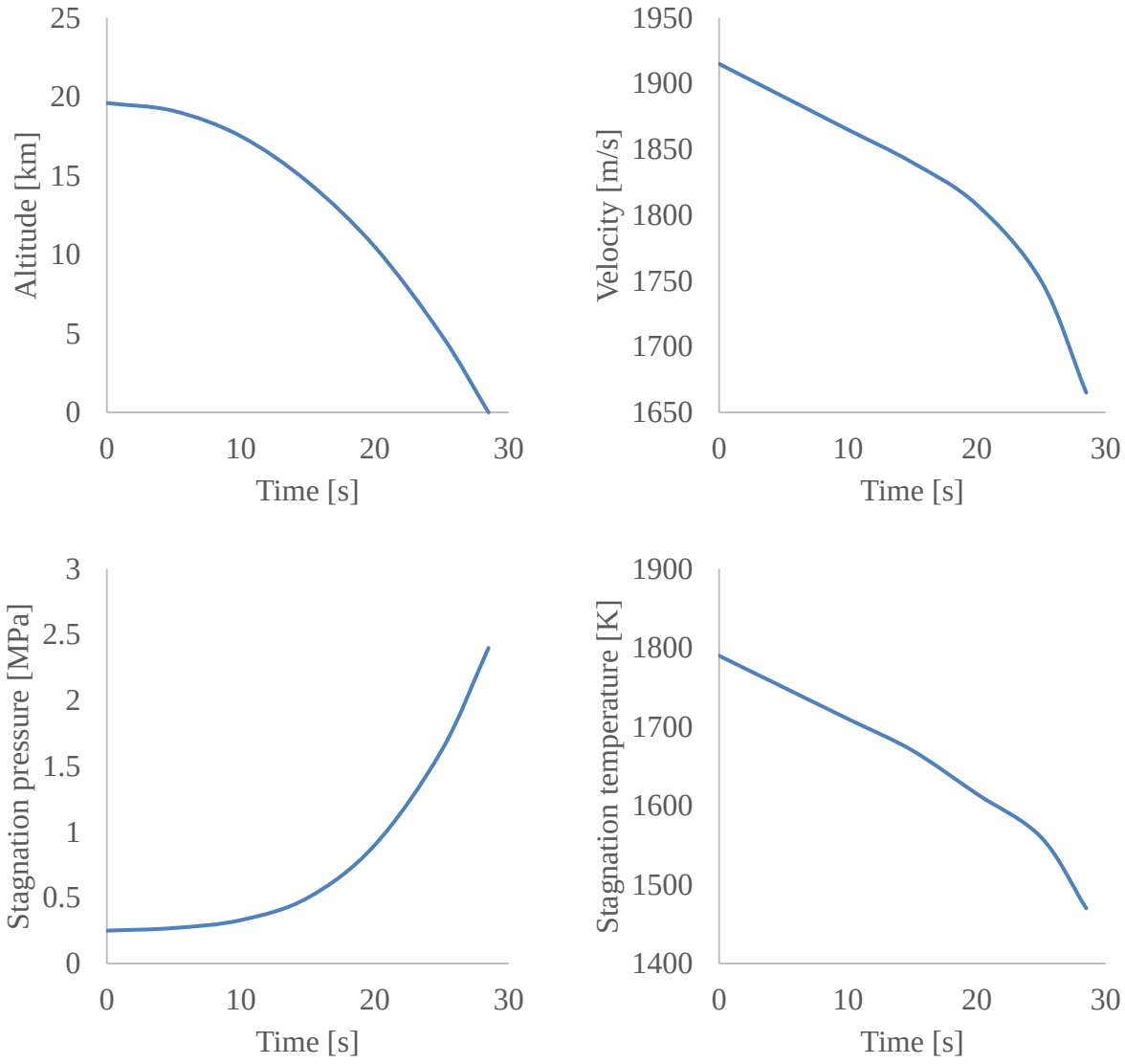

Figure 1.2: Representative hypersonic terminal trajectory[3]

A summary of the driving disciplines and their couplings is shown by Collar's triangle,[4] modified to a tetrahedral with the inclusion of thermal considerations in Figure 1.3.

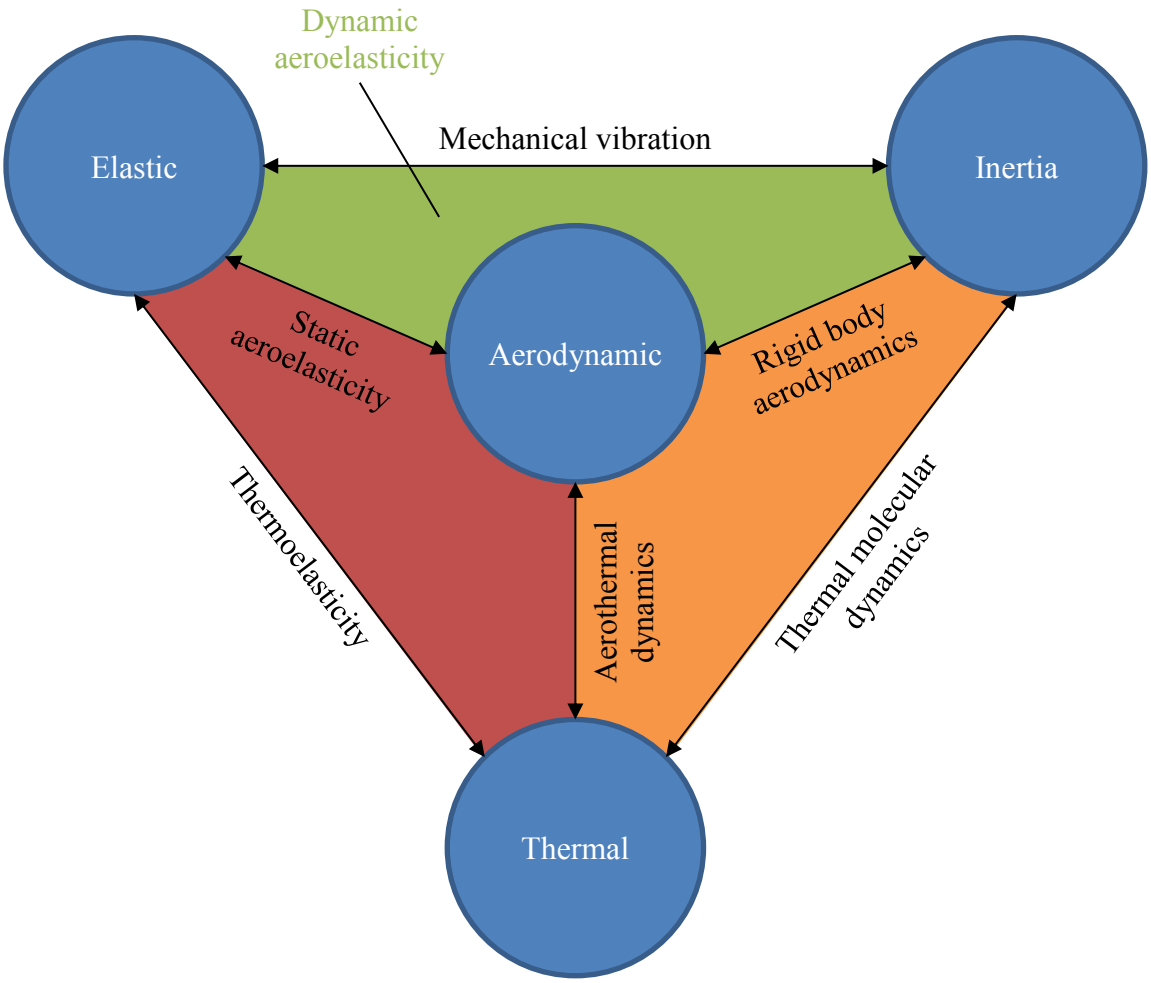

Figure 1.3: Modified Collar's triangle of aerothermoelasticity

The four primary disciplines to consider are elastic, inertial, aerodynamic, and thermal. Collar's triangle originally described the interactions of these disciplines for the consideration of dynamic aeroelasticity, shown as the green face of the tetrahedral. By way of exemplifying how these disciplines interact in practice, consider a flexible vehicle traveling at hypersonic velocities. Aerodynamic pressures load the outer surface and deform the vehicle's shape. The aerodynamics then responds to the newly deformed shape by modifying the pressure loads. The rigid body velocities and rotations are then modified due to the new net external loads and further change the pressure loads. Meanwhile, flow compression and viscous heating are quickly warming the outer

surface. This heat seeps into the vehicle's structure and changes the stiffness of its materials while uneven thermal expansion warps the vehicle's shape, further modifying the structure's response to the pressure loading, modifying the pressure field, leading to new heating patterns, changing the shape further, resulting in new rigid body motions, modifying the pressure field, and so on. If one is to design effectively such a vehicle, a robust understanding of each discipline in isolation and when interacting with others is necessary.

Humanity's foray into hypersonic flight began in the latter part of World War II with the use of Nazi Germany's V-2 rocket. The sub-orbital trajectories of these rockets sometimes included a phase during reentry into the upper atmosphere that induced low-hypersonic thermoelastic effects which could lead to the loss of the vehicle.[5] Following the defeat of Nazi Germany, a United States appropriated V-2 was used as a boost-stage to a WAC Corporal rocket which achieved 5,150 miles per hour, in excess of Mach 6.7, over the White Sands Missile Range, New Mexico, February 24th, 1949.[2,6] However, the vehicle was destroyed on reentry and only charred remains were recovered. Several years later the U.S. – U.S.S.R. space race commenced and the consideration of HSVs, particularly for spaceflight and reentry, found new urgency.

As a product of the space race came the development of the NASA X-15 rocket plane proposed in 1954, which eventually traveled up to 67 miles in altitude, reached Mach 6.7[7] and featured a blunted nose for thermal management with wedge airfoil stabilizers that would be characteristic of many HSVs for the decades to come. Lifting bodies were introduced soon after with experimental studies focused on manned space access such as the Boeing X-20 Dyna-Soar in 1957, which featured a large delta wing for hypersonic glide and controlled speed bleed-off.[8] Such an approach to controlled and lifting reentry would be seen again in the design of the NASA Space Shuttles in 1981.[9] The Rockewell X-30 National Aero-Space Plane (NASP) in 1986 was the next

major attempt at hypersonic flight and featured a super-sonic combustion ramjet (scramjet) propulsion system to assist in its acceleration to upwards of Mach 20, so to provide single-stage to orbit space access. As a byproduct of the scramjet system, some conceptions of NASP were also wave-rider type HSVs that trapped a shock wave beneath the fuselage and rested on the resulting high-pressure flow to generate lift. However, the development of high temperature materials and development of feasible scramjet propulsion systems proved too difficult for the time and lead to the cancellation of the unrealizable NASP project.[10,11]

It was not until the successful flight of the unmanned NASA X-43 in 2004, as part of the NASA Hyper-X program, that the scramjet design limitations of the past were overcome. After separation from a Pegasus solid-rocket booster, the wedge-type X-43 HSV accelerated under scramjet power for 11 seconds to reach Mach 6.8.[12] A later flight of a revised vehicle, the X-43A, would reach Mach 9.6.[6,13] The success of the X-43 spurred the development of the Boeing X-51 WaveRider that was designed in 2005 and first flown in 2010. Whereas the X-43 was simply to prove the practicality of air-breathing hypersonic flight, the X-51 was to prove its feasibility by using JP-7 fuel and eventually kept the scramjet active for up to 210 seconds.[14–16]

1.2 Literature Review

Although the prospect of hypersonic aerothermoelastic modeling is daunting, the last six decades of literature provide a rich collection of techniques specific to the aerodynamic, thermal dynamic, and structural dynamic disciplines, as well as their couplings. A multitude of model reduction and surrogate model methods are also available, and range from general tools for arbitrary systems to discipline-specific approaches that leverage properties of the governing

equations to limit the number of degrees of freedom to be considered. The techniques, models, and methods leveraged in this thesis and by related studies are reviewed.

1.2.1 Aerothermoelasticity

As described in the introduction, the field of aerothermoelasticity is composed of a collection of coupled disciplines whose interactions must be understood if effective HSV models are to be formulated. Integral to this is understanding simply how coupled each discipline must be to the others for accurate simulation. Numerous studies[17–22] have attempted to implement various levels of coupling and can be distilled into Figure 1.4.

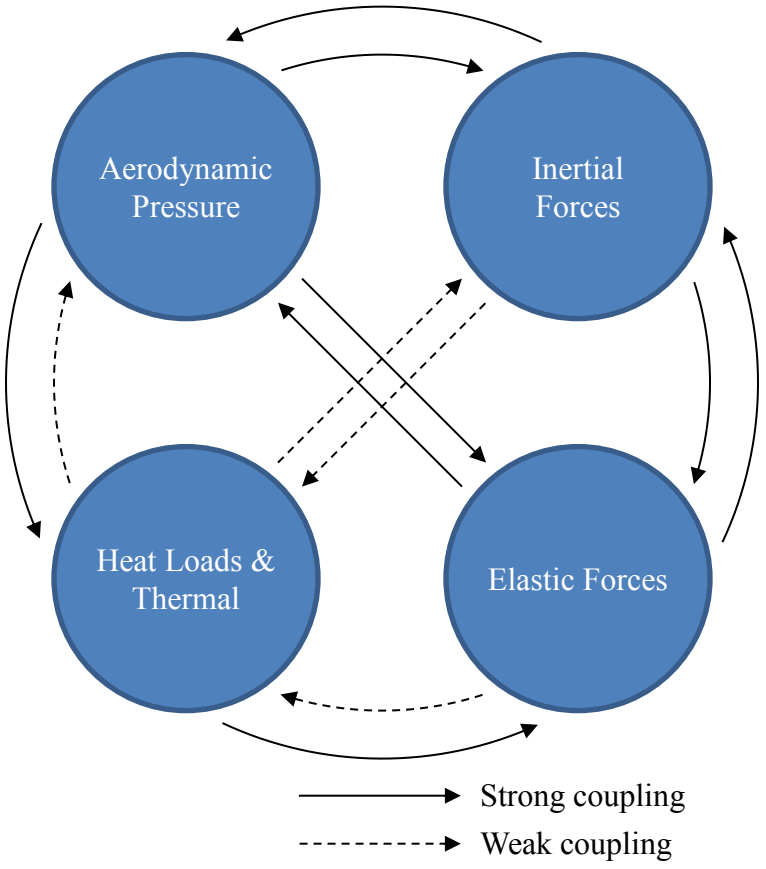

Figure 1.4: Coupling strength between disciplines[23]

Aerodynamic pressure loads, inertial forces, and elastic forces are all strongly interdependent, as a change in shape or motion of a body will immediately result in a new pressure field which in turn drives a new shape or motion. Heat loads and the thermal system, however, are somewhat less coupled. For a body of considerable thermal capacity, a change in the temperature occurs on a slower time scale than the inertial or elastic dynamics, and so receives only weak influences from these systems. Aerodynamic pressure does play a meaningful role in the determination of heat flux on the boundary conditions, but the temperature does not strongly influence pressure. The thermal solution does strongly affect material properties and so has a strong influence on the elastic forces.

Work by Culler and McNamara[19] evaluated the levels of coupling required to simulate a carbon-carbon panel characteristic of a hypersonic vehicle's skin. Oblique shock[1] and piston theory[24] were used to determine unsteady aerodynamic pressure loads, Eckert's reference enthalpy method[25] was used for the thermal loads, and finite element models were used to integrate the thermal and elastic solutions. It was found that coupling between the aerodynamic heating and elastic deformation resulted in low to moderate increases in surface temperature on the order of 10% and large increases on the order of 100% in the surface ply failure index due to thermal expansion compared to the uncoupled solution. The expanded panel also exhibited snap-through behavior when there was no coupling between the surface deformation and aerodynamic pressure during long duration simulations; however, with additional pressure due to deformation, snap-through was shown to onset much sooner. Including aerodynamic heating effects into the coupled pressure and deformation was also shown to prevent snap-through altogether under some conditions.

Miller et al.[20,21,26] built upon this work to demonstrate that time simulation of aerothermoelastic systems could be carried out, this time with CFD pressure solutions, with a loosely coupled scheme that used multi-cycling during integration to emphasize pressure calculations with the most iterations, structural deformation with fewer, and finally thermal with the least. Near second-order accuracy was maintained for all three disciplines compared to more tightly coupled, non-multi-cycling solutions. This approach of multiple time cycles for different processes was later shown to work well for more complex, built-up structures and a completely ROM-based analysis by Gogulapati et al.[17]

1.2.2 Hypersonic Flight Dynamics

Research by Bolender and Doman[27] described a two-dimensional longitudinal flight dynamics model that employed a combination of oblique shock, Prandtl-Meyer expansion, and a quasi-one-dimensional duct with heat addition[1] to determine the stability characteristics of a two-dimensional HSV. The inclusion of shock-expansion theory, rather than the previously studied[28] Newtonian impact theory,[29–31] allowed for the consideration of engine inlet spillage and inlet shock patterns which are both considered with respect to a movable inlet door intended to maintain a shock-on-lip condition. Pressures on the aft body resulting from the propulsion exhaust are also considered. Flat plates are used to approximate control surfaces positioned near the tail of the vehicle, which also employed shock-expansion theory in order to determine lift and drag characteristics during simulation. Vehicle flexibility was approximated by a pair of cantilevered beams, one reaching fore and the other aft, joined at the center of mass of the vehicle. The frequency response of the joined-beam model was then analyzed to determine the main vibrational modes of the beam structure and used to generalize the equations of motion for the vehicle. The

equations of motion were linearized about a trim condition and used to show unstable short period and phugoid modes.[32] Bolender and Doman[27] concluded that research into a closed-loop control system would be required. However, consideration of only two-dimensional flight limited the development of HSV control laws, which would ultimately be required to operate in full three-dimensional, six-degree-of-freedom environments where both longitudinal and lateral flight characteristics must be considered.

In order to explore the characteristics of a three-dimensional vehicle flight, Frendreis, Skujins, and Cesnik[33] conducted a full six-degree-of-freedom analysis of a generic hypersonic vehicle which included a rigid vehicle structure, two-dimensional shock expansion theory for the external panel pressures, and a one-dimensional area ratio model of the propulsion system. This work was then expanded by Falkiewicz, Frendreis, and Cesnik[34] to include the effects of a flexible fuselage, flexible control surfaces, the resulting inertial coupling, unsteady aerodynamics, and aerothermal effects by partitioning the HSV into discrete component regions among which information was exchanged to maintain vehicle continuity. The work by Falkiewicz et al.[35–38] focused on enhancing the fidelity of the HSV control surfaces by considering the unsteady aerodynamics, aerothermal heating, and the resulting material property degradation of the control surface structure by way of structural Ritz modes and proper orthogonal decomposition (POD) of the dominant thermal modes. Meanwhile Frendreis and Cesnik[39] focused on the application of vehicle flexibility to the three-dimensional model by a modal representation of the fuselage deformations. Work by Dalle et al.[40] applied the two-dimensional Michigan-AFRL Scramjet In Vehicle (MASIV)[41–46] propulsion model to three-dimensional flight of a rigid HSV to determine vehicle trim. Further work by Dalle and Driscoll[47] eventually led to the continuous differentiation of a HSV system for flight trajectory simulation, stability analysis, and model parameter sensitivity

analysis for a simple rigid six-degrees-of-freedom on an ellipsoidal Earth, as well as optimization of ascent trajectories, coordinated turns, and ramjet to scramjet mode transitions.[48–51]

1.2.3 Trajectory Optimization

It is often the case during model reduction that not only the system dynamics need to be considered, but also the expected system inputs. For HSVs, this is particularly true for the thermal model, which is a slow integration of heat loads, exhibits strong hysteresis, and is highly path dependent. Thus significant model reduction can be achieved if the trajectory of the HSV can be identified *a priori*. For several of the studies described in this thesis, a representative trajectory was required, for which to tailor structural, thermal, and thermo-structural reduced order models (ROMs). In the literature, the optimization of hypersonic trajectories for a wide range of vehicle and mission types has been approached using many different optimization tools.[52–54] Zhao and Zhou[55] employed a multiple phase Gauss Pseudospectral method to maximize cross range and minimize trajectory time for a reentering hypersonic vehicle subjected to heating, loading, waypoint, and no-fly zone constraints. This was done by partitioning the trajectory into segments with matching final/initial conditions at the segment interfaces to create a continuous trajectory while refining the Legendre-Gauss sample density around periods of constraint influence. Rao and Clarke[56] used the Legendre Pseudospectral method to optimize a hypersonic reentry trajectory, however with a focus on maximizing control margin that would allow for unmodeled perturbations to the vehicle during an actual flight. The possibility of using the pseudospectral method as a guidance law was also discussed. An intelligent method based on multi-objective particle swarm optimization was developed by Grant and Mendeck[57] to explore the design space of the Mars Science Laboratory entry trajectory in terms of parachute deployment altitude, range error, and

acceleration loading. This method was especially well-suited to handle Pareto fronts, solution loci in the design space along which even trade-offs occur between multiple objective functions and provide no single superior solution. Also available is the Optimal Trajectories by Implicit Simulation (OTIS) software by Hargraves et al.[58] which can generate open-loop control functions based on Hermite interpolation of the trajectory and nonlinear programming. Many types of point-mass and rigid-body problems have been considered using the OTIS tools including single- and multi-stage-to-orbit hypersonic vehicle trajectories.

For the work presented in this thesis, the General Pseudospectral Optimization Software (GPOPS-II) was used to apply the Radau Pseudospectral method,[59] previously used by Rexius et al.[60] to optimize the launch, staging, and descent of a rocket-boosted hypersonic glider similar to the common aero vehicle (CAV).[61] GPOPS-II was viewed by the authors as a suitable trajectory optimizer due to similar flight constraints during the final descent phase of the CAV presented by Rexius[60] and the sample HSVs considered in this work, as well as the ease of use due to its Matlab based implementation.

1.2.4 Reduced Order Modeling

It is often noted in literature that full-order simulation, particularly computational fluid dynamics (CFD) and finite element analysis (FEA) for aerodynamic, structural dynamic, and thermodynamic coupled systems, can be prohibitively costly in terms of computational reasources.[62–65] To reduce the computational cost associated with obtaining a thermal solution for a vehicle structure using traditional finite element analysis, ROMs are often employed. A straightforward ROM approach is to use eigenmode analysis as described by Shore,[66] which is analogous to the derivation of free-vibration modes for a structure, except that thermal

conductivity and capacity are considered in place of the stiffness and inertia matrices. This leads to a set of basis modes from which a subset of temperature distributions may be selected and used as generalized degrees of freedom of the thermal problem. This approach may be extended with the component mode synthesis method described by Craig and Bampton.[67] In component mode synthesis, a structure is first partitioned into a set of interfacing substructures. Each substructure's eigenmodes are determined with fully constrained boundary conditions at the interfaces to form a basis set for each substructure. The basis sets are then augmented with boundary modes derived from perturbation of the substructure interfaces, which are selected to ensure continuity between substructures. By reducing the order of the basis sets of each substructure, the number of degrees of freedom of the overall structure may be reduced. This approach is useful for structures with a small number of components that have dissimilar properties, but can be cumbersome as the number of interfaces increases, requiring more and more boundary modes. The Guyan reduction method[68] is possible if the thermal loading locations are known *a priori* and may be used to construct matrices whose entries only pertain to degrees of freedom that are known to vary and yet sacrifices none of the structural complexity. This approach is useful for thermal problems in which there are a few localized heat sources, but is poor at reducing the model complexity in scenarios with widely distributed loads, such as aerodynamic heating of a vehicle. Another possible technique to reduce the thermal problem is the modal identification method.[69] In this approach, a set of eigenmodes of a state-space representation of the full-order system are identified through minimization of a criterion related to the difference between the outputs of the full and reduced-order systems. This is useful when a full eigenmode analysis of the state-space is computationally infeasible and the thermal conductivity and capacity matrices are unknown. However, for the studies in this thesis, the thermal matrices will be known and thus, the advantage is inconsequential. Furthermore, the

modal identification method has been shown to be effective for systems with low numbers of thermal loads (1 to 3), but will become infeasible for the thousands of loads considered over the entire outer surface of a hypersonic vehicle.[35]

Nearly all of these ROMs involve the transformation of a governing system of equations into modal space and differ in the identification of the basis set and correction for nonlinear effects. However, these methods largely rely on the matrices of the governing systems of equations rather than the actual response of the system when observed during simulation or experimentation. Furthermore, eigenvector bases may not be optimal in the sense of capturing the most system energy with the fewest number of modes. If the transient responses of the thermal system can be characterized *a priori*, as is the case in this thesis by beginning with known structural models, the method of Proper Orthogonal Decomposition (POD) may be used.[35] The POD method provides an inherent optimality condition of providing the most efficient capture of the dominant energy modes of a system with a finite number of basis modes[70] and has been widely used in literature to reduce both linear[71,72] and nonlinear[73] thermal problems.

For structural dynamics, ROMs are often applications of the Rayleigh-Ritz/Galerkin methods[74] and matrix transformation to the eigenvalue and eigenvector form.[75] Once expressed as a set of eigenvectors or modes, the basis set is truncated to reduce the degrees of freedom of the system and thus reduce the effort of integrating the structural equations of motion. However, as a goal of this thesis is to capture the coupling of thermal and structural effects, this approach cannot be applied directly to the problem studied here because of the change of the structural stiffness from geometric stiffening and material degradation effects. Instead, the approach taken in this thesis is to perform an initial calculation of the free-vibration mode shapes at some reference thermal state. These mode shapes are then to be used as the modal basis for simulation with updates

to the stiffness matrix from a kriging surrogate model based on training samples in different thermal states described by the thermal POD basis modes.[36]

1.2.5 Surrogate Modeling

Sometimes a system's governing equations are not well understood or are not readily reduced by the techniques previously described. In these cases, it is advantageous to substitute the high-order governing equations with a low-order surrogate function that can be trained or tuned to imitate the full solution for a greatly reduced computation cost.[76–85] For nearly all surrogate techniques, this is done by exposing the model to a training set of high-order solutions that span the design space that the model will be expected to operate in. There is a rich array of surrogate model techniques in the literature, many of which are general, and many of which offer specialized functions suited to capture a particular flavor of dynamics. However, these models broadly fall into one of several category types. Perhaps the simplest type of such surrogate model are the regression models[86–90] which contain some base function that describes a response surface and has one or more tuning parameters. These tuning parameters are varied so to minimize the total error of the surface to a set of training samples. Regression models are best used when the modeled system order is at least approximately known and when it is desirable to have a surrogate with predictable computational cost that does not vary with the number of training samples. Some limited extrapolation can also be considered, depending on the base function. However, regression models often reach convergence with relatively few training points and do not improve further with additional samples.

Radial basis functions (RBF)[91–95] offer a second form of surrogate that is based on one or more kernel functions. Each of the training samples are used as the center of a kernel function that

occupies some portion of the design space. Interpolation is done by a weighted sum of the kernel functions, whose influence is some variant of inversely proportional to the distance between the training samples and the sought point in the design space. This approach is ideal when the order of the modeled system is unknown but training samples are plentiful and one desires the solution at any training point to be recoverable. RBF surrogates will typically improve asymptotically to the behavior of the modeled system when given more training samples, but increase in computational expense linearly with the number of training samples. Extrapolation outside of the training set is typically not possible.

Kriging[96–101] is a combination of regression and radial basis functions that leverages the strengths of each to produce a response surface that quickly converges and maintains the solutions of the training samples. A regression process is first used to fit a base function to the training samples as best as possible in order to identify the underlying trends. Error corrections are then applied via radial basis kernels that augment the surface so to pass through the training samples. Under most circumstances, a kriging model will improve in accuracy when provided with additional samples and offers limited extrapolation. However, too many training samples will increase computational cost as the kriging begins to behave more as a radial basis model.

Artificial neural networks (ANN)[102–106] are a numerical model inspired by the connectivity of biological neurons in a brain or nervous system. It consists of an array of bounded activation functions (neurons), such as sigmoid or hyperbolic tangent, that are interconnected along linear gains that sum at the input of each neuron (synapses). At model initiation, random gains are assigned to each synapse. The ANN is then used to predict one or more output values when given an input to a training sample. The error between the prediction and training sample solution is then distributed across the synapses according to the product of the synapse gains connecting the output

to a given synapse (back-propagation). Repeated prediction of training samples, determination of error, and back-propagation causes the ANN to converge onto the behavior of the training set. ANNs are ideal when considering highly nonlinear systems that are not well understood and have high-dimensional inputs. The number of training samples required to converge an ANN grows exponentially with the number of neurons if the network is fully connected, and thus vast numbers of samples are required to model complex systems.

Finally, space mapping[107–110] is a hybrid type of surrogate model which is useful when one has access to only a space training set of high-fidelity solutions, but a rich set of simplified solutions. The assumption is that the simplified solutions capture the general behavior of the modeled system, and can be used to make a response surface with one of the aforementioned surrogate techniques. A global correction is then performed to adjust the response surface to agree with the high-fidelity solutions. This results in a model that exactly reproduces the high-fidelity training data and the overall trends despite the sparse training set.

1.2.6 Material Thermal Property Modeling

The variation of material thermal properties has been considered in literature, although often in a limited capacity. In a study by McMasters et al.[111] of nonlinear thermal diffusion, an exact analytical solution was derived with a thermal conductivity that varied linearly with temperature and was later used to verify the results of a finite element thermal analysis code, CALORE.[112] While thermal conductivity was variable, all other thermal properties were assumed to be constant.

Matney et al.[113] considered the variation of thermal properties for the problem of hypersonic flow over a panel with underlying stiffeners in the development of an adaptive thermal

basis set. In their study, aerodynamic pressure was modeled using piston theory[24] and heat flux was modeled using the Eckert reference enthalpy method.[114] These aerodynamic and thermal loading solutions were then applied to a finite element model (FEM) to observe structural and thermal responses. Variation of the in-plane thermal conductivity with respect to the temperature of the panel was modeled using a property lookup table. Each element of their panel FEM was identical and could use the same lookup table for all elements. This approach to modeling the variation of material thermal properties with respect to temperature was therefore limited to very simple geometries where uniform finite elements could be used.

The force-derivative method originally developed by Camarda[115,116] for nonlinear structural dynamics has also been shown by Balakrishnan, Hou, and Camarda[117] to work well for nonlinear thermal problems by modifying the heat load based on previously linearized thermal capacity and conductivity properties. In this approach, variation of the thermal properties of both structures and materials could be considered but required repeatedly solving an eigenproblem and inverting a variable FEM conductivity matrix. This allows for transient thermal solutions more quickly than a full FEM simulation but not without its own overhead that could become prohibitive if more than a couple degrees of freedom are considered.

1.2.7 Estimation of State Spaces

Methods of combining ROM techniques and linear parameter-varying (LPV) models have often begun with already determined state spaces with many degrees of freedom and sought to reduce the number of degrees of freedom while retaining the dominant behavior of the system in order to produce control laws. Such methods include modal reduction,[118] balanced realization and truncation,[118,119] Krylov methods,[120] and others.[121,122] It is not uncommon to use multiple

techniques in combination when considering systems of very high order, such as in aeroelastic analyses of flexible aircraft. A recent example has been the simulation of the X-56A flight model where the influence of the airspeed and fuel weight was considered.[122] In that work, a collection of state space matrices was first reduced by a combination of regular state truncation, modal reduction, and balanced truncation from 180 to 21 states. However, in this reduction process, the final 21 states did not have consistent meaning for all state spaces. To remedy this, a common subspace was determined, from which all the state space matrices could be recovered. Matrices for state spaces outside of the original collection were determined through linear interpolation between nearest neighbor samples and shown to correctly predict the frequency response of most retained states.

A different model reduction technique was developed by Carlson et al.[123] in which the partial differential equations (PDEs) of motion for an F-16 similar aircraft were generalized using proper orthogonal decomposition (POD) modes derived from high-fidelity flight simulations of the maneuvering aircraft. The PDEs considered contained both linear and bi-linear terms in order to model some nonlinear behaviors including post-stall and aeroelasticity effects. Comparison of the reduced model and Kestrel[124,125] flight simulation results showed good agreement, but with some loss of high-frequency dynamics.

1.2.8 Aeroelastic Stability of Pressurized Cylindrical Shells

In the experimental and analytical work of Olson and Fung,[126] a low-aspect ratio cylindrical copper shell was exposed to supersonic flow ranging from Mach 2.5 to 3.5. The behavior of the shell's flutter motion was studied and the effect of internal pressure and axial load on the flutter boundary was investigated. It was found that the nonlinear geometric behavior of a cylindrical

shell induced a series of circumferentially travelling waves whose amplitudes eventually grow at the onset of flutter.[127] Axial load reduced the flutter boundary until the shell buckled, later reproduced by Barr and Stearman[128] and Bismarck-Nasr.[129] After buckling, the new corrugated shape was stable. Internal pressure was shown to initially have a destabilizing effect, reducing the flutter boundary, but stabilized the shell at sufficiently high pressures. Early analytical solutions based on shallow shell theory were unable to reconcile the destabilizing and then restabilizing behavior observed in experiments.[126]

Evensen and Olson[127,130] later refined the analysis of the cylindrical shells using a nonlinear four-mode approach to study the limit cycle oscillation and traveling circumferential waves.[126] The works of Barr and Stearman[128,131] and later Amabili and Pellicano[132,133] showed how shell imperfections can account for the disagreement between theory and experiment and that the application of nonlinear piston theory did not appear to affect the onset of flutter.

Several works have also studied the application of finite element methods and were summarized by Bismarck-Nasr.[134] Sabri and Lakis[135] appears to be the most recent study which focused on the development of a finite element specialized for circular cylindrical shells. Sander's thin shell theory was used to determine displacement fields from exact solutions of the governing equations after which the classical finite element method was applied. The resulting flutter boundary predication was an improvement over past analysis,[126] but failed to reproduce experimental results.

1.3 Objectives of this Dissertation

As the previous section shows, many advances have been made in the literature toward the efficient modeling of individual aerothermoelastic disciplines and some coupled. However, a

unified framework for modeling HSVs has yet to be established and shown to model accurately full six degree-of-freedom flight for general-purpose analyses. It is therefore the objectives of this thesis to

1. enhance an aerothermoelastic reduced-order model framework capable of producing numerically efficient flight simulations of supersonic and hypersonic vehicles. This framework was outlined by Falkiewicz and Cesnik[136] with preliminary development performed by Frendries et al.[33,39,40,137] Generalization of this framework for all high-speed vehicles will be carried out and comparisons made to classical methods for verification.
2. develop an all-in-one reduced-order model to simulate aero-servo-thermo-elastic HSVs faster than real-time. While the framework previously described may be efficient on a model-by-model basis, moderate to tight coupling still requires online convergence iterations present computational overhead and increases processing time. Estimation of the HSV and a unified system relieves this overhead and accelerates processing.
3. demonstrate the importance of temperature dependent material thermal properties for heat transfer systems and investigate modeling techniques to capture the property variations. Several surrogate modeling approaches will be compared and contrasted based on accuracy and computational cost.
4. investigate the aeroelastic stability of pressurized vehicles on terminal trajectories and when maneuvering.

CHAPTER II

Foundational Theory

The theories that underpin this dissertation and were present at the onset of this study are overviewed in the context of the University of Michigan High Speed Vehicle Simulation Framework. These theories include analytical models of aerodynamics and aerodynamic heating, as well as model reduction techniques for heat transfer, structural dynamics, and thermoelastic coupling. Ramjet and scramjet models are also visited, which use combinations of the aforementioned theories along with models of combustion and heat addition.

2.1 University of Michigan High Speed Vehicle Simulation Framework

The simulation of high-speed flight vehicles involves the consideration of multiple, highly coupled disciplines. Each of these disciplines can be daunting to consider with a realistic level of fidelity individually, and combined, they present a virtually intractable problem that is extremely difficult to numerically integrate and analyze. An information flowchart of the discipline interactions is shown in Figure 2.1. The University of Michigan High Speed Vehicle (UM/HSV) framework strives to couple one or more families of reduced-order and surrogate models in order to simulate such high-speed vehicles. To reduce the numerical burden of individual disciplines, a suite of model reduction techniques are used to identify dominant modes of physical processes, determined from observations of high order solutions. When high order solutions are not available,

fundamental models may be used in their place. For especially complex systems where the underlying governing processes are not well understood or not readily condensed, surrogate models may be introduced which provide best-guess approximations to high fidelity solutions, but do not require the numerical overhead typically required. The three primary disciplines and their interactions are shown in Figure 2.2 along with the types of models available in this thesis to represent each process.

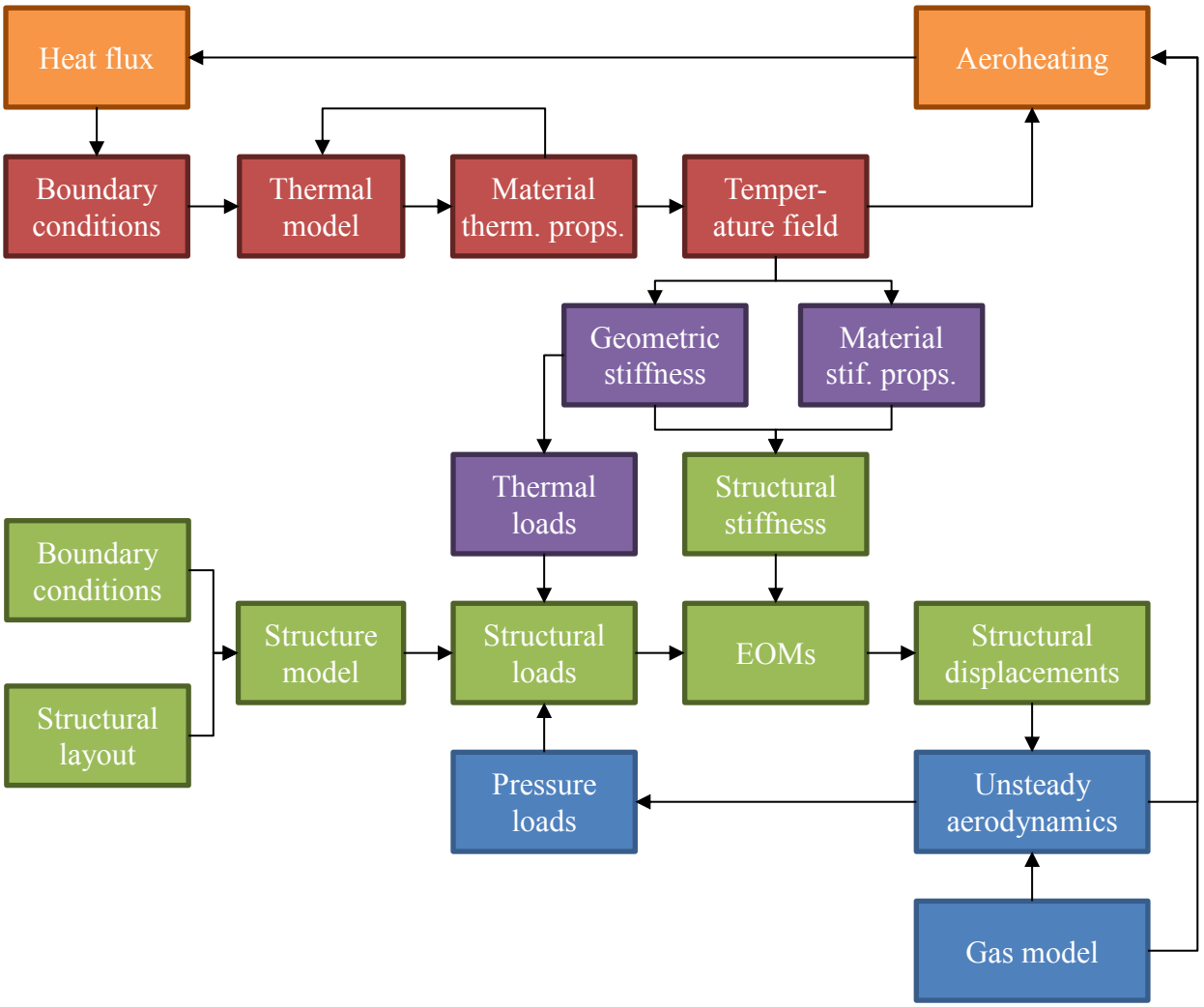

Figure 2.1: Information flow between aerothermoelastic disciplines

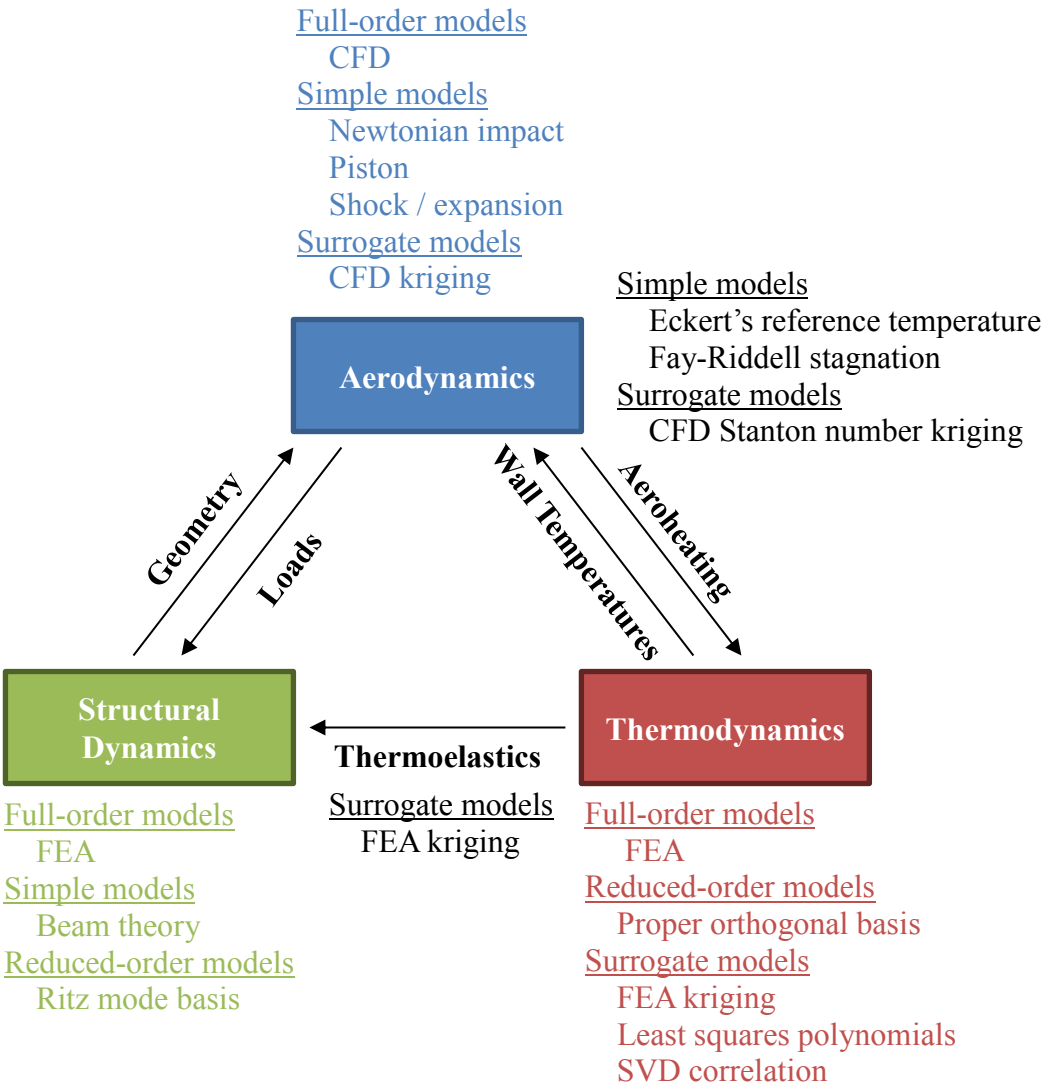

Figure 2.2: Collar's triangle of aerothermoelastic processes with related models

While it is possible to develop models for each discipline that apply to an entire vehicle, it may not be possible to emphasize the driving processes of a particular component of the vehicle without significantly increasing the numerical cost. Furthermore, not all models need be applied to all components, e.g. a thermoelastic model for a structure that does not experience significant temperature changes, a combustion model for a control surface, etc.

2.2 Partitioned Solution Approach

A primary feature of the simulation framework described in this thesis is the implementation of a partitioned approach to vehicle modeling and simulation. In this approach, a vehicle is divided into a number of different components with uncommon aerothermoelastic characteristics. A main body is chosen to provide a body-fixed frame for the flight mechanics portion of analysis. At predetermined time intervals, the motion of the main body is transferred to attached components. Each component's behavior is then integrated independently before forces and moments at the interfaces are transferred back to the main body as shown in Figure 2.3.

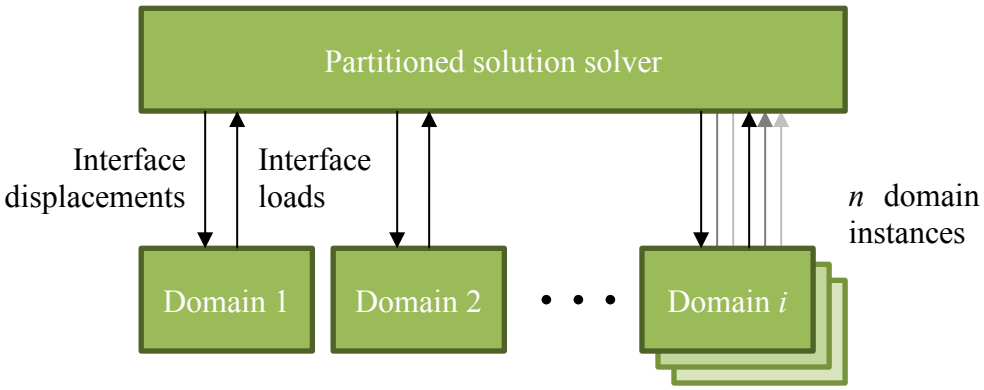

Figure 2.3: High-level overview of information exchange between partitioned domains

The partitioned approach removes the need to couple directly the models of each component and presents several advantages over a single monolithic vehicle model. Since each component may treat the other components as "black-boxes," the models used within each may be very different and tailored to best capture the relevant physics for that component. Physical processes that are unimportant for a particular component need not be modeled. Alternatively, processes that are the primary performance drivers may be emphasized with higher fidelity models or finer integration. Thus, the computational cost may be minimized while increasing overall fidelity.

Furthermore, the partitioned approach permits entire components to be exchanged, removed, or isolated without affecting the operability of the others. This enables fast trade studies for various component types and models of varying fidelity.

2.3 Model Reduction and Surrogate Techniques

In many cases, it is possible to reduce the order or number of degrees of freedom of a given dynamics formulation by identifying the underlying modes or trends of the system to be represented. This identification can be done through inspection of the dynamic equations, observation of the system behavior during integration, or some combination thereof. Once the dominant trends are determined, then they may be used to generalize the dynamic equations or used to fit some representative simple model.

2.3.1 Modal Basis Projection

Many dynamic systems may be represented in the form

$$M\ddot{x}(t) + C\dot{x}(t) + Kx(t) = F(t) \ , \tag{2.1}$$

where $x(t)$ is a column matrix of some degrees of freedom (DOFs) to be tracked over the integration of t, M is an inertial matrix which represents a systems resistance of changes to the DOF rates, C is a damping matrix which represents a systems resistance to the DOF rates, K is a stiffness matrix which represents how any one DOF influences the other DOFs, and F is some external forcing represented by a column matrix. In a full- or high-order system, there may be hundreds of thousands to millions of unique DOFs to consider, which cause matrices M, C, and

K to be prohibitively large for timely integration of the dynamics. However, in many cases, it is possible to identify or assume some basis set of vectors which approximates the DOFs as a sum of weighted mode shapes, i.e.,

$$x \approx \Phi \, \eta \left(t \right) \ , \tag{2.2}$$

where η are the mode shape weights which vary along t and Φ is a matrix whose columns are constant mode shapes, i.e.,

$$\Phi = \begin{bmatrix} \phi_1 & \phi_2 & \cdots & \phi_m \\ \vdots & \vdots & & \vdots \end{bmatrix} . \tag{2.3}$$

Critical to the reduction of the system is that the number of mode shapes m is significantly smaller than the number of DOFs initially considered. Substituting (2.2) into (2.1) and pre-multiplying by Φ^T yields

$$\Phi^T M \, \Phi \, \ddot{\eta} \left(t \right) + \Phi^T C \, \Phi \, \dot{\eta} \left(t \right) + \Phi^T K \, \Phi \, \eta \left(t \right) = \Phi^T F \left(t \right) \ . \tag{2.4}$$

Multiplication of the matrices then yields

$$\Phi^T M \, \Phi = m \ , \tag{2.5}$$

$$\Phi^T C \Phi = c \ , \tag{2.6}$$

$$\Phi^T K \Phi = k \ , \tag{2.7}$$

$$\Phi^T F(t) = f(t) \ , \tag{2.8}$$

where the number of entries in m, c, and k are significantly smaller than their full order counterparts and $f(t)$ represents generalized forces to the newly defined basis set. Pictorially this process is shown in Figure 2.4.

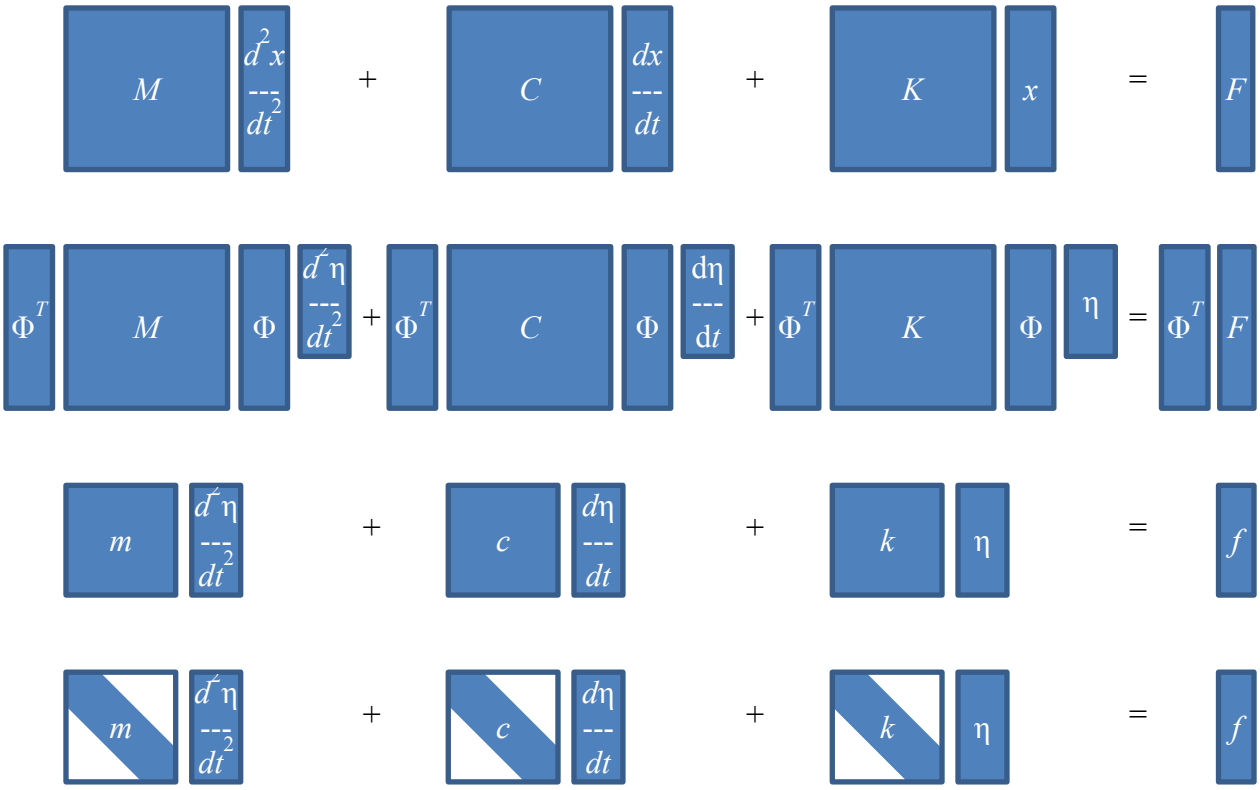

Figure 2.4: Visual representation of the reduction of system dynamics by modal projection

One may notice that in the fourth row of equation blocks in Figure 2.4, the generalized matrices have been diagonalized. This may be achieved by selection of orthogonal mode shapes for the basis set. This transforms the dynamic equations into a series of independent ordinary differential equations that can be easily processed compared to the full order, coupled equations. Selection of the appropriate basis set is highly dependent on the system that is to be represented and will be revisited in the following sections for the systems considered in this thesis.

2.3.2 Kriging

Kriging, sometimes called Gaussian process regression, is a statistical method for interpolating between *n*-dimension data samples through a combination of regression and correlation kernels.[138,139] It provides a flexible and computationally efficient approximation that is particularly suited to numerical experimentation, where there is no random perturbations to the samples, by maintaining the ability to exactly reproduce the data points to which the response surface was fitted.[140] A kriging model takes the form of

$$\hat{y}(b) = R_{krig}(b, X) + Z(b, X) , \tag{2.9}$$

where $\hat{y}$ is the kriging estimation of some output vector, b is a vector of inputs for the sought kriging estimation, R_{krig} is a chosen regression function, Z is a chosen correlation function, and X is a collection of training points to which the regression function was fitted and with which the correlation function weights determined. It is assumed that the underlying trends of the data

samples are determined by the regression function and that the mean error of the samples is zero about the fitted regression surface.[141] Error corrections are then applied to the regression surface by way of correlation functions local to each data sample. Many regression functions can be used, but in many applications are considered as polynomials. Similarly, there are a wide selection of correlation functions from which to choose. Popular methods include Gaussian, exponential, spherical, spline, and linear distributions. For further details on the fitting of the regression coefficients and optimization of the correlation weighting parameters, the reader is encouraged to review the work by Sacks, Welch, and Mitchell.[139] An interesting aside of the kriging method is that when the regression function is chosen to be a 0^{th}-order polynomial that produces a constant mean value of the data samples, then the method reduces to another popular interpolation method know as radial basis functions. In this case, the correlation functions serve as the radial basis kernels and their weighting parameters specify the kernels' range in the design space.

2.4 Aerodynamic Models

To determine the flow properties on the outer mold-line (OML) of a vehicle or body, an aerodynamic model is required. These models can range in fidelity and numerical cost from the simple and inexpensive Newtonian impact theory up to the expensive but accurate direct numerical simulation. Regardless of which aerodynamic model is used, the surface pressure, viscous traction, near-surface Mach number, and near-surface temperature must be determined. These flow properties will be used as the inputs to the thermodynamic and structural dynamic models described later in this chapter.

2.4.1 Newtonian Impact Theory

For high Mach numbers and sharp leading edged vehicles where the shock lies close to the OML, Newtonian impact theory may be used. The utility of Newtonian impact theory is derived from the simplicity of its formulation. That is, the pressure coefficient is a function only of the local surface geometry and freestream as

$$c_p = k\left(u \cdot \hat{n}\right)^2 , \tag{2.10}$$

where u is the freestream flow vector, $\hat{n}$ is the unit normal to the local surface, and the coefficient k is 2 in the classical Newtonian equation or the coefficient of pressure at the stagnation of the flow for a blunt body with a detached shock. However, this formulation only applies to surfaces that the flow can "see" and are not shadowed either by a surface upstream or on the leeward side of a body. For shadowed surfaces

$$c_p = 0 . \tag{2.11}$$

The local pressure of a surface is then

$$p = p_\infty + \frac{1}{2}\rho_\infty u^2 c_p , \tag{2.12}$$

where p_∞ and ρ_∞ are the freestream pressure and density respectively, and u is the magnitude of the freestream flow velocity.

2.4.2 Shock-Expansion Theory

For a planar panel exposed to a steady, inviscid, supersonic flow at an angle, θ, measured between the panel and freestream flow vector, there are four possible solution types for determining the flow conditions on the panel. These flow types are shown in Figure 2.5.

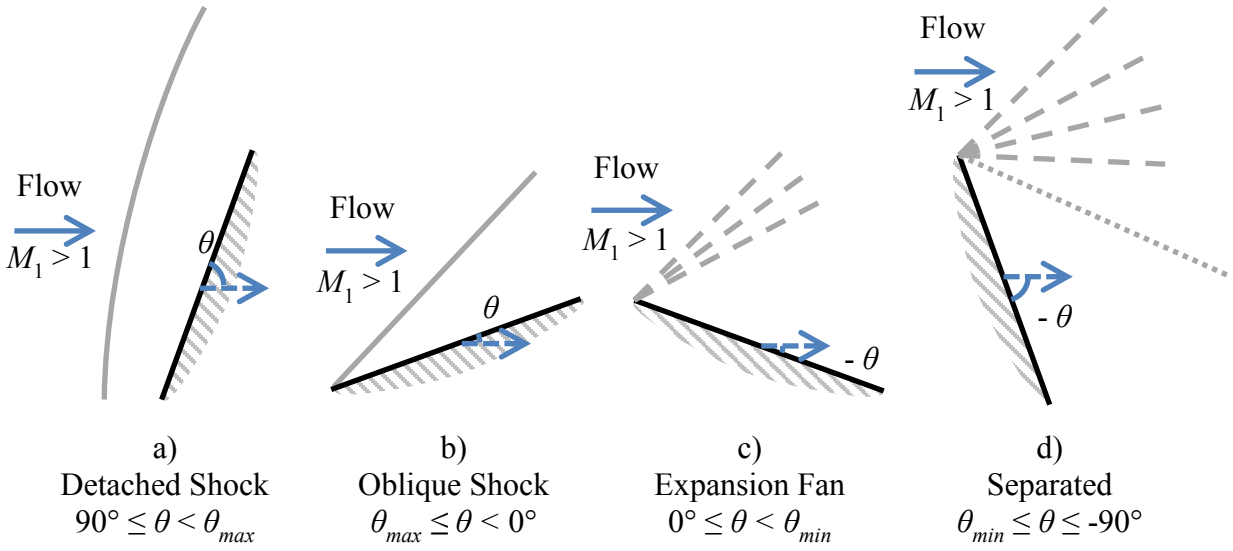

Figure 2.5: Panel flow solution types

The first flow type is a detached shock, shown in Figure 2.5 a, which occurs when the deflection angle, θ, is between 90° and a maximum deflection angle, θ_{max}, determined by[1]

$$\theta_{max} = \tan^{-1}\left[\frac{2\cot(\beta_{max})\left(M_1^2 \sin^2 \beta_{max} - 1\right)}{M_1^2\left(\gamma + \cos 2\beta_{max}\right) + 2}\right], \tag{2.13}$$

where

$$\beta_{max} = \sin^{-1} \sqrt{\frac{bM_1^2 - 4 + c}{a}} \quad , \tag{2.14}$$

where

$$a = 4M_1^2 \gamma \quad , \tag{2.15}$$

$$b = \gamma + 1 \quad , \tag{2.16}$$

$$c = \sqrt{\left\{16 + M_1^2 \left[8(\gamma - 1) + M_1^2 b\right]\right\}} \quad , \tag{2.17}$$

where β_{max} is the maximum attached shock wave angle, M_1 is the Mach number upstream of the panel, and γ is the ratio of specific heats. To determine the ratio of conditions pre- and post-shock, one first determines the wave angle by

$$\beta = \beta_{max} + (\theta - \theta_{max}) \frac{\frac{\pi}{2} - \beta_{max}}{\pi - \theta_{max}} \quad . \tag{2.18}$$

Then the Mach number upstream and normal to the shock wave, M_{1_n}, is determined by

$$M_{1_n} = M_1 \sin \beta \quad . \tag{2.19}$$

Using the normal shock relations, the ratios of the conditions pre- and post-shock are found to be

$$\frac{p_2}{p_1} = \frac{2\gamma M_{1_n}^2 - (\gamma - 1)}{\gamma + 1} \ , \tag{2.20}$$

$$\frac{\rho_2}{\rho_1} = \frac{(\gamma + 1) M_{1_n}^2}{(\gamma - 1) M_{1_n}^2 + 2} \ , \tag{2.21}$$

$$\frac{T_2}{T_1} = \frac{p_2 / p_1}{\rho_2 / \rho_1} \ . \tag{2.22}$$

The second flow type is an oblique shock, shown in Figure 2.5 b, which occurs when the deflection angle, θ, is between a maximum deflection angle, $\theta_{\max}$, determined by (2.13) and 0°. To determine the ratios of conditions, one again first determines the wave angle approximated by the root of[142]

$$X^3 + bX^2 + cX + d = 0 \ , \tag{2.23}$$

where

$$X \equiv \sin^2 \beta \ , \tag{2.24}$$

$$b = -\left[\frac{M_1^2 + 2}{M_1^2} + \gamma \sin^2\theta\right], \tag{2.25}$$

$$c = \frac{2M_1^2 + 1}{M_1^4} + \left[\frac{(\gamma+1)^2}{4} + \frac{\gamma - 1}{M_1^2}\right]\sin^2\theta, \tag{2.26}$$

$$d = -\frac{\cos^2\theta}{M_1^4}. \tag{2.27}$$

As (2.23) is a cubic polynomial, it is expected that three roots exist. Of these roots, there is a complex pair and two real solutions. The complex pair solution is nonphysical. The greater real solution corresponds to the strong shock angle that manifests when the backpressure following the shock is unusually high. One takes the lesser real solution corresponding to the weak shock angle which is typical of supersonic flow on the outer surface of a vehicle. With the wave angle, β, determined, (2.19), (2.20), (2.21), and (2.22) may be used to determine the ratios of flow properties across the shock.

The third flow type is an expansion fan, shown in Figure 2.5 c, which occurs when the deflection angle, θ, is between 0° and minimum deflection angle, $\theta_{\min}$, determined by

$$\theta_{\min} = \nu(M_1) - \nu_{\min}, \tag{2.28}$$

where

$$\nu(M) = \sqrt{\frac{\gamma+1}{\gamma-1}}\tan^{-1}\sqrt{\frac{\gamma-1}{\gamma+1}\left(M^2-1\right)} - \tan^{-1}\sqrt{M_2-1}\ , \tag{2.29}$$

$$\nu_{\min} = \frac{\pi}{2}\left(\sqrt{\frac{\gamma+1}{\gamma-1}}-1\right)\ , \tag{2.30}$$

To determine the ratio of flow properties across the expansion fan, one determines the Mach number, M_2, following the expansion using

$$\theta = \nu(M_1) - \nu(M_2)\ , \tag{2.31}$$

where the Prandtl-Meyer function, $\nu(\ )$, is given in (2.29). Since a flow expansion is isentropic, once the post-expansion Mach number, M_2, is known, the isentropic relations yield

$$\frac{p_2}{p_1} = \left[\frac{1+\frac{\gamma-1}{2}M_1^2}{1+\frac{\gamma-1}{2}M_2^2}\right]^{\frac{\gamma}{\gamma-1}}\ , \tag{2.32}$$

$$\frac{\rho_2}{\rho_1} = \left[\frac{1+\frac{\gamma-1}{2}M_1^2}{1+\frac{\gamma-1}{2}M_2^2}\right]^{\frac{1}{\gamma-1}}\ , \tag{2.33}$$

$$\frac{T_2}{T_1} = \frac{1 + \frac{\gamma - 1}{2} M_1^2}{1 + \frac{\gamma - 1}{2} M_2^2} \,. \tag{2.34}$$

The fourth flow type is separated flow, shown in Figure 2.5 d, which occurs when the deflection angle, θ, is less than the minimum deflection angle, $\theta_{\min}$, determined by (2.28). In this scenario, the supersonic flow is unable to expand quickly enough to remain flush with the panel and instead juts off at an angle equal to the minimum deflection angle, $\theta_{\min}$. The region in contact with the panel is typically highly turbulent and low pressure. Accurate description of this region is beyond the scope of the basic engineering theory used in this section. Thus it is assumed that in regions of supersonically separated flow, the pressure, p_2, temperature, T_2, and density, ρ_2, are zero.

2.4.3 Piston Theory

The term "piston theory", as used in this section, refers to any method for calculating the aerodynamic loads in which the local pressure generated by the body's motion is related to the local normal component of fluid velocity in the same way these quantities are related at the face of a piston moving in a one-dimensional channel. In general, piston theory may be employed for high flight Mach numbers or high reduced-frequencies of unsteady motion, whenever the surface involved is nearly a plane and not inclined too sharply to the direction of the free stream. The foregoing shape conditions are fulfilled by all but the immediate tip (and possibly leading edge) regions of most supersonic wings. In most aeronautical applications, the normal component of fluid velocity is the given quantity and the surface pressure is the unknown to be determined, so

that a point-function relationship between the two is a great convenience. These observations, coupled with the fact that arbitrary small deformations and arbitrary time-dependent unsteady motions can be taken into account, make piston theory a powerful tool for analyzing high-speed problems.

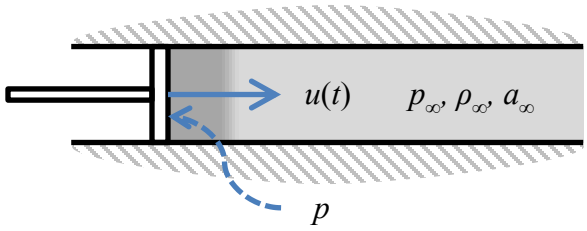

Figure 2.6: Piston in a one-dimensional channel

Figure 2.6 depicts a piston moving with velocity $u(t)$ in the end of a channel containing perfect gas, whose undisturbed pressure, density, and speed of sound are p_∞, ρ_∞, and a_∞. Provided that the piston generates only simple waves, the darkly shaded region of Figure 2.6, and produces no entropy change, the exact solution for the instantaneous pressure, $p(t)$, on its face is[24]

$$\frac{p}{p_\infty} = \left[1 + \frac{\gamma - 1}{2}\frac{u}{a_\infty}\right]^{\frac{2\gamma}{\gamma - 1}} . \qquad (2.35)$$

Depending on the magnitude of the ratio, u / a_∞, (2.35) may be approximated by the linear relation

$$p - p_\infty = \rho_\infty a_\infty u \quad , \tag{2.36}$$

by its second-order binomial expansion

$$p - p_\infty = \rho_\infty a_\infty^2 \left[\frac{u}{a_\infty} + \frac{\gamma + 1}{4} \left(\frac{u}{a_\infty} \right)^2 \right] , \tag{2.37}$$

or by its third-order expansion

$$p - p_\infty = \rho_\infty a_\infty^2 \left[\frac{u}{a_\infty} + \frac{\gamma + 1}{4} \left(\frac{u}{a_\infty} \right)^2 + \frac{\gamma + 1}{12} \left(\frac{u}{a_\infty} \right)^3 \right] . \tag{2.38}$$

Reasoning from a suggestion by Hayes,[143] Lighthill[144] pointed out that (2.38) can be used with excellent accuracy even under non-isentropic conditions to calculate the pressure on an airfoil in steady or unsteady motion whenever the flight Mach number has such an order of magnitude that $M^2 \gg 1$. An additional limitation is that the product of $M\delta$ cannot be too large, where δ is the thickness ratio of the airfoil or the ratio of the maximum amplitude of unsteady motion to airfoil chord length.

At hypersonic flight speeds, one can imagine a column of air passing over a sharp edged, narrow-bodied vehicle as remaining essentially intact, providing an analog to the one-dimensional channel of air. The boundary of the vehicle then acts as the piston face advancing into and retreating from the flow.

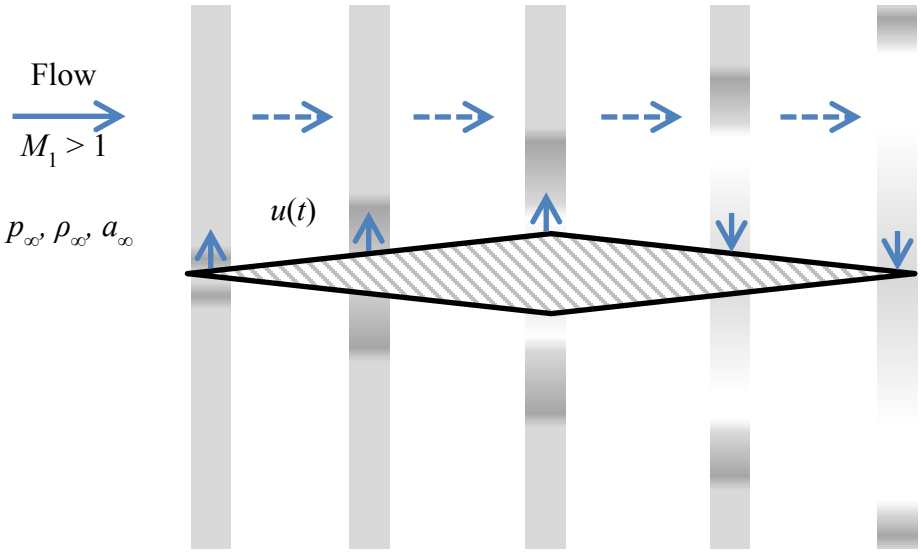

Figure 2.7: Shaded columns of air as they flow past a slender body

Figure 2.7 depicts a hypersonic diamond airfoil passing through a series of air columns. As the airfoil presses into each column, a darkly shaded compression wave is formed and moves along the air column. After mid-chord, the airfoil retreats from the column and a lightly shaded set of expansion waves are formed and also move along the air column. The speed, w, which the airfoil surface moves into the air columns is

$$w = M_1 a_\infty \tan^{-1}\theta + u_u \quad , \tag{2.39}$$

where θ is the deflection angle due to an inclined surface and u_u is any unsteady motion of the surface due to vibration, vehicle maneuvers, etc., which is handled on a case-by-case basis depending on the type of analysis performed. The local surface pressures can then be solved using (2.38). Note that a sharply inclined surface, such that the piston speed is greater than or equal to

the speed of sound, $w \geq a_\infty$, exceeds the scope of piston theory since it is assumed that only simple waves are generated.

2.4.4 Shock-Expansion Theory with Unsteady Piston Theory Correction

To overcome the limitation of piston theory for a steeply inclined panel whose normal velocity component exceeds the speed of sound or highly unsteady motions where u_u of (2.39) exceeds the speed of sound, a combination of the shock-expansion theory previously described and an unsteady correction term derived from piston theory may be used. Given a planar surface inclined to a supersonic flow, one of the four shock-expansion scenarios previously described and shown in Figure 2.5 will exist and may be used to determine a steady component of the aerodynamic pressure on the surface. In all scenarios except the separated flow, where the speed of sound at the surface is undefined due to the lack of medium, once the flow is processed by the leading shock or expansion, piston theory may be applied given the local speed of sound and density as shown in Figure 2.8.

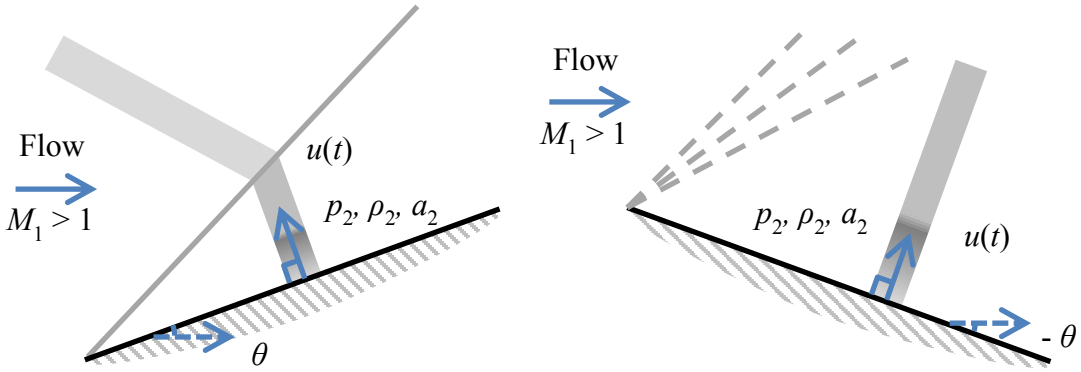

a) Steady Shock with Unsteady Piston Correction

b) Steady Expansion with Unsteady Piston Correction

Figure 2.8: Steady shock and expansion scenarios with unsteady piston theory corrections

To determine the steady component of the pressure and local flow conditions, one of the following equation sets in Table 2.1 are used.

Table 2.1: Equation sets to determine steady pressure and surface local flow properties

Scenario	Equations
Detached shock $(90° \le \theta < \theta_{max})$	(2.14), (2.20), (2.21), and (2.22)
Oblique shock $(\theta_{max} \le \theta < 0°)$	(2.23), (2.20), (2.21), and (2.22)
Expansion fan $(0° \le \theta < \theta_{min})$	(2.31), (2.32), (2.33), and (2.34)

Once the steady component of the pressure is determined, (2.38) may be modified slightly to[40]

$$\Delta p_2 = \rho_2 a_2^2 \left[\frac{u}{a_2} + \frac{\gamma + 1}{4} \left(\frac{u}{a_2} \right)^2 + \frac{\gamma + 1}{12} \left(\frac{u}{a_2} \right)^3 \right], \tag{2.40}$$

where ρ_2 and a_2 are the local flow density and speed of sound respectively after the flow is processed by the leading edge wave system. The local speed of sound, a_2, is determined by

$$a_2 = \sqrt{\gamma R T_2}, \tag{2.41}$$

where $\gamma = 1.4$ is the ratio of specific heats for air as an ideal gas, but approaches 1 when real gas effects are taken into account, and $R = 287.1$ J/kg/K is the specific gas constant for air, but may also change if dissociation and ionization modify the flow species interacting with the surface. The overall pressure on the surface accounting for both steady and unsteady effects is then

$$p_{2,overall} = p_1 \left(\frac{p_2}{p_1} \right) + \Delta p_2 \ , \tag{2.42}$$

2.5 Aerodynamic Heating Models

Once the surface flow conditions are determined by the aerodynamic models and the temperature of the vehicle OML is known or assumed, the surface heat flux may be determined. Two primary regions of a given vehicle often require unique aerodynamic heating models. The first region is the stagnation point and is usually where the greatest heat flux is experienced. Here the flow is processed by a nearly normal shock wave close to the surface of the vehicle, creating a nonequilibrium flow, meaning that flow chemistry is particularly important. The second region is the bulk of the body, where the flow direction is nearly parallel to OML in any given location. Here the behavior of the boundary layer is most important and governs the heat flux to the OML.

2.5.1 Eckert Reference Temperature

With the Eckert reference temperature method, variations in the flow properties across a boundary layer are accounted for by a reference temperature which is used to determine integrated properties through the thickness of the boundary layer. The precise profile of the properties cannot be determined with this method, but this approach has been shown to provide surface quantities such as skin friction and heat transfer with acceptable accuracy.[145]

To begin, the static pressure p, Mach number M, and static temperature T local to each panel of the OML is determined from the aerodynamics model any time the surface heat flux is required. These values are treated as the outer flow conditions of a turbulent boundary layer. A

turbulent boundary layer is assumed due to the yet unknown transition characteristics of the flow, and thus provided a worse-case scenario for the heat transfer. This lead to a recovery factor of

$$r_f = \mathrm{Pr}^{1/3} , \tag{2.43}$$

where Pr is the Prandtl number which is assumed to be constant at 0.7. By definition, the recovery temperature is

$$T_r = r_f \left(T_0 - T \right) + T , \tag{2.44}$$

which allowed Eckert's reference temperature to be found as

$$T^* = T + 0.5 \left(T_w - T \right) + 0.22 \left(T_r - T \right) , \tag{2.45}$$

where T_w is the local wall temperature on the OML. The reference boundary layer flow properties are

$$\rho^* = \frac{p}{R T^*} , \tag{2.46}$$

$$\mu^* = \mu_{ref} \frac{T_{ref} + S}{T^* + S} \left(\frac{T^*}{T_{ref}} \right)^{3/2} , \tag{2.47}$$

$$\mathrm{Re}^* = \frac{\rho^* u x}{\mu^*} \,. \tag{2.48}$$

Here the reference density ρ^* is found using the ideal gas law. The reference dynamic viscosity μ^* is found using Sutherland's law of viscosity with Sutherland's reference temperature $T_{ref} = 288\ \mathrm{K}$ and Sutherland's constant for air $S = 110\ \mathrm{K}$. The reference Reynolds number Re^* is then determined by definition using the local steady flow velocity u outside of the boundary layer and distance along the body from the stagnation point, x. The coefficient of skin friction was then determined by the Blasius relation for $\mathrm{Re}^* \le 4.56 \times 10^6$,[146]

$$c_f = \frac{0.0592}{\left(\mathrm{Re}^*\right)^{0.2}} \,, \tag{2.49}$$

and the Schultz-Grunow equation[147] for $\mathrm{Re}^* > 4.56 \times 10^6$,

$$c_f = \frac{0.37}{\left(\log_{10} \mathrm{Re}^*\right)^{2.584}} \,. \tag{2.50}$$

The recommended Reynolds number to transition between the skin friction models is 10^7 by Arthur, Schultz, and Guard,[147] however for the work presented in this thesis, this threshold is adjusted to have a continuous transition between the models. Both models are necessary since a vehicle 1 to 10 meters in length, traveling at low hypersonic velocities, and stratospheric altitudes

will encounter Reynolds numbers on the orders of 10^6 to 10^8. The Stanton number is determined by the Colburn-Reynolds analogy,

$$\mathrm{St} = k \frac{c_f}{2} \mathrm{Pr}^{-2/3} , \tag{2.51}$$

where k is a geometry dependent coefficient. For a flat plate $k = 1$, and for a cone $k = 1.28$, as shown by Young and Van Driest.[148] The heat transfer coefficient can be found from the definition of the Stanton number

$$c_h = \mathrm{St}\, c_p \rho^* u , \tag{2.52}$$

where the constant pressure specific heat capacity c_p can be found using the simple harmonic vibrator model for air

$$c_p = \left(c_p\right)_{perf} \left\{ 1 + \frac{\gamma - 1}{\gamma} \left[\left(\frac{\Theta}{T^*} \right)^2 \frac{\exp\left(\Theta / T^*\right)}{\left(\exp\left(\Theta / T^*\right) - 1\right)^2} \right] \right\} , \tag{2.53}$$

where $\left(c_p\right)_{perf} = 1006 \text{ J/K/kg}$ is the constant pressure specific heat capacity of calorically perfect air and $\Theta = 2778 \text{ K}$ is the characteristic temperature of the diatomic vibrational mode of air. Finally, the heat flux to the surface is given by

$$q = c_h \left(T_r - T_w \right) + \sigma \varepsilon \left(T_\infty{}^4 - T_w{}^4 \right) \text{ ,} \tag{2.54}$$

where $\sigma = 5.6704 \times 10^{-8}$ W/m^2/K^4 is the Stefan-Boltzmann constant, ε is the emissivity of the surface material, and T_∞ is the far-field freestream temperature from the 1976 standard atmospheric model,[149] thus accounting for the conductive and radiative heat transfer.

2.5.2 Fay-Riddell Stagnation Heating

While the Eckert reference temperature method is well suited for regions of the vehicle where the flow is nearly parallel to the surface, it fails to provide accurate heat flux estimates when the surface is steeply inclined to the flow, such as around the stagnation point and on the leading edges of wings. In these regions, it is considerably better to use the Fay-Riddell heat flux equation.[150,151]

To begin, one must first determine if the flow near the stagnation point is frozen or at equilibrium. It is very likely that the flow is in neither of these conditions, but solution to a non-equilibrium flow that has only partially relaxed its energy modes is beyond the scope of this simple formulation. To determine the flow properties just beyond the shock if the flow is considered frozen, the normal shock relations of (2.14), (2.20), (2.21), and (2.22) may be used. If the flow is considered to be at equilibrium, then the post-shock temperature T_2 may be used as an initial guess to a convergence problem match the flow enthalpy h, which is conserved across the shock, since the pressure-specific heat capacity c_p is a function of temperature T_2, i.e.,

$$h = c_p(T_2)T_2 \ . \tag{2.55}$$

The NASA thermodynamic coefficients data tables[152] may be used to approximate the heat capacity as

$$c_p = \frac{1000R_u\left[o_1T_2^{-2} + o_2T_2^{-1} + o_3 + o_4T_2 + o_5T_2^{2} + o_6T_2^{3} + o_7T_2^{4}\right]}{M_W} \ , \tag{2.56}$$

where R_u is the universal molar gas constant, each o is an empirical coefficient from the NASA data tables,[152] and M_W is the molecular weight of the gas species. Once T_2 and c_p have been determined, other post-shock flow properties may be determined by

$$\gamma_2 = \frac{c_p}{c_p - R} \ , \tag{2.57}$$

$$a_2 = \sqrt{\gamma_2 R T_2} \ , \tag{2.58}$$

$$u_2 = \frac{u_1\rho_1}{\rho_2} \ , \tag{2.59}$$

$$M_2 = \frac{u_2}{a_2} \ . \tag{2.60}$$

The stagnation properties are then determined by the isentropic relations, i.e.,

$$\rho_0 = \rho_2 \left(1 + \frac{\gamma_2 - 1}{2} M_2^2 \right)^{\frac{1}{\gamma_2 - 1}} , \tag{2.61}$$

$$T_0 = T_2 \left(1 + \frac{\gamma_2 - 1}{2} M_2^2 \right) , \tag{2.62}$$

$$p_0 = p_2 \left(1 + \frac{\gamma_2 - 1}{2} M_2^2 \right)^{\frac{\gamma_2}{\gamma_2 - 1}} . \tag{2.63}$$

Sutherland's formula (2.47) is then used to determine the stagnation flow viscosity μ_0 and wall flow viscosity μ_w using the stagnation temperature T_0 and wall temperature T_w, respectively. The density of the flow at the wall is then determined by

$$\rho_w = \frac{p_2}{R T_w} , \tag{2.64}$$

Next, the flow velocity gradient near the stagnation point is assumed to be the modified Newtonian flow solution over a hemisphere, i.e.,

$$\frac{du}{dx} = \frac{1}{r} \sqrt{\frac{2 (p_0 - p_2)}{\rho_0}} , \tag{2.65}$$

where r is the radius of the hemisphere. Finally, the Fay-Riddell heat flux equation is used to determine the heat flux as[153]

$$q = \frac{0.763}{\mathrm{Pr}^{0.6}}\left(\rho_w \mu_w\right)^{0.1}\left(\rho_0 \mu_0\right)^{0.4}\left[1+\left(L^{0.54}-1\right)\frac{h_D}{h_0}\right]\left(h_0 - h_w\right)\sqrt{\frac{du}{dx}}\ , \tag{2.66}$$

where the Fay-Riddell Lewis number is assumed $L = 1$ for an atom-molecule mixture and the dissociation enthalpy is taken to be $h_D = 24.657$ MJ/kg for air.

2.5.3 Stanton Number Kriging

When the properties of the flow and surface temperatures are known over a body, the Stanton number St may be used to determine the surface heat flux due to aerodynamic heating q_{aero} by[154]

$$q_{aero}\left(x,y,t\right) = c_p u_\infty \rho_\infty \mathrm{St}\left(x,y,t\right)\left[T_w\left(x,y,t\right) - T_0\right]\ , \tag{2.67}$$

where c_p is the constant pressure heat capacity, u_∞ is the freestream velocity, ρ_∞ is the freestream density of the flow, T_w is if the surface temperature of the body, and T_0 is the total temperature of the flow. To model the Stanton number, the work of Crowell and McNamara[155] is considered, in which a kriging surrogate model is trained on CFD solution samples.

A flowchart of the process used to model steady CFD data is provided in Figure 2.9. First, the input parameters and bounds for the steady model are established. Latin hypercube sampling

(LHS) is then used to identify a diverse set of sampling points. Next $n + K$ sample aerothermodynamic responses are computed from CFD solutions to the Navier-Stokes equations at each of the sample points; n sample points for model construction, and K sample points for evaluation. If further accuracy is desired, more sample responses are added and the process is repeated.

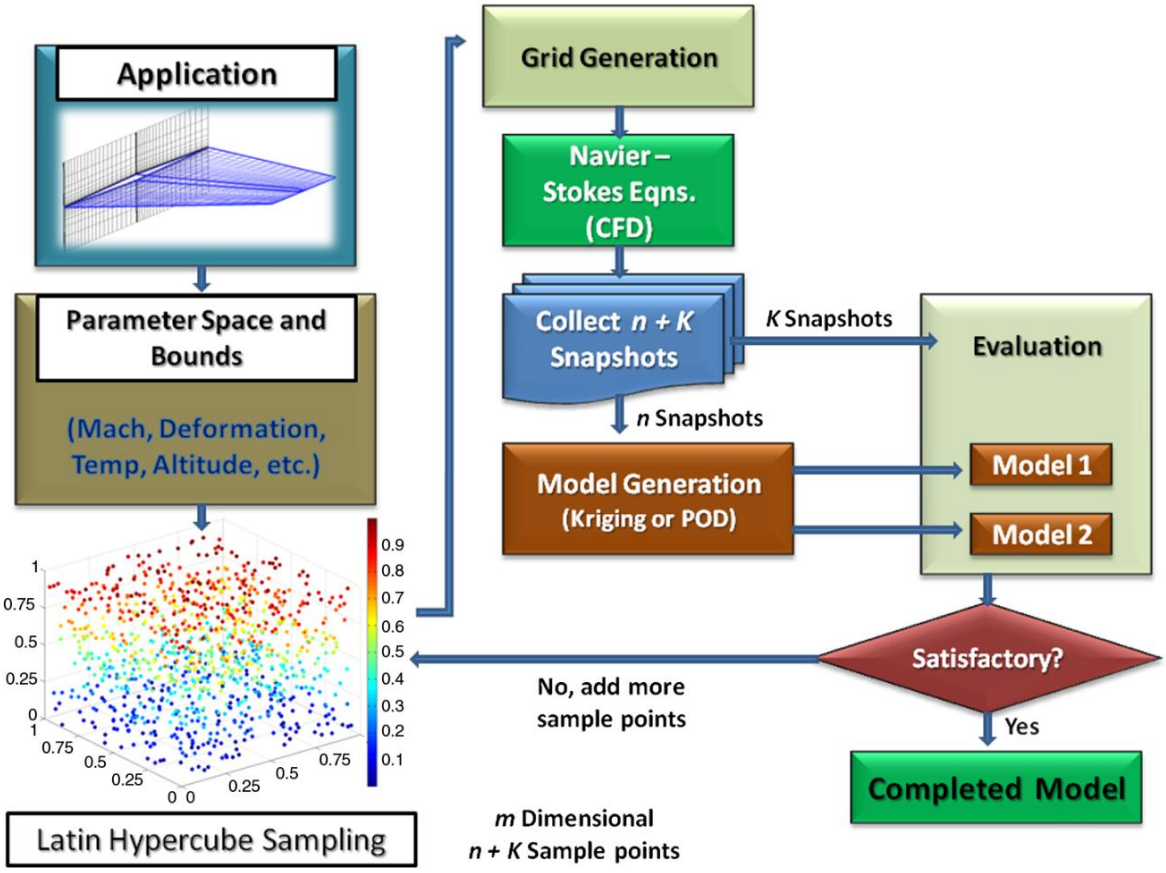

Figure 2.9: Schematic of the process for modeling steady CFD data[155]

2.6 Thermal Models

The heat flux on the OML serves as the boundary conditions to the heat transfer problem in which the internal temperature distribution of a structure is determined. The method of finite

elements is the standard approach to solving for the internal temperature, but can be too computationally costly to perform quickly for a realistic structure. In this section, model reduction techniques are described to simplify the governing equations while sacrificing as little accuracy as possible. The nonlinear effects of temperature dependent material properties are also considered.

2.6.1 Thermal Basis Identification

To reduce the order of the thermal model, the work of Falkiewicz and Cesnik[35] is considered which expresses the temperature distribution of the vehicle structure as the sum of a small number of basis vectors multiplied by time varying coefficients, i.e.,

$$\begin{Bmatrix} T_1 \\ \vdots \\ T_s \end{Bmatrix} = c_1(t)\begin{Bmatrix} \phi_1^{(1)} \\ \vdots \\ \phi_s^{(1)} \end{Bmatrix} + c_2(t)\begin{Bmatrix} \phi_1^{(2)} \\ \vdots \\ \phi_s^{(2)} \end{Bmatrix} + \cdots + c_r(t)\begin{Bmatrix} \phi_1^{(r)} \\ \vdots \\ \phi_s^{(r)} \end{Bmatrix}, \tag{2.68}$$

where T_i is the temperature of the *i*th of *s* nodes in the structure model, $c_j(t)$ is the *j*th of *r* time-varying coefficients of the thermal basis vectors, and $\phi_i^{(j)}$ is the *i*th entry of the *j*th thermal basis vector. To determine the thermal basis vectors ϕ, the method of snapshots is used. With the method of snapshots, a high-fidelity thermal model is simulated using finite element analysis (FEA) software. Given a surface heat flux derived from the aerodynamic and aeroheating models, a transient heat transfer solver can be used to simulate the thermal state forward in time. Snapshots of the temperature of each node in the finite element model (FEM) are taken at prescribed time intervals and used to form the snapshot matrix

$$A = \begin{bmatrix} T_1^{(1)} & T_1^{(2)} & \cdots & T_1^{(n)} \\ T_2^{(1)} & T_2^{(2)} & \cdots & T_1^{(n)} \\ \vdots & \vdots & \ddots & \vdots \\ T_s^{(1)} & T_s^{(2)} & \cdots & T_s^{(n)} \end{bmatrix}, \tag{2.69}$$

where each column is a vector of the FEM nodal temperatures at a single moment in the simulation, $T_i^{(j)}$ is the *i*th of *s* node temperatures at the time the *j*th of *n* snapshots of the thermal state. A correlation matrix C, is then formed from the snapshot matrix A as

$$C = \frac{1}{n} A^T A \ . \tag{2.70}$$

The eigenvectors and eigenvalues of the covariance matrix C are found from

$$Cs = \lambda s \ , \tag{2.71}$$

where s is a matrix whose columns are the eigenvectors corresponding to the entries of the diagonal matrix λ which contains the eigenvalues of C arranged in decreasing magnitude. The thermal basis vectors are then determined as

$$\phi_k = \frac{1}{\sqrt{n\lambda_k}} A s_k \ . \tag{2.72}$$

where ϕ_k is the *k*th thermal basis vector, *n* is the number of snapshots originally taken, λ_k is the *k*th diagonal entry of the eigenvalue matrix, and s_k is the *k*th column of the eigenvector matrix. Arranging the base thermal modes as the columns of a matrix gives the thermal basis matrix, Φ ,

$$\Phi = \begin{bmatrix} \phi_1^{(1)} & \cdots & \phi_1^{(n)} \\ \vdots & \ddots & \vdots \\ \phi_s^{(1)} & \cdots & \phi_s^{(n)} \end{bmatrix} = [\phi_1, \ldots, \phi_n] \ . \tag{2.73}$$

Note that *n* thermal basis vectors are determined since *n* thermal snapshots were considered by the snapshot matrix. With this thermal basis matrix, the snapshot matrix may be reproduced exactly as[72]

$$A = \Phi \eta \ , \tag{2.74}$$

where η is an *n*-dimensional square matrix of coefficients of the thermal basis vectors ϕ_k which, when summed, reproduce the thermal state at that time. Thus, row *k* of η is a time history of the magnitude of basis ϕ_k during simulation at each of the original snapshots.

To reduce the order of the thermal basis matrix, consider that λ_1 is the largest magnitude eigenvalue and thus ϕ_1 contains the most dominant thermal basis. Correspondingly, λ_n was the smallest magnitude eigenvalue and ϕ_n contains the least dominant thermal basis. Truncating the thermal basis matrix by removing the least dominant thermal modes allows one to reduce the number of thermal degrees of freedom while preserving the most dominant features of the thermal state,

$$\Psi = \begin{bmatrix} \phi_1^{(1)} & \cdots & \phi_1^{(m)} \\ \vdots & \ddots & \vdots \\ \phi_s^{(1)} & \cdots & \phi_s^{(m)} \end{bmatrix} = \left[\phi_1, \ldots, \phi_m \right] \; ; \; m < n \; , \tag{2.75}$$

where Ψ is the truncated thermal basis matrix. By truncating the thermal basis, one loses the ability to reproduce exactly the snapshot matrix. However, the snapshot matrix can still be approximated by

$$A \approx \Psi c \; , \tag{2.76}$$

where c is now an *m* by *n* matrix of the coefficients of the truncated thermal basis vectors. The error incurred by truncation of the thermal basis matrix may be interpreted as the relative energy lost ε_{rel} by projecting the snapshot matrix A of *n* dimension onto the *m* dimensional space spanned by the truncated thermal basis matrix Ψ, given by[156]

$$\varepsilon_{rel} = \frac{\left\| A - \Psi \Psi^T A \right\|^2}{\left\| A \right\|^2} \; . \tag{2.77}$$

2.6.2 Generalization of the Thermal Problem

Once an appropriate thermal basis is determined, one may generalize the governing system of equations for the thermal problem

$$M\left(T\left(t\right)\right)\dot{T}\left(t\right)+K\left(T\left(t\right)\right)T\left(t\right)=F\left(t\right)\ , \tag{2.78}$$

into

$$m\left(c\left(t\right)\right)\dot{c}\left(t\right)+k\left(c\left(t\right)\right)c\left(t\right)=f\left(t\right)\ , \tag{2.79}$$

where

$$m\left(c\left(t\right)\right)=\Psi^{T}M\left(\Psi c\left(t\right)\right)\Psi\ , \tag{2.80}$$

$$k\left(c\left(t\right)\right)=\Psi^{T}K\left(\Psi c\left(t\right)\right)\Psi\ , \tag{2.81}$$

$$f\left(t\right)=\Psi^{T}F\left(t\right)\ , \tag{2.82}$$

and where $M\left(T\right)$ and $K\left(T\right)$ are the thermal capacity and conductivity matrices, each a function of the time varying temperature vector $T\left(t\right)$, and $F\left(t\right)$ is the time varying thermal load vector.

2.6.3 Numerical Integration

To numerically integrate the generalized thermal problem forward at discrete times t_n and t_{n+1}, separated by the time interval Δt, the Crank-Nicolson algorithm is considered due to its known unconditional stability for both linear and nonlinear heat conduction systems.[157] This results in

$$c\left(t_{n+1}\right)=\left[\frac{k}{2}+\frac{m}{\Delta t}\right]^{-1}\left\{\left[-\frac{k}{2}+\frac{m}{\Delta t}\right]c\left(t_{n}\right)+\frac{f\left(t_{n}\right)+f\left(t_{n+1}\right)}{2}\right\}\ . \tag{2.83}$$

2.7 Structural Dynamics Models

A variety of reduced structural model methods are described which together fit the framework of a partitioned approach to simulating structural dynamics. Elastic equations of motion for free-free and displacement driven structures are generalized by modal bases.

2.7.1 Ritz Modes Generalization of Free Structures

Application of the partitioned approach creates two distinct types of elastic model requirements. For the main body, the elastic model is a free structure that will have forces imposed upon it by the interfaces to the sub-bodies, aerodynamic pressures, and thermal stresses. To reduce the order of a free structural model, the structural equations of motion may be generalized by a basis of assumed mode shapes. These shape bases are often composed of free-vibration modes and can be enhanced by including static loading shapes which capture deformation due to specific loading conditions of interest[36] or higher-order mode shapes which capture geometric nonlinearities.[158–160] Consider the undamped full-order structural dynamic equations

$$M\ddot{x}\left(t\right)+Kx\left(t\right)=F\left(t\right)\ , \tag{2.84}$$

where M is the mass matrix, K is the stiffness matrix, F is the load vector, $x(t)$ are the physical degrees of freedom, and t is time. The free-vibration mode shapes may be determined from the solution of the eigenproblem

$$\left(-\omega_j^2 M + K\right)\xi_j = 0 \ , \tag{2.85}$$

where ω_j is the frequency and ξ_j is the corresponding j^{th} mode. Truncation of the shape bases is carried out by excluding modes outside of some frequency range of interest. The physical degrees of freedom are then expressed as a linear combination of these modes such that

$$x(t) = \begin{bmatrix} \xi_1 & \cdots & \xi_n \\ \vdots & \cdots & \vdots \end{bmatrix} d(t) = \Phi\, d(t) \ , \tag{2.86}$$

where Φ is the modal matrix whose columns are the mode shape column vectors ξ. Substituting (2.86) into (2.84) and pre-multiplying by Φ^T yields

$$\Phi^T M \Phi \ddot{d}(t) + \Phi^T K \Phi\, d(t) = \Phi^T F(t) \ , \tag{2.87}$$

$$m\ddot{d}(t) + k_S d(t) = f(t) \ , \tag{2.88}$$

where the modal terms m, k, and f have lower rank compared to their full-order counterparts.

2.7.2 Displacement Driven Structures

The second elastic model requirement created by the application of the partitioned approach is for a model that can take in prescribed accelerations and displacements and return the

forces and moments in response to that motion and other external forces. For a sub-body with prescribed accelerations and displacements at selected degrees of freedom (DOFs), r, the equations of motion can be partitioned as

$$\begin{bmatrix} M_{rr} & M_{ru} \\ M_{ur} & M_{uu} \end{bmatrix} \begin{Bmatrix} \ddot{x}_r \\ \ddot{x}_u \end{Bmatrix} + \begin{bmatrix} K_{rr}(T) & K_{ru}(T) \\ K_{ur}(T) & K_{uu}(T) \end{bmatrix} \begin{Bmatrix} x_r \\ x_u \end{Bmatrix} = \begin{Bmatrix} F_r \\ F_u^H + F_u^A \end{Bmatrix}, \tag{2.89}$$

where M_{rr}, M_{ru}, M_{ur}, and M_{uu} are the physical mass matrices, x_r and x_u are the physical degrees of freedom, $F^H(T)$ is the load vector due to heating, $F^A(t)$ is the load vector due to aerodynamic pressure, the subscript r corresponds to the restrained DOFs (those with the prescribed accelerations and displacements), and the subscript u corresponds to the unrestrained DOFs (those without prescribed accelerations and displacements). The modified stiffness matrix, $K(T)$, is given by

$$K(T) = K_C(T) + K_G(T), \tag{2.90}$$

where $K_C(T)$ is the conventional stiffness matrix that varies due to the temperature-dependence of the material properties and $K_G(T)$ is the geometric stiffness matrix resulting from thermal stresses. In this formulation, the equations of motion for the unrestrained control surface DOFs are cast in terms of the elastic displacements relative to the constraint motion caused by the enforced displacements at the restrained DOFs. The term "constraint motion" refers to the displacements that the structure would undergo if the prescribed motion were applied statically

and inertial effects were not present. Note that the term "constraint motion" is specifically used instead of "rigid body motion" because the number of DOFs with prescribed motion is greater than that required to constrain rigid body motion in this case. Such a formulation is advantageous because the constraint motion is accounted for separately and the equations of motion are associated only with the elastic response, the structural modal matrix does not need to be modified to include constraint modes. Therefore, the sub body modal matrix is composed only of elastic modes in this formulation. The first step is to calculate the constraint motion due to enforced motion at the unrestrained DOFs, denoted by x_u^C . This quantity is obtained by neglecting inertial loads and external loads in the second row of (2.89) and solving for x_u , i.e.,

$$x_u^C = -\left(K_{uu}\right)^{-1} K_{ur} x_r \equiv U x_r \ , \tag{2.91}$$

If the number of DOFs with prescribed motion were exactly equal to the minimum number of DOFs required to constrain rigid body motion, the columns of U would represent rigid body modes. Because in this case the number of DOFs with prescribed motion is greater than that required to constrain rigid body motion, the columns of U represent constraint modes.

The next step is to derive the equations governing the elastic deformation of the unrestrained DOFs, x_u^E , relative to the constraint motion. Expanding (2.89), one obtains

$$M_{rr}\ddot{x}_r + M_{ru}\ddot{x}_u + K_{rr}x_r + K_{ru}x_u = F_r \ , \tag{2.92}$$

$$M_{ur}\ddot{x}_r + M_{uu}\ddot{x}_u + K_{ur}x_r + K_{uu}x_u = F_u^H + F_u^A \ . \tag{2.93}$$

Recall that the total motion of the unrestrained DOFs is the sum of the constraint motion plus the elastic motion, i.e.,

$$x_u = x_u^C + x_u^E \quad . \tag{2.94}$$

Substituting (2.94) into (2.93), one obtains

$$M_{ur}\ddot{x}_r + M_{uu}\left(\ddot{x}_u^C + \ddot{x}_u^E\right) + K_{ur}x_r + K_{uu}\left(x_u^C + x_u^E\right) = F_u^H + F_u^A \quad , \tag{2.95}$$

and using (2.91) in (2.95), the system becomes

$$M_{ur}\ddot{x}_r + M_{uu}\left[-\left(K_{uu}^*\right)^{-1}K_{ur}\ddot{x}_r + \ddot{x}_u^E\right] + K_{ur}x_r + K_{uu}\left[-\left(K_{uu}\right)^{-1}K_{ur}x_r + x_u^E\right] = F_u^H + F_u^A \quad . \tag{2.96}$$

Bringing all terms associated with the restrained DOFs to the right-hand side of (2.96), the equation becomes

$$M_{uu}\ddot{x}_u^E + K_{uu}x_u^E = -M_{ur}\ddot{x}_r + M_{uu}\left(K_{uu}\right)^{-1}K_{ur}\ddot{x}_r - K_{ur}x_r + K_{uu}\left(K_{uu}\right)^{-1}K_{ur}x_r + F_u^H + F_u^A \quad , \tag{2.97}$$

and simplifying the right-hand side of (2.97) results in

$$M_{uu}\ddot{x}_u^E + K_{uu}x_u^E = \left[M_{uu}\left(K_{uu}\right)^{-1} K_{ur} - M_{ur} \right] \ddot{x}_r + F_u^H + F_u^A \quad . \tag{2.98}$$

The relation given by (2.98) is the system to be solved for the relative elastic motion of the unrestrained DOFS, x_u^E. Note that the solution to (2.98) requires only the accelerations of the restrained DOFs, $\ddot{x}_r$, and not the displacements. However, x_r is required to compute the constraint motion, x_u^C.

2.7.3 Ritz Modes Generalization of Displacement Driven Structures

As with the free main-body, due to the large number of degrees of freedom typical of sub body structures, direct solution of (2.98) within the aerothermoelastic sub-body framework is not desirable. A common approach to reduce the order of such a system is to employ a modal transformation in which the structural displacements are expressed as a linear combination of a small number of basis vectors that are the free vibration mode shapes of the structure. However, this approach cannot be applied directly for (2.98) as the mode shapes change over time due to modification of the stiffness from geometric stiffness and material degradation effects associated with temperature changes. The approach taken in this work follows the approach introduced in Falkiewicz and Cesnik.[36] It first performs an off-line calculation to select a reduced number of Ritz modes based on free vibration modes and load-dependent Ritz vectors evaluated at a reference thermal state. These Ritz modes are then used as the modal basis for solution of the structural response throughout the simulation. This procedure is applicable as the Ritz modes need only to satisfy the geometric boundary conditions,[161] which will always be the case regardless of the stiffness distribution. The modal matrix containing the structural reference modes, Φ, is held

fixed throughout the simulation, thus preventing the need to solve an eigenvalue problem of the full system as time evolves. Though the reference modes will not be updated throughout the simulation, the stiffness matrix will be updated each time the structural dynamic response is calculated to account for temperature-dependent material properties and geometric stiffening. Updating of the conventional stiffness matrix is performed using the temperature-dependence of the material properties of the various materials. The geometric stiffness matrix is updated by solving a static finite element problem based on the thermal loads from temperatures at the current time step and the material coefficients of thermal expansion. As discussed previously, an important result of solving only for the elastic response in (2.98) is that the structural basis must only contain elastic modes. Because the remainder of the motion is accounted for in (2.94), the structural modal matrix need not contain constraint modes.

The reduced-order system is obtained by first representing the elastic motion, $x_u^E(t)$, as a linear combination of Ritz modes such that

$$x_u^E(t) = \Phi d(t) \ , \tag{2.99}$$

where d represents the modal coordinates of the Ritz modes which are stored as columns of the modal matrix, Φ. Note that since the number of Ritz modes used in the model expansion is much less than the number of physical degrees of freedom in the model, the computational cost of the solution is reduced. Once the modified stiffness matrix is known at a given time, the system is reduced by substituting (2.99) into (2.98) and pre-multiplying the system by Φ^T to project the system onto the basis, i.e.,

$$\Phi^T M_{uu} \Phi \ddot{d}(t) + \Phi^T K_{uu} \Phi d(t) = \Phi^T \left(\left[M_{uu} \left(K_{uu}(T) \right)^{-1} K_{ur}(T) - M_{ur} \right] \ddot{x}_r(t) + F_u(t,T) \right) , \quad (2.100)$$

where the net force, $F_u(t,T)$, is defined as

$$F_u(t,T) = F_u^H(T) + F_u^A(t) . \quad (2.101)$$

The generalized mass matrix, m_{uu}, generalized stiffness matrix, k_{uu}, and generalized net force vector, f_u, are then identified from (2.100) as

$$m_{uu} = \Phi^T M_{uu} \Phi , \quad (2.102)$$

$$k_{uu}(T) = \Phi^T K_{uu}(T) \Phi , \quad (2.103)$$

$$f_u(t,T) = \Phi^T F_u(t,T) , \quad (2.104)$$

and the reduced system in modal form is given as

$$m_{uu} \ddot{d}(t) + k_{uu}(T) d(t) = f_u(t,T) + \Phi^T \left(\left[M_{uu} \left(K_{uu}(T) \right)^{-1} K_{ur}(T) - M_{ur} \right] \ddot{x}_r(t) \right) . \quad (2.105)$$

As the mass of the structure is taken to be constant in this work, the reference modes are orthogonal with respect to the mass matrix and the generalized mass matrix, m_{uu}, reduces to the identity

matrix. Since the modified stiffness matrix is continuously changing due to transient heating, there is no guarantee of orthogonality of the reference modes due to stiffness, and the equations are coupled. As such, the reduced-order system of equations in modal space is integrated numerically to calculate $d(t)$ at each aerothermoelastic time step.

2.7.4 Integration Method

The numerical integration method employed for the sub-bodies is similar to the Newmark-β method except that the load vector is averaged over three time instants and the stiffness matrix is modified such that the dynamic equation of motion reduces to a static solution if no inertial effects or damping exist.[162] The scheme uses a central finite difference representation for the velocity and acceleration at discrete times, given by

$$\dot{d}^{(n)} = \frac{d^{(n+1)} - d^{(n-1)}}{2\Delta t_{AE}} \,, \tag{2.106}$$

$$\ddot{d}^{(n)} = \frac{d^{(n+1)} - 2d^{(n)} + d^{(n-1)}}{\Delta t_{AE}^2} \,, \tag{2.107}$$

where the superscript (n) refers to the time level. The initial conditions, $d^{(0)}$ and $\dot{d}^{(0)}$, are used to generate the vectors $d^{(n-1)}$, $f_u^{(n-1)}$, and $f_u^{(n)}$ for the initial time step, $n = 0$, i.e.,

$$d^{(-1)} = d^{(0)} - \dot{d}^{(0)}\Delta t_{AE} \,, \tag{2.108}$$

$$f_u^{(-1)} = k_{uu} d^{(-1)} \quad , \tag{2.109}$$

$$f_u^{(0)} = k_{uu} d^{(0)} \quad . \tag{2.110}$$

Note that this formulation assumes that the initial acceleration for all points is zero (initial velocity is constant). In order to maintain consistency with the central difference approximation for the modal accelerations, the enforced acceleration in (2.105), $\ddot{x}_r(t)$, is approximated at time level (n) using a central difference formula, i.e.,

$$\ddot{x}_r(t) = \frac{x_r^{(n+1)} - 2x_r^{(n)} + x_r^{(n-1)}}{\Delta t_{AE}^2} \quad . \tag{2.111}$$

Substituting the finite difference approximations of the velocities and accelerations, (2.106), (2.107), and (2.111), into the equations of motion, (2.105), and averaging the applied loads over three adjacent time instants, the equations of motion are re-written as

$$H_1 d^{(n+1)} = H_2 + H_3 d^{(n)} + H_4 d^{(n-1)} \quad , \tag{2.112}$$

where

$$H_1 = \frac{1}{\Delta t_{AE}^2} m_{uu} + \frac{1}{3} k_{uu} \quad , \tag{2.113}$$

$$H_2 = \frac{1}{3}\left(f_u^{(n+1)} + f_u^{(n)} + f_u^{(n-1)} \right) + \Phi^T \left[M_{uu} \left(K_{uu}(T) \right)^{-1} K_{ur}(T) - M_{ur} \right] \frac{x_r^{(n+1)} - 2x_r^{(n)} + x_r^{(n-1)}}{\Delta t_{AE}^2} \quad , \tag{2.114}$$

$$H_3 = \frac{2}{\Delta t_{AE}^2} m_{uu} - \frac{1}{3} k_{uu} \quad , \tag{2.115}$$

$$H_4 = -\frac{1}{\Delta t_{AE}^2} m_{uu} - \frac{1}{3} k_{uu} \quad . \tag{2.116}$$

The vector of structural modal coordinates at the end of the time step, $d^{(n+1)}$, is obtained by decomposing H_1 and applying it to the right-hand side of (2.112). Once $d^{(n+1)}$ is obtained, the total motion of the unconstrained degrees of freedom in physical space is computed via (2.91), (2.94), and (2.99) using

$$x_u^{(n+1)} = -\left(K_{uu} \right)^{-1} K_{ur} x_r^{(n+1)} + \Phi d^{(n+1)} \quad . \tag{2.117}$$

2.7.5 Interface Forces

Once the displacements of the unrestrained DOFs are known at a given time t, the force contribution due to the sub body motion, F_r^W, can be calculated at time t by computing the quantity

$M_{ru}\ddot{x}_r + K_{ru}x_u$ from the first row of (2.89) and moving it to the right-hand side to treat as a forcing function acting on the main body at the interface. This force contribution is computed using

$$F_r^W(t,T) = -M_{ru}\frac{x_u^{(n+1)} - 2x_u^{(n)} + x_u^{(n-1)}}{\Delta t_{AE}^2} - K_{ru}\frac{x_u^{(n+1)} + x_u^{(n)} + x_u^{(n-1)}}{3}, \tag{2.118}$$

where the accelerations of the unrestrained DOFs, $\ddot{x}_u$, are calculated using central difference and the displacements are averaged over three adjacent time instants in order to maintain consistency with the numerical integration scheme. Once $F_r^W(t,T)$ is known, it can then be passed to the main body equations of motion in order to update the loads. In order to compute the net external force that the sub body exerts relative to the main body, $F_r^{W/B}$, the elastic motion of the unrestrained sub body DOFs relative to the interface DOFs is utilized. Therefore, $F_r^{W/B}$ is given by

$$F_r^{W/B} = -K_{ru}\left(x_u^E - x_{u,T}^E\right), \tag{2.119}$$

where $x_{u,T}^E$ is the elastic deformation caused by thermal loads. Note that $x_{u,T}^E$ must be subtracted from x_u^E because thermal loads are internal to the system and do not result in external forces being exerted on the main body.

2.8 Thermoelastic Model

Even after fixing the Ritz modes to be used throughout the simulation, repeatedly solving for the stiffness matrix given some thermal state at every time step is undesirable and may take

significant time to complete for each change to the thermal state. Instead, a surrogate model which can be solved on the order of a fraction of a second is desirable. Kriging is chosen for this section since it does not require a priori assumptions on the form of the full solution and is easily implement through the Design and Analysis of Computer Experiments (DACE) toolbox[141] in Matlab®. This toolbox solves for the optimum tuning coefficient of the kriging surrogate through efficient maximum likelihood estimation, and provides several different options for regression models and correlation functions.

Generation of the sample set is done by taking N Latin hypercube samples of the parameter space that characterizes the thermal state of the structure. In this work, the thermal state is expressed through the summation of proper orthogonally decomposed (POD) thermal modes $\phi_{POD}(x,y)$ with time-varying coefficients $c(t)$, i.e.,

$$T_s(x,y,t) = c_1(t)\phi_{POD,1}(x,y) + \cdots + c_N(t)\phi_{POD,N}(x,y) \ . \tag{2.120}$$

Thus, the coefficients $c(t)$ provide a parameterization of the thermal state. Bounding of the parameter space is accomplished by considering the range of temperatures of interest for the thermal model, which are typically taken to be between the minimum freestream temperature and maximum stagnation temperature of the flow for the entire flight regime of interest. For each of the N samples, the stiffness of the structure is evaluated by solving a static FEM problem and then pre-multiplied by the modal matrix to determine the modal stiffness matrix. After the N LHS samples have been collected and used to create the kriging model, an additional K LHS samples are taken to evaluate the accuracy of the kriging model. If the accuracy in insufficient, the value

of N is increased, the kriging model is recreated, and then reevaluated for accuracy until the some accuracy threshold determined by the researcher is met. This process is outlined in Figure 2.10.

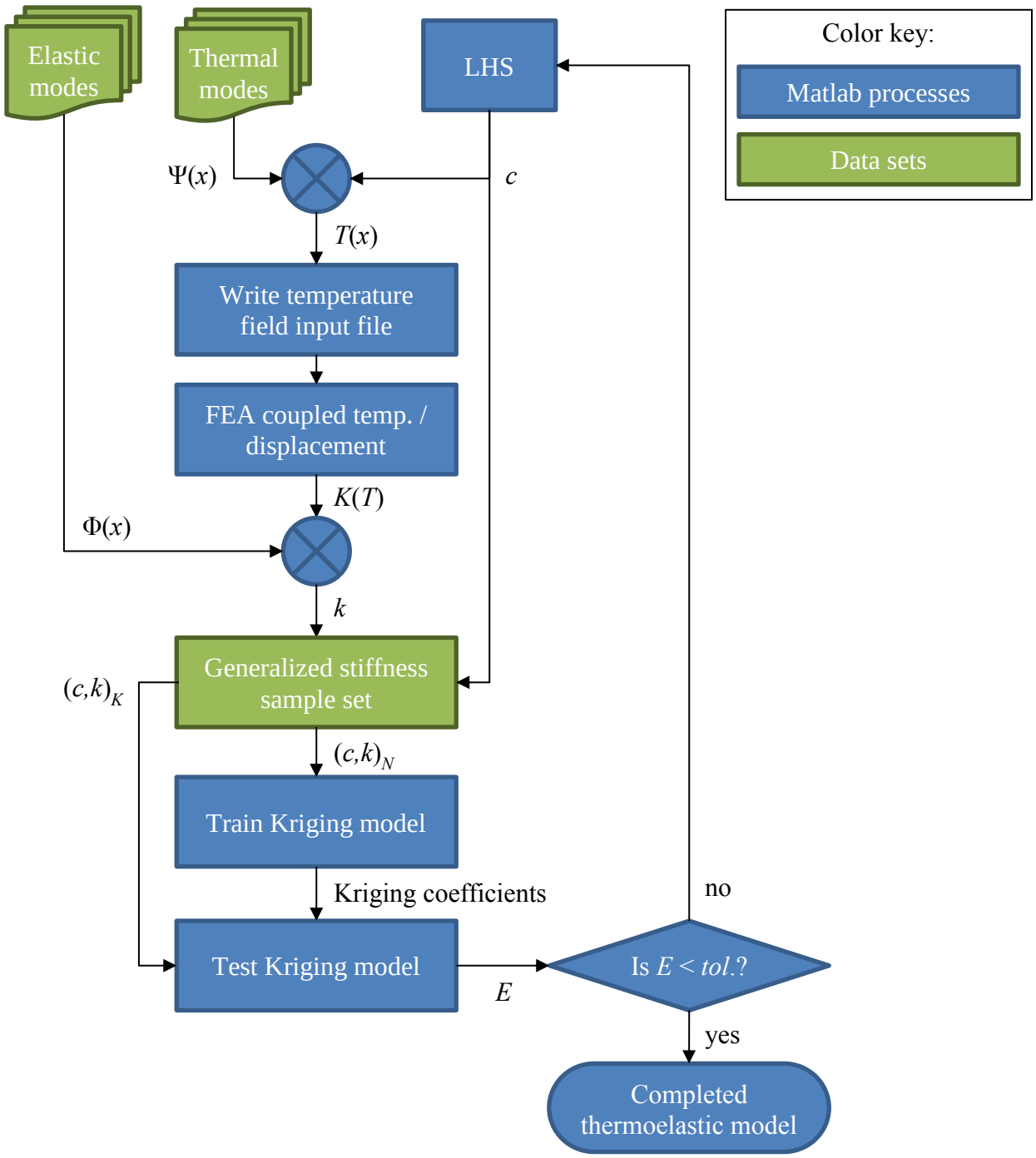

Figure 2.10: Flowchart of the thermoelastic kriging surrogate training

2.9 Propulsion Models

Propulsion forces on the vehicle are estimated using one of two methods that are capable of modeling ramjet or scramjet performance. These methods range from a low-fidelity 1-D area ratio model with Rayleigh flow assumptions to a medium-fidelity 2-D method of characteristics model with flamelet chemistry. In either model, the flow conditions into the inlet of the propulsion system and the fuel-air equivalence ratio are used to determine the forces, moments, pressure field, and started condition.

2.9.1 1-D Area Ratios with Heat Addition

The flow path schematic used for the 1-D area ration model is shown in Figure 2.11 and was presented by Bolender and Doman[27] and is similar to that used by Chavez and Schmidt.[28] The conditions given at the engine inlet (station 1) are primarily determined by the Mach number and angle of attack at which the aircraft is flying. These parameters determine, in part, the properties of the bow shock and reflected shock. The flow through the diffuser is assumed isentropic. The two control variables that determine the thrust setting are the diffuser area ratio and the equivalence ratio. The fuel-air equivalence ratio, Φ , effectively determines the change in total temperature that results from the combustion process. Choosing Φ as a control parameter is the same as controlling the fuel flow, because one can calculate how much air is captured by the propulsion system. Controlling A_d allows one to modulate the Mach number and the static pressure of the air entering into the combustion chamber. Ideally, the air remains supersonic to avoid significant ram drag penalties. Because the air entering the combustor is supersonic, the heat release due to fuel combustion reduces the Mach number of the airstream that is passing through the engine.

Care must be taken to ensure that the amount of heat added does not thermally choke the combustor flow.

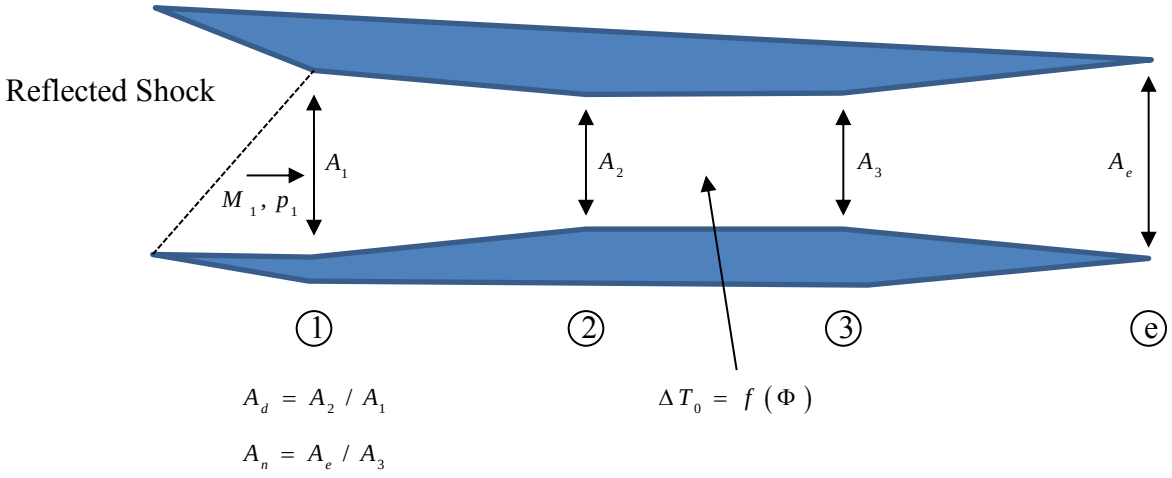

Figure 2.11: Scramjet cross section[27]

The first stage of the engine is the isentropic diffusor, which is represented by the isentropic mass continuity as

$$\frac{\left[1+\frac{\gamma-1}{2}M_2^2\right]^{\frac{\gamma+1}{\gamma-1}}}{M_2^2} = A_d^2 \frac{\left[1+\frac{\gamma-1}{2}M_1^2\right]^{\frac{\gamma+1}{\gamma-1}}}{M_1^2}, \tag{2.121}$$

where M_1 is the pre-diffuser Mach number, M_2 is the post-diffuser/pre-combustor Mach number, and A_d is the diffuse area ratio. The combustor is treated as a constant area, frictionless duct with heat addition. The total temperature change in the combustor is governed by

$$\frac{T_{0_3}}{T_{0_2}} = \frac{1 + \dfrac{H_f \eta_c f_{st}}{c_p T_{0_2}}}{1 + f_{st}\Phi} , \tag{2.122}$$

where T_{0_2} and T_{0_3} are the respective pre- and post-combustor total temperatures, c_p is the specific heat capacity of air, H_f is the lower heating value of the fuel, η_c is the combustor efficiency, f_{st} is the stoichiometric fuel-to-air mass ratio, and Φ is fuel equivalence ratio. Using the total temperature change, the post-combustor Mach number M_3 of the flow is given by

$$\frac{M_3^2\left(1 + \dfrac{\gamma - 1}{2} M_3^2\right)}{\left(\gamma M_3^2 + 1\right)^2} = \frac{M_2^2\left(1 + \dfrac{\gamma - 1}{2} M_2^2\right)}{\left(\gamma M_2^2 + 1\right)^2} + \frac{M_2^2}{\left(\gamma M_2^2 + 1\right)^2} \frac{T_{0_3} - T_{0_2}}{T_2} . \tag{2.123}$$

Using the pre- and post-combustor Mach numbers, the post-combustor pressure and temperature are determined by the Rayleigh line relations

$$p_3 = p_2 \frac{1 + \gamma M_2^2}{1 + \gamma M_3^2} , \tag{2.124}$$

$$T_3 = \frac{M_3^2}{M_2^2} \frac{\left(1 + \gamma M_2^2\right)^2}{\left(1 + \gamma M_1^2\right)^2} , \tag{2.125}$$

where p_2 and T_2 are the pressure and temperature before combustion, and p_3 and T_3 are the pressure and temperature after combustion, respectively. The final stage of the engine is an

isentropic supersonic nozzle. Since it is assumed isentropic, it is also governed by (2.121). However M_1 is replaced by M_3, M_2 is replaced by the engine exit Mach number M_e, and A_d is replaced by the nozzle area ratio, A_n. Using momentum mechanics, the propulsive force magnitude, F^P, is determined by

$$F^P = \dot{m}_a \left[(1 + \Phi) u_e + u_\infty \right] + (p_e - p_\infty) A_e - (p_1 - p_\infty) A_1 \ , \tag{2.126}$$

where $\dot{m}_a$ is the engine inflow mass flow rate, Φ is the fuel-air ratio, u_e is the flow's exit velocity, u_∞ is the vehicle freestream velocity, p_e is the exit pressure, p_∞ is the freestream air pressure, A_e is the engine exit area, and A_1 is the engine inlet area.

2.9.2 2-D Michigan-AFRL Scramjet in Vehicle (MASIV)

The MASIV code[42] provides an analysis tool for air-breathing hypersonic vehicles. The vehicle must have an approximately two-dimensional inlet and an approximately two-dimensional nozzle. In other words, it is designed for analysis of vehicles with geometry similar to that of an X-43. The primary purpose of MASIV is to analyze the thrust of the combined flow path. This includes the inlet, isolator, combustor, and nozzle. The code uses a two-dimensional implementation of the method of characteristics to determine the wave structure in the inlet and nozzle, and is the reason for the limitation of the vehicle geometry.

The engine analysis is split into four parts: the inlet, the isolator, the combustor, and the nozzle. When MASIV runs in scram mode, the isolator does not play a significant role. Both the inlet and the nozzle rely on a two-dimensional flow analysis tool called Supersonic Aerodynamic

Model Using Riemann Interactions (SAMURI). This mode is essentially a discretized and automated method of characteristics in which the fundamental quantities are shock waves, expansion waves, vehicle surfaces, and contact discontinuities. Instead of relying on a grid and solving for the flow condition in each cell, SAMURI calculates where waves should occur and allows them to intersect. Whenever two waves come into contact, a Riemann problem is solved, which results in two new waves and a contact discontinuity. This technique is limited to two-dimensional, supersonic flows, but it can analyze a wide variety of geometries within these constraints. An example flow solution is shown in Figure 2.12.

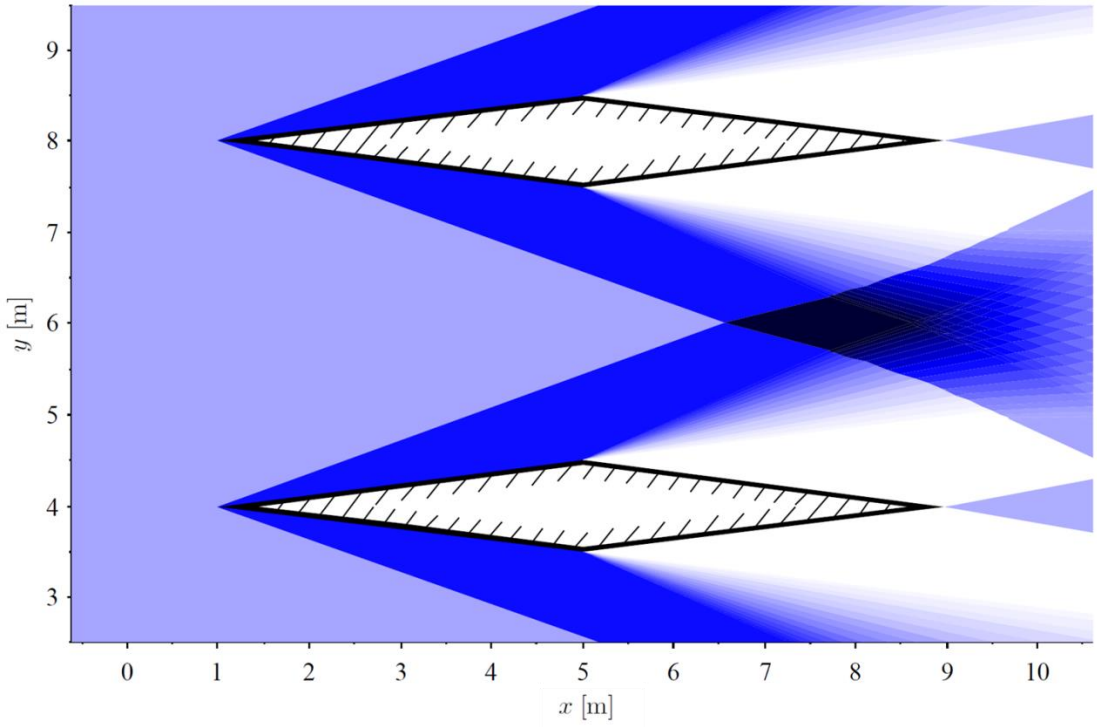

Figure 2.12: Mach 5 flow over two diamond airfoils colored by pressure[43]

The combustor is analyzed using a quasi-one-dimensional technique that includes a model for three-dimensional mixing and uses flamelet chemistry. This means that the calculation of the

state variables, i.e. pressure, temperature, mass fractions, etc., is done using one-dimensional ordinary differential equations. However, the rate change of the mass fractions is calculated according to a model that captures the mixing of a fuel jet injected into an air crossflow.

For brevity, the entire theory behind the MASIV code is not described here. However, the reader is encouraged to read several papers written by the authors of the MASIV model. A detailed description of the inlet model is given by Dalle, Fotia, and Driscoll,[41] and a similar description of the combustor model is given by Torrez et al.[163] with a discussion of the ram-mode solver by Torrez, Dalle, and Driscoll.[164] A paper dedicated to the scramjet nozzle presented by Dalle, Torrez, and Driscoll.[165] Finally, Dalle et al.[40] describes how these components may be integrated into a full vehicle model.

Since the MASIV code analyzes only two-dimensional flow paths, yet the vehicles simulated by the UM/HSV code are three-dimensional, a vehicle is sliced leading to trailing edge at several span-wise locations as shown in Figure 2.13.

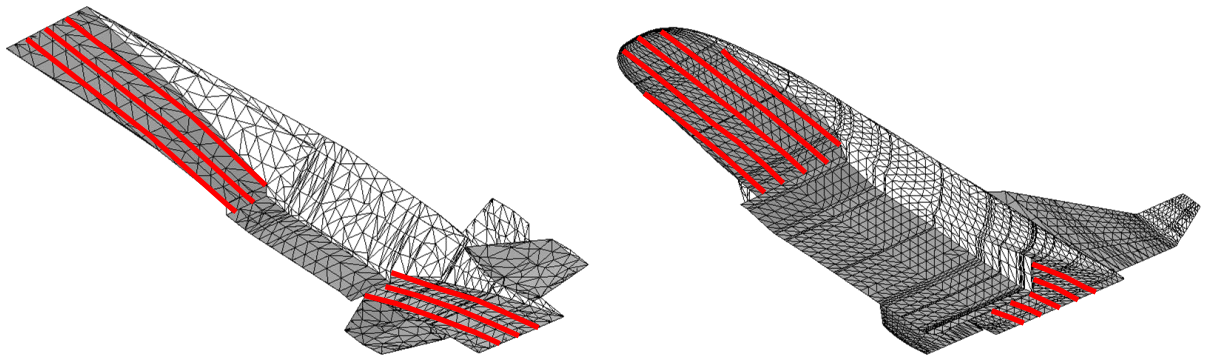

a)
AFRL Strike/Cruise Vehicle
with three flowpath sections

b)
NASA Vision Vehicle
with five flowpath sections

Figure 2.13: Sample 2-D flowpath sections highlighted in red[40]

Each slice is used to create a two-dimensional model of the flow path, accounting for deformation of the main body, flight angles, and the freestream flow conditions. The shape of the inlet, the cowl, and the nozzle are determined by creating a polygon with nodes at the intersections of the vehicle OML mesh edges and the cross section plane as shown in Figure 2.14. It is important to note that the cross section plane is always oriented normal to the y-axis of the body frame. This does not allow for the consideration of sideslip by the propulsion system, however is necessary to ensure that the flow paths provided to MASIV are truly two-dimensional.

If the cross section plane intersects an OML face very close to one of the OML nodes, at least two cross section nodes will be generated that are very close together, as shown in Figure 2.15. If this happens, each cross section node does not contribute much definition to the flow path shape and in the event that the cross section nodes are extremely close, within numerical rounding error, a small ridge or step may be produced on the surface. If the ridge or step is sharp enough, the SAMURI flow solver will create a small region of flow separation, with undefined flow properties that invalidate the overall force and moment calculations later performed by MASIV. To mitigate this computational limitation, cross section nodes that are within 1 millimeter of each other are reduced to a single node. Once the cross section nodes of the inlet, the cowl, and the nozzle are determined, they are used to modify the MASIV default inlet and nozzle geometry variable structures.

The isolator section is considered to be of constant area with only deformation along its length due to the main body. The isolator flow path remains otherwise straight and a constant fraction of the total flow path length housed within the cowl. The combustor section is allowed to deform in both length and angle of the expansion region so to join flush with the beginning of the

nozzle section. As with the isolator, the combustor flow path otherwise remains straight and is the remaining length fraction housed within the cowl that is not occupied by the isolator. Placement of the fuel injectors is left as the default MASIV locations.

With the inlet, isolator, combustor, and nozzle flow paths determined, the sections are stacked end to end to form the overall flow path for a given cross section of the vehicle, as shown in Figure 2.16 b. Note that the upper surfaces of the flow path polygons do not match the contour of the vehicle body. Similarly, the lower surfaces of the cowl do not match the contour of the cowl. This is because these surfaces do not contribute to the internal flow path shape and are ignored by MASIV during force and moment calculations. The flow pattern solutions from SAMURI are shown in Figure 2.16 c for the inlet and nozzle sections.

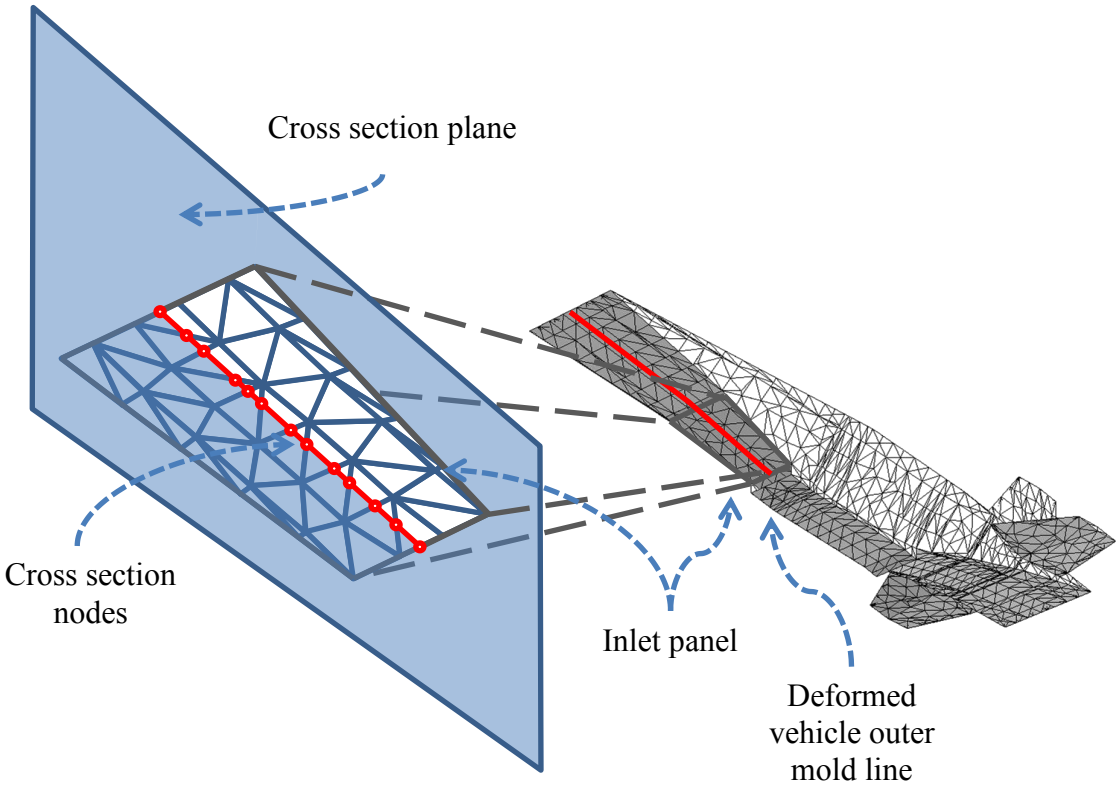

Figure 2.14: Generation of propulsion section nodes

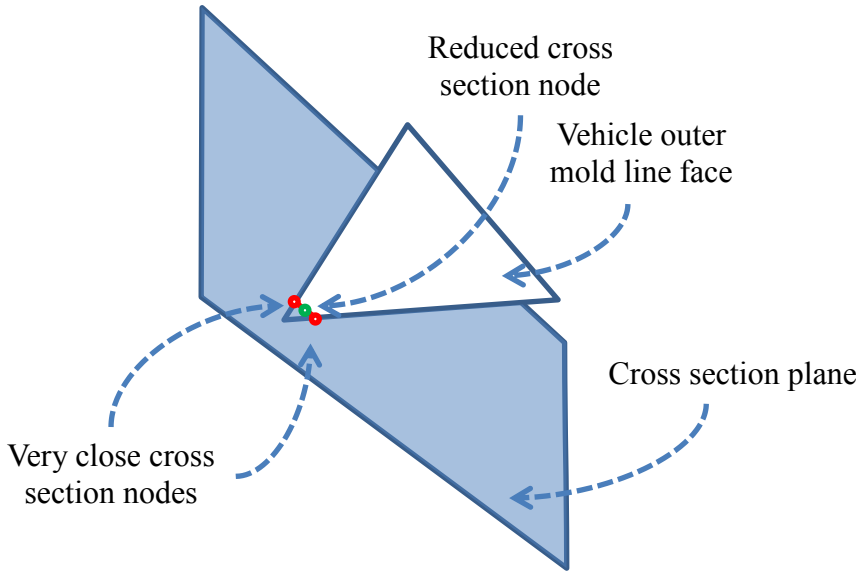

Figure 2.15: Generation of cross section nodes near an outer mold line node

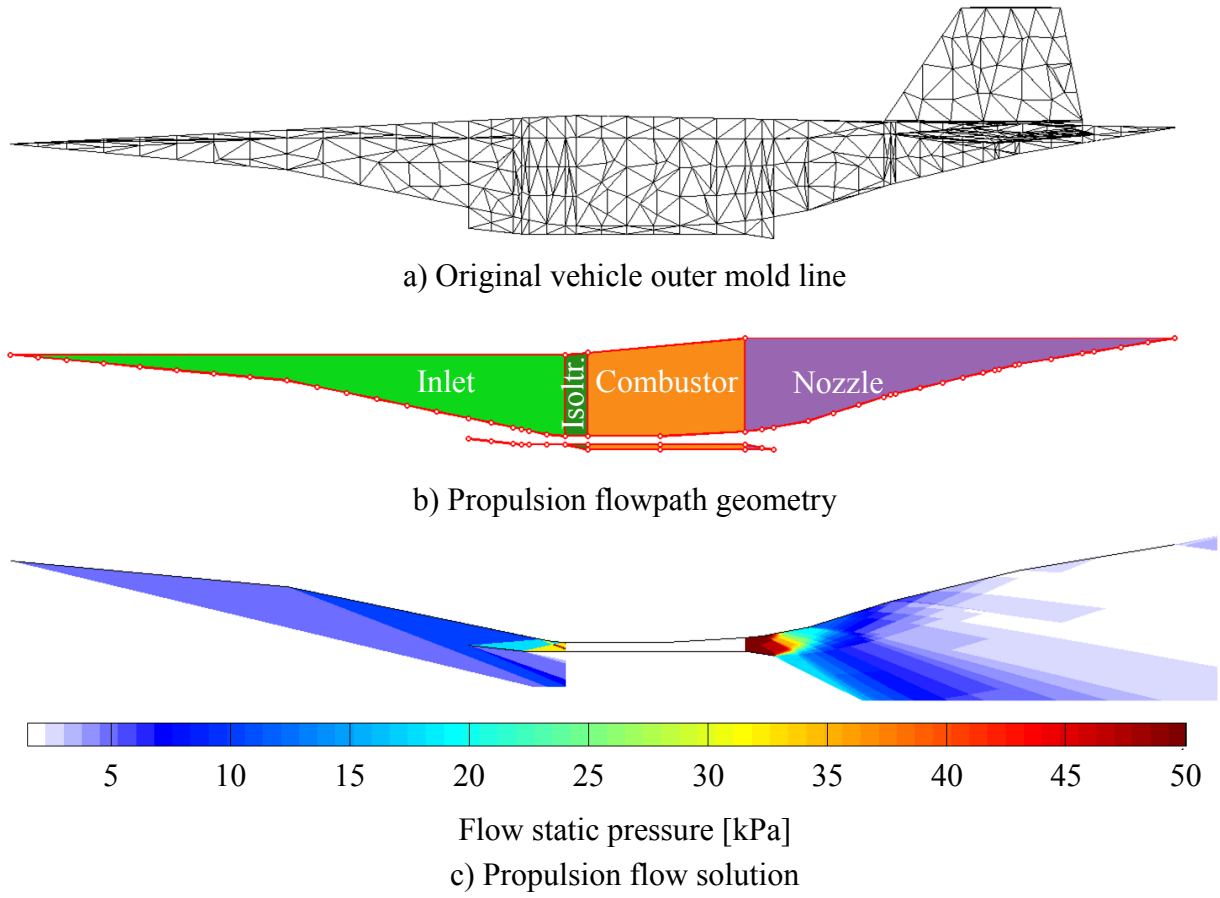

a) Original vehicle outer mold line

b) Propulsion flowpath geometry

c) Propulsion flow solution

Figure 2.16: Propulsion cross section creation process

To avoid double counting some pressure loads on the main body by considering both the main body aerodynamics and the propulsion models, two considerations were made. First, the force and moment contributions by the inlet and nozzle are not included in the output of MASIV. Only the forces and moments generated by the isolator and combustor sections are taken from MASIV's forces solutions. Second, on the regions of the main body designated as either the inlet or nozzle, the surface pressures from the SAMURI flow solution are applied to the main body outer mold line. Since the SAMURI pressure solutions exist only on the cross section planes used to determine the flow path geometries, pressures between the cross sections are interpolated using a cubic spline.

CHAPTER III

Theory Enhancements

Enhancements to the theory are overviewed in this chapter. These include the development of a general surrogate modeling technique via singular value decomposition and singular vector regression, the addition of nonlinear material thermal property models when considering generalized heat transfer equations, model linearization techniques for aerothermoelastic systems, and a nonlinear state space model which can be used to quickly simulate highly nonlinear dynamic systems. A framework for a ramjet/scramjet propulsion surrogate model is also described along with a method of basis reprojection for a change of vehicle models due to stage separation.

3.1 Singular Value Decomposition and Regression

A method of surrogate model generation through singular value decomposition and function regression to right singular vectors is developed based on the work of Lillian, McDaniel, and Morton.[166] The first step of this method is to produce a set of training samples from a system to be considered. These samples may be derived from any source so long as the system inputs and outputs are recorded in a consistent manner. It is also advantageous that the samples span the design space approximately uniformly for the best overall model accuracy; however, uniform sample spacing is not a mathematical requirement of this approach. Once collected, the training samples are arranged into a sample matrix S by

$$S = \begin{bmatrix} y_1\left(x^{(1)}\right) & y_1\left(x^{(2)}\right) & \cdots & y_1\left(x^{(s)}\right) \\ \vdots & \vdots & & \vdots \\ y_m\left(x^{(1)}\right) & y_m\left(x^{(2)}\right) & \cdots & y_m\left(x^{(s)}\right) \end{bmatrix}, \tag{3.1}$$

where y_i is the i^{th} entry of m of output vector y when given input vector $x^{(k)}$ of s samples to be considered. The input matrix d is then formed by concatenating a constant vector of 1's onto a permutation of the input vector entries. The length of the constant 1's vector should be equal to the length of the input vectors. For the work presented in this thesis, permutations of the input vectors were limited to complete polynomials of the inputs, i.e.,

$$d_{\text{const}} = \begin{bmatrix} 1 & 1 & \cdots & 1 \\ \vdots & \vdots & & \vdots \\ 1 & 1 & \cdots & 1 \end{bmatrix}_{n \times s}, \tag{3.2}$$

$$d_{\text{linear}} = \begin{bmatrix} 1 & 1 & \cdots & 1 \\ \vdots & \vdots & & \vdots \\ x_1^{(1)} & x_1^{(2)} & \cdots & x_1^{(s)} \\ \vdots & \vdots & & \vdots \\ x_n^{(1)} & x_n^{(2)} & \cdots & x_n^{(s)} \end{bmatrix}_{(2n) \times s}, \tag{3.3}$$

$$d_{\text{quad}} = \begin{bmatrix} 1 & 1 & \cdots & 1 \\ \vdots & \vdots & & \vdots \\ x_1^{(1)} & x_1^{(2)} & \cdots & x_1^{(s)} \\ \vdots & \vdots & & \vdots \\ x_1^{(1)}x_1^{(1)} & x_1^{(2)}x_1^{(2)} & \cdots & x_1^{(s)}x_1^{(s)} \\ x_1^{(1)}x_2^{(1)} & x_1^{(2)}x_2^{(2)} & \cdots & x_1^{(s)}x_2^{(s)} \\ \vdots & \vdots & & \vdots \\ x_n^{(1)}x_n^{(1)} & x_n^{(2)}x_n^{(2)} & \cdots & x_n^{(s)}x_n^{(s)} \end{bmatrix}_{\left(2n+n^2/2+n/2\right)\times s}, \tag{3.4}$$

where $x_j^{(k)}$ is the j^{th} entry of the k^{th} input vector. The subscript appended to each of the input matrices (3.2) through (3.4) indicate the number of entries in the matrix for s samples of input vectors with length n. Note that higher order polynomial representations of the inputs may be considered and follow the same multiplication pattern. Up to 6$^{\text{th}}$-order is considered in this thesis. However, these input matrices become unwieldy to typeset and have been omitted for brevity.

Using singular value decomposition, sample matrix S may be expressed as

$$S = U \Sigma V^T, \tag{3.5}$$

where U is a square matrix whose columns are the left singular vectors of S, Σ is a rectangular diagonal matrix of the singular values ranked in descending magnitude, and V is a square matrix whose columns are the right singular vectors. Due to the arrangement of the samples in matrix S U may be considered as a set of normalized basis matrices which can be used to construct the training samples y, whose magnitudes in each of the samples is given by ΣV^T. Furthermore, Σ gives the relative importance of each of the basis matrices in reconstructing the sample matrix. Provided the samples adequately populate the state space, then the bases of the sample matrices

may also be used to describe the state space as a whole. If there are a large number of states that result in a large number of basis matrices, then truncation of the bases may be performed by removing the least important bases according to the singular values contained in Σ.

The next step is to relate the right singular vectors of V to the input vectors contained in d. A coefficient matrix R_{svd} is defined using a least squares approach such that

$$d^T R_{svd} = V \quad , \tag{3.6}$$

and determined by

$$R_{svd} = \left(d d^T \right)^{-1} d V \quad . \tag{3.7}$$

Now, given any unsampled input vector $\tilde{x}$ expressed as a vector of $\tilde{d}$ with a consistent permutation scheme as the training inputs d, an approximate sample matrix $\tilde{S}$ may be estimated as

$$\tilde{S} = U \Sigma R_{svd}^T \tilde{d} \quad , \tag{3.8}$$

which contains the entries of the unsampled output $\tilde{y}$ corresponding to $\tilde{x}$. Due to the regression process, some information was lost and the training samples generally cannot be perfectly reproduced. However, the matrices U, Σ, and R_{svd}^T remain fixed after model construction and can be premultiplied into a single matrix $U \Sigma R_{svd}^T$. Estimation of any unsampled points may be

determined very quickly with a single matrix-vector multiplication by $\tilde{d}$. This operation is very amenable to modern-day graphical processing units (GPUs) and can be computed rapidly with vectorized array programing.

3.2 Material Thermal Property Models

As was noted in the thermal models section of the previous chapter, the thermal capacity and conductivity matrices that describe a heat transfer system are in general a function of temperature, depending on the material properties and temperature range to be considered. However, generalization of the heat transfer equations obfuscate the relationship between the thermal matrices and the thermal mode amplitudes. Yet, it is important that a thermal model can account for such dependencies. Three methods are considered to account for the temperature dependence of generalized material thermal properties.

3.2.1 Least Squares Regression of High-Dimensional Polynomials

The first method considered is to approximate each entry of the generalized thermal matrices using polynomials formed from the thermal mode coordinates, i.e.

$$B \approx R_{ls}\left[1 \quad \cdots \quad 1 \quad c_1 \quad \cdots \quad c_r \quad c_1c_1 \quad c_1c_2 \quad \cdots \quad c_rc_r \quad c_1c_1c_1 \quad c_1c_1c_2 \quad \cdots\right]^T = R_{ls}\overline{c} \ , \tag{3.9}$$

where R_{ls} is a matrix of coefficients for each permutation of thermal mode coordinates c_i, where i varies from 1 to r for each thermal basis, and B contains the entries of the thermal matrices k and m stored as column vectors

$$B = \begin{bmatrix} k_{1,1} & k_{1,2} & \cdots & k_{r,r} & m_{1,1} & m_{1,2} & \cdots & m_{r,r} \end{bmatrix}^T . \tag{3.10}$$

The coefficient matrix R_{ls} is determined by the solution to the least-squares problem:

$$R_{ls} = \left(\overline{c}\,\overline{c}^T \right)^{-1} \overline{c}\,\overline{B} , \tag{3.11}$$

where $\overline{c}$ is a matrix whose columns are vectors of the thermal mode coordinates for each snapshot expanded to include all powers and combinations of the modal coordinates desired for the polynomial to be fit and $\overline{B}$ is a matrix whose columns are vectors of the entries of the thermal matrices k and m corresponding to each set of thermal coordinates.

3.2.2 Kriging of Material Thermal Properties

The second method considered to capture the variation of the thermal capacity and conductivity matrices with respect to the thermal modal coordinates, $m(c)$ and $k(c)$, is kriging.[139] To create the kriging model, a set of training samples of thermal conductivity and capacity matrices is produced from a heat-transfer FEM based on coordinates of the thermal modal basis. Selection of the modal coordinates is determined by Latin hypercube sampling[167,168] (LHS) within thermal coordinate bounds determined by the extremes observed in the POD snapshot matrix previously described. Upon collection of a number of model training and testing samples, several Kriging models may be constructed based on different combinations of regression and correlation functions, many of which are available in the Matlab® DACE Toolbox.[141] Each model can then be tested for accuracy in reproducing the test samples.

3.2.3 Application of Singular Value Decomposition and Regression

For the application of determining the entries of the generalized thermal capacity and conductivity matrices, a sampling of the FEM solutions is first required. These can be taken using the same LHS as the Kriging ROM generation for direct comparison of the methods. A snapshot matrix S is constructed with the entries of $k(c)$ and $m(c)$ as column vectors at each LHS point and may be represented as

$$\overline{B} = \begin{bmatrix} m_{1,1}\left(c^{(1)}\right) & m_{1,1}\left(c^{(2)}\right) & \cdots & m_{1,1}\left(c^{(s)}\right) \\ m_{1,2}\left(c^{(1)}\right) & m_{1,2}\left(c^{(2)}\right) & \cdots & m_{1,2}\left(c^{(s)}\right) \\ \vdots & \vdots & & \vdots \\ m_{n,n}\left(c^{(1)}\right) & m_{n,n}\left(c^{(2)}\right) & \cdots & m_{n,n}\left(c^{(s)}\right) \\ k_{1,1}\left(c^{(1)}\right) & k_{1,1}\left(c^{(2)}\right) & \cdots & k_{1,1}\left(c^{(s)}\right) \\ k_{1,2}\left(c^{(1)}\right) & k_{1,2}\left(c^{(2)}\right) & \cdots & k_{1,2}\left(c^{(s)}\right) \\ \vdots & \vdots & & \vdots \\ k_{n,n}\left(c^{(1)}\right) & k_{n,n}\left(c^{(2)}\right) & \cdots & k_{n,n}\left(c^{(s)}\right) \end{bmatrix}, \tag{3.12}$$

where $m_{i,j}\left(c^{(k)}\right)$ is the i,j^{th} entry of the generalized heat capacity matrix m when the temperature field is described by the k^{th} temperature coordinates c. The SVD model approach is then applied as described in section 3.1. If the space spanned by the sample vectors is large, i.e. each snapshot contains a large number of degrees of freedom, the problem may be reduced by removing the smallest singular values in Σ as well as the corresponding columns of U and V. In this way,

dimensions of the snapshots which are least important to the representation of S may be neglected and the order of the eventual model is reduced.

A correlation matrix R_{svd} is determined which relates the basis amplitudes in V to the thermal mode coordinates c as previously described. Then, given any additional set of thermal mode coordinates $\tilde{c}$, not necessarily included in the snapshot matrix, estimated thermal matrices $\tilde{m}$ and $\tilde{k}$ may be found by

$$\begin{bmatrix} \tilde{m}_{1,1} \\ \tilde{m}_{1,2} \\ \vdots \\ \tilde{m}_{n,n} \\ \tilde{k}_{1,1} \\ \tilde{k}_{1,2} \\ \vdots \\ \tilde{k}_{n,n} \end{bmatrix} = U \Sigma R_{svd}^{T} \tilde{c} \quad . \tag{3.13}$$

3.3 State Space Identification and Estimation

Identification of the vehicle state space aims to represent the non-linear vehicle's behavior in a linearized form, i.e.,

$$\dot{x}(t) = A\{x(t) - x_e\} + B\{u(t) - u_e\} \quad , \tag{3.14}$$

where $x(t)$ is a column vector of the vehicle's *n* states, $u(t)$ is a column vector of the vehicle's p control inputs, $\dot{(\,)}$ denotes the derivative with respect to time, x_e is a column vector of some

reference state, u_e is a column vector of some reference control input, A is the $n \times n$ linear time invariant state matrix, and B is the $n \times p$ linear time invariant input matrix. Analysis of the matrices A and B is a common approach to study vehicle stability and is used heavily in the design of vehicle control laws.

To determine the entries of the state matrix, it is first necessary to understand the meaning of each entry. Of the $n \times n$ state matrix A, the *i*,*j* entry corresponds to the *i*th state's derivative in response to a perturbation of the *j*th state away from a reference state. Thus, each column of the state matrix contains the derivatives of all n states in response to perturbation of the state corresponding to that column and is the Jacobian matrix of the equations of motion of the vehicle bodies.

There are three primary methods for determination of such derivatives and are finite difference, complex-step, and symbolic differentiation.[169] Symbolic differentiation will not be considered here due to a lack of tractability that comes from the simulation framework implementation architecture described later.

3.3.1 Finite Difference Method

Finite difference formulas are derived by combining Taylor series expansions. Using the right combinations of these expansions, it is possible to obtain finite difference formulas that estimate an arbitrary order derivative with any required order of truncation error. Determination of each column of A begins with the identification of some reference vehicle state vector x_e and reference control input vector u_e, typically those of some trim state. A small perturbation h is then added to and subtracted from the *j*th entry of the reference vector and a central difference scheme is used to estimate each state's sensitivity to the perturbation, yielding

$$A_j = \frac{f\left(x_e + e_j h, u\right) - f\left(x_e - e_j h, u_e\right)}{2h} \quad , \tag{3.15}$$

where A_j is the *j*th column vector of the A matrix and e_j is a column vector of 0 except for a value of 1 in the *j*th entry. Note that (3.15) provides second-order accuracy with respect to h, but higher orders of accuracy are possible with larger expansions. Next, consider the form of the function f as

$$\dot{x} = f(x, u) \quad . \tag{3.16}$$

To determine the vector $\dot{x}$, a pseudo-time simulation of the vehicle is performed and the states x at two or more instances in time are used in a finite difference scheme to approximate $\dot{x}$. Since the UM/HSV framework is intended to include many types of models, backwards integration of the governing equations may not be guaranteed. Therefore a central difference scheme is not desirable, and one must use a forward difference, despite it being less accurate than central difference for a given number of observations of x. This loss of accuracy may be mitigated by using a high order scheme. Up to a sixth order scheme is given by

$$f(x, u) \approx \frac{\left(-x^{(0)} + x^{(1)}\right)}{\Delta t_{AE}} \quad , \tag{3.17}$$

$$f(x,u) \approx \frac{\left(-\frac{3}{2}x^{(0)} + 2x^{(1)} - \frac{1}{2}x^{(2)} \right)}{\Delta t_{AE}}, \tag{3.18}$$

$$f(x,u) \approx \frac{\left(-\frac{11}{6}x^{(0)} + 3x^{(1)} - \frac{3}{2}x^{(2)} + \frac{1}{3}x^{(3)} \right)}{\Delta t_{AE}}, \tag{3.19}$$

$$f(x,u) \approx \frac{\left(-\frac{25}{12}x^{(0)} + 4x^{(1)} - 3x^{(2)} + \frac{4}{3}x^{(3)} - \frac{1}{4}x^{(4)} \right)}{\Delta t_{AE}}, \tag{3.20}$$

$$f(x,u) \approx \frac{\left(-\frac{137}{60}x^{(0)} + 5x^{(1)} - 5x^{(2)} + \frac{10}{3}x^{(3)} - \frac{5}{4}x^{(4)} + \frac{1}{5}x^{(5)} \right)}{\Delta t_{AE}}, \tag{3.21}$$

$$f(x,u) \approx \frac{\left(-\frac{49}{20}x^{(0)} + 6x^{(1)} - \frac{15}{2}x^{(2)} + \frac{20}{3}x^{(3)} - \frac{15}{4}x^{(4)} + \frac{6}{5}x^{(5)} - \frac{1}{6}x^{(6)} \right)}{\Delta t_{AE}}. \tag{3.22}$$

3.3.2 Complex Step Method

The complex-step derivative approximation, like the finite difference formulas, can also be derived using a Taylor series expansion. Rather than using a real perturbation h, a purely imaginary ih is used. If f is a real function in real variables and is analytic, one can expand it in a Taylor series about a real reference vector x as

$$f\left(x + ihe_j\right) = f\left(x\right) + ih\frac{\partial f}{\partial x_j} - \frac{h^2}{2}\frac{\partial^2 f}{\partial x_j^2} - \frac{ih^3}{6}\frac{\partial^3 f}{\partial x_j^3} + \cdots \quad . \tag{3.23}$$

By taking the imaginary parts of both sides of (3.23) and dividing by h, yields

$$\frac{\partial f}{\partial x_j} = \frac{\mathrm{Im}\left[f\left(x + ihe_j\right)\right]}{h} + O\left(h^2\right) \quad . \tag{3.24}$$

Hence, the complex-step approximation is an $O\left(h^2\right)$ estimate of the derivative. Like a finite difference formula, each evaluation gives one column of the Jacobian, the state matrix A. However, because there is no subtraction operation, the only source of numerical error is the truncation error. By decreasing h to a small enough value, one can ensure that the truncation error is of the same order as the numerical precision of the evaluation of f.

3.3.3 Full Nonlinear Model Development Based on Multiple Linearized Samples

Once a number of samples of A and B have been collected, it is possible to quickly estimate state space representations of a system. Each sample is combined into a single matrix by rearranging the entries A and B into columns, which then become the columns of a sample matrix

$$S = \begin{bmatrix} A_{1,1}\left(x^{(1)},u^{(1)}\right) & A_{1,1}\left(x^{(2)},u^{(2)}\right) & \cdots & A_{1,1}\left(x^{(s)},u^{(s)}\right) \\ A_{1,2}\left(x^{(1)},u^{(1)}\right) & A_{1,2}\left(x^{(2)},u^{(2)}\right) & \cdots & A_{1,2}\left(x^{(s)},u^{(s)}\right) \\ \vdots & \vdots & & \vdots \\ A_{1,n}\left(x^{(1)},u^{(1)}\right) & A_{1,n}\left(x^{(2)},u^{(2)}\right) & \cdots & A_{1,n}\left(x^{(s)},u^{(s)}\right) \\ A_{2,1}\left(x^{(1)},u^{(1)}\right) & A_{2,1}\left(x^{(2)},u^{(2)}\right) & \cdots & A_{2,1}\left(x^{(s)},u^{(s)}\right) \\ \vdots & \vdots & & \vdots \\ A_{n,n}\left(x^{(1)},u^{(1)}\right) & A_{n,n}\left(x^{(2)},u^{(2)}\right) & \cdots & A_{n,n}\left(x^{(s)},u^{(s)}\right) \\ B_{1,1}\left(x^{(1)},u^{(1)}\right) & B_{1,1}\left(x^{(2)},u^{(2)}\right) & \cdots & B_{1,1}\left(x^{(s)},u^{(s)}\right) \\ \vdots & \vdots & & \vdots \\ B_{n,m}\left(x^{(1)},u^{(1)}\right) & B_{n,m}\left(x^{(2)},u^{(2)}\right) & \cdots & B_{n,m}\left(x^{(s)},u^{(s)}\right) \end{bmatrix}, \tag{3.25}$$

where $A_{i,j}\left(x^{(k)},u^{(k)}\right)$ is the *i,j* entry of matrix $A\left(x^{(k)},u^{(k)}\right)$ which is the state matrix A for the k^{th} sample state vector $x^{(k)}$ and input vector $u^{(k)}$ for a total of *s* samples. Similar for $B_{i,j}\left(x^{(k)},u^{(k)}\right)$ for n states and m inputs. The sample state vectors are also combined into one of the sample point matrix permutations, d from equations (3.2) through (3.4).

Determining the state rates $\dot{x}$ in (3.14) during integration of the equations of motion is then a 2-step process. In step 1, the state matrices are determined from the SVD method, followed by step 2, where the state matrices are multiplied by the state vector x. It is also possible to use the SVD method to estimate the state rates $\dot{x}$ in a 1-step process by replacing the columns of matrix S in (3.25) with the $\dot{x}$ vectors corresponding to each sampled state x, i.e.,

$$S = \begin{bmatrix} \dot{x}\left(x^{(1)}\right) & \dot{x}\left(x^{(2)}\right) & \cdots & \dot{x}\left(x^{(s)}\right) \end{bmatrix}. \tag{3.26}$$

During integration of the equations of motion, the state rates $\dot{x}$ are then determined directly from the SVD method without the need to consider the state matrices. If the d_{lin} input matrix is used to contain the state vectors, then this approach produces a single linear, time-invariant representation equivalent to equation (3.14), which represents a mean behavior of the system.

3.4 Propulsion Surrogate Model

While the 2-D MASIV propulsion model for ramjet and scramjet simulation is a highly effective tool and greatly reduces the computational cost of determining propulsion performance over CFD analysis, it lacks the necessary robustness for online simulation. Subtle elastic deformation of the inlet or nozzle regions can produce weak waves that in reality would not significantly influence the model solution, but can create overlapping wave patterns that do not have a unique solution. Furthermore, the method of characteristics used for the flow field in the inlet and nozzle sections relies on upstream flow solutions in order to determine downstream properties. This severely limits computational parallelization that is key to reducing processing time. In response to these limitations, a surrogate model was desired based on MASIV force, moment, and pressure field solutions. However, since the surrogate methods considered thus far are based on continuous regression and correlation functions, they are ill suited to consider the discontinuous nature of scramjet choke, blowout, or unstart in the performance space. Kriging could possibly be used, but dense sampling around the started boundaries would be required in order to approximate the infinitely steep gradient of the discontinuities and would result in a computationally expensive surrogate model.

To mitigate these shortcomings, a kriging model is proposed with a secondary correlation function such that

$$\hat{y}(b) = \left(R_{krig}(b, X_1) + Z_1(b, X_1)\right)\lfloor Z_2(b, X_2)\rfloor \ , \tag{3.27}$$

where X_1 is the training set containing all continuous values, i.e., forces, moments, pressure fields, which will be represented using correlation function Z_1, X_2 is the training set containing discontinuous propulsion started flags 0 or 1, taken at the same sample points as X_1 and will be represented using correlation function Z_2, and $\lfloor\ \rfloor$ is the floor function. Each of the functions composing the kriging model are fitted using the classical approach where R_{krig} and Z_1 are considered in tandem, and Z_2 is considered as though its partner regression function is a constant 0. By introducing the floored correlation function that is modeling a binary response surface, a sharp started boundary can be represented without additional sample locations. To avoid erroneous non-started conditions within the started boundaries, a linear Z_2 correlation function is recommended.

3.5 Stage Separation Basis Reprojection

Representing the elastic and thermal DOFs via a pair of corresponding basis sets is an effective means of reducing the model order and complexity. However with increased simplicity comes a loss of model flexibility. This is especially evident during a staging event in which the vehicle geometry may change drastically in an instant and the basis sets are no longer valid. The post-stage geometry may have its own basis sets that do not span the mode space defined by the pre-stage sets. Thus, a method for transitioning the energy represented in the pre-stage mode coordinates is introduced to the post-stage mode space. Consider a pre-stage DOF field described

by x_1 represented by the pre-stage basis Φ_1. Also, consider the post-stage DOF field x_2 to be a subset of the DOFs contained in x_1 where the maintained DOFs are identified by an index list ν_2 and also represented by the post-stage basis Φ_2. One can express this as

$$\Phi_1(\nu_2)\eta_1 = x_1(\nu_2) \approx x_2 = \Phi_2\eta_2 \ . \tag{3.28}$$

The pre-stage mode coordinates η_1 are known. To estimate the post-stage mode coordinates η_2 while minimizing energy loss during projection, consider

$$\eta_2 \approx \left(\Phi_2^T\Phi_2\right)^{-1}\Phi_2^T\Phi_1(\nu_2)\eta_1 \ . \tag{3.29}$$

Modal rates may be similarly determined by substituting η for $\dot{\eta}$. For the sake of simulation, the prospect of multiplying sizable basis matrices and then performing an inversion may not be appealing while online. However, since the bases are typically known *a priori*, the basis projection matrix $\left(\Phi_2^T\Phi_2\right)^{-1}\Phi_2^T\Phi_1(\nu_2)$ may be pre-computed and stored in memory.

CHAPTER IV

Numerical Implementation

This chapter describes the implementation of the models described in the previous chapters for the University of Michigan High Speed Vehicle (UM/HSV) code. Through coupling and integration of various engineering, surrogate, and reduced order models, a supersonic or hypersonic vehicle may be evaluated for flight trimming, time simulation in open or closed loop control, or stability analysis.

4.1 Architecture Overview

The following sections overview the architecture and implementation of the key elements of the UM/HSV code. The division of the various process models and body models is performed by the partitioned solution approach first proposed by Falkiewicz and Cesnik.[136] Numerical implementation is done using a publish-subscribe framework for flexibility in analysis and code development.

4.1.1 Partitioned Solution Approach

To effectively bring together a wide spectrum of numerical models, each focusing on a particular portion of a HSV, the partitioned solution approach has been developed. With this approach, the HSV is divided into *n* components of interfacing models as shown in Figure 4.1.

Each model is a self-contained system of equations tailored to capture the relevant related physics. Each region's models are integrated in time and at predefined time increments, information between regions is exchanged across interfaces. An example of such physical partitioning is shown in Figure 4.2 with more details of the partitioned regions given in following sections.

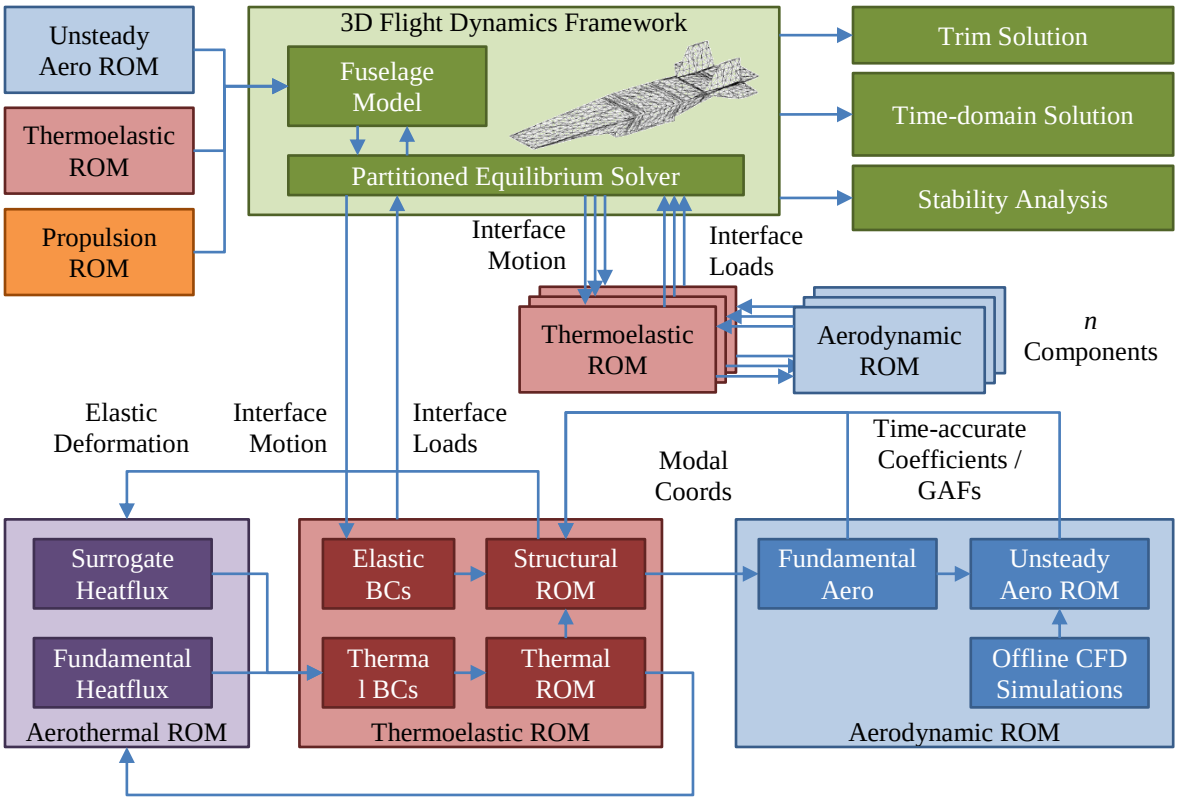

Figure 4.1: Block diagram of the partition solution approach

There are several advantages to the partitioned solution simulation over a single monolithic simulation. Firstly, entire regions of the HSV may be exchanged, removed, or isolated without affecting the operability of the others. This enables fast trade studies of various component types and models of varying fidelity. Different phenomena such as divergence or flutter of a lifting surface, shock interaction in the propulsion system, or a multitude of other possible problems can

be analyzed within the same simulation architecture. Secondly, physical processes that are unimportant to the dynamics of a particular region need not be modeled, while processes that are the primary performance drivers for other regions may be emphasized with higher fidelity models or finer discretization. This reduces computational cost while increasing overall HSV model fidelity.

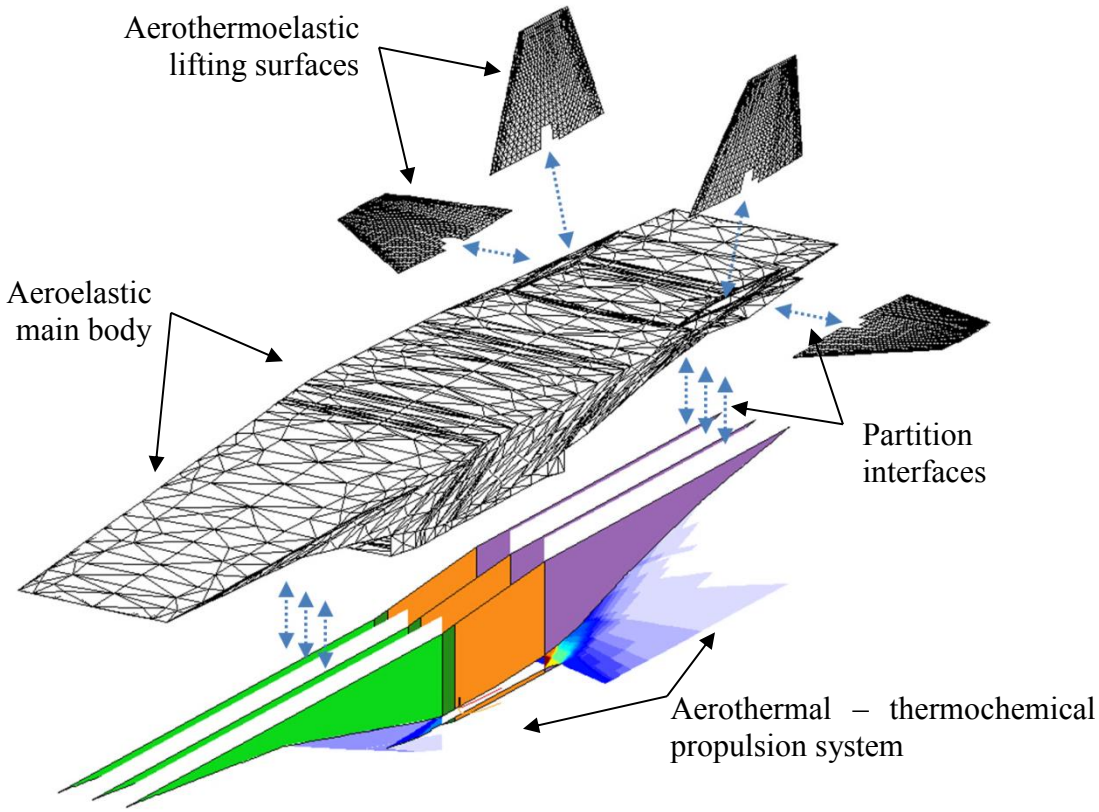

Figure 4.2: Graphical layout of sample partitioned HSV regions

4.1.2 Publish-Subscribe Architecture

The publish-subscribe (PS) code architecture is adopted in this work to implement the partitioned solution approach. In PS architecture, each function sends and receives relevant data through communication with a global data structure. An individual function does not require knowledge of how the information was first published to the data structure, but only that the

information is available for subscription. After processing, each function then publishes its results back to the data structure for use by other functions. Since no data is specifically sent between high-level functions, functions may be added, exchanged, or removed without significant impact on the operation of other code processes. This permits one to exchange freely the number and arrangement of components and models used during simulation and process a wide variety of different HSV geometries and simulation fidelities without rewriting any low-level code. A high level overview of the code layout is shown in Figure 4.3.

Each of the dark process blocks outlined in Figure 4.3 represent a high-level function that performs its named task. To initiate any analysis, the user inputs are read by the "Load Inputs" process that parses a user provided input file and locates any associated data files. The inputs, data file addresses, and analysis requests are then published to the global data structure. Next, the "Initialize Fuselage" process sets up the main body by subscribing to the initial conditions and file addresses written into the data structure, and loads all data files associated to the main body. These files include a mesh geometry, elastic mode shape basis, inertial properties, stiffness properties, thermal basis, heat capacity properties, thermal conductivity properties, and any other information that may be required for the requested analysis. Similarly, "Initialize Lifting Surfaces" loads the files relevant to the sub-bodies, often lifting or control surfaces, and pre-deforms the sub-bodies by converging on a static elastic solution. "Assemble Interfaces" then links the constrained portions of the sub-bodies to the main body and initializes the variables in the data structure for motion and force communication between partitions.

If requested in the input file, the "Trim Vehicle" process is called to configure the HSV to achieve a set of goal states and rates. Further description of the trim process is given in section 4.2. The "Identify State Space" process is next if requested in the input file, and estimates the state

space representation of an HSV in $\dot{x} = Ax + Bu$ form using a selection of three methods, i.e. forward-difference, complex step, and direct identification for single body HSV models.

Finally, if requested, the time simulation analysis is performed. This analysis consist of three nested convergence loops that manage the aerothermal, aeroelastic, and partition interfaces. The inner-most loop, the "Interfaces Loop" contains two processes. The first is "Integrate Fuselage Motion" which integrates the equations of motion for the main body, given the external and interface forces of the previous loop. The second is "Integrate Lifting Surface Motion" which considers the motion at the interfaces imposed by the main body and external forces, integrates the sub-bodies' equations of motion, and returns the forces and moments at the interface. The new interface forces are then applied to the main body and "Integrate Fuselage Motion" is repeated. New interface motions are determined and the process of integrating the sub-bodies and main body is iterated until a convergence criterion is met. Further details can be found in section 4.3.2.

Once the partition interfacial motions and forces have been brought to an equilibrium, the time simulation enters the "Aeroelastic Loop." At the initiation of any given aeroelastic loop, the "Control Inputs" process is called to determine if there are any open-loop or closed-loop control inputs to be implemented before the interface loop is called. The "Actuator Dynamics" process follows the integration of the main and sub-bodies' motion in the interface loop, and contains any transfer model that might be implemented to represent the difference between a command signal and the actual actuation of a control surface due to forces, torques, friction, rate limits, etc. The aerodynamic loads and surface flow conditions for any sub-bodies are then determined by "Lifting Surface Aerodynamics," which can use simplified engineering formulations and/or ROMs that were trained off-line and loaded as a data file with the other inputs.

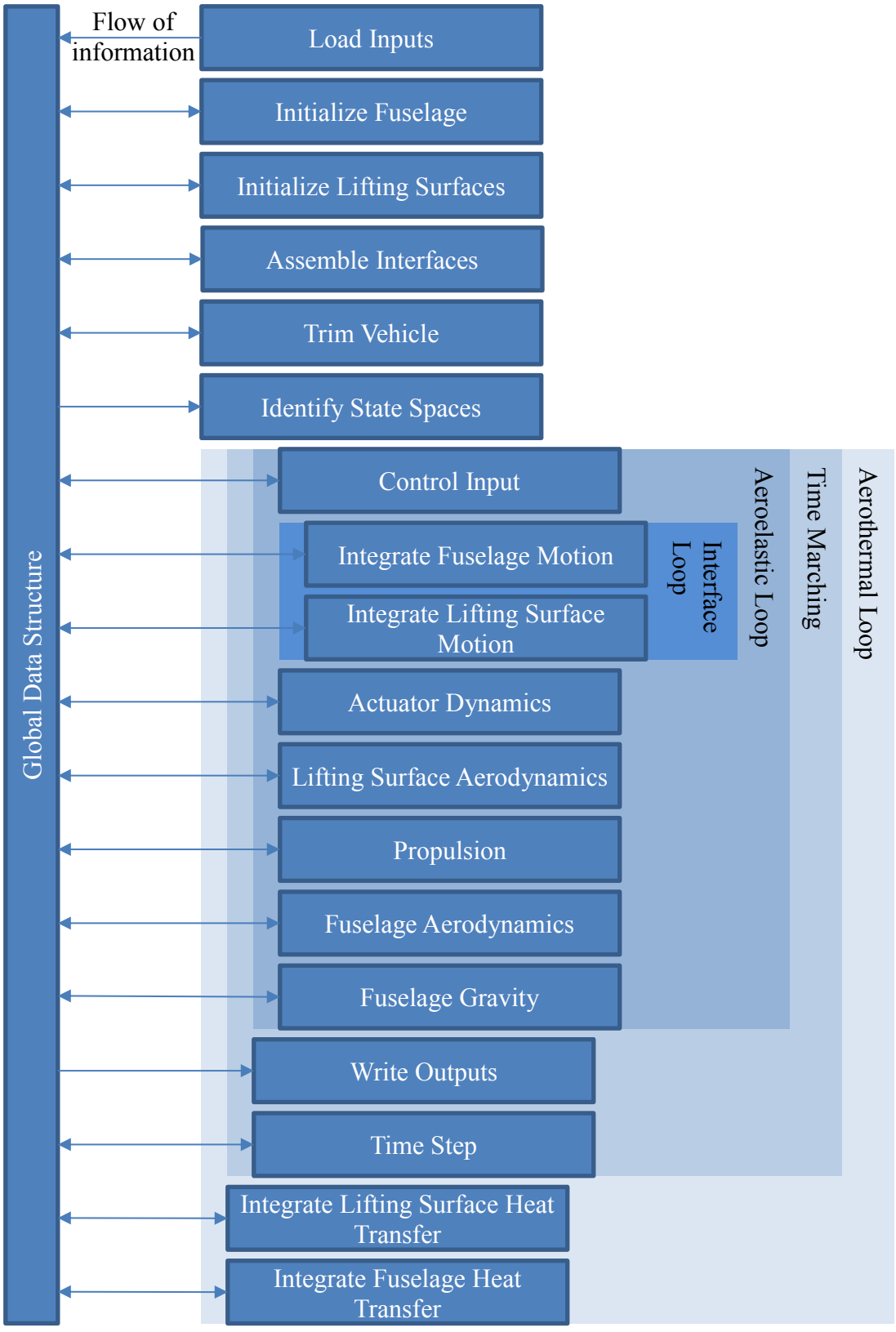

Figure 4.3: High-level overview of the UM/HSV code architecture

The “Propulsion” process is next and models the forces, moments, and modifications to the surface pressure distribution on the main body due to any ramjet, scramjet, or rocket propulsion system that may be present. “Fuselage Aerodynamics” then determines the flow conditions surrounding the main body and “Fuselage Gravity” determines the influence of gravitational acceleration. “Write Outputs” records the progress of the simulation and any information that was requested in the input file. Since writing to disk can be a slow process, the “Write Outputs” process can be super-iterated, meaning that it does not have to be invoked during the aeroelastic loop. Provided that the aeroelastic loop convergence residuals are acceptably low, the “Time Step” process can be called to shift the time levels of the main and sub-bodies’ states and index the time counter.

The outer-most loop is the “Aerothermal Loop,” which contains the “Integrate Lifting Surface Heat Transfer” and “Integrate Fuselage Heat Transfer” processes. As the names suggest, the processes integrate the heat transfer equations of the main and sub-bodies. During typical time simulations, the heat transfer equations are much less dynamic than the aeroelastic or interface matching equations, and therefore do not require as fine of a time increment during integration in order to yield accurate results. As such and to save numerical resources, the heat transfer equations are integrated on a time step that is an integer multiple of the aeroelastic time step. In the rare event that the heat transfer rates are on the order of the aeroelastic state rates, then this integer multiple may be 1, but often 10 or 100 is used, depending on the scale of the HSV to be considered.

4.2 Vehicle Trim

The process used to trim a given vehicle is outlined in Figure 4.4. The process begins with an initial guess of the vehicle’s trim state characterized by the angle-of-attack, propulsion system’s

fuel equivalence ratio, deflection angles of all control surfaces, and amplitudes of the main body structural modes. These trim states are then applied to the vehicle's data structure. Next, the given flight conditions in terms of altitude and Mach number are used to determine the freestream conditions surrounding the main and sub bodies. These freestream conditions are then used to determine the aerodynamic pressure over each sub-body's surface. The structural models of each sub-body are then invoked to determine the structural response to the surface pressure in terms of displacements and velocities over a small time step, typically one order of magnitude less than the shortest elastic mode period included in the model. The sub-bodies' structural velocities are then zeroed to damp out any oscillatory motion. A displacement residual r_{disp} is computed as the $L_{2,1}$ norm of the difference between the $n+1$ and n time step solutions, i.e.,

$$r_{disp} = \left\| x_u^{(n+1)} - x_u^{(n)} \right\|_{2,1} , \tag{4.1}$$

where x_u are the unrestrained displacements of the a given sub-body. In this way, the static elastic deformation of the sub-bodies are dependent variables of the main body shape and flight conditions, thus reducing the number of independent variables that must be considered during trim.

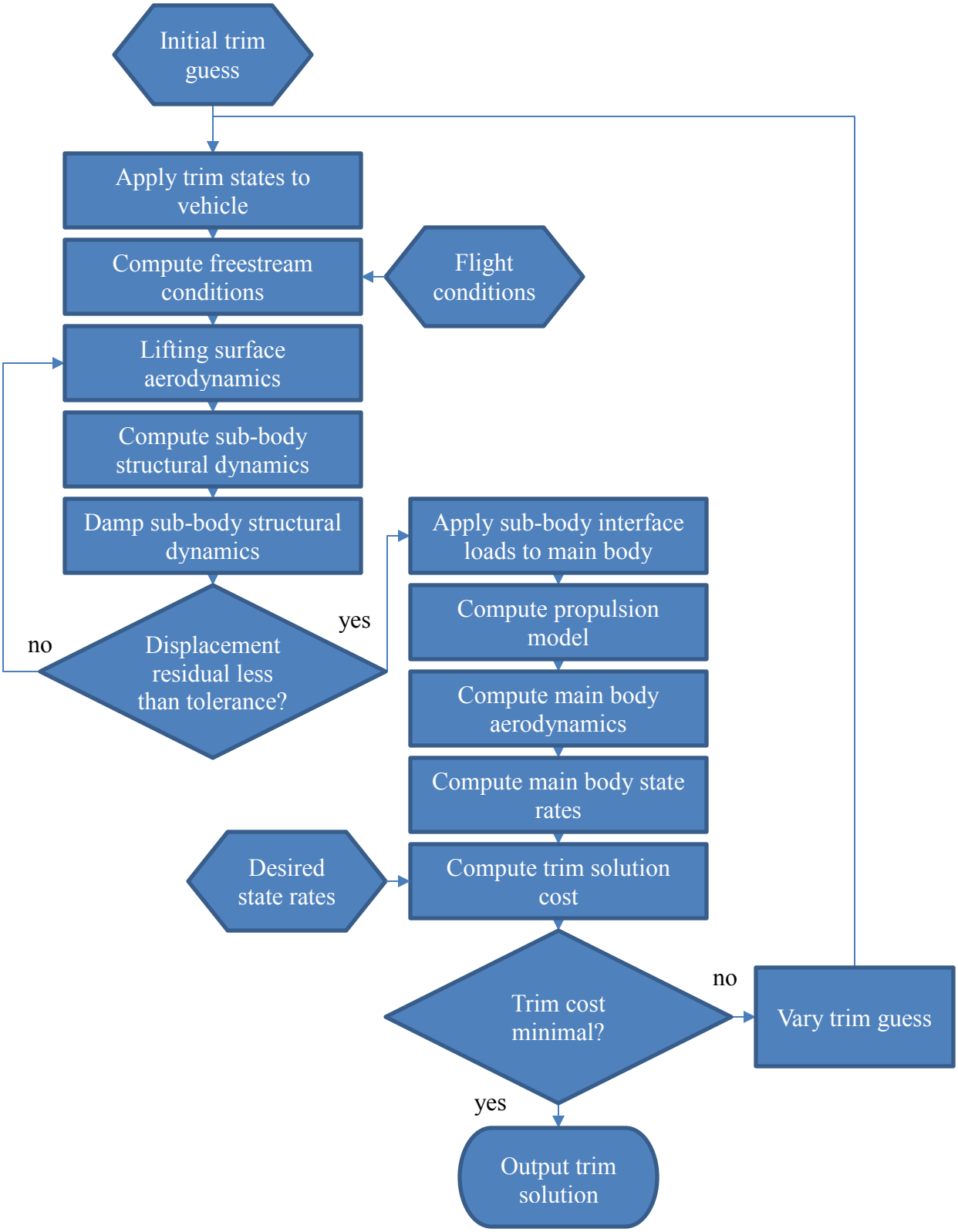

Figure 4.4: Flowchart of the vehicle trim process

If r_{disp} is greater than some tolerance value (typically 10^{-5} to 10^{-9} meters or radians, depending on degree of freedom), then sub-body surface pressures and structural dynamics are recomputed, using the previous displacements solution as the initial condition. If r_{disp} is less than the tolerance value, then the interface loads are computed and applied to the main body. The propulsion model is then considered and the propulsion forces, moments, and nozzle surface pressures applied to the main body. The main body aerodynamics is then computed to determine the surface pressures, before the main body's state rates are determined from the equations of motion that are of the form

$$\dot{x} = f(x) + g(F) \quad , \tag{4.2}$$

where x and $\dot{x}$ are vectors of the main body states and state rates, respectively, F is a vector of the generalized forces on the main body, and $f(\ )$ and $g(\ )$ are some arbitrary functions. A vector of the desired state rates is then subtracted from the solution to (4.2), i.e.,

$$\dot{x}_{cost} = \dot{x} - \dot{x}_{desired} \quad , \tag{4.3}$$

where the subscript *cost* denotes the state rate vector that will later be used in calculation of the trim solution cost and the subscript *desired* denotes a vector of target state rates specified by the user. For many cases, the $\dot{x}_{desired}$ vector will simply contain zeros, and will thus lead the trim solution to be for steady, straight line, (and level if the vehicle is symmetrical) flight. However,

for the cases where one desires to trim the vehicle for a turn, loop, roll, acceleration, etc., this vector provides an easy method of expressing them in the trim cost function. The cost of the trim solution r_{trim} is then given by

$$r_{trim} = \dot{x}_{cost}^{T} [I] \dot{x}_{cost} \quad , \tag{4.4}$$

where $[I]$ is the identity matrix of dimension equal to the length of $\dot{x}_{cost}$.

Given the determination of the cost r_{trim} of a trim solution, the Nelder-Mead simplex method as described by Lagarias et al.[170] is used to find the trim state which minimizes r_{trim}. This method is implemented through the *fminsearch* function of Matlab® and operates as follows:

> "If n is the length of x, a simplex in n-dimensional space is characterized by the $n+1$ distinct vectors that are its vertices. … At each step of the search, a new point in or near the current simplex is generated. The function value at that new point is compared with the function's values at the vertices of the simplex and, usually, one of the vertices is replaced by the new point, giving a new simplex. This step is repeated until the diameter of the simplex is less than the specified tolerance."[171]

Due to the highly nonlinear and often discontinuous nature of hypersonic vehicle flight characteristics, after the *fminsearch* function has reached an exit criteria, r_{trim} is compared to a specified tolerance (typically 10^{-9} mixed units) to determine if the minimization has become stuck at some local minima. Ideally r_{trim} should be driven to zero, however in the event that it is not

below the tolerance, all inputs of the trim solution may be multiplied by pseudo-random numbers between 0.9 and 1.1, or in the event of a zero value to 0.1, in an attempt to "shake" the solution loose from the local minima. The shaken trim inputs are then rerun as the initial guesses of the trim solution by the *fminsearch* function. To prevent this randomization from continually driving the solution away from the global minimum, a log of the trim inputs and related costs is kept for review. Should one notice that the solution continues to converge on some non-zero r_{trim} value, a new initial guess is needed.

4.3 Time Simulation

During a time simulation, the states of an HSV are integrated forward in time for a specified period given generalized forces for each DOF. After integration, the generalized forces and HSV properties are updated. A series of convergence loops are nested around the integration of the states since the states, rates, and forces can be interdependent.

4.3.1 Integration of States

At the heart of the UM/HSV code is a pair of numerical integration routines that integrate the main body EOMs. For most HSV time simulations, the Matlab® function *ode45* is used to run the Runge-Kutta 4th order with Dormand-Prince 5th order error estimation algorithm.[172] In cases where the system is stiff, such as when considering a high-frequency mode basis, then the *ode15s* function may be used.

Within each global time step may be a dozen sub-iterations by the ODE solver and depends on aeroelastic time step size and dynamics of the HSV for a given period of time. Periods of high rates of change in the EOM states, such as during an aggressive maneuver or stage separation,

often require $O(10^1)$ to $O(10^2)$ sub-iterations to achieve the default normalized error tolerance of 10^{-9}. However, the ODE solvers are only used to integrate the EOM of the main body. When sub-bodies are included, the interfacial forces and moments must be considered and they are often a function of the motion of the interface, and therefore depend on the integration of the main body solution. This creates an interdependency of the main body and sub-bodies' solutions.

To account for the interdependence of the main and sub-bodies' solutions, an inner interface-convergence loop is constructed. The aerodynamic and propulsive forces may also be a function of the EOM solutions of their parent bodies, and therefore require an aeroelastic-convergence loop. Finally, an outer aerothermal-loop is used for the aerothermal and heat transfer equations, which often do not require the same time resolution as the aeroelastic dynamics, and so can be super-iterated to save computational resources.

4.3.2 Interface Loop

A summary of the algorithm used to bring the main body and a sub-body into equilibrium within each aeroelastic time step is given in Table 4.1 and is based on the work of Falkiewicz, Frendries, and Cesnik.[173] The iteration procedure begins with the determination of the main body motion in the sub-body frame at the location of the interface. The transformation matrix from the main to sub body frame, T_{rot}, is combined with the relative rotation of the frames due to the deformation of the main body, $\psi_i \eta_i$, where i is the index of the main body elastic mode. This involves use of the skew-symmetric operator, which for a three dimensional problem is given by

$$Skew_3\begin{Bmatrix} x_1 \\ x_2 \\ x_3 \end{Bmatrix} = \begin{bmatrix} 0 & -x_3 & x_2 \\ x_3 & 0 & -x_1 \\ -x_2 & x_1 & 0 \end{bmatrix}. \tag{4.5}$$

The velocity of the restrained DOFs, $\dot{x}_r^{(n+1)}$, in the sub-body frame due to the deformation, $\phi\dot{\eta}$, and rotation, $\zeta \times r$, of the main body is then determined and transformed into the sub-body frame with matrix C in step 2. The displacement of the restrained DOFs at the next time level, $x_r^{(n+1)}$, is determined based on the current displacement, $x_r^{(n)}$, and an average of the velocity between the current and next time levels, $\left(\dot{x}_r^{(n+1)} + \dot{x}_r^{(n)}\right)/2$, and multiplied by the aeroelastic time step, Δt_{AE} in step 3. Next is to determine H_2 of the sub-body equations of motion in step 4 and to find the displacements of the sub-body structure in modal space, $d^{(n+1)}$, in step 5. The unrestrained DOFs are determined in physical space in step 6, followed by the forces on the root, $F_r^W(t,T)$ in step 7. The residual, R, of the interface equilibrium is then determined by comparing the unrestrained DOFs of the current iteration, $x_{u,1}^{(n+1)}$, to the previous iteration, $x_{u,0}^{(n+1)}$ in step 8. If R is less than a tolerance value, tol, then the process concludes. If R is greater than tol, the main body EOMs are integrated over the aeroelastic time step, Δt_{AE}, using the new interface forces from the sub-body, $F_r^W(t,T)$, in the main body frame before step 1 through 9 are repeated until R is less than tol. At which point, the main body and sub-body have been brought into equilibrium.

Table 4.1: Iteration scheme used for bringing main and sub-bodies interfaces into equilibrium[173]

1. $C = T_{rot}\left[I - Skew_3\left(\sum_{i=1}^{m} \psi_i \eta_i \right) \right]$
2. $\dot{x}_r^{(n+1)} = C\left[\sum_{i=1}^{m} \phi_i \dot{\eta}_i + (\zeta \times r) \right]$
3. $x_r^{(n+1)} = x_r^{(n)} + \frac{\dot{x}_r^{(n+1)} + \dot{x}_r^{(n)}}{2} \Delta t_{AE}$
4. $H_2 = \frac{1}{3}\left(f_u^{(n+1)} + f_u^{(n)} + f_u^{(n-1)} \right) + \Phi^T \left[M_{uu} \left(K_{uu}^*(T) \right)^{-1} K_{ur}^*(T) - M_{ur} \right] \frac{x_r^{(n+1)} - 2x_r^{(n)} + x_r^{(n-1)}}{\Delta t_{AE}^2}$
5. $d^{(n+1)} = H_1^{-1}\left(H_2 + H_3 d^{(n)} + H_4 d^{(n-1)} \right)$
6. $x_{u,1}^{(n+1)} = -\left(K_{uu}^* \right)^{-1} K_{ur}^* x_r^{(n+1)} + \Phi\, d^{(n+1)}$
7. $F_r^W(t,T) = -M_{ru} \frac{x_u^{(n+1)} - 2x_u^{(n)} + x_u^{(n-1)}}{\Delta t_{AE}^2} - K_{ru}^* \frac{x_u^{(n+1)} + x_u^{(n)} + x_u^{(n-1)}}{3}$
8. $R = norm\left(x_{u,1}^{(n+1)} - x_{u,0}^{(n+1)} \right)$
9. $x_{u,0}^{(n+1)} = x_{u,1}^{(n+1)}$
10. While $R > tol$
11. $\int_t^{t+\Delta t_{AE}} (\text{Main Body EOMs})\, dt$
12. Repeat steps 1 through 9
13. End

4.3.3 Aeroelastic Loop

Enclosing the interface convergence loop is the aeroelastic convergence loop that considers the interdependency of the EOMs and external forces. During the interface convergence loop, the structural motions of the main and sub-bodies are brought into equilibrium. However, the motion of these bodies affects the aerodynamic and propulsive loads. A summary of the algorithm used to update the external loads and bring the system into equilibrium before incrementing the aeroelastic time step is given in Table 4.2.

At the beginning of each aeroelastic loop, the main body states $x_{mb,1}^{(n+1)}$ and unrestrained displacements of each sub-body $x_{u,1}^{(n+1)}$ at time-instant $n+1$ are determined in the interface loop of

the previous section. In the case when one or more of the sub-bodies are a control surface, actuation δ_i is determined by some function $f(\ )$ given the states, actuation rate, time, temperature, pressure load, etc. at the current time in step 2. Step 3 determines the aerodynamic load F^A on the main and sub-bodies; step 4 determines the propulsive load F^P, given there is a propulsion system; and step 5 determines the gravitational or other body loads F^G. The full equations for steps 3 through 5 are found in Chapter II. The residual R_{mb} is determined as the 2-norm of the difference between the main body state vector of the current loop $x_{mb,1}^{(n+1)}$ and of the previous loop $x_{mb,0}^{(n+1)}$. If R_{mb} is less than an error tolerance tol_{mb} then the aeroelastic loop is complete and time is incremented by one aeroelastic time step Δt_{AE}. If R_{mb} is greater than tol_{mb}, then steps 1 through 9 are repeated with the updated external loads.

Table 4.2: Iteration scheme to converge on aeroelastic solution

1. $x_{mb,1}^{(n+1)} = \int_t^{t+\Delta t_{AE}} (\text{Main Body EOMs})\, dt$, $x_{u,1}^{(n+1)} = -\left(K_{uu}^*\right)^{-1} K_{ur}^* x_r^{(n+1)} + \Phi\, d^{(n+1)}$
2. $\delta_i = f\left(x, \dot{\delta}, t, T, p\right)$
3. $F^A = f\left(x, M, T\right)$
4. $F^P = f\left(x, M, T, \lambda\right)$
5. $F^G = f\left(x\right)$
6. $R_{mb} = norm\left(x_{mb,1}^{(n+1)} - x_{mb,0}^{(n+1)}\right)$
7. $x_{mb,0}^{(n+1)} = x_{mb,1}^{(n+1)}$
8. While $R_{mb} > tol_{mb}$
9. Repeat steps 1 through 7
10. End

4.3.4 Aerothermal Loop

The aerothermal loop is the outmost loop of the three. Unlike the interface and aeroelastic loops, the aerothermal loop does not seek to reduce a residual below some tolerance. It is implemented to permit the super-iteration of the aerothermal and heat transfer equations, whose dynamics are typically some orders of magnitude slower than the aeroelastic dynamics. Thus, to reduce computational cost, the aerothermal loop is only executed once for every heat transfer time step Δt_{HT}. The heat transfer Δt_{HT} time step must be some integer multiple of the aeroelastic time step Δt_{AE}, even if that integer is 1.

CHAPTER V

Sample Cases

This chapter describes the two major families of sample cases used in the numeric investigations. The first is the Air Force Research Laboratory's (AFRL) Intelligence, Surveillance, and Reconnaissance (ISR) cruiser that is designed for multi-mission, round-trip, long-duration flights over contested air spaces. Along with studying the vehicle as a whole, several components-level studies are presented, including isolated lifting surfaces and the propulsion system. The second is the AFRL Initial Concept 3.X (IC3X) vehicle that is designed for strike missions on time-sensitive ground targets. Again, the vehicle is studied as a whole, before being broken down into sections of interest, including the thermal protection system and mid-body shell.

5.1 Intelligence, Surveillance, and Reconnaissance Cruiser

The AFRL ISR cruiser is a wedge-type hypersonic vehicle akin to the NASA X-43 and is based on a 2D hypersonic cruise vehicle presented by Bolender and Doman,[27] augmented with lifting surfaces introduced by Falkiewicz and Cesnik.[36] The straight leading edge of the vehicle maintains an attached oblique shock wave that is deflected under the fuselage. This provides lift for the forebody and compresses the flow for intake into the dual-mode ramjet/scramjet propulsion system located on the underside of the fuselage. Ingested flow is further compressed by an isolator assembly before mixing with hydrogen or kerosene fuel and combusting. The combustion products

are exhausted from the propulsion system and onto an expansion ramp comprising the aft body. As the combusted flow expands outward into the freestream, it presses against the expansion ramp and provides lift for the aft body. Attached to the aft body are a pair of all-movable elevon surfaces and a pair of vertical rudders that provide stability and control.

5.1.1 Vehicle Properties

A summary of the AFRL cruiser vehicle's dimensions and inertial properties is given in Table 5.1 and shown in Figure 5.1. The vehicle is partitioned into a main body that includes the fuselage and scramjet propulsion system, and sub-bodies that include four all-movable lifting surfaces. While the internal structure of the fuselage code have been modeled with 3-D mode shapes, however, for this configuration the fuselage is modeled as a pair of Euler-Bernoulli beams joined at the center of the vehicle and used to model the elastic deformation of the structure. Each *x*-axis cross section of the vehicle is maintained rigid during deformation and follows the displacement of the local beam section. Mass and rotational inertia is distributed along each beam as shown in Figure 5.2 and connections to the sub-body interface locations are considered rigid. Three elastic mode shapes are derived from the beam structure model: a torsion, longitudinal bend, and lateral bend. These mode shapes are shown in Figure 5.3.

Table 5.1: AFRL cruiser selected geometric and structural parameters

Parameter	Description	Value
L_{fore}	Forebody length	15.2 m
L_{aft}	Aftbody length	15.2 m
μ_{fore}	Forebody mass / unit length	838 kg/m
μ_{aft}	Aftbody mass / unit length	1250 kg/m
I_x	Rotational inertial about the vehicle length / unit length	3280 kg m^2/m
EI_{zz}	Lateral bending stiffness	5.06×10^{10} Nm^2
EI_{yy}	Longitudinal bending stiffness	6.32×10^{9} Nm^2
GJ	Torsional stiffness	4.74×10^{9} Nm^2

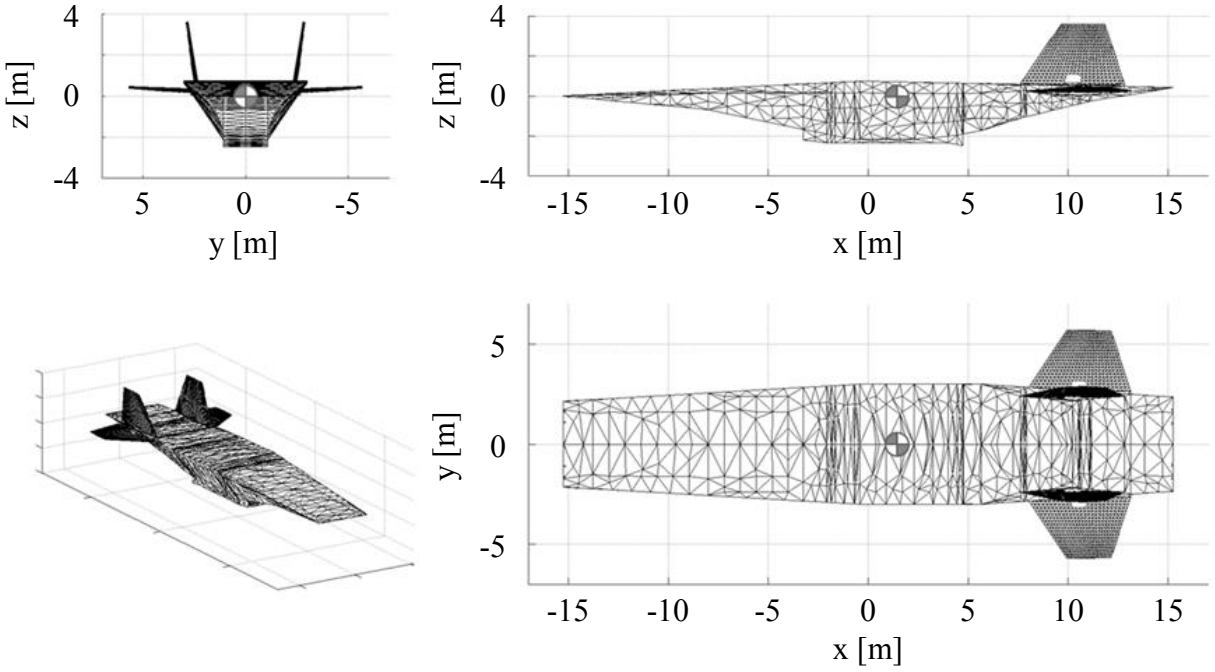

Figure 5.1: AFRL cruiser vehicle configuration

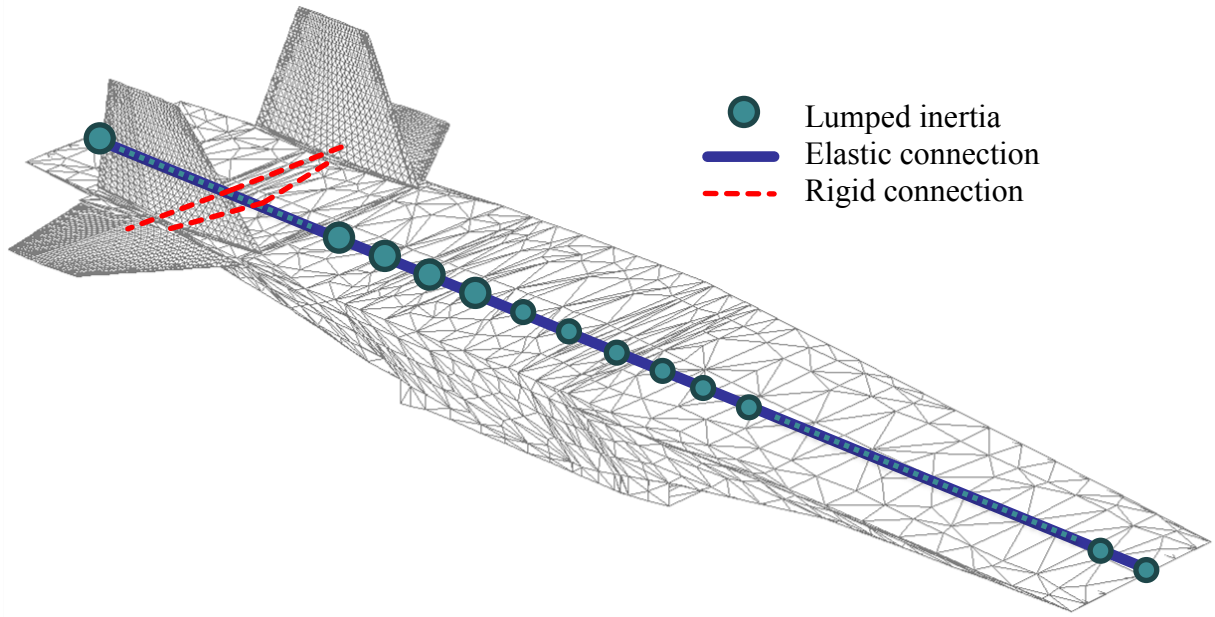

Figure 5.2: Internal structure of the AFRL cruiser vehicle model

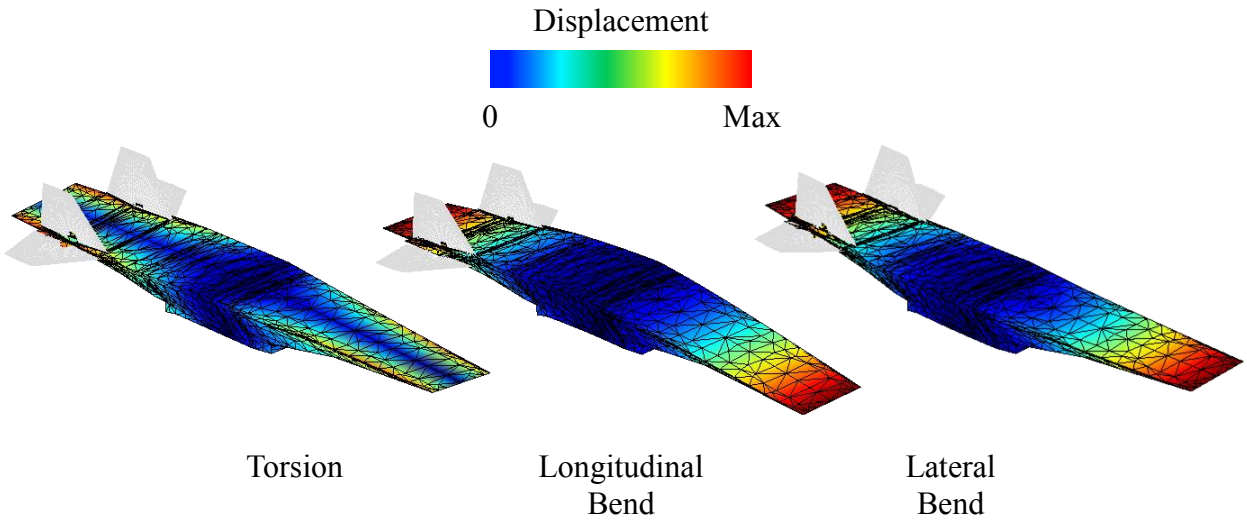

Figure 5.3: Main body elastic mode shapes

The outer-mold line (OML) is comprised of exclusively triangular panels so that deformation of the OML does not produce any nonplanar surfaces. This allows each surface panel to maintain a unique outward normal that may be used for aerodynamic and aeroheating calculations.

5.1.2 Control Surfaces

At the aft of the vehicle are four all-movable surfaces. Two nearly horizontal surfaces are used as elevons while two nearly vertical surfaces are used as rudders. The planform is loosely based on the F-104 Starfighter wing and is shown in Figure 5.4. The airfoil is a symmetric double-wedge or diamond with a 4.3% thickness to chord ratio. Twenty-three evenly spaced spars and nineteen chord-wise stiffeners of 25.4 mm thick titanium alloy 834, make up the internal structure.[36] The skin is a three system of an external refractory metal heat shield of Renè 41,[174] Min-K® insulation,[175] and titanium alloy 834 skin. The skin system is shown in Figure 5.5 with material properties in Table 5.2.

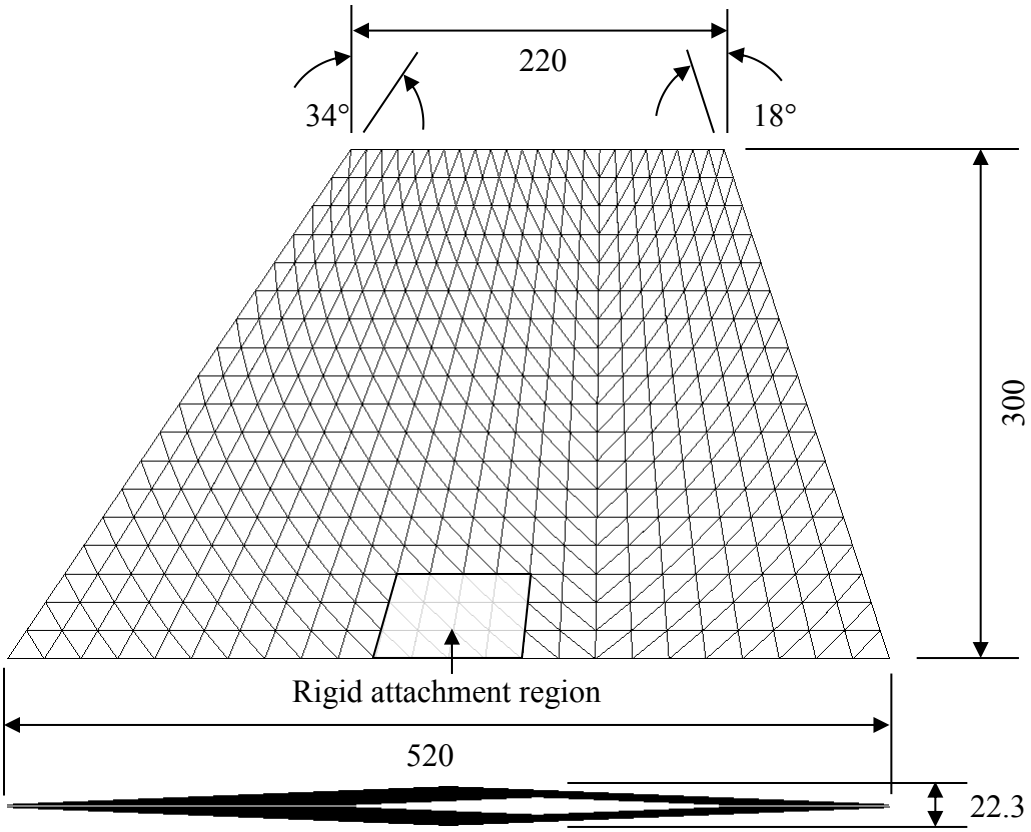

Figure 5.4: Basic control surface model[36]

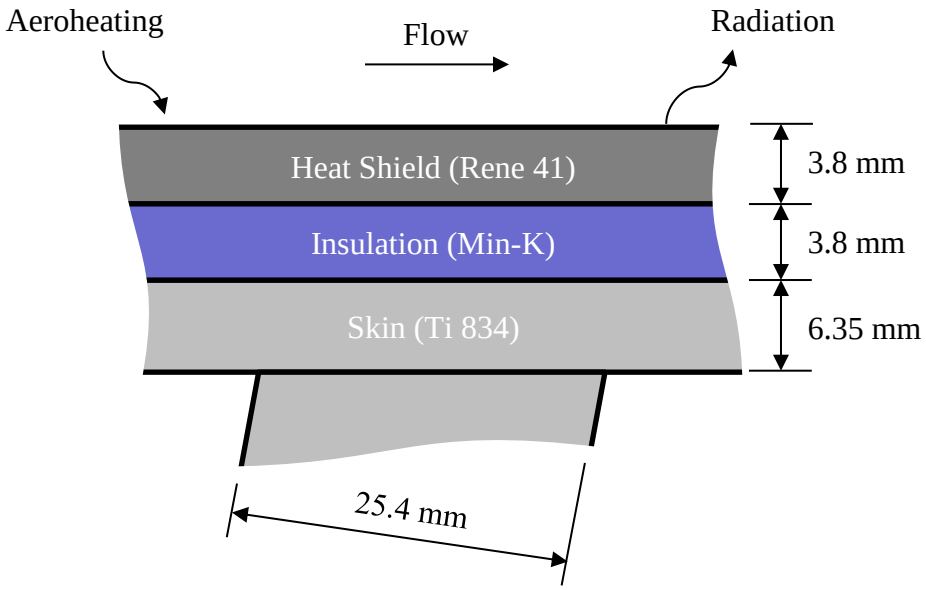

Figure 5.5: Control surface skin system[36]

Table 5.2: Control surface material properties

(T-dep. = temperature dependent, Neg. = negligible)

	ρ [kg/m^3]	E [GPa]	ν	α_T [μm/m/K]	k_T [W/m/K]	c_p [J/kg/K]	T_{max} [K]
Renè 41	8240	T-dep.	0.31	T-dep.	18	541	1500
Min-K®	256	Neg.	Neg.	Neg.	0.052	858	1250
Ti 834	4550	T-dep.	0.31	11	7	525	837

As with the fuselage, the control surfaces express deformation via a basis of mode shapes. These are derived from both free vibration and static loading at a reference tempearture,[36] and are shown in Figure 5.6. Due to the temperature dependent nature of the material properties, the mode shapes do not have unique frequencies. The full process used to select these mode shapes and the loading conditions considered are described in Falkiewicz and Cesnik.[36]

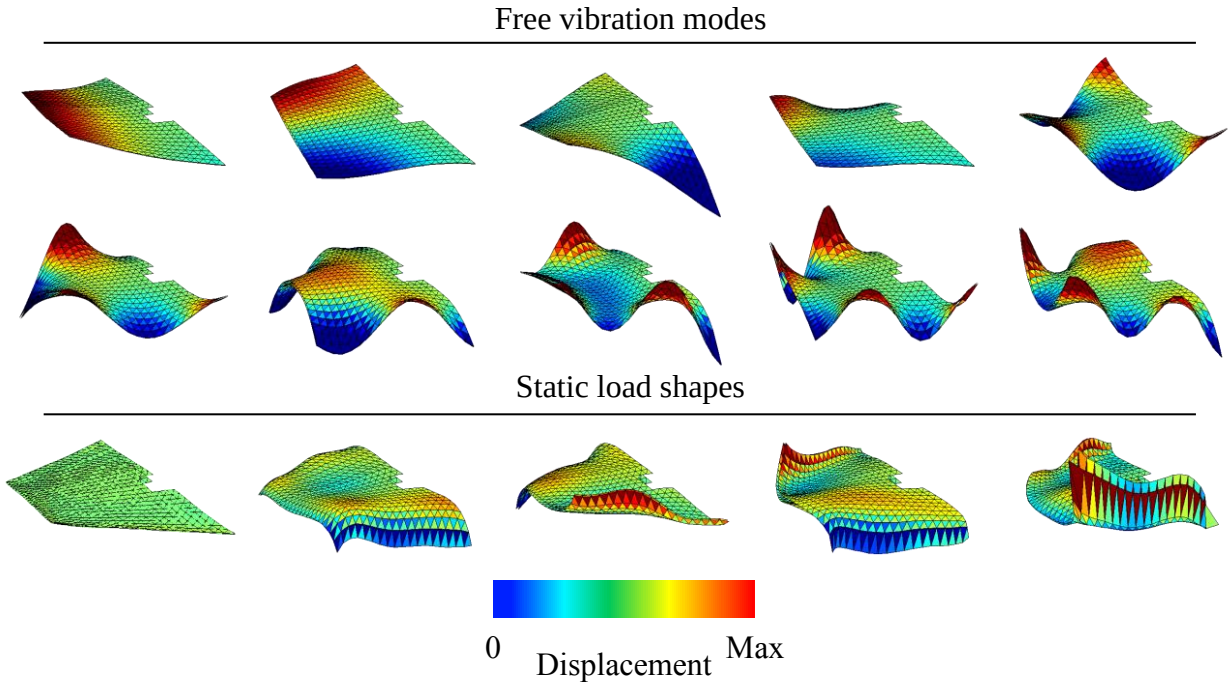

Figure 5.6: Control surface elastic basis mode shapes

5.1.3 Propulsion System

Nearly the entire underbelly of the vehicle consists of a dual-mode ramjet/scramjet propulsion system with the dimensions shown in Figure 5.7. The double-ramp inlet section produces a pair of oblique shock waves that pass just outside or on the lip of the cowl. These shock waves provide the initial compression of the flow to ensure efficient combustion and lift for the forebody. A short isolator section is used to increase the flow temperature and pressure of the flow via a train of shock waves. In ramjet mode, the shock train terminates in a normal shock that brings the flow subsonic before entering the combustor section. However, in scramjet mode, the flow remains supersonic into the combustor section where hydrogen or kerosene fuel is injected and combusts. The exhaust products are then expanded in the nozzle section to provide thrust and lift.

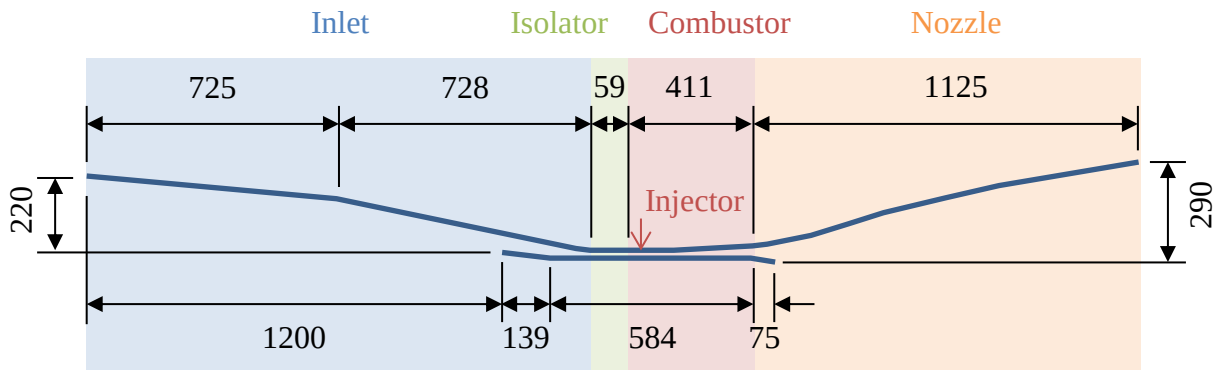

All dimensions in centimeters

Figure 5.7: Ramjet/scramjet propulsion system dimensions

5.2 Initial Concept 3.X Vehicle

An initial sizing study by the AFRL Munitions Directorate led to the creation of a representative configuration.[176,177] This vehicle was to be an air-launched, rocket-scramjet combined cycle propelled vehicle that performed a three-phase trajectory. Shown in Figure 5.8,

the vehicle would first be boosted by rocket propulsion up to a cruising altitude of more than 50 kft (15.2 km) and Mach number greater than 5. A spent rocket booster would then be jettisoned and a scramjet propulsion system engaged to maintain a cruise condition for the majority of the overall trajectory. Finally, after exhausting the scramjet fuel supply, the vehicle would enter a terminal phase in a hypersonic glide condition to reach a ground target some distance downrange.

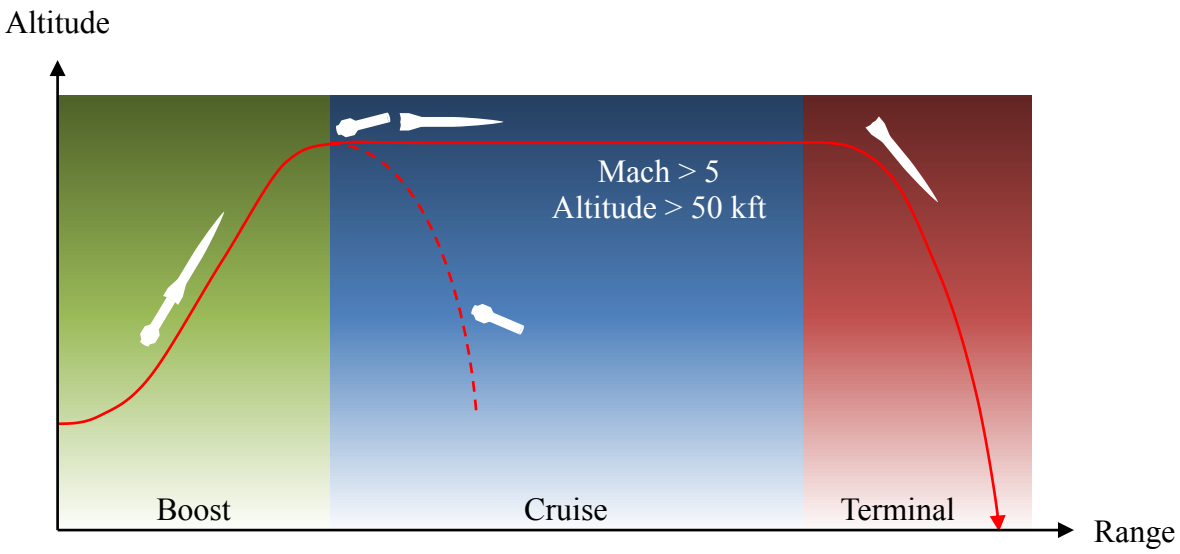

Figure 5.8: Basic outline of a boost-cruise-terminal mission profile for an air-launched, rocket-boosted hypersonic vehicle

5.2.1 Vehicle Properties

The IC3X vehicle configuration was largely established by Witeof and Neergaard[177] using the Preliminary Aerothermal Structural Simulation (PASS) code suite[176] and is shown in Figure 5.9, Figure 5.10, and Figure 5.11. Basic properties are given in Table 5.3 and component materials in Table 5.4.

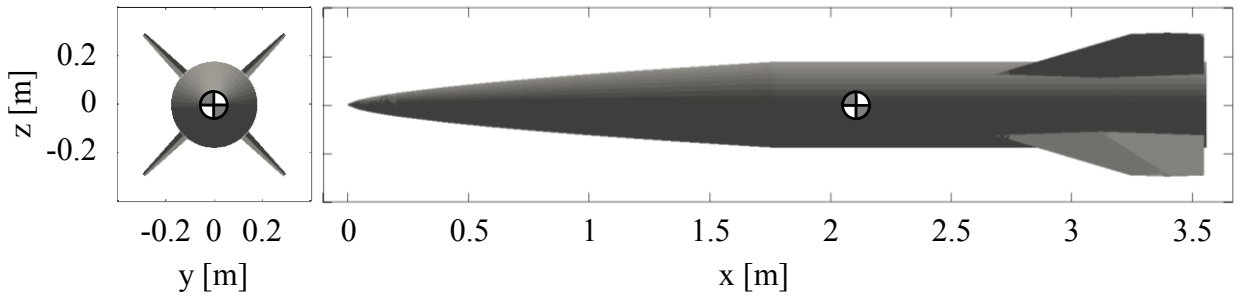

Figure 5.9: Representative vehicle dimensions

Table 5.3: Basic properties

Property	Fully Fueled	Reserve Fuel Only
Body length (m)	3.56	3.56
Body diameter (m)	0.36	0.36
Wingspan (m)	0.82	0.82
Center of gravity (m)	2.09, 0, 0	2.06, 0, 0
Mass (kg)	375	307
I_x (about CG) (kg m^2)	9.42	7.37
I_y (about CG) (kg m^2)	345	338
I_z (about CG) (kg m^2)	345	338

The body is axisymmetric with four aft all-movable fins for stability and control. Beginning at the nose tip, the OML starts with a 10-mm diameter hemisphere tangent-transitioned to power-law forebody following the relation:

$$r = 0.126x^{0.6}, \tag{5.1}$$

where r is the radius in meters of the OML x meters along the axis of symmetry from the nose. At 1.78-m from the nose, the body transitions to a 0.36-m constant diameter cylinder, which continues until the trailing end, 3.56-m from the nose tip. The fins, shown in Figure 5.10, are diamond airfoils with a maximum thickness at 50% chord. The maximum thickness is 5% of the

chord, plus a 1 mm TPS layer. Internally, the fins are solid QISO^{TM} triaxial weave carbon-carbon composite that is assumed quasi-isotropic. The root chord is 86.4-cm and tapers down to a 30.4-cm chord at the tip. The leading edge is swept back 67.3° and the trailing edge is unswept. The fins are attached to the body by 17.8-cm long, 2.0-cm diameter solid shafts, 51.8 cm from the leading edge and formed from the same carbon-carbon composite as the internal fin structure. The center of each fin shaft is attached to the body 3.2 m from the nose tip.

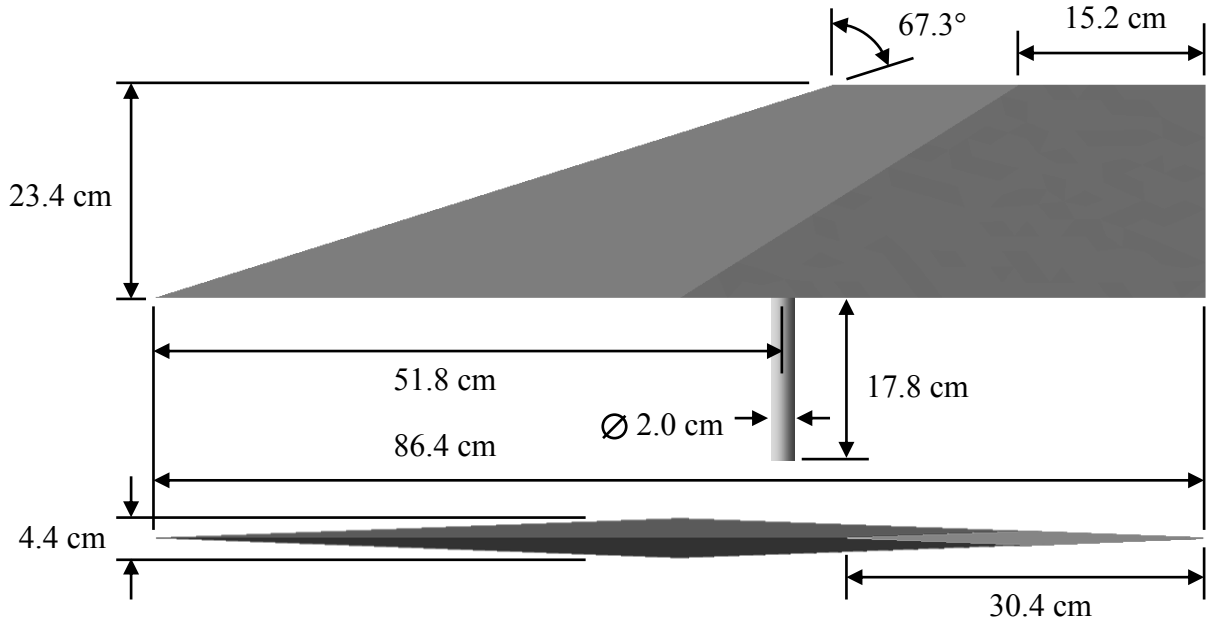

Figure 5.10: Fin OML dimensions

Shown in Figure 5.11, the internal structure is a titanium alloy monocoque with additional stiffeners between a fin root box and trailing end. The purpose of the stiffeners is to support the body during the boost phase of flight when a rocket motor mounted to the trailing end is used to bring the vehicle to cruising speed. The thickness of the monocoque skin varies between 1.3 mm and 3.1 mm according to an optimization performed previously using the PASS code suite.[176]

Covering the monocoque skin is a TPS of Exelis™ Acusil-II[178] material. Like the monocoque skin, the TPS varies in thickness according to optimization results from the PASS code suite,[176] but generally is thicker near the nose, thins along the body toward the tail, and thickens again aft of the fin root shafts to permit a cooler, stiffer structure near the fin root box. At the nose is a solid, tungsten ballast that forms the first 20 cm of the nose that bears the stagnation heat flux during hypersonic flight and brings the center of gravity forward. Within the body is also a 90-kg steel casing that acts as a thermal sink for temperature sensitive components. During analysis, the steel casing is considered only as a thermal sink and its mass is not directly used. Instead, nonstructural masses are distributed along the monocoque skin to account for various internal subsystems. Although a scramjet propulsion system is assumed to maintain the cruise conditions, no flow path geometry is defined.

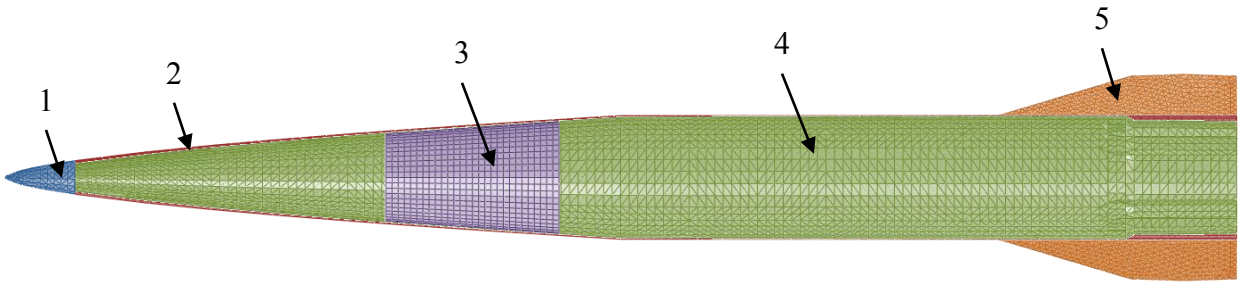

Figure 5.11: IC3X internal structure mid-span cross-section and FEM

Table 5.4: IC3X materials (see Figure 5.11)

ID	Component	Material(s)
1	Nose ballast	Tungsten
2	Thermal protection system	Acusil-II
3	Casing	Carbon steel
4	Monocoque	Titanium alloy
5	Control fins	QISO carbon-carbon composite & Acusil-II

5.2.2 Material Properties

It is expected that the operating temperatures will be sufficient to cause significant changes to the properties of its constituent materials. Thus, data for material properties over a wide range of temperatures are required and given in Table 5.5 and Figure 5.12. The TPS material, Acusil-II,[178] is assumed to not contribute to the structural stiffness and is assigned a Young's modulus of 0.01 GPa, so to be low but not cause numerical instability. Material properties were found from a variety of sources.[178–185]

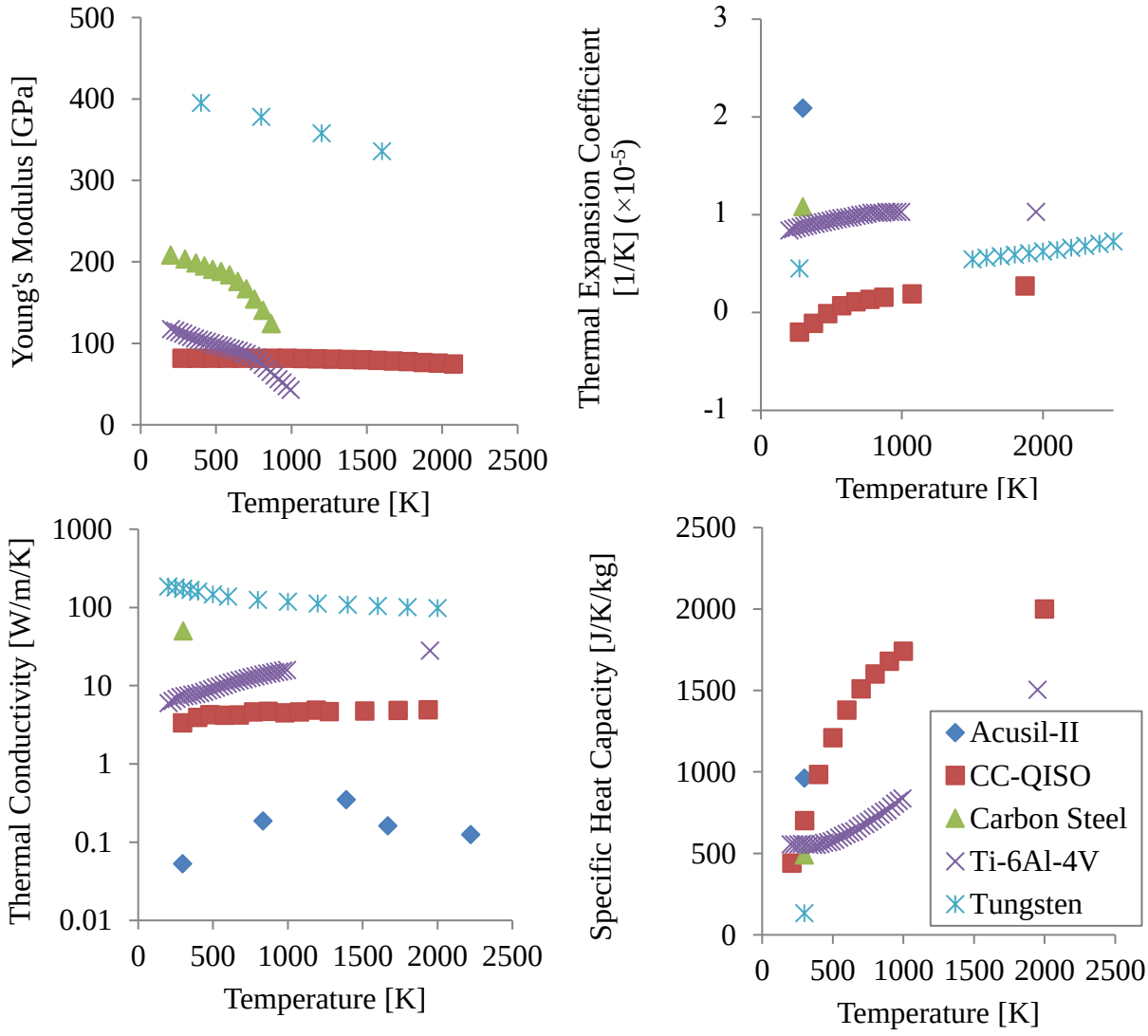

Figure 5.12: Temperature dependent material properties[178–185]

Table 5.5: Temperature independent material properties

	Density [kg/m^3]	Poisson's Ratio
Acusil-II	256.3	0.30
CC-QISO	1650.0	0.21
Carbon Steel	7900.0	0.30
Ti-6Al-4V	5199.4	0.31
Tungsten	19250.0	0.26

5.2.3 Sample Substructure

To quickly perform representative thermal analyses, a sample FEM was established which is representative of a small portion of the IC3X. This substructure is located at the interface of the vehicle nose ballast and fore-body, on the Earth-facing side during typical flight conditions, in a region that was shown to experience high thermal loads and also contain several different materials.[3] For simplicity, this substructure is considered to be approximately 2D, despite the curvature of the vehicle's body in this region. The vehicle, sample substructure, and FEM grid are shown in Figure 5.13. The FEM consisted of 6478 nodes and 3040 linear hexahedral solid elements clustered near regions where high temperature gradients are expected due to external heat flux or material interfaces. Three materials are considered: elemental tungsten in the nose ballast, Exelis Inc.'s Acusil-II® material in the thermal protection layer covering the fore-body, and titanium alloy Ti-6Al-4V that comprised the structural monocoque of the vehicle. For simplicity, neighboring materials are considered to be perfectly bonded and no joiner or fastener geometry was included. Boundaries of the FEM that are not exposed to the external heat flux are adiabatic.

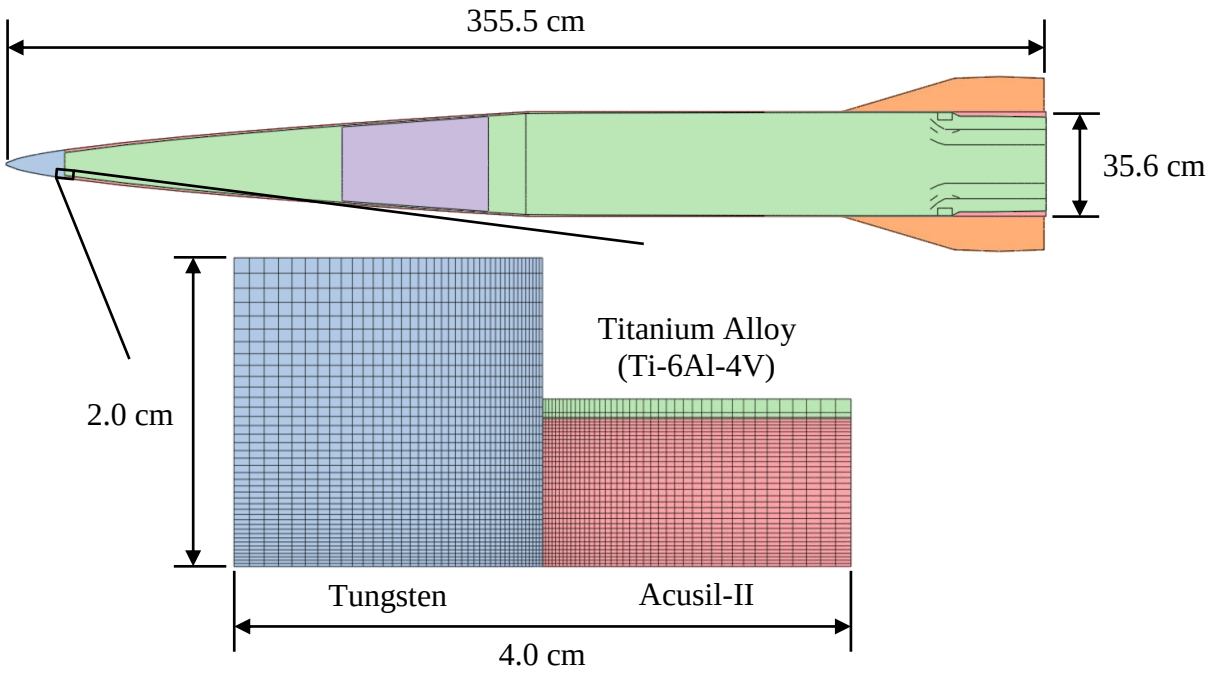

Figure 5.13: Sample substructure with overlaid FEM grid and its location on the vehicle

5.2.4 Cylindrical Shell Model

It was anticipated that the nose and cylindrical sections of the IC3X might be subjected to an aeroelastic instability akin to panel flutter during the terminal phase of flight. An experimental configuration previously investigate in literature[126,127,130] was considered to characterize the nature of this instability and determine if the reduced order model methods developed as part of this study are appropriate. A finite element model (FEM) is constructed to match the materials, dimensions, and boundary conditions described in literature which consisted of a circular cylindrical shell formed from electroplated copper with dimensions shown in Figure 5.14 and whose properties are given in Table 5.6. The shell section was welded to copper rings on each end which were held to the test mount by 4.763-mm diameter rubber tubing.[126] The boundaries of the shell were approximately clamped except for axial displacement, which allowed the length of the shell to

vary under load. Axial flow was passed over the outer surface while stagnant air was held in a cavity within the shell. Inner surface pressure and freestream flow conditions are summarized in Table 5.7.

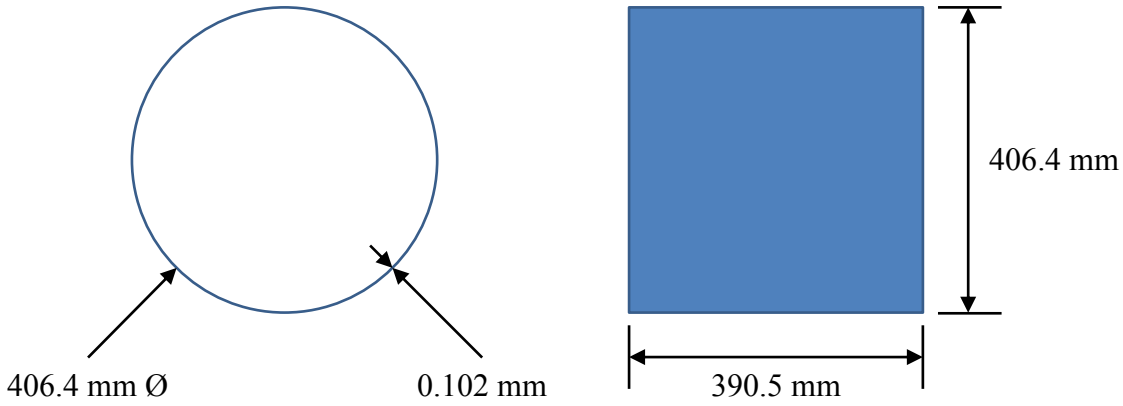

Figure 5.14: Dimensions of the test cylindrical shell[126]

Table 5.6: Material properties of copper[186,187]

Property	Symbol	Value	
Modulus of elasticity	E	115	GPa
Density	ρ	8960	kg/m^3

Table 5.7: Test condition ranges of the cylindrical shell case[126]

Flow condition	Minimum	Maximum
Freestream Mach number	2.5	3.5
Freestream total pressure (kPa)	84.7	135.4
Freestream total temperature (K)	322.0	322.0
Inner gauge pressure (kPa)	-0.3	27.6

CHAPTER VI

Numerical Studies

The partitioned approach to hypersonic vehicle simulation is implemented and verified using the University of Michigan High Speed Vehicle simulation code. Trim and time simulations of monolithic and partitioned aeroelastic models of the Air Force Research Laboratory's Intelligence, Surveillance, and Reconnaissance Hypersonic Vehicle are compared. Stability analysis of an aerothermoelastic control surface is also performed to demonstrate the thermal and thermoelastic capabilities of the simulation code. Model reduction techniques are then applied to the Initial Concept 3.X vehicle. Fundamental shock, expansion, and piston theory aerodynamic models are compared to Euler CFD solutions and used along with three degree-of-freedom equations of motion to optimize a family of terminal trajectories for maximum final kinetic energy. Outer mold-line flow conditions are determined along a representative terminal trajectory selected from the optimized family, and Eckert's reference temperature method is used to determine surface heat fluxes to a FEM of the vehicle. Integration of the heat transfer equations provides a set of temperature snapshots that, once proper orthogonally decomposed, provide a modal basis set with which to reduce the heat transfer equations. Free vibration mode shapes are also determined from the FEM at a reference temperature distribution and used as a basis to reduce the elastic equations of motion. Finally, a kriging surrogate model is trained to capture the thermoelastic effects that arise from material property degradation and geometric stiffening due to temperature.

Next, it is shown that the assumption of constant material thermal properties when using the proper orthogonal decomposition derived thermal basis may result in significantly inaccurate temperature solutions. High dimensional polynomials, the kriging method, and a novel method based on singular value decomposition (SVD) are compared to capture the variation of generalized thermal capacity and conductivity based on thermal basis coordinates. The SVD-based method is shown to be superior and the resulting enhanced thermal model system is shown to agree well with high-fidelity finite element solutions.

The SVD-based method is then combined with the complex-step method of state space identification to estimate nonlinear state space representations of dynamic systems. A simple nonlinear-spring, mass, and damper system is used to investigate the method's training and stability characteristics before being applied to the IC3X vehicle. Time simulation results are compared with UM/HSV solutions and shown to be highly accurate while requiring an order of magnitude less processing time during integration.

Finally, terminal trajectory simulations of the IC3X with the UM/HSV code indicated a unique form of aeroelastic instability characteristic of cylindrical shells. To determine if the UM/HSV code and model reduction techniques are adequate for the prediction of this instability, the experimental results of Olson and Fung[126] are numerically reproduced using nonlinear FEA to model an internally pressurized cylindrical shell section in supersonic flow. Reduced order models derived from the FEM are used within the UM/HSV code and shown to capture the unpressurized shell stability boundary, but lack the ability to represent a destabilizing effect of moderate internal pressure that was observed by Olson and Fung[126] and the nonlinear FEA results.

6.1 Partitioned Model of the Intelligence, Surveillance, and Reconnaissance Vehicle

To verify that the partitioned approach to vehicle simulation is valid, trim and time simulation results for the AFRL cruiser are compared with its monolithic counterpart. No thermal model was developed for the fuselage of the AFRL cruiser, thus the comparison was performed as purely aeroelastic. Furthermore, to allow each model to have the same number of elastic degrees of freedom, the lifting surfaces are assumed rigid for this comparison. To demonstrate the thermodynamic capabilities of the UM/HSV code, an aerothermoelastic stability analysis is performed for one of its aft control surfaces.

6.1.1 Vehicle Trim

Using the Matlab function *fminsearch*, the following cost function J_{trim} can be minimized:

$$J_{trim} = \begin{bmatrix} \dot{u} \\ \dot{v} \\ q \\ \dot{\eta}_y \end{bmatrix} \begin{bmatrix} \\ I \\ \\ \end{bmatrix} \begin{bmatrix} \dot{u} & \dot{v} & q & \dot{\eta}_y \end{bmatrix}, \tag{6.1}$$

where $\dot{u}$ and $\dot{v}$ are forward and lateral accelerations, respectively, q is pitch acceleration, $\dot{\eta}_y$ is the longitudinal bending rate, and I is the identity matrix. To avoid local minima, the solution of *fminsearch* is randomly perturbed by up to 10% for each parameter and reentered as the initial guess for another minimization. The two solutions are then compared for agreement. If the maximum residual is less than 1%, the solution is considered to represent a global minimum. The trim conditions for both a rigid and flexible AFRL cruisers are considered in the sample simulation for steady level flight at Mach 6.0 and altitude of 26 km are given in Table 6.1.

Table 6.1: AFRL cruiser steady level flight trimmed conditions, Mach 6, 26 km altitude

		Rigid Vehicle		Flexible Vehicle	
Symbol	Description	Partitioned Solution	Monolithic Solution	Partitioned Solution	Monolithic Solution
α	Angle of attack (deg)	–0.64	–0.61	–0.66	–0.61
η_1	Lateral bending mode amplitude	–	–	0	0
η_2	Longitudinal bending mode amplitude	–	–	–0.003	–0.004
η_3	Torsion mode amplitude	–	–	0	0
δ_e	Horizontal elevon deflection (deg)	1.49	1.49	2.06	1.61
ϕ	Fuel equivalence ratio	0.126	0.126	0.139	0.122
	Minimized Parameters				
$\dot{u}$	Forward acceleration (m/s^2)	2.4×10^{-1}	1.6×10^{-2}	2.5×10^{-1}	3.1×10^{-5}
$\dot{w}$	Vertical acceleration (m/s^2)	2.4×10^{-2}	1.5×10^{-3}	1.8×10^{-2}	-7.5×10^{-5}
$\dot{\omega}_y$	Pitch angular acceleration (deg/s^2)	7.2×10^{-3}	4.9×10^{-4}	7.0×10^{-3}	9.2×10^{-7}
$\ddot{\eta}_{lon}$	Longitudinal bending mode acceleration ($1/s^2$)	-	-	9.2×10^{-3}	1.6×10^{-5}

One can see from Table 6.1 that for the rigid vehicle cases, the partitioned and monolithic trim solutions match very well with only minor differences in the angle of attack and the minimization parameter values. This result supports that in steady cases the partitioned solution matches the monolithic solution. The flexible cases do not agree as well as the rigid ones, particularly for the elevon deflection angle with a 28% error and 14% error in fuel equivalence ratio. However, the error normalization can be misleading as these disagreements are small in magnitude, not exceeding 0.45° and 0.017, respectively, and it is the division by small reference values that inflate the percentage errors. It is likely that these differences arose from the fact that in the monolithic solution, the all-movable surfaces are deformed slightly by the longitudinal bending mode of the fuselage. Since the entire vehicle has been considered as one object, this bending mode also applies to the control surfaces; whereas the partitioned solution control surfaces

do not deform with the fuselage. A true monolithic model of the AFRL cruiser would have to be created independently from the simulation architecture presented here to eliminate these differences.

6.1.2 Time Simulation

By iteratively computing the EOMs, component models, and generalized forces, the simulation is marched forward in time. Time simulation results may be viewed as either video, snapshot of it exemplified in Figure 6.1, or time history plots as shown in Figure 6.3 through Figure 6.6. The partitioned and monolithic solutions are each simulated starting at their respective trim conditions outlined in Table 6.1. The flight conditions and simulation parameters are listed in **Error! Reference source not found.**. Note that since the monolithic solution is treated as a main body object, the only time step of significance is the aeroelastic time step. The heat transfer time step, aerothermal time step, and residual displacement tolerance are only used for the partitioned solution.

Table 6.2: Sample AFRL cruiser simulation parameters

Parameter	Description	Value
M	Initial flight Mach number	6.0
h	Initial flight altitude	26.0 km
Δt_{AE}	Aeroelastic time step	0.001 s
Δt_{HT}	Heat transfer time step	0.001 s
Δt_{AT}	Aerothermal time step	0.010 s
R_{tol}	Fuselage/control surface residual displacement tolerance	10^{-5} m

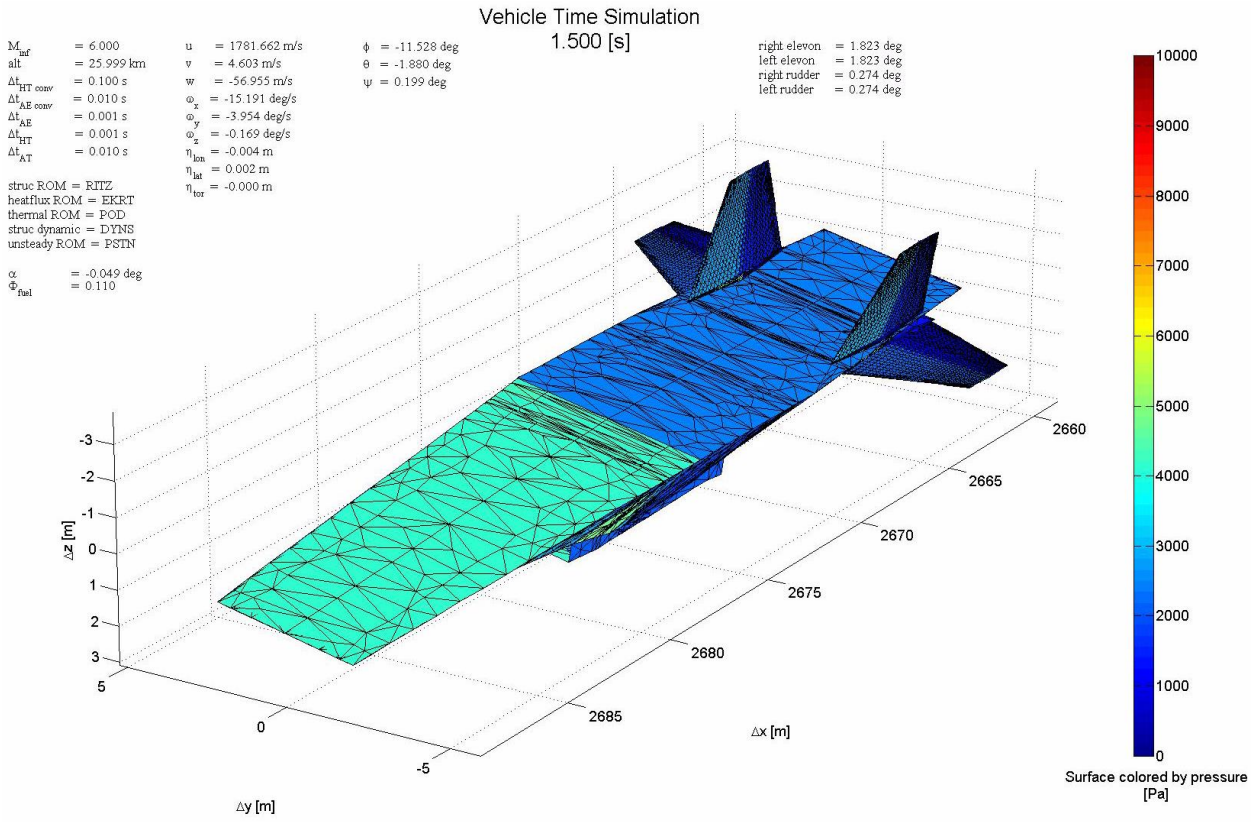

Figure 6.1: Sample AFRL cruiser simulation video rendering during a roll maneuver

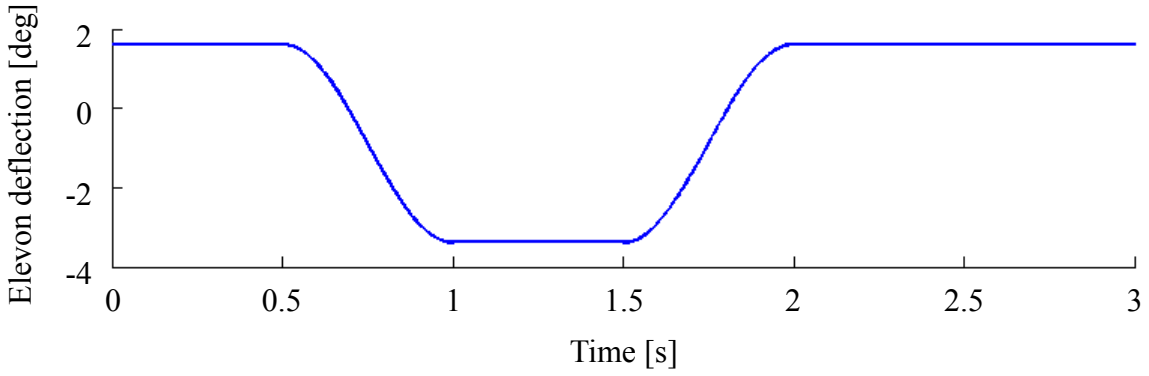

Figure 6.2: Commanded horizontal elevon deflection for the rigid partitioned solution case

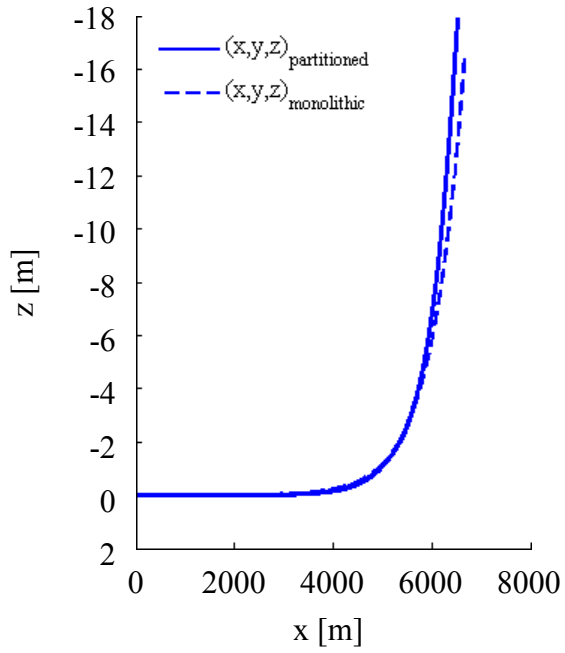

Figure 6.3: Rigid body position

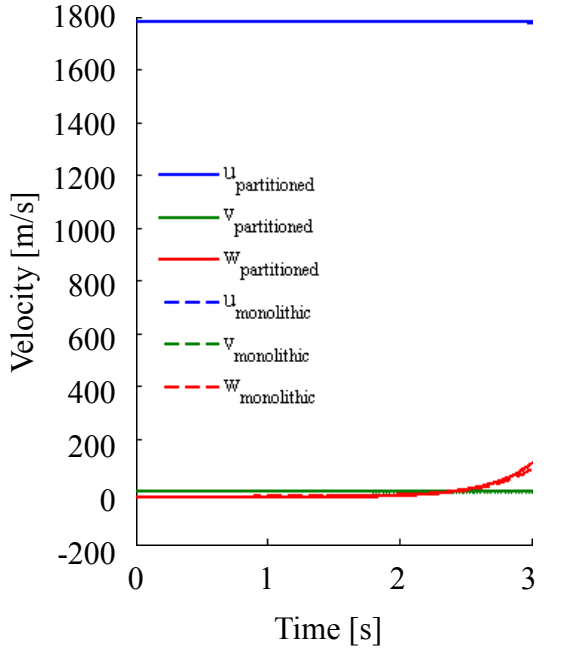

Figure 6.4: Rigid body velocity

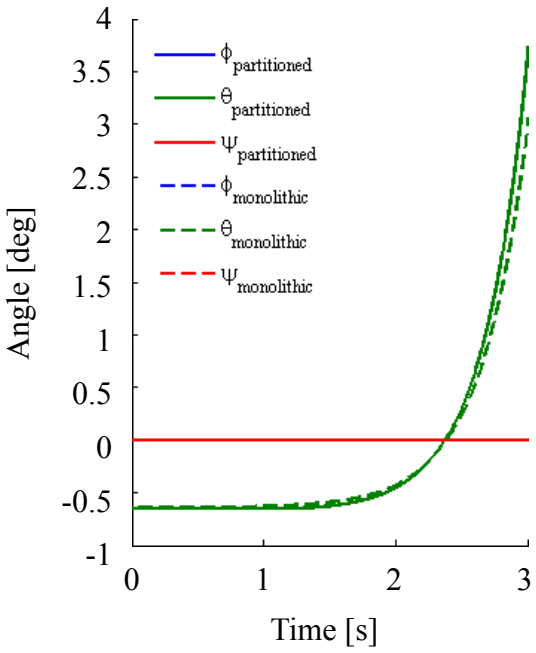

Figure 6.5: Rigid body Euler angles

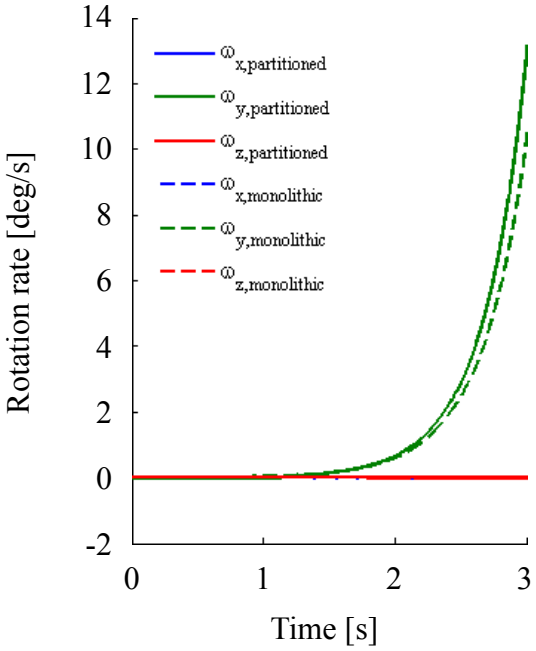

Figure 6.6: Rigid body angular rates

Figure 6.3 through Figure 6.6 show that the partitioned and monolithic solutions generally match in form and behavior. Some slight differences can be seen in the pitch angle and rotation rate, θ and ω_y respectively. These differences are within what was expected and are likely due to the actuation torques at the root of the elevon for the partitioned solution. These actuation torques are not captured by the monolithic solution since the OML mesh is directly modified to effect the change in elevon deflection.

The simulations were carried out on an Asus Workstation computer with an 8-core 2.00 GHz Intel Xeon processor and 32 GB RAM. For 3 seconds of simulation, the partitioned solution was completed in ~32 minutes and the monolithic solution in ~14 minutes. The additional time required for the partitioned solution was largely due to iteration of the interface convergence loop, which requires at least two loops in order to find a residual value to confirm that the interface motions and forces have met the specified tolerance.

6.1.3 Control Surface Stability Analysis

Determining the aeroelastic stability of a vehicle is critical in establishing the flight envelope of the vehicle. For the AFRL cruiser model, early time simulations at high Mach numbers (approximately Mach 8 or greater) and low altitude (approximately 10 km) showed possible control surface flutter. To characterize its dynamic response in flight a linear representation of the control surface motion can be established as

$$\dot{x}(t) = Ax(t) \ , \tag{6.2}$$

where $x(t)$ is the state vector, taken to be the amplitudes of 15 elastic structural Ritz modes and their 15 respective time derivatives, and A is the linear state matrix. The entries of A are approximated from time simulations of the control surface as

$$\dot{x} = f(x) \ , \tag{6.3}$$

$$A(:,k) \simeq \frac{f(x_e + \Delta_{xk}) - f(x_e - \Delta_{xk})}{2\varepsilon_{xk}} \ , \tag{6.4}$$

where $A(:,k)$ denotes the k^{th} column of A, x_e is the trim state such that $f(x_e) = 0$, and the perturbation Δ_{xk} is of the form

$$\Delta_{xk} = \begin{bmatrix} 0 & \cdots & \varepsilon_{xk} & 0 & \cdots & 0 \end{bmatrix}^T \ , \tag{6.5}$$

where ε_{xk} is 1% of the k^{th} trim state or a small value if the k^{th} trim state is zero. The function $f(x_e \pm \Delta_{xk})$ is approximated by a 6^{th}-order forward difference of 7 time steps of the control surface simulation.

The structural properties of the control surface will vary over time due to the exposure to the hypersonic flow. Aerodynamic heating will degrade the material stiffness and uneven thermal expansion will create both geometric stiffening and thermal loads on the surface. To account for these effects, the solutions uses the Eckert reference temperature method and the POD thermal ROM to time march the thermal analysis of the control surface starting at the reference state of

uniform 293-K structure. Without loss of generality, to decrease the computational burden for this study, the control surface is flown at 10-km altitude. This altitude is not typical of most hypersonic vehicles, air-breathing or otherwise, due to thermal and scramjet performance issues that would arise from passing through the denser lower atmosphere. Altitudes of 20 to 30 km are more typical for hypersonic vehicles, however these would result in higher flutter Mach numbers and lower aeroheating, requiring longer simulation runtimes to heat the control surface sufficiently for thermal effects to make a similar impact.

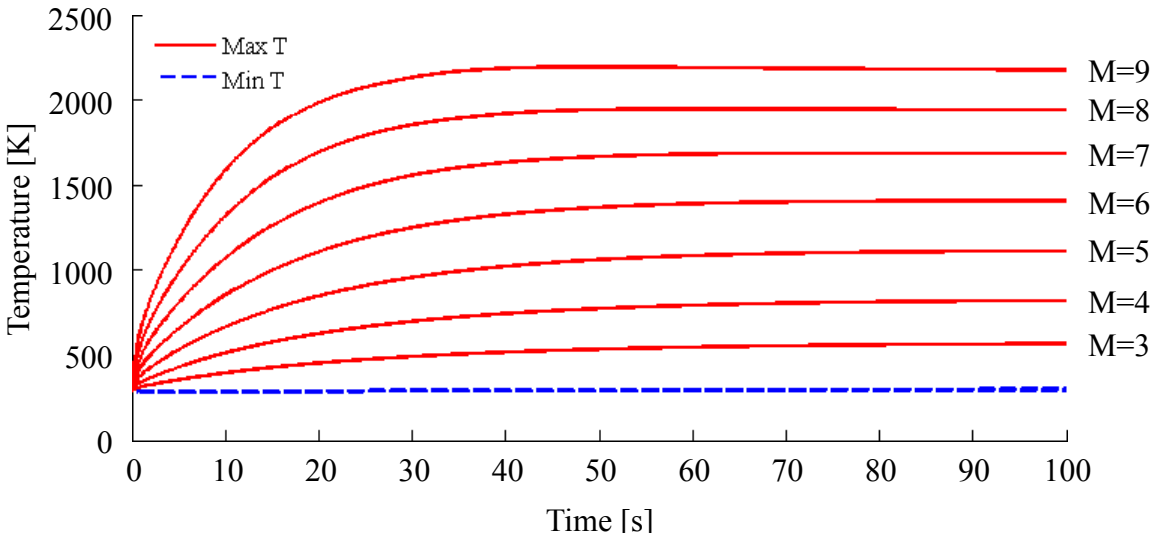

Figure 6.7: Temperature range of all points of the control surface structure for prolonged cruise at an altitude of 10 km

The stability of the control surface at a given Mach number and time exposed to flow is determined by the relation of the eigenvalues λ of A of the form

$$As = \lambda s \ , \tag{6.6}$$

where s are the associated eigenvectors. A mode of the control surface is deemed to be unstable when the corresponding root crosses to the positive real half plane. For the case of the control surface used as part of the AFRL cruiser, started at a uniform 293 K and instantaneously exposed to the hypersonic flow, the behavior of the unstable (first vibration) mode is shown in Figure 6.8 and Figure 6.9.

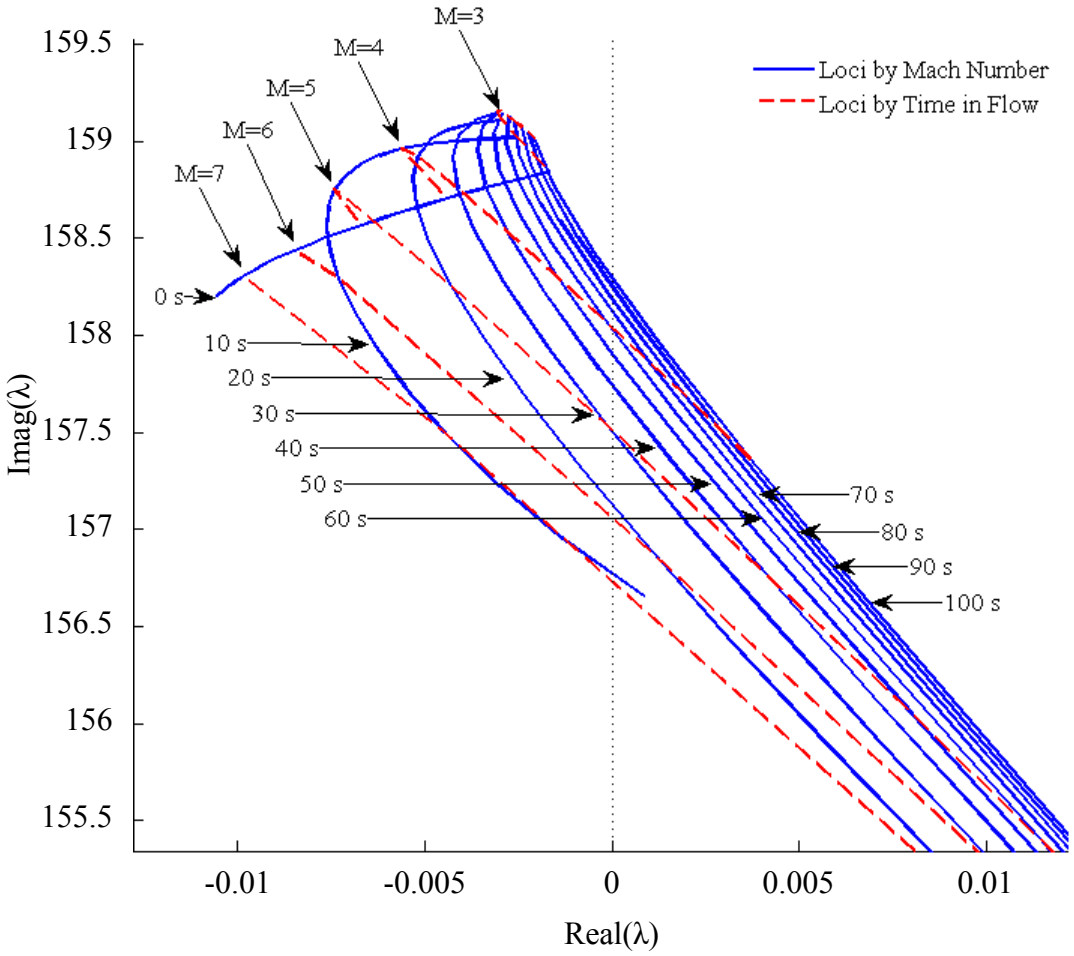

Figure 6.8: Root loci for various Mach numbers and flow exposure times for the first free vibrational mode, 10 km altitude

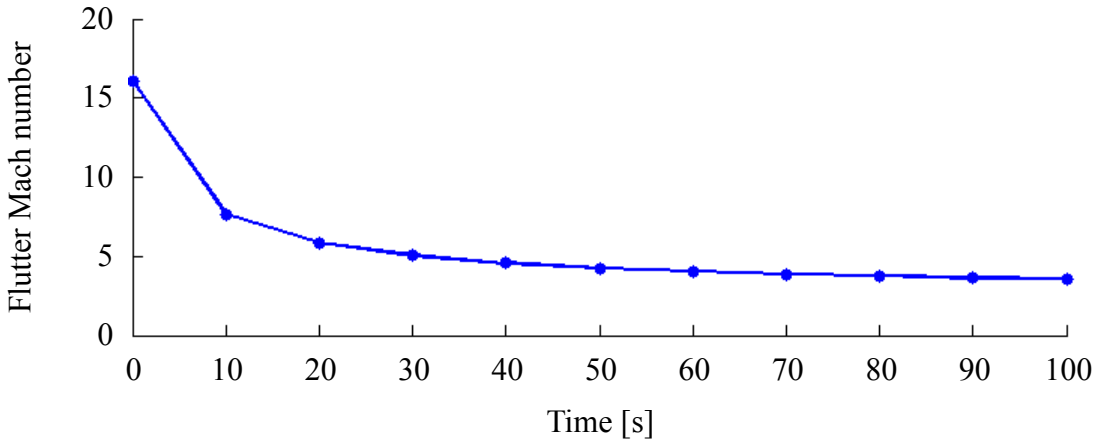

Figure 6.9: Time history of flutter Mach number, 10 km altitude

Figure 6.8 and Figure 6.9 show that, as the control surface is first exposed to the flow, the control surface is relatively rigid and presents a flutter Mach number of 16.1. However, as the control surface heats, there is a loss of stiffness, lowering the flutter Mach number. This loss of stiffness also lowers the frequency of the modes describing the elastic deformation of the control surface, corresponding to the negative slope of the loci by time in flow shown in Figure 6.8. Also for lower Mach numbers, 3 though ~5.5, one can see a temporary increase in frequency likely due to geometric stiffening from the thermal gradients present in the control surface. As the control surface temperatures begin to stabilize after exposure to the flow, the flutter Mach number asymptotes to ~3.5, corresponding to a loss of over 78% of the initial flutter margin.

As a way to verify these stability results, a time simulation of the control surface was performed at the initial temperature distribution while flying at 10-km altitude. The Mach number was varied and time traces of the modal amplitudes were recorded, as shown for mode 1 in Figure 6.10. An exponential curve was then fit to the peaks of the amplitude trace by least-squares, to estimate the damping ratio of the mode. A fast-Fourier transform was also performed to estimate the trace frequency. This was performed for Mach numbers ranging from 10 to 19. The frequencies

and damping ratios of modes 1, 2, and 3 are shown in Figure 6.11. As can be seen, the damping ratio becomes negative just beyond Mach 16. This result agrees well with the previous result found by the finite-difference and eigenvalue approach and serves to verify the solution.

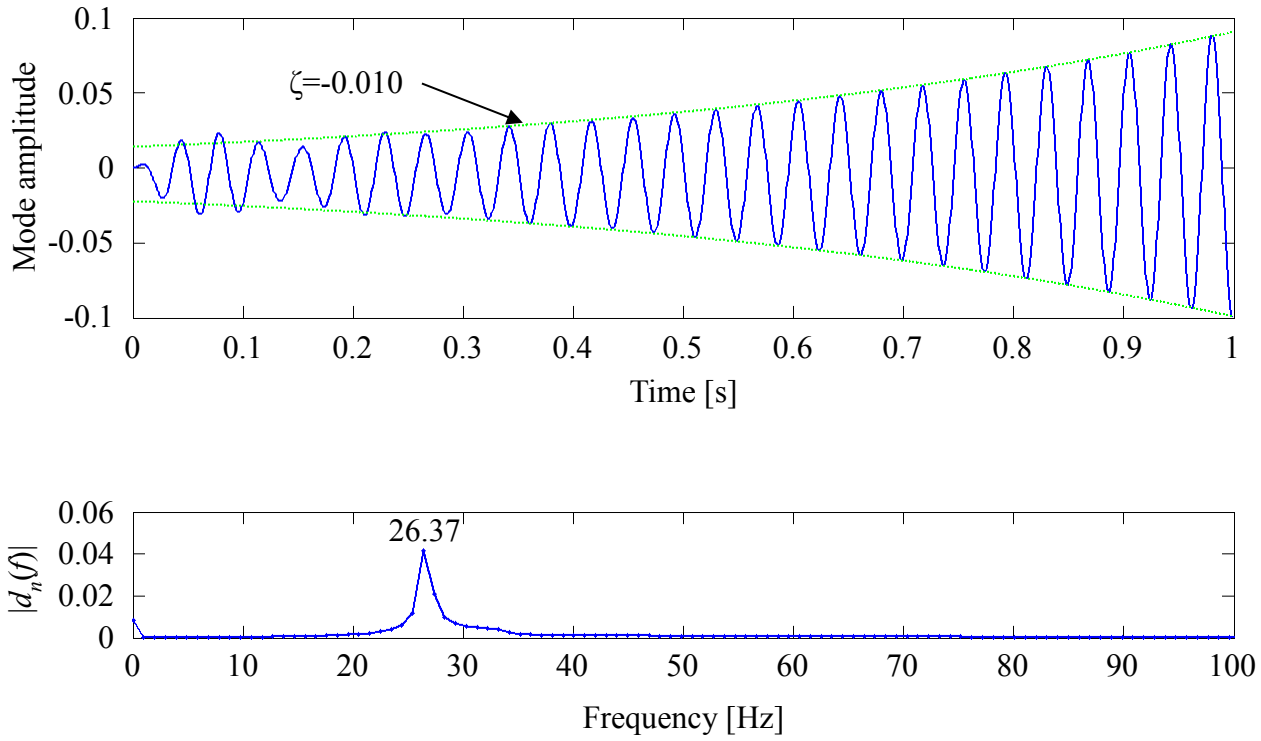

Figure 6.10: Mode damping and frequency characterization from time trace

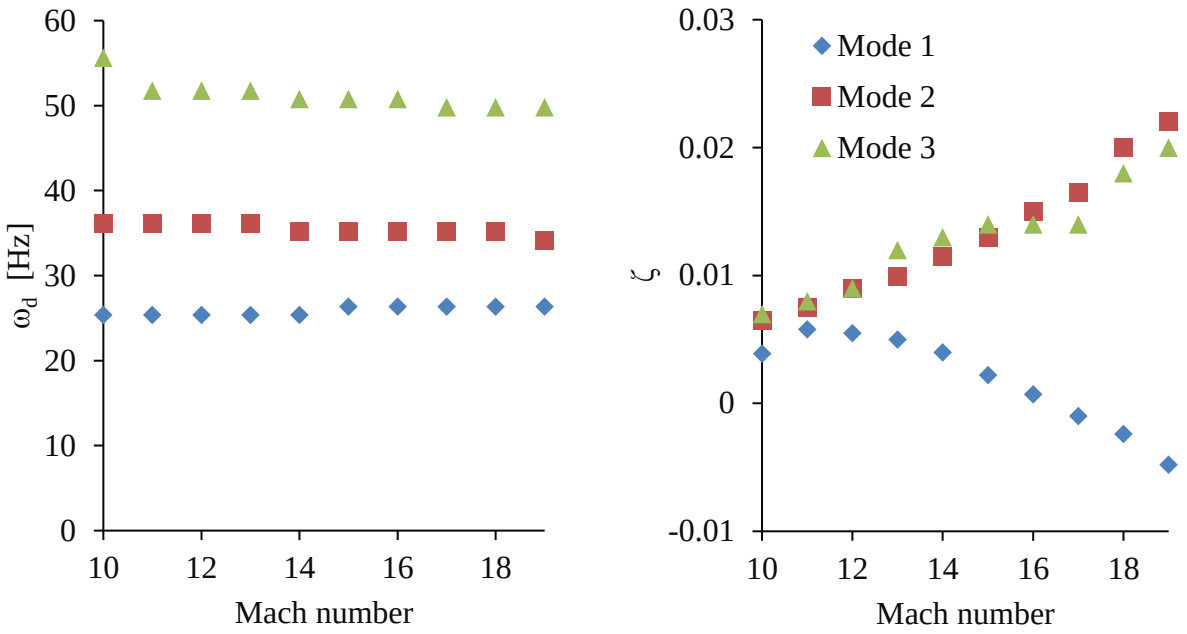

Figure 6.11: Damped frequency and damping ratio for control surface elastic modes 1-3

6.2 Model Reduction of the IC3X Vehicle

Model reduction techniques are applied to the AFRL Initial Concept 3.X (IC3X) vehicle on terminal trajectories to capture the aerodynamic, thermodynamic, and structural dynamic system evolution and couplings. The General Pseudospectral Optimization Software (GPOPS-II) is used to determine a set of terminal trajectories that maximized impact velocity. Shock, Prandtl-Meyer expansion, and piston theory were combined to create an approximate flow solution over the outer mold line that was then compared to Fully Unstructured Navier-Stokes 3-Dimensional (FUN3D) computational fluid dynamics solutions. Proper orthogonal decomposition (POD) of the thermal state of the vehicle was conducted leading to 33 thermal degrees of freedom rather than approximately 28,000 contained by a representative finite element model (FEM), while sacrificing negligible system energy. Free vibration mode shapes are derived and used to generalize the

structural dynamics equations of motion reducing the number of structural degrees of freedom to 8 from the original 130,000.

6.2.1 Finite Element Model

To provide a reference and training sample source for model reduction, a pair of FEMs were created. The first was a structural model for vibration mode analysis and load testing. The second was a thermal model for heat transfer analysis. Both models are based on the work of Witeof and Neegard,[177] however mesh refinement and other adjustments were made to the previous work to permit thermal analyses pertaining to both FEMs. A summary of the node count, element count, and element types used in each components of the FEM is given in Table 6.3 and Table 6.4. For the structural FEM, thick components such as the ballast and body TPS, were modeled with solid elements. Thin-walled components, such as the monocoque, steel casing, fin structures, and fin TPS were modeled with shell elements. The fin root shafts joining the fins to the body were modeled as cubic beam elements. For the thermal FEM, heat transfer between the fins and the body was assumed negligible and the fin root shafts were neglected. All components were modeled using solid elements so to have a more accurate representation of the through-thickness temperature profiles of thin-walled components. For the structural FEM, the mass contribution of the steel casing was already accounted for by the distributed non-structural masses added to the monocoque skin, thus the casing mesh was unnecessary. Cross sections of both FEMs are shown in Figure 6.12.

Table 6.3: Structural Abaqus FEM mesh details

Component	Node count	Element count	Element type	Element code
Ballast	2,177	1,279	quadratic tetrahedral	C3D10
Monocoque	5,509	11,096	linear triangular	S3R
TPS	14,620	7,267	linear hexahedral	C3D8
Fin	1,300	3	cubic beam	B33
		2,371	linear triangular	S3R

Table 6.4: Thermal Abaqus FEM mesh details

Component	Node count	Element count	Element type	Element code
Ballast	2,230	1,315	quadratic tetrahedral	DC3D10
Monocoque	96,224	76,360	linear hexahedral	DC3D8
TPS	14,620	7,267	linear hexahedral	DC3D8
Casing	1,386	660	linear hexahedral	DC3D8
Fin	6,470	9,460	linear wedge	DC3D6

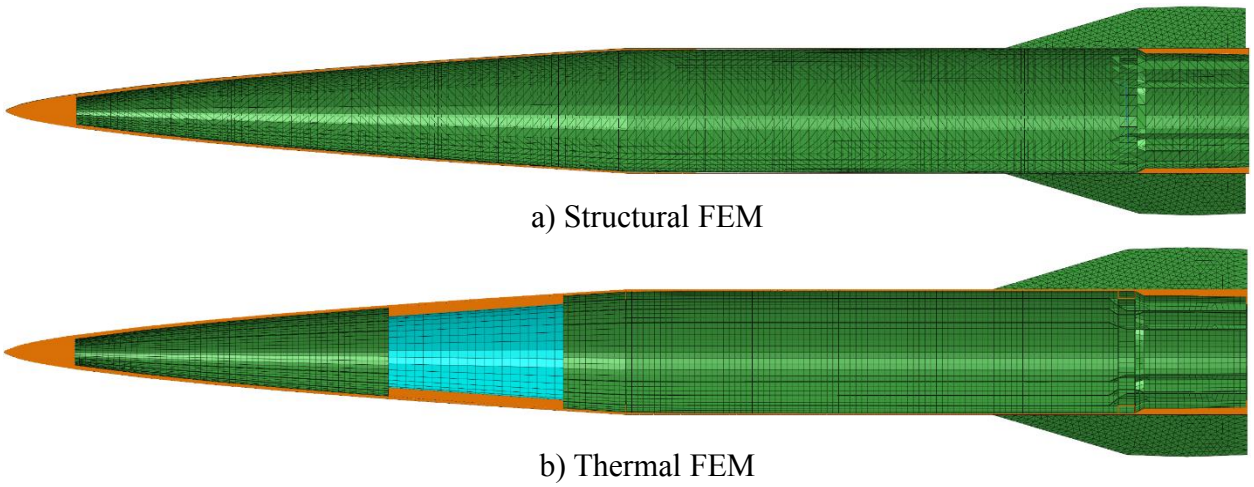

a) Structural FEM

b) Thermal FEM

Figure 6.12: Mid-span cross sections of the IC3X vehicle FEMs

6.2.2 Cruise Phase

While analysis of the terminal phase trajectory was the primary goal, the thermal initial conditions to the terminal phase are established by the cruise phase. Thus, trimming for steady-level flight in the cruise was required to determine the flow conditions over the OML required to determine the surface heat flux. During the cruise phase, an undescribed propulsion system is active to maintain flight. It is assumed that this propulsion system consumes all non-reserve fuel linearly over the duration of a 500-nautical-mile cruise phase. This cruise phase is assumed greater than Mach 5, and above 50 kft (15.2 km) in altitude.

6.2.2.1 Aerodynamics Model

The OML was extracted from the structural and thermal FEMs and used to determine the surface pressures for flight at Mach 6.5 and $65{,}000\,\mathrm{ft}$ altitude for various angles of attack. The surface pressure distributions were then compared to Euler CFD simulations processed by the FUN3D code suite by Dreyer.[188] The SEP and CFD solutions for surface pressure are shown in Figure 6.13.

It can be seen that overall the SEP solutions qualitatively match well with the Euler CFD solutions for surface pressure. However, there are minor differences including the over-prediction of pressure at the nose tip by the SEP model due to the neglect of 3D pressure relief effects for conical bodies. In addition, the shock wave interactions between the fins and the body are neglected since the SEP model considers panels of the OML individually, with no account for the regions of dependence or influence in the supersonic flow. That said, calculation of each SEP pressure distribution required ~6 seconds on 1 Intel E5 2.0 GHz core while calculation of each Euler CFD solution required ~300 seconds on 128 Intel E5 2.6 GHz cores.

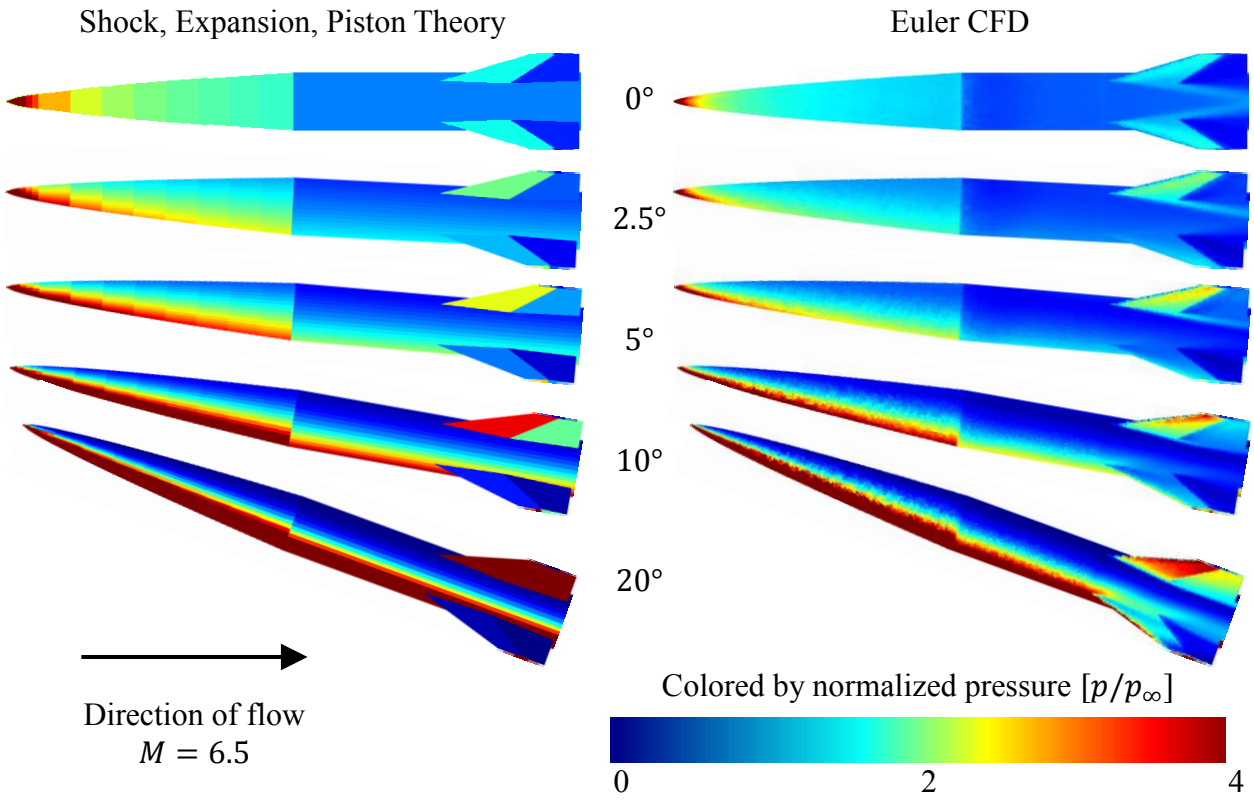

Figure 6.13: Comparison of SEP to Euler CFD surface pressures

The pressure solution at the centroid of each panel of the SEP solution is then quantitatively compared with the spatially nearest panel of the CFD solution. The normalized root-mean-square error (NRMSE) is used,

$$\mathrm{NRMSE} = \frac{\sqrt{\left[\frac{1}{n}\sum_{i=1}^{n}\left(p_{SEP,i} - p_{CFD,i}\right)\right]^2}}{\max\left(p_{CFD}\right) - \min\left(p_{CFD}\right)}, \tag{6.7}$$

where n=21315 is the number of panels comprising the SEP OML, $p_{SEP,i}$ is the surface pressure at the centroid of the ith panel of the SEP OML, and $p_{CFD,i}$ is the surface pressure at the spatially nearest CFD panel to the SEP panel. The NRMSE for each angle of attack is given in Figure 6.14.

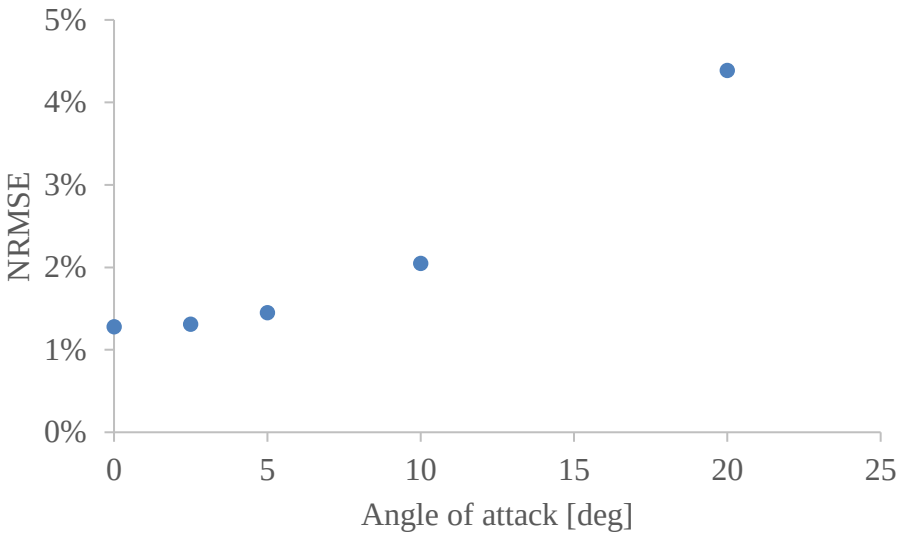

Figure 6.14: Comparison of the SEP and CFD pressure solutions

6.2.2.2 Vehicle Trim

Trimming was conducted by minimizing the summed magnitudes of the body forces and moments for a number of time instances along the cruise phase using the simplex method implemented through the *fminsearch* built-in function of Matlab.[31] Inputs to the minimization were the angle of attack and fin deflection. The fin deflection was applied to each fin symmetrically across the plane of symmetry for longitudinal flight to reduce all fin deflections to a single angle. A thrust force was applied as an axial force along the vehicle's axis of symmetry and was scaled

to cancel the component of the weight along the axis of the vehicle plus the drag in the body frame after the aerodynamic model was applied,

$$T = D + mg\cos(\alpha) \ , \tag{6.8}$$

where T is the thrust magnitude, m is the mass of the vehicle, g is the acceleration due to gravity, α is the angle of attack, and D is the drag, taken to be the x component of the net aerodynamic forces in the body frame obtained from the SEP aerodynamics model. Note that the SEP aerodynamic model used in this work was akin to an Euler solution in that it ignored viscous effects and accounted only for pressure drag. To ensure that the neglect of the viscous drag would not significantly affect the trim solution, a set of trim solutions including the skin friction coefficients derived from the Eckert reference temperature method were considered for a uniform OML temperature of 273 K. While the required thrust increased, sometimes by as much as 38%, the angle of attack and fin deflection angles varied by less than 4% compared to the inviscid trim solution. Since the incident angle of the OML to the freestream flow is the primary driving factor for the surface heat flux considered later in this chapter, the inviscid trim solutions were considered adequate. The aerodynamic forces in the body frame are found by

$$F = -\begin{bmatrix} p_1 A_1 \hat{n}_x^{(1)} & p_1 A_1 \hat{n}_y^{(1)} & p_1 A_1 \hat{n}_z^{(1)} \\ \vdots & \vdots & \vdots \\ p_n A_n \hat{n}_x^{(n)} & p_n A_n \hat{n}_y^{(n)} & p_n A_n \hat{n}_z^{(n)} \end{bmatrix} , \tag{6.9}$$

and aerodynamic moments in the body frame are found by

$$M = [x_c]_\times F \quad , \tag{6.10}$$

where F is a $n \times 3$ matrix of forces on each OML panel, p_i is the pressure on the *i*th OML panel determined from the SEP aerodynamics model, A_i is the surface area of the *i*th OML panel, $\hat{n}_x^{(i)}$, $\hat{n}_y^{(i)}$, $\hat{n}_z^{(i)}$ are the components of the outward facing unit normal vector of the *i*th OML panel, M is a $n \times 3$ matrix of moments about the nose tip, x_c is a $n \times 3$ matrix of the body frame locations of the OML panel centroids from the nose, and $[\ ]_\times$ is the skew-symmetric matrix operator. Total drag D and lift L are the sums of the first and third columns of the force matrix F, respectively. Total pitching moment is the sum of the second columns of the moment matrix. The net forces and moments relevant for steady-level flight, assuming lateral symmetry, are then

$$F_{x,net} = \sum_{i=1}^{n} F_{i,1} + mg\sin(\alpha) - T \quad , \tag{6.11}$$

$$F_{z,net} = \sum_{i=1}^{n} F_{i,3} + mg\cos(\alpha) \quad , \tag{6.12}$$

$$M_{y,net} = \sum_{i=1}^{n} M_{i,2} + x_{CG} mg\cos(\alpha) \quad , \tag{6.13}$$

where $F_{i,j}$ is the *i,j*th entry of F, $M_{i,j}$ is the *i,j*th entry of M, and x_{CG} is the distance of the center of gravity from the nose tip. Note that eq. (38) is identically 0 under all conditions due to the

definition of the thrust T in eq. (35). Thus only $F_{z.net}$ and $M_{y,net}$ must be minimized to obtain the trim state. Since at this point, the elastic and thermal models were not yet developed and the structure was considered perfectly rigid. Shown in Figure 6.15 is a sample lift and drag distribution along the body length for the end of the cruise phase at Mach 6 and an altitude of 75 kft (22.9 km). Figure 6.16 shows the trim conditions for the beginning and end of the cruise phase at the flight conditions described.

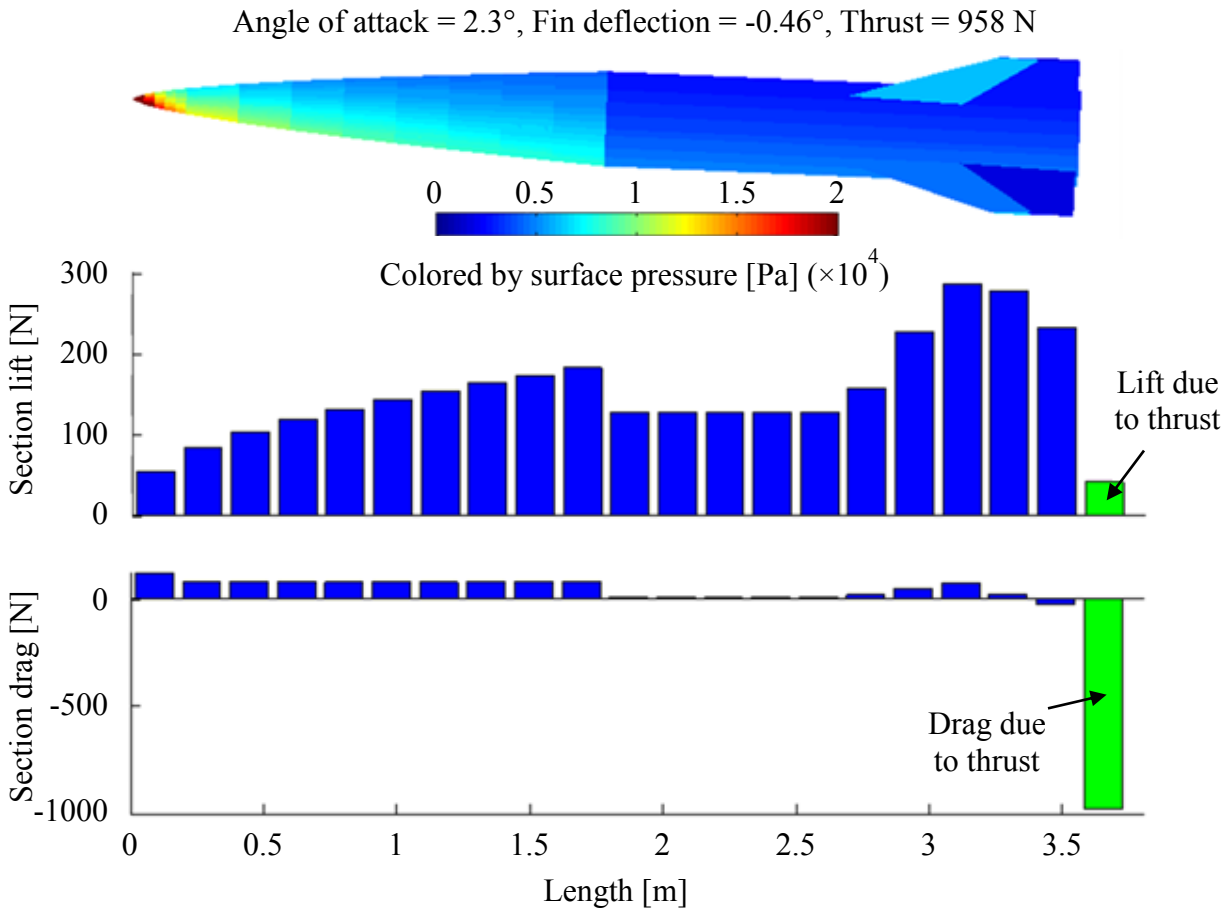

Figure 6.15: Sample lift and drag distribution for Mach 6, 75 kft (22.9 km) altitude, end of cruise phase

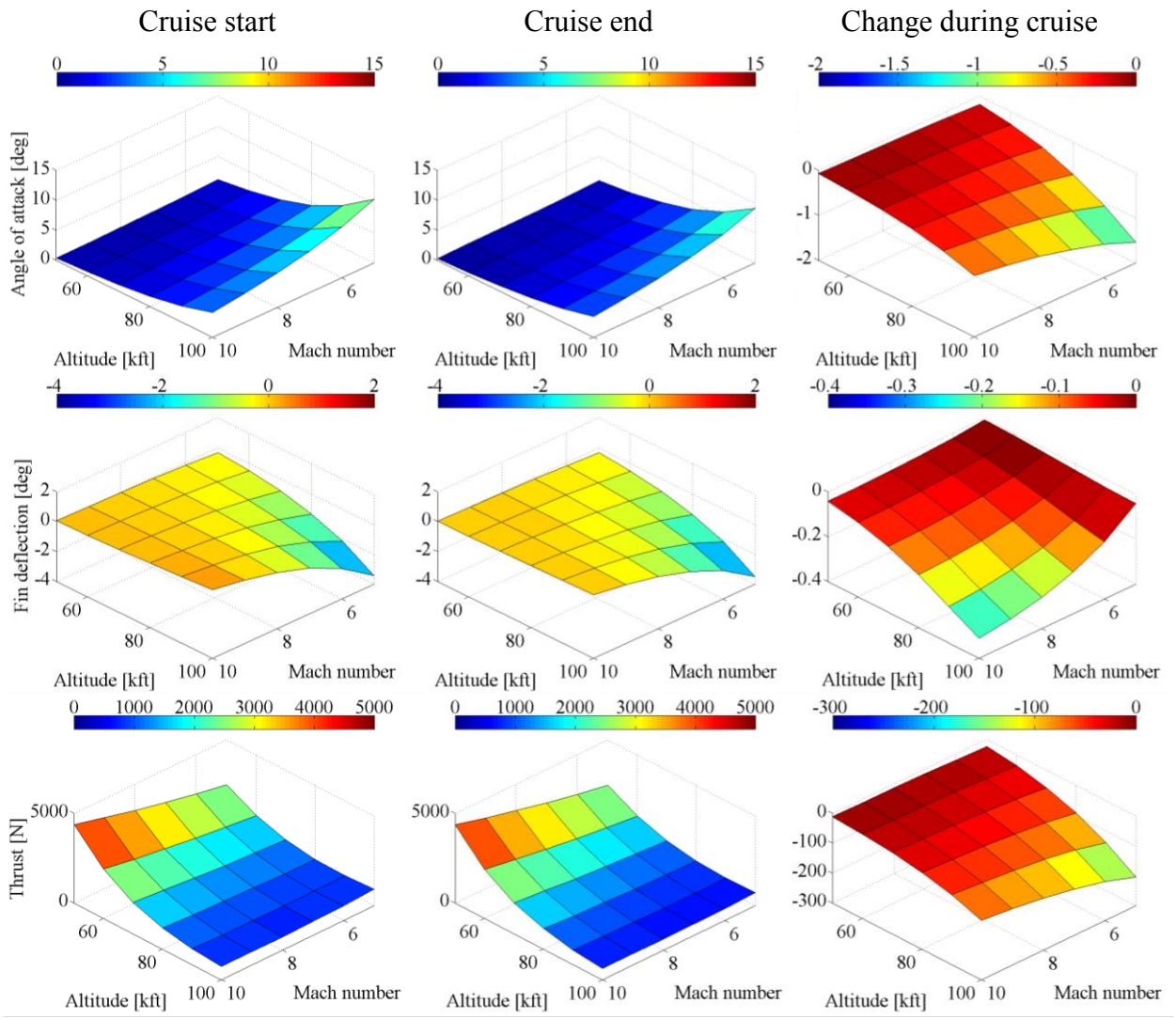

Figure 6.16: Cruise phase trim states for a range of Mach numbers and altitudes

6.2.3 Terminal Phase Trajectory Optimization

The vehicle enters the terminal phase of the trajectory following the cruise phase and pitches downward to begin its descent toward the ground. In order to tailor thermal and structural modal solutions, a representative terminal trajectory was required. To determine a realistic trajectory, an optimization of the vehicle flight dynamics was carried out to maximize the kinetic

energy of the vehicle upon reaching the ground. The General Purpose Optimal Control Software (GPOPS-II)[189] was used with the 3 degree of freedom equations of motion

$$\dot{r} = v \sin(\beta) \,, \tag{6.14}$$

$$\dot{x}_{lon} = \frac{v \cos(\beta)}{r} \,, \tag{6.15}$$

$$\dot{v} = -\frac{D}{m} - g \sin(\beta) \,, \tag{6.16}$$

$$\dot{\beta} = \frac{\frac{L}{m} - \cos(\beta)\left(g - \frac{v^2}{r}\right)}{v} \,. \tag{6.17}$$

Here r is the radius from the center of the Earth to the body center, x_{lon} is the longitude in the Earth frame, v is the speed, β is the flight path angle, g is the acceleration due to gravity, D is the drag force, L is the lift force, and m is the vehicle mass. The vehicle was considered to be on a spherical Earth with gravitational acceleration as a function of altitude, lift and drag coefficients derived from the shock, expansion, and piston (SEP) theory aerodynamics model previously described, and atmospheric conditions based on the 1976 standard atmospheric model.[149] Control was effected by varying the angle of attack which varied the drag *D* and lift *L*.

To integrate equations of motion (6.14) through (6.17), lift and drag polars were required. The SEP aerodynamics model was used to vary the angle of attack at Mach 6.5, and record the variation of the coefficients of lift and drag. The results are shown in Figure 6.17.

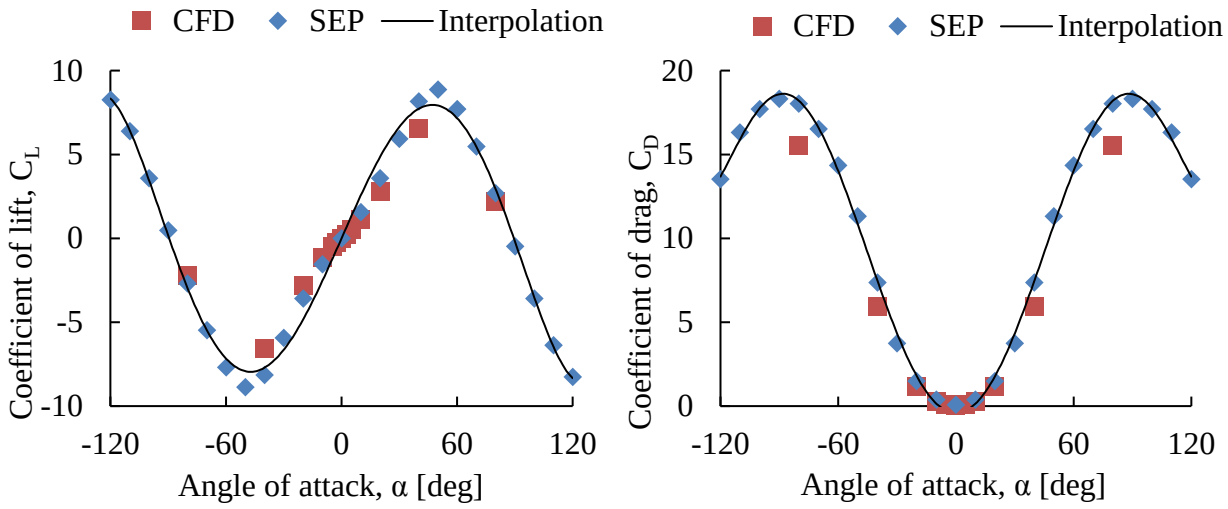

Figure 6.17: Vehicle lift and drag polars for Mach 6.5

A sparse sampling of CFD solutions taken from Dreyer[188] are also shown in Figure 6.17 for comparison to the SEP solutions. Overall, both solutions match well for both moderate and extreme angles of attack. The least-squares method was then used to fit fifth and sixth order polynomials to each polar, yielding

$$C_L(M = 6.5) = \left(2.603\times10^{-1}\right)\alpha^5 + \left(-4.456\times10^{-5}\right)\alpha^3 + \left(1.504\times10^{-9}\right)\alpha \ , \tag{6.18}$$

$$C_D(M = 6.5) = \left(8.478\times10^{-2}\right)\alpha^6 + \left(5.450\times10^{-3}\right)\alpha^4 + \left(-4.908\times10^{-7}\right)\alpha^2 + \left(3.482\times10^{-2}\right) \tag{6.19}$$

where C_L is the coefficient of lift, C_D is the coefficient of drag, and M is the Mach number. The Prandtl-Glauert factor for supersonic flight was then used to approximate C_L and C_D for Mach numbers other than 6.5

$$C_L(M) = \frac{C_L(M = 6.5)\sqrt{(6.5)^2 - 1}}{\sqrt{M^2 - 1}}, \tag{6.20}$$

$$C_D(M) = 1.5 \times \frac{C_D(M = 6.5)\sqrt{(6.5)^2 - 1}}{\sqrt{M^2 - 1}}. \tag{6.21}$$

A factor of 1.5 was also applied to C_D to account for additional drag generated by an undescribed scramjet inlet. Given C_L, C_D, and the equations of motion, the terminal trajectories shown in Figure 6.18 for initial Mach numbers 5, 6, 7, 8, 9, and 10 and initial altitudes of 50, 60, 70, 80, 90, and 100 kft (15.2, 18.3, 21.3, 24.4, 27.4, and 30.5 km, respectively) were generated by the GPOPS-II code to maximize final kinetic energy.

A representative trajectory starting at Mach 6, 75 kft (22.9 km) altitude was selected for further analysis. The trajectory is overlaid and bolded onto Figure 6.18 for comparison to the sample set of trajectories. The time histories of the altitude, flight speed, angle of attack, and flight path angle of the representative trajectory are shown in Figure 6.19. The total flight time of the representative terminal trajectory is 37.5 s, covering a range of 49.1 km. The final Mach number is 2.6, which at sea level is equivalent to 887 m/s.

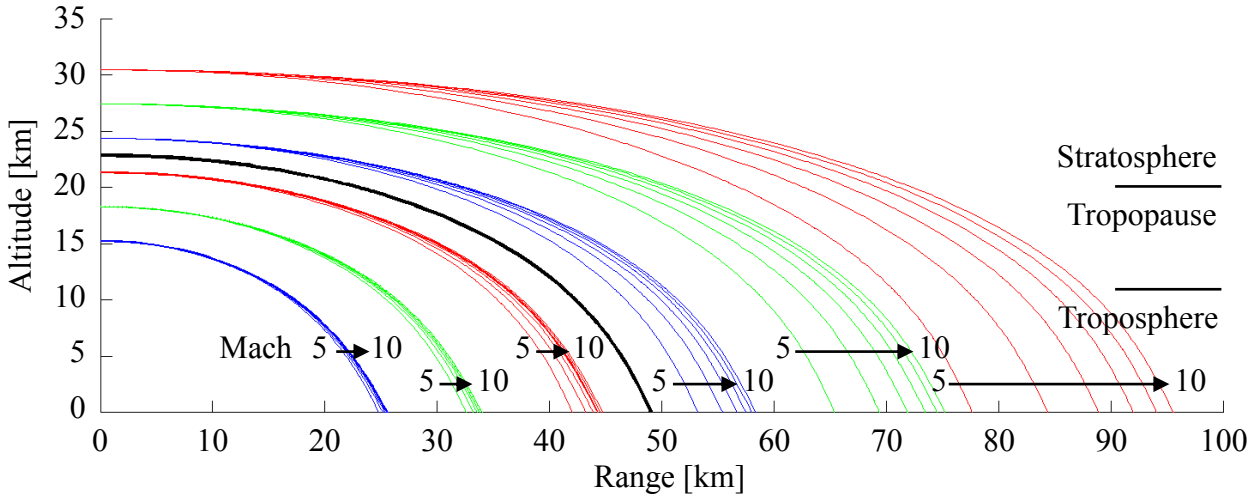

Figure 6.18: Selection of terminal trajectories optimized for maximum final kinetic energy

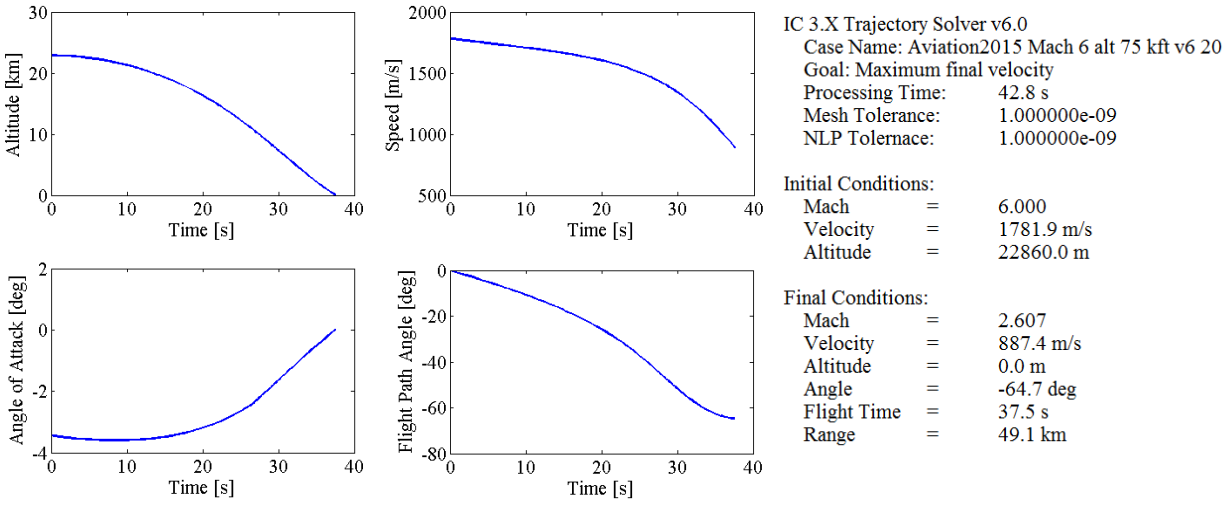

Figure 6.19: Representative terminal trajectory (initial Mach 6 and 75 kft altitude)

6.2.4 Heat Transfer Simulation

To employ the method of snapshots to the thermal state in the terminal trajectory phase, a high-fidelity heat-transfer simulation of the structure was required. However, simply simulating the terminal phase is insufficient due to the thermal hysteresis. The cruise phase was also simulated to determine the initial terminal phase heat transfer conditions.

An Abaqus user-defined subroutine (UDS) was written to interface the heat-transfer FEA with the SEP aerodynamic model and trim solver. Within the UDS, the Eckert aeroheating model was implemented and used to determine the surface heat flux across the aerodynamic boundary layer given flow conditions determined *a priori* and wall temperatures determined during the heat-transfer FEA. The process flow chart is shown in Figure 6.20.

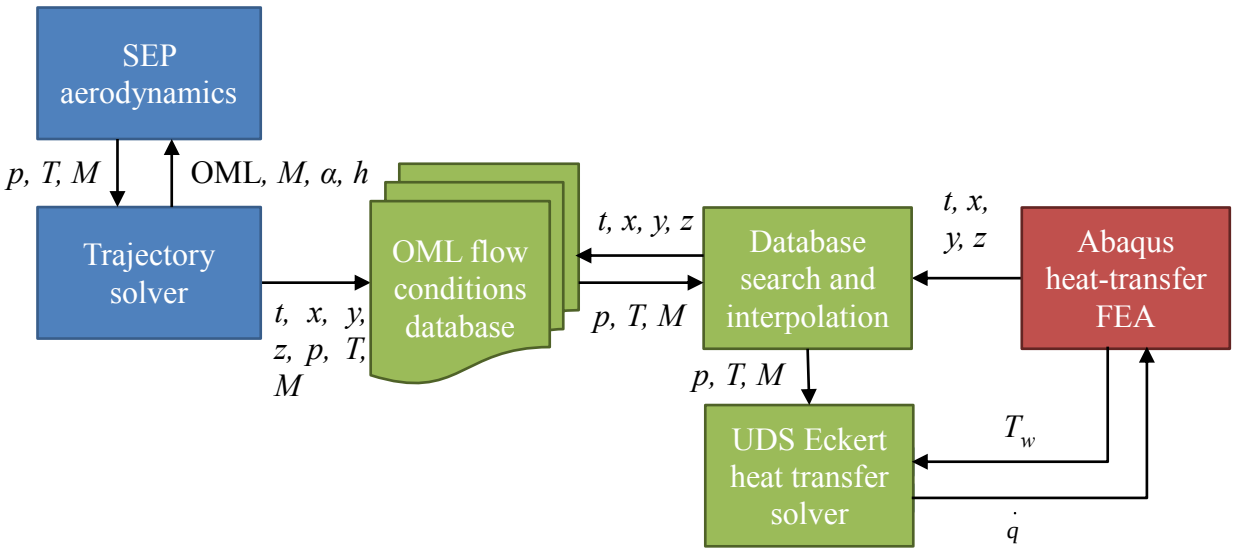

Figure 6.20: Process for coupling aerodynamic model and structure heat-transfer FEA

During preprocessing, the trajectory solver, which during cruise is the trim solver, passes the OML geometry, flight Mach number, angle of attack, and altitude to the SEP aerodynamics model. The aerodynamics model then returns pressure, outer temperature, and outer Mach number

at the centroid of each OML panel. Upon determining the vehicle is trimmed for a given instant in the cruise phase, time, spatial coordinates, pressure, outer temperature, and outer Mach number for each panel are written to a database. During the heat-transfer FEA, the time and spatial coordinates of a node on the FEM are passed by Abaqus to the database searcher and interpolator. Since the aerodynamic solutions are considered at the OML panel centroids and the heat-transfer simulation temperature solutions are considered at the element nodes, interpolation of the flow properties is implemented by averaging the flow solutions of all spatially adjacent panel centroids to an element node, i.e.,

$$\{ p, T, M \}_{node} = \frac{1}{n} \sum_{i=1}^{n} \{ p, T, M \}_{centroid} \quad , \tag{6.22}$$

where n is dependent on the element type of the associated node. For quadrilateral elements, $n = 4$, while for tetrahedral and triangular elements, $n = 6$. No interpolation was considered temporally. Instead, trim and aerodynamic solutions were determined at intervals of 0.1-s and flow conditions were taken at the nearest recorded time in the OML flow conditions database. This approach was viable since a time interval of 0.1-s was much too fine of an interval to appear in the heat-transfer simulation due to the long characteristic times of thermodynamic processes.

A Mach 6, 75 kft (22.9 km) altitude cruise heat-transfer simulation was begun with the structure at a uniform 238 K. The cruise phase covered 500 nautical miles (926 km) over approximately 520 s. Temperature profiles for the OML and bond-line between the monocoque skin, fin structure, and TPS are shown in Figure 6.21. Maximum and minimum temperatures of each component during simulation are shown in Figure 6.22. To increase the processing rate of the heat-transfer simulation, the body and fins were simulated separately. Since the fins have less

thermal capacity and a larger relative surface area than the body, they tend to experience rapid heating initially, requiring fine time steps, but quickly stabilize and can be integrated with larger time steps. On the other hand, the body does not heat as rapidly, allowing for larger time steps than the fins initially, but spends a longer time in a transient state, thus not allowing the time steps to be lengthened as significantly as with the fins. This separation of the body and fins implies the neglect of gap heating at the joint between the fins and body. While gap heating is a significant source of heat flux, a model for it has not been developed in this work.

During the cruise phase, the nose and fore-body experience the greatest heating due to the more inclined OML surfaces. This was expected, as the TPS is thicker in these areas than the mid-body. The ballast bears the greatest heating due to the stagnation point, but heats relatively slowly compared to the TPS slightly aft due to its greater thermal capacity. One may see that the mid-body monocoque bound line is the first to experience the heating effects at approximately 16 s into the cruise phase, where the TPS is the thinnest, but ultimately the highest bound line temperature was found on the windward fore-body, despite the thicker TPS on the fore-body. The fin TPS heated nearly as quickly as the stagnation point on the ballast, but quickly reached a maximum and then began to cool slightly as the fins assumed new angles of attack to trim the vehicle.

Following the cruise phase heat-transfer simulation is terminal phase heat-transfer simulation with initial thermal states determined by the final states of the cruise phase. Linking between the SEP aerodynamics model and the Abaqus FEA was nearly identical to what was done for the cruise phase, except that rather than the trajectory being determined by the trim solver, the GPOPS-II optimized terminal trajectory states are used. Transition from the trim condition at the end of cruise to the condition at the beginning of the terminal phase is considered instantaneous.

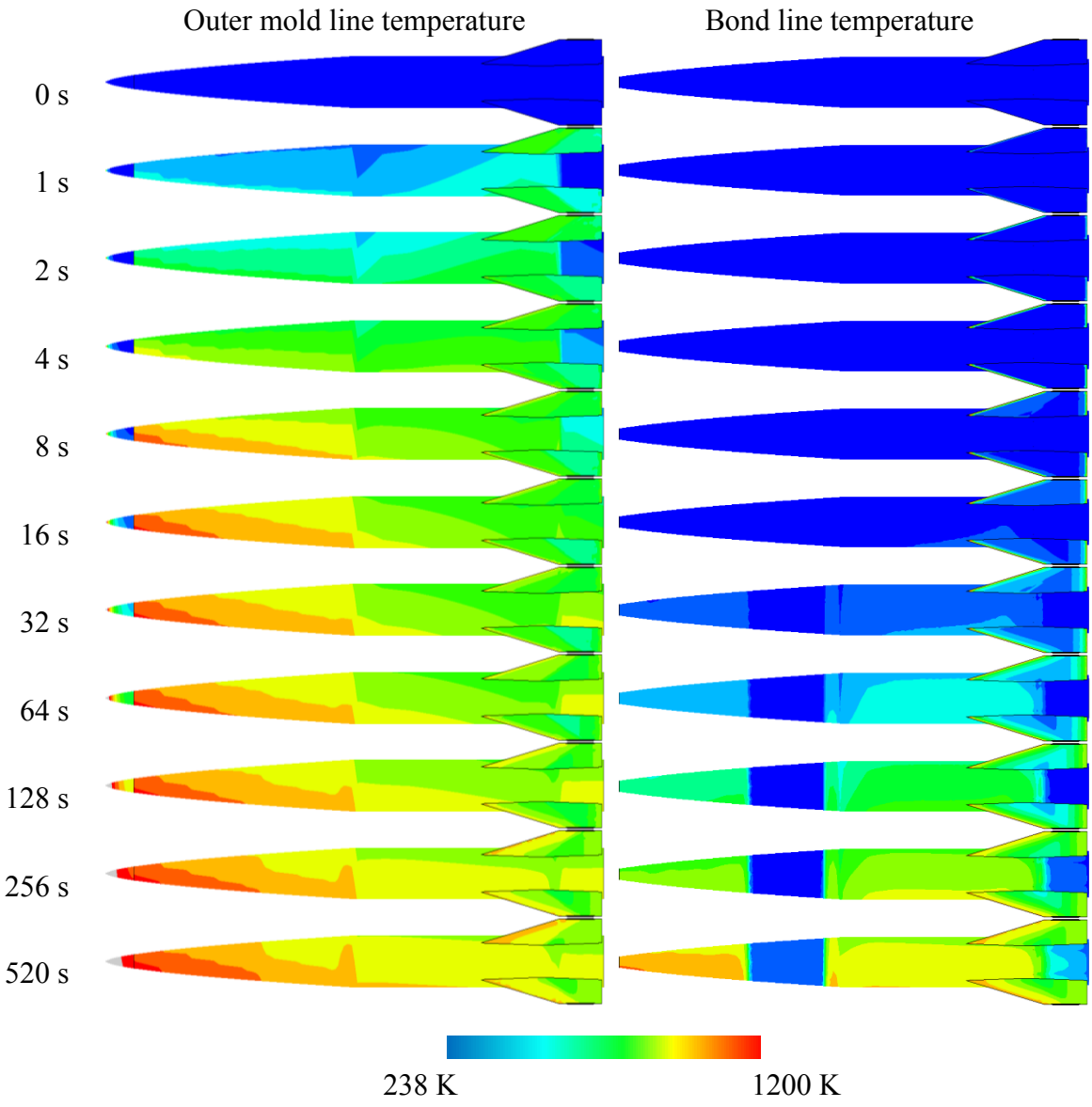

Figure 6.21: Cruise phase temperature profiles for Mach 6, 75 kft (22.9 km) altitude

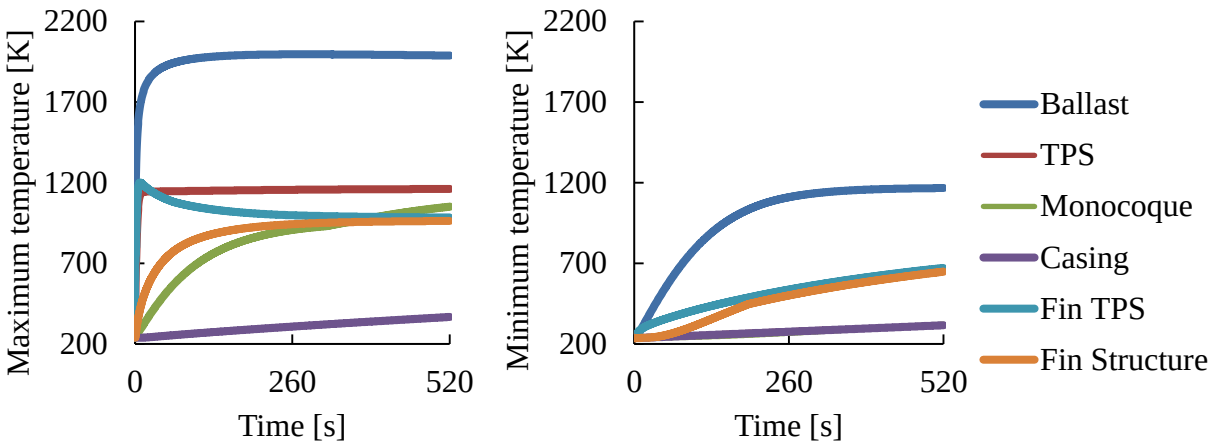

Figure 6.22: Extreme temperatures in cruise by component

In reality, the pitch-over maneuver from the cruise to terminal phase would require some finite amount of time, but the duration of this maneuver was assumed small compared to the characteristic time of the thermal solution. As with the cruise phase, aerodynamic solutions in the terminal phase were considered at intervals of 0.1 s and written to the OML flow conditions database and the fin and body heat-transfer simulations were run separately. Temperature profiles for the OML and bond-line between the monocoque skin, fin structure, and TPS are shown in Figure 6.23 and temperature ranges by component are shown in Figure 6.24.

The heating effects of the pitch-over maneuver at the initiation of the terminal phase can be seen in the inversion of the maximum heating location on the fore-body OML in the first 4 s. The OML then continues to heat until about 24 s when the vehicle enters the troposphere and the combination of lower Mach number and higher density atmosphere begins to quench its surface. The duration of the terminal phase appears to be insufficient to significantly alter the thermal state of the monocoque bond line while the fin bound line did experience some cooling near the leading and trailing edges due to the locally low heat capacity of the fin structure. Several sharp “kinks”

in the extreme temperature plots of Figure 6.24 may be seen. These are the result of the extreme temperature point changing to a new location in the structure which experienced a different cooling rate than the previous location, resulting in a discontinuity in the slope of the plotted results.

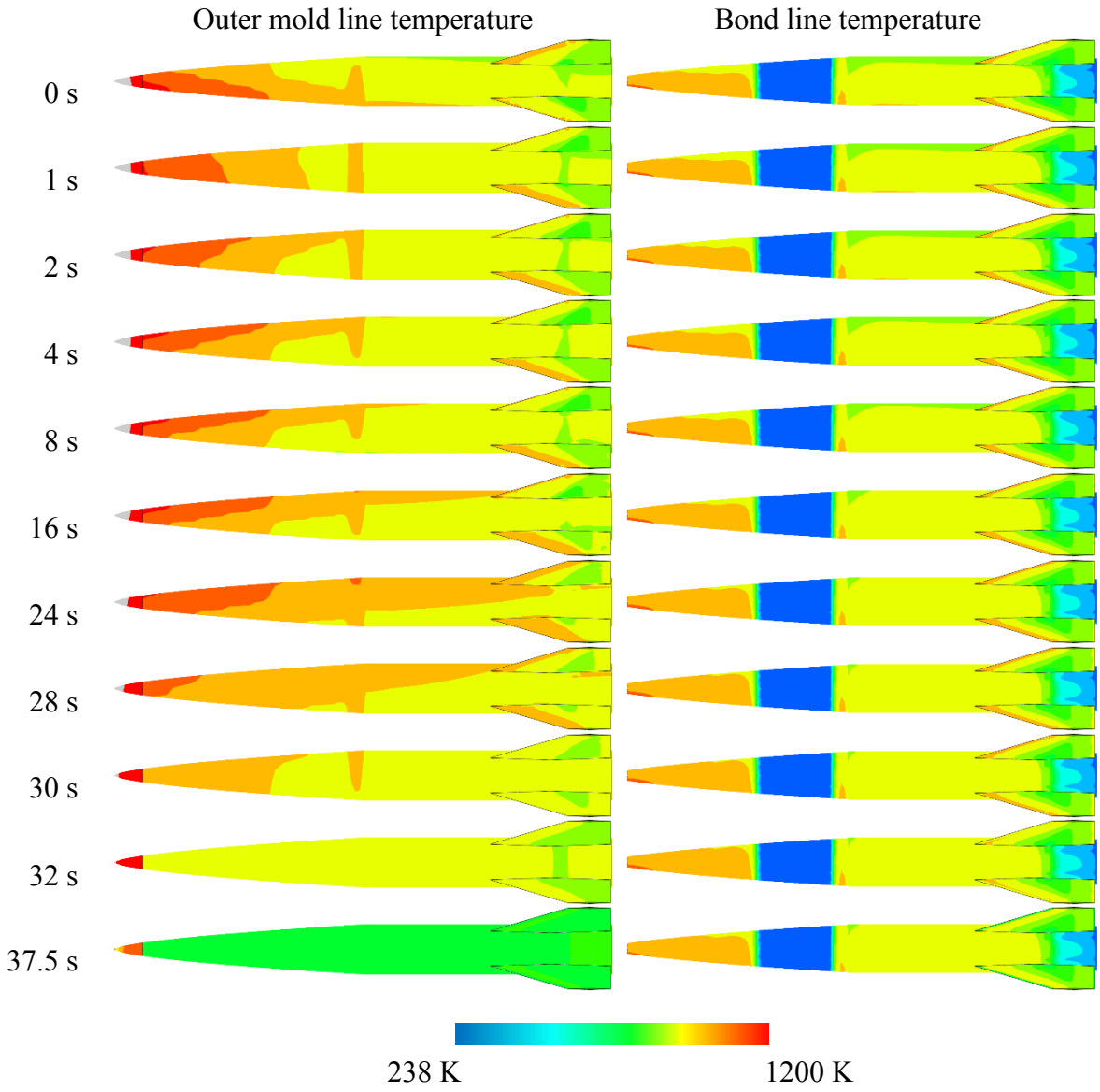

Figure 6.23: Terminal phase temperature profiles for Mach 6, 75 kft (22.9 km) altitude

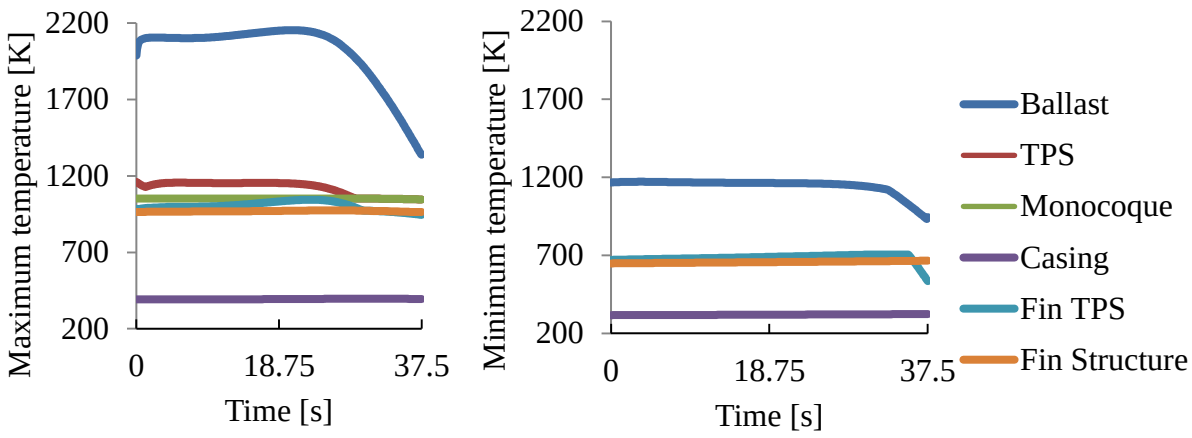

Figure 6.24: Extreme temperatures in terminal phase by component

Throughout both the cruise and terminal phases, one can see the effects of the relative thermal capacities of different components, primarily the ballast and steel casing. The ballast bears the greatest surface heat fluxes, both in heating and cooling, but tended to change overall temperature slowly. The steel casing is protected from the surface heating and remains relatively cool. The lower temperature of the structure near the casing even extends through the monocoque and TPS and is visible in the OML temperature distributions.

6.2.5 Thermal Model Reduction

With the thermal states known for the terminal phase, the method of snapshots is then applied. Since the ultimate goal is to truncate the resulting modal basis to reduce the number of thermal degrees of freedom, selecting modes which contain the most system energy is desirable. It has been previously shown by Falkiewicz and Cesnik[22] that, in some cases, taking more snapshots to derive the modal bases can result in a less accurate thermal model due to the spreading of energy to higher modes that are then neglected during truncation. Ideally, enough thermal modes

are retained to achieve machine accuracy or roughly 15 significant figures. To determine the accuracy of a truncated mode set, the relative energy loss ε_{rel} is used. If it is found that the relative energy loss is approximately 15 orders of magnitude less that the total system energy, $\varepsilon_{rel} \approx 10^{-15}$ then one could consider the energy loss by truncation of the modal basis to be negligible. Thermal snapshots were considered at several time intervals ranging from 10 s to 0.1 s. The relative energy loss was then determined for truncation of each modal basis compared to the snapshot matrix used to form them. The number of retained modes required to achieve negligible energy loss given the number of snapshots taken is shown in Figure 6.25. Once the number of bases retained from each snapshot matrix was determined, the relative energy loss was investigated further by projecting the 0.1-s time interval snapshot matrix onto the space spanned by the retained bases and reevaluating the relative energy loss of each basis set. The results are shown in Figure 6.26.

It can be seen from Figure 6.25 that taking more snapshots indeed results in more bases required to capture the target system energy, which indicates a spreading of energy to higher modes.[22] However, this spread of energy appears to asymptote to approximately 30 to 35 modes for large numbers of snapshots. From Figure 6.26, one can see that the relative energy loss decreased steadily for larger numbers of snapshots, which eventually reached the target of $\varepsilon_{rel} \approx 10^{-15}$ for snapshots taken at 0.1-s intervals. Thus, it was determined that the 33 basis modes derived from the 376 snapshots taken at 0.1-s intervals provided an adequate representation of the thermal solution in the terminal phase. The first 10 thermal basis modes are shown in Figure 6.27 with the eigenvalue magnitudes of each mode and relative energy loss ε_{rel} due to truncation error shown in Figure 6.28 and Figure 6.29.

From the OML column in Figure 6.27, it can be seen that the most dominant thermal basis, mode 1, emphasizes the influence of the relative thermal capacities of the structure near the steel

casing, mid-chord of the fins, and TPS near the tail. Mode 2 emphasizes the difference in thermal properties between the ballast and TPS as well as stagnation point heating. Mode 4 emphasizes the difference in temperatures between the windward and leeward sides while modes 8 and 9 almost exclusively focus on fine temperature gradients near the nose stagnation point. From the bond line column, it can be seen that the relatively subtle temperature change of the skin during the terminal phase leads to basis modes that only emphasize the effect of the steel casing in modes 1 and 2 and some slight differences between the windward and leeward sides in modes 3, 4, and 5.

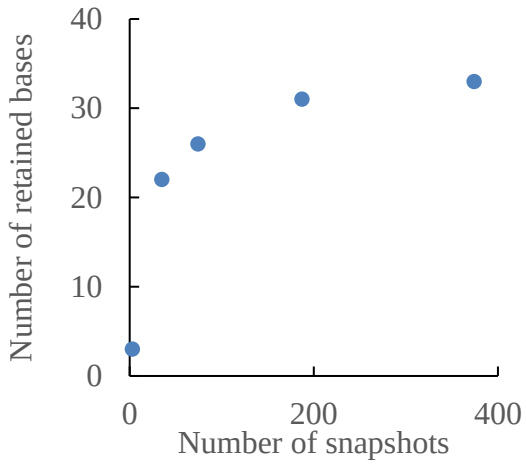

Figure 6.25: Number of bases to achieve negligible energy loss

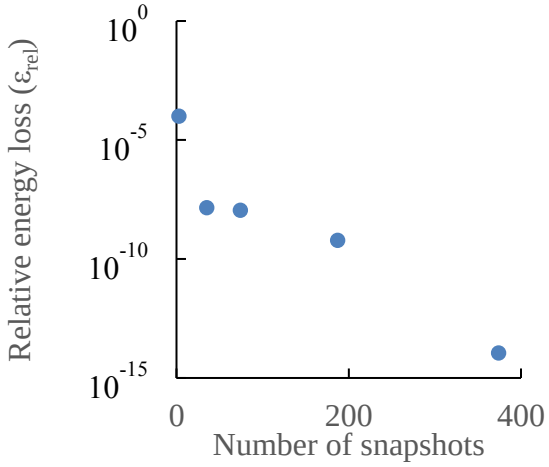

Figure 6.26: Energy loss compared to 0.1-s interval snapshot matrix

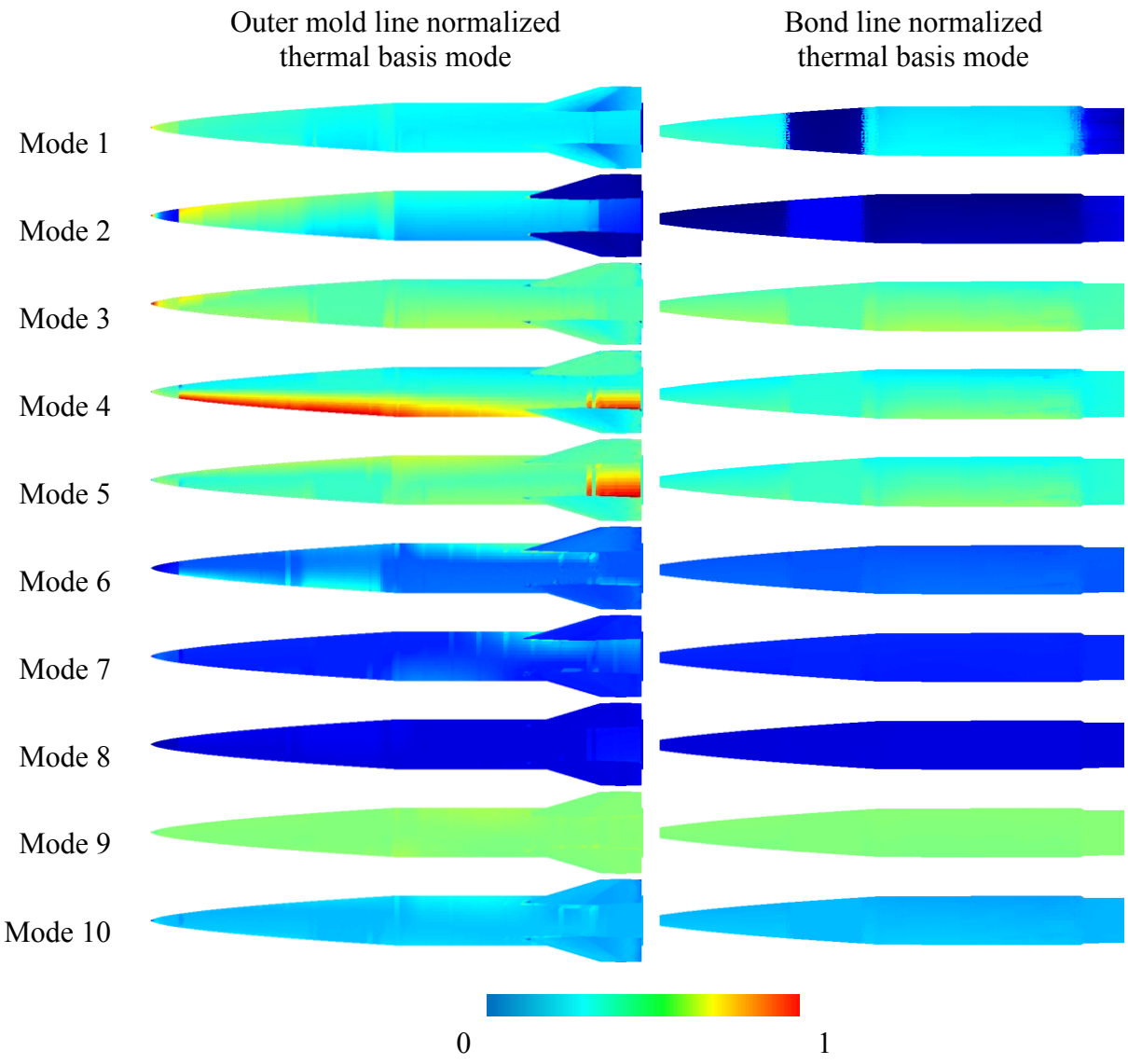

Figure 6.27: First 10 thermal basis modes normalized by maximum temperature

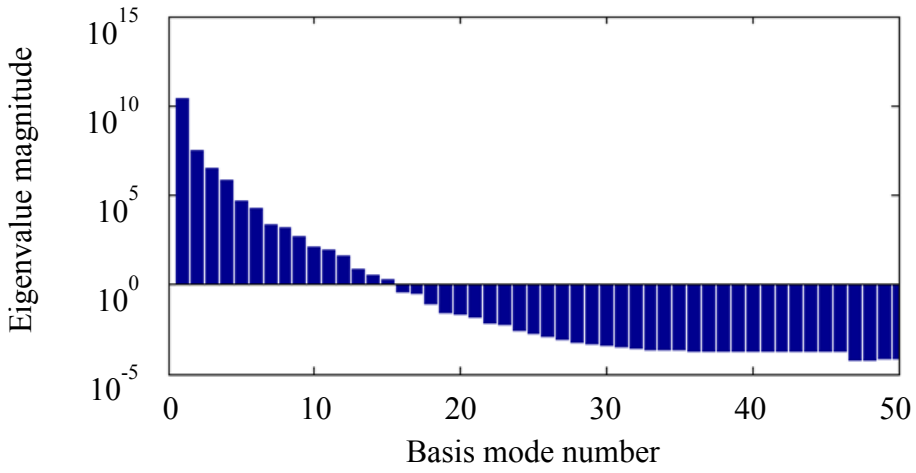

Figure 6.28: Eigenvalue magnitudes of the first 50 thermal basis modes (0.1-s snapshot sampling)

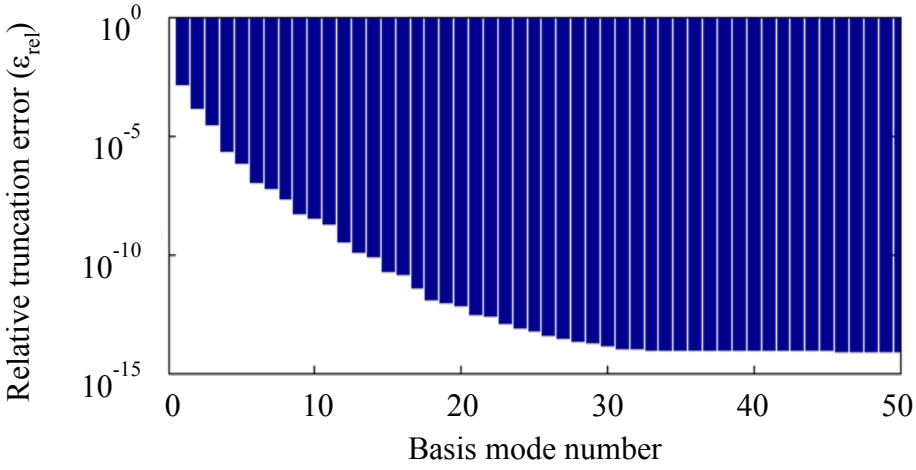

Figure 6.29: Relative truncation error associated with retaining up to the first 50 thermal basis modes (0.1-s snapshot sampling)

By projecting the 0.1-s interval snapshot matrix A into the space spanned by the first 33 basis modes Ψ, the variation of the amplitude of each mode c can be seen along the terminal phase of the trajectory. In general, since the basis modes have been truncated, some information

has been lost. Therefore, the snapshot matrix will not project perfectly onto the truncated modal space and an error ε can be introduced. However, since it has been shown that projection of the snapshot matrix A onto 33 basis modes of Ψ produces relative errors on the order of 10^{-15}, from a numerical standpoint it is possible to project the snapshot matrix directly within computer accuracy, i.e.

$$c = \Psi^{-1} A + \varepsilon \quad , \tag{6.23}$$

where ε is approximately 15 orders of magnitude smaller than $\Psi^{-1} A$ and may be neglected. The coordinates of the first 9 thermal basis modes throughout the terminal phase are shown in Figure 6.30. Overall, mode 1 dominates throughout much of the terminal phase and begins to yield to mode 2 at 28 s following the transit to the troposphere and final quenching of the OML. Mode 3 appears to vary in response to a combination of angle of attack and atmospheric conditions. Modes 4, 5, 6, and 7 are more dynamic than the lower modes and are especially active during the pitch-over maneuver at the initiation of the terminal phase. Mode 8, which contributes almost exclusively to the stagnation point temperature profile, shows the exact time of troposphere transit with a sudden change in slope at 26.4 s.

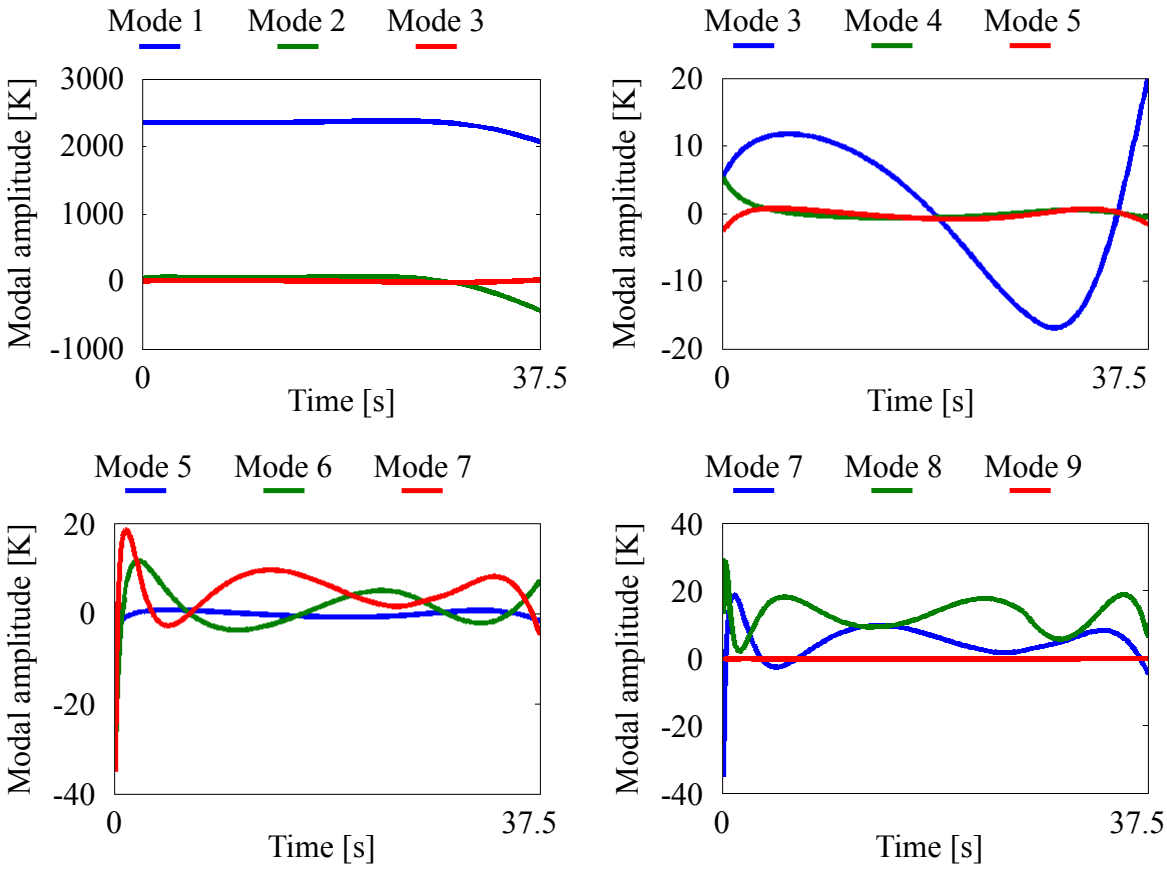

Figure 6.30: Thermal basis modal amplitude variation in the terminal phase

6.2.6 Structural Model Reduction

To reduce the number of degrees of freedom of the structural model, the structural equations of motion were generalized into a modal form. A common set of mode shapes to use for such generalization are the free vibration mode shapes. However, due to the degradation of the material stiffness at elevated temperatures and geometric stiffening of the structure due to thermal gradients and dissimilar interface materials, the normal modes will change in time. Instead, modes determined at a reference thermal state will be used as a set of Ritz modes for model reduction. Thus, a reference thermal state was determined by taking the median temperatures of each FEM node throughout the terminal phase. The median temperatures were considered rather than the

mean temperatures since the final quench of the OML skewed the temporal distribution of temperatures toward a lower value that was not representative of the majority of the terminal phase. This reference thermal state is shown in Figure 6.31.

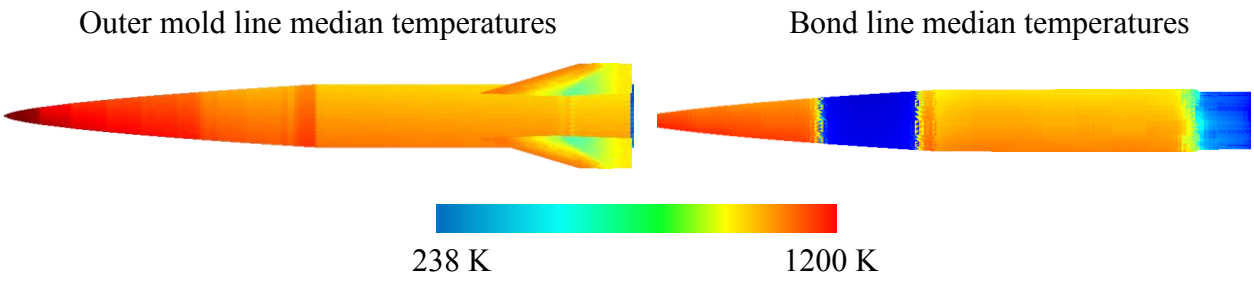

Figure 6.31: Reference thermal state for structure modal identification

Using the Abaqus[30] linear perturbation, frequency analysis with the Lanczos[32] solver, 102 mass-normalized mode shapes and frequencies for 1 to 200 Hz were obtained and a subset are shown in Figure 6.32. The 200 Hz upper limit was determined by the maximum frequency that could realistically be acted upon by a hypothetical flight controller and fin actuator. No intermittent contact effects where considered between the fins and the body, which allow the fins to intersect the body in the cases of the 2nd and 3rd bending as well as the 1st extension modes in case deformation becomes large enough.

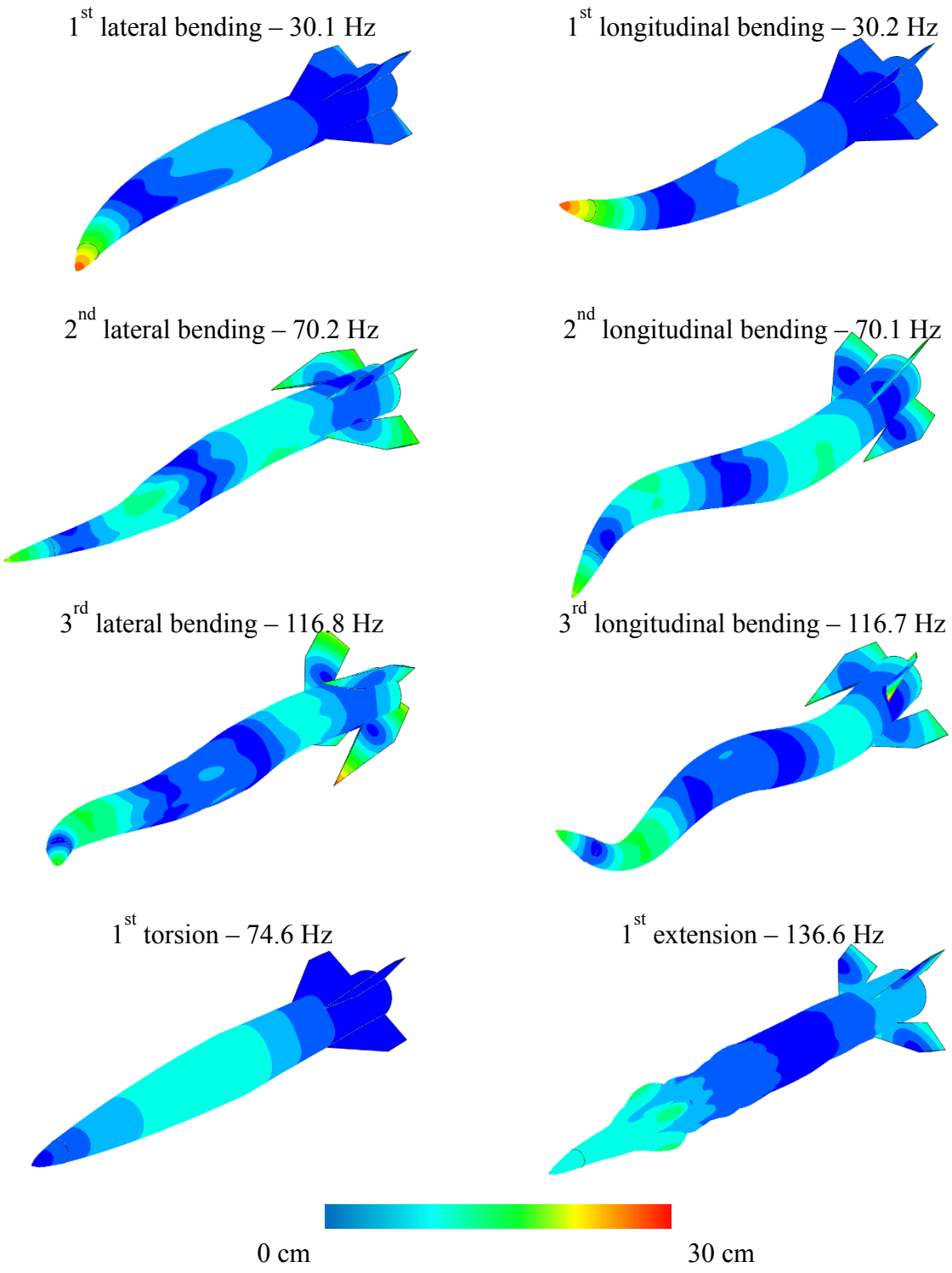

Figure 6.32: Free vibrational modes at the reference thermal state

6.2.7 Thermoelastic Coupling

While the Ritz modes determined in the previous section are orthogonal at the reference thermal state, there is no guarantee that these modes will remain orthogonal as the stiffness and mass properties vary during flight or along trajectories different from the one selected for this study. The loss of orthogonality is acceptable when integrating the structural equations of motion so long as the variations of the stiffness and mass matrices are modeled. For the terminal phase of the trajectory, it is assumed the propulsion system is inactive and there are no changes to the vehicle mass. For the stiffness part, a Kriging model was used for the approximation of the stiffness properties, as introduced by Falkiewicz and Cesnik.[36] An outline of the Kriging training process is given in Figure 6.33 and begins with the selection of thermal modes and thermal mode coordinates. The 5 most dominant thermal modes, $\Psi(x)$, were selected to achieve a relative temperature field error of $O\left(10^{-6}\right)$. Thermal coordinates, c, were selected by Latin hypercube sampling.[190] The product of the thermal modes and coordinates yields a temperature field in physical coordinates, $T(x)$ which is written into an Abaqus FEA input file that also includes the vehicle mesh and material properties. A coupled temperature and displacement analysis is performed and the global stiffness matrix, $K(T)$, is extracted. The stiffness matrix is generalized by the elastic modes, $\Phi(x)$, and the generalized stiffness matrices, k, and corresponding thermal coordinates, c, are paired to form a sample set. From this sample set, all but 100 of the samples are used to train the Kriging model using the *dacefit* function of the DACE toolbox.[141] The remaining samples are then used as testing points to evaluate the error of the model. The error is determined by the normalized root-mean-square of (6.7) and L_∞ methods. If the error is below some tolerance, $E < tol.$, then the model is complete. If not, then further training samples are selected and the model training process is iterated. The error for 18 combinations of regression

and correlation functions within the Kriging model are show for various training set sizes in Figure 6.34.

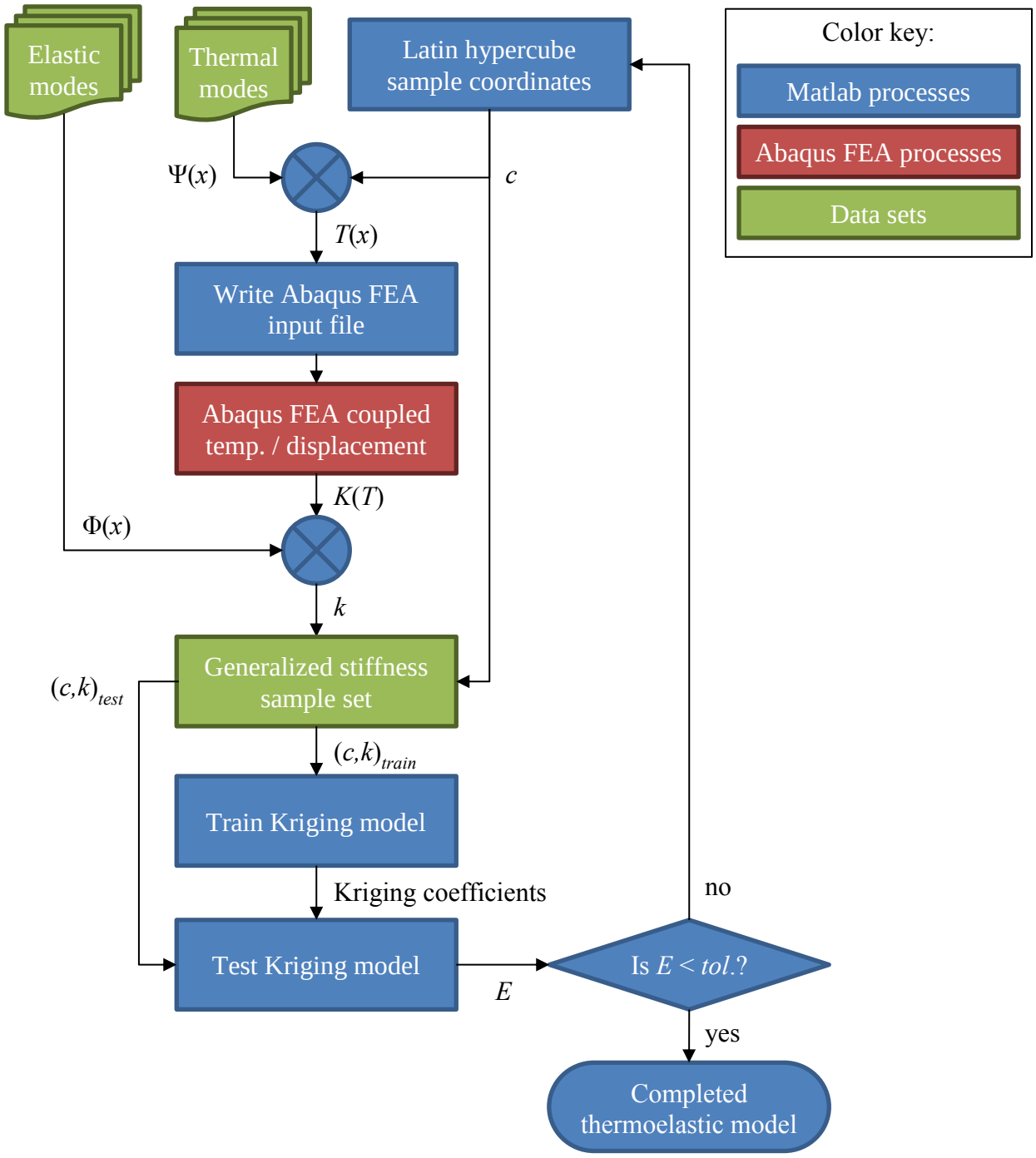

Figure 6.33: Thermoelastic Kriging model training

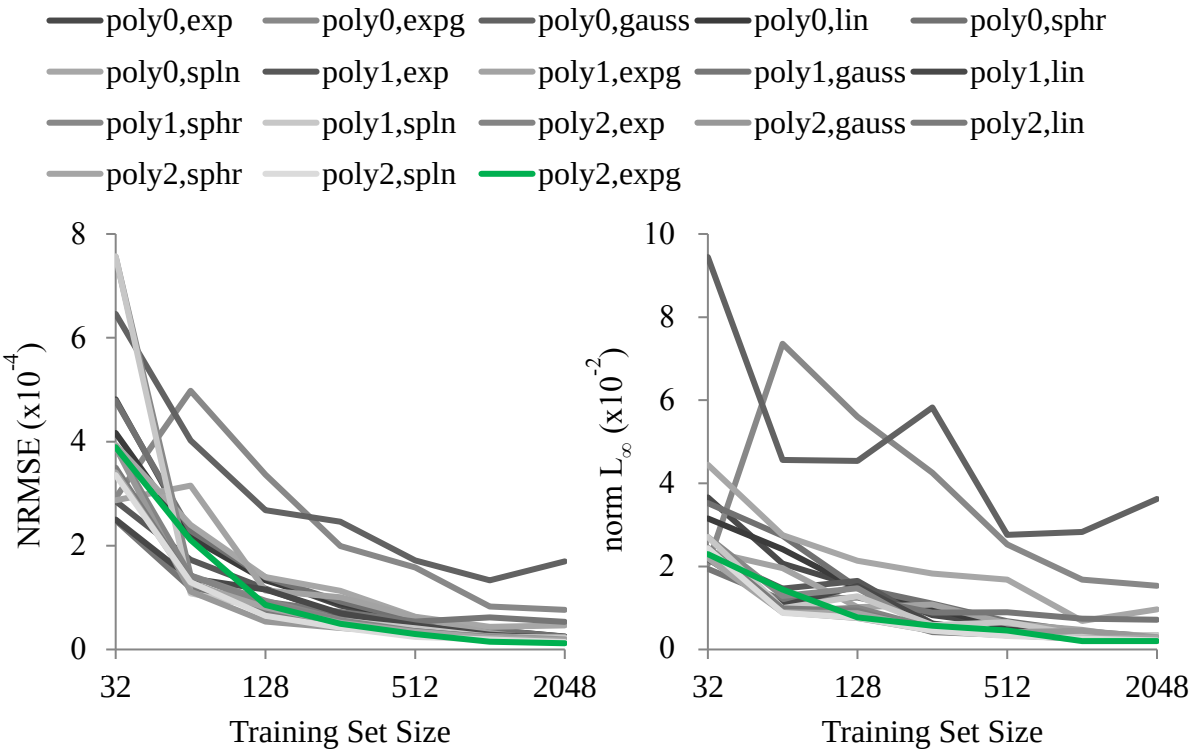

Figure 6.34: Thermoelastic Kriging training errors

6.3 Nonlinear Thermal Reduced Order Models

A set of reduced order models are considered to determine the variation of the material thermal capacity and thermal conductivity with respect to temperature for a representative hypersonic vehicle structure on a terminal trajectory. The number of thermal degrees of freedom is first reduced by projecting the thermal state of a sample structure into a modal space whose bases are determined using proper orthogonal decomposition. A numerical integration scheme based on the Crank–Nicolson algorithm is used to simulate the thermal state forward in time. Models for the generalized material thermal properties are based on the method of Kriging, a least-squares polynomial approximation, and a singular value decomposition approach. The resulting thermal models are compared in terms of accuracy and computational efficiency. The singular

value decomposition approach is shown to be the superior overall reduced-order model to capture the variation of thermal properties with temperature when compared to a full-order finite element solution. The effects of varying the number of retained thermal modes and thermal property eigenvectors on the singular value decomposition model are then considered. It is shown that only a few eigenvectors need to be considered to achieve excellent agreement with finite element analysis.

6.3.1 Sample Collection

To create the thermal property ROMs, a number of training and testing samples were required. The process used to collect these samples is outlined in Figure 6.35 and begins with considering the thermal bases Ψ and thermal mode ranges $\min(c)$ and $\max(c)$ resulting from a POD of an FEA heat transfer simulation of the substructure. Latin hypercube sampling was used to determine a uniformly random set of thermal coordinates c that were then converted to physical temperature distributions T within the FEM. These were then passed to an FEA solver which assembled the full thermal property matrices M and K, which were then exported and generalized according to the thermal bases Ψ into m and k. Each generalized thermal property matrix was then paired with its corresponding thermal coordinates c and sent to each of three ROM training functions to be incorporated into a thermal property ROM.

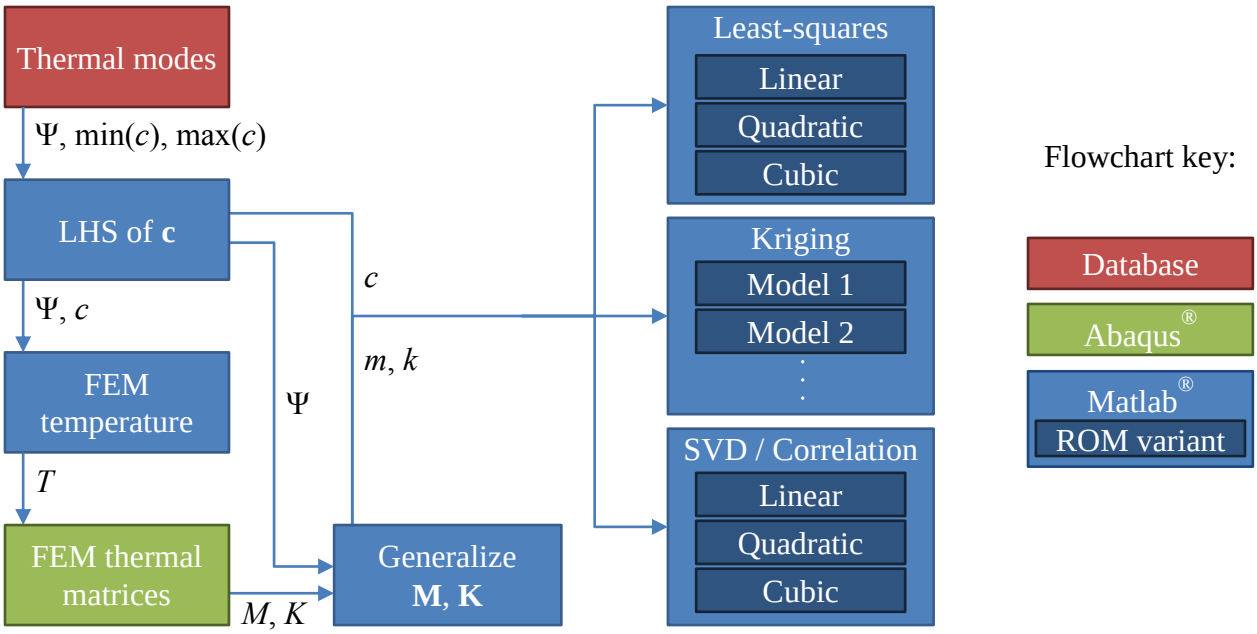

Figure 6.35: Training sample collection process

Within each ROM training function the c, m, k samples are divided into two groups. One group of n training samples was used to train each model within the ROM type. For the least-squares ROM, three models were considered: linear, quadratic, and cubic polynomials of the thermal coordinates c. The Kriging ROM contained eighteen combinations of three regression functions: constant, linear, and quadratic polynomials and six correlation functions: pure exponential, general exponential, Gaussian, linear, spherical, and spline. Each of these regression and correlation functions were default forms provided with the Matlab® DACE toolbox.[141] The SVD and linear correlation ROM contained three models: linear, quadratic, and cubic polynomials of the thermal coordinates.

Another group of testing samples was then used to test the accuracy of each model in prediction of samples not contained in the training set. The model which contained the least single entry maximum error (L_∞) normalized by the value each entry was considered the most accurate

and exported for comparison against the other ROM types. The L_∞ error metric was selected to compare the different ROM variants within a training function since it is the most conservative measure of error. A flowchart of this process is shown in Figure 6.36.

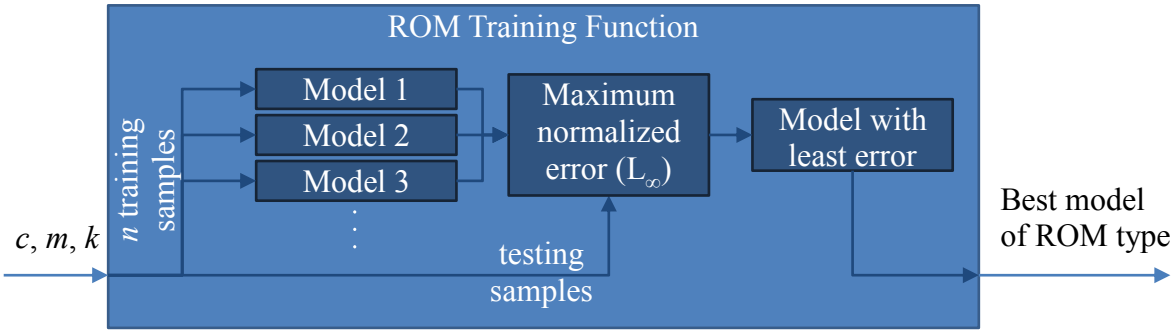

Figure 6.36: ROM training, testing, and selection for each ROM type

6.3.2 Finite Element Analysis Heat Transfer Simulation

To determine a suitable POD basis set for the substructure, a high-fidelity heat transfer simulation was performed using the Dassault Systèmes Inc.'s Abaqus® FEA[191] heat transfer solver. During simulation, at every time step the wall temperature T_w, time t, and spatial locations x, y, z of every node exposed to flow were exported to a Fortran user-defined subroutine and used to search for a corresponding node in a preprocessed database of flow conditions; namely pressure p_e, temperature T_e, and Mach number M_e. This database was determined *a priori* by an in-house unsteady aerodynamics code employing oblique shock, Prandtl-Meyer expansion, and third-order piston theory.[24] The flight trajectory consisted of a 520 second, Mach 6, 75 kft (22.9 km) altitude cruise phase during which the vehicle was trimmed for propelled steady and level flight, followed by a 37.5 second unpropelled terminal phase along a path optimized for maximum final kinetic energy. Details of this trajectory and optimization process may be found in the previous chapter.

Once the flow properties near a node of interest were found, the Eckert reference temperature[25] and black-body radiation methods were used to determine the heat flux $\dot{q}_w$ to the node. The heat flux was imported back to the FEA heat transfer solver as a boundary condition and the solution was moved ahead in time. A flowchart of this process is shown in Figure 6.37. The resulting temperature profiles of the substructure during the cruise and terminal phases are shown in Figure 6.38 and Figure 6.39, respectively.

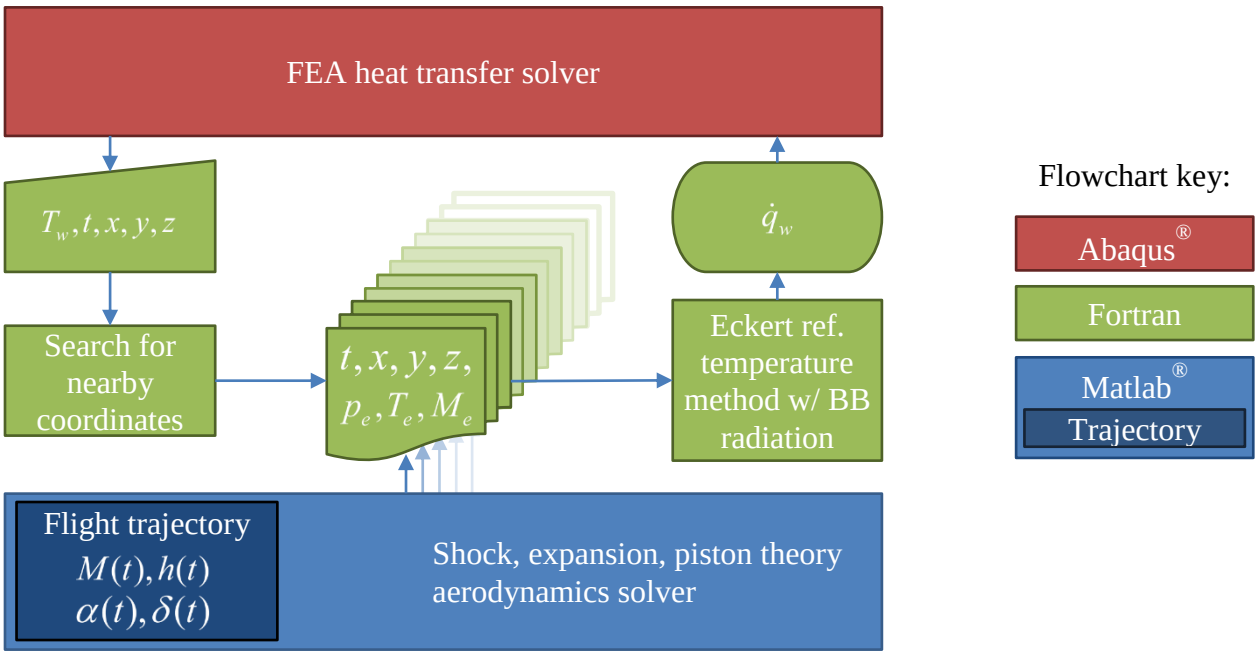

Figure 6.37: FEA heat transfer simulation along flight trajectory

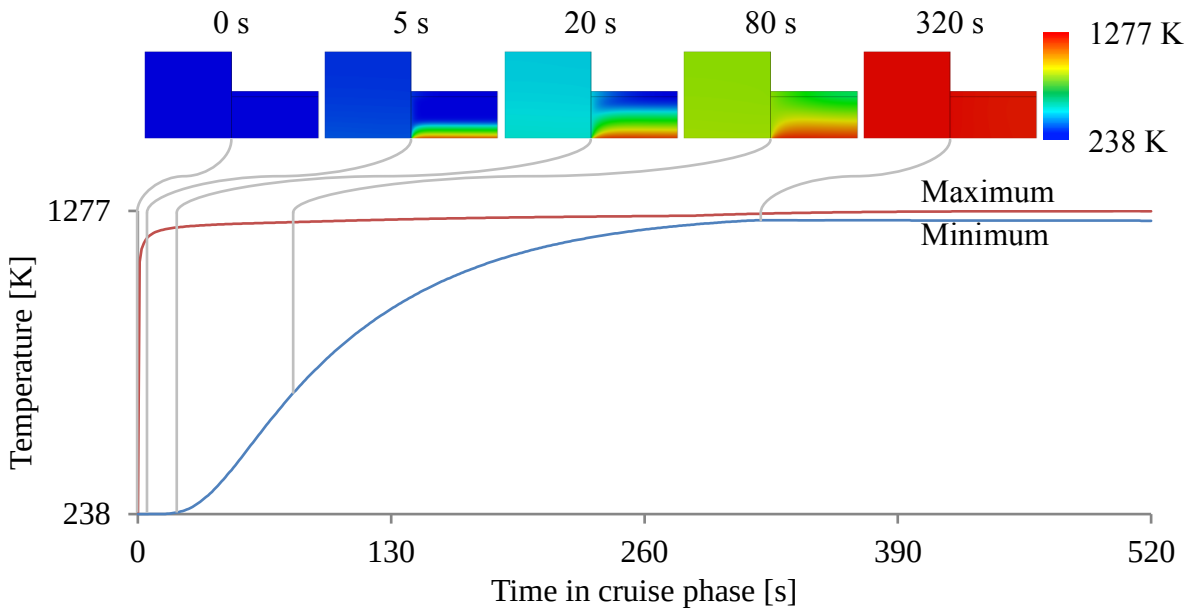

Figure 6.38: Temperature range in substructure during cruise phase

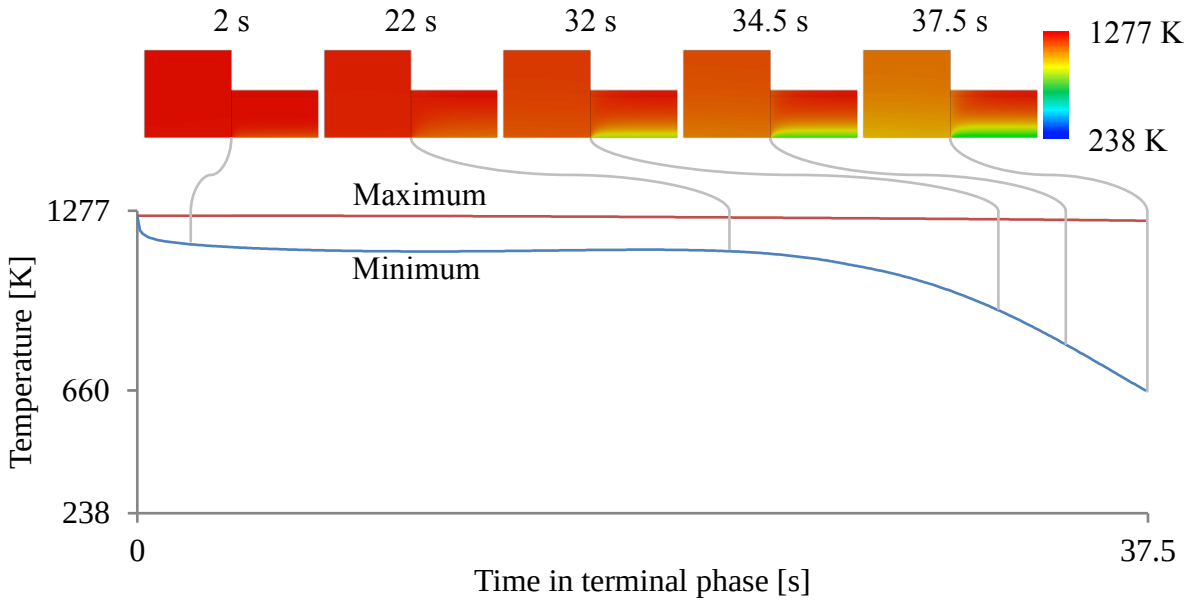

Figure 6.39: Temperature range in substructure during terminal phase

During the cruise phase, the substructure is initially a uniform 238 K. The outer surface of the TPS quickly warms to nearly 1277 K and begins slowly conducting heat inward toward the

skin. The ballast meanwhile has a high thermal conductivity and warms almost uniformly. Protected by the TPS, the skin is the slowest to warm, however after roughly 320 s the substructure became completely thermally soaked, meaning nearly a uniform 1277 K. Upon entering the terminal phase, the vehicle switched from a nose-up to a nose-down angle of attack. Thus the substructure which was initially on the highly thermal loaded windward side of the vehicle was then on the less loaded leeward side which caused as a small initial drop in the outer TPS temperature. After about 32 s, the vehicle had sufficiently slowed to allow additional cooling of the TPS until the end of the terminal phase at 37.5 s. Throughout the terminal phase the skin remained nearly at 1277 K since insufficient time passed to conduct its heat back out through the TPS.

6.3.3 Thermal Bases

After performing a simulation of the sample structure along the cruise and terminal phase trajectories, thermal bases were determined using the method of POD for the terminal phase. The first 5 bases are shown in Figure 6.40 with the relative eigenvalue magnitudes and basis truncation error shown in Figure 6.41. Figure 6.40 reveals that almost the entirety of all modes focus on describing the temperature gradient in the TPS of the model due to the low conductivity of the Acusil-II® material compared to the tungsten and titanium alloy of the ballast and skin, respectively. Some detail is afforded for the titanium alloy skin; however, this is largely to enforce the temperature continuity between the skin and TPS. Despite placing almost all focus on the TPS, Figure 6.41 shows that the truncation of the bases to the first 5 modes provided a relative error of $\sim 10^{-8}$, which is typically sufficient to accurately represent the thermal state of the structure. Thus, one may use these bases to generalize the rank 6478 thermal problem considered by the FEA to a

rank 5 problem and be confident that reasonable solution accuracy may still be obtained if similar thermal loading is simulated.

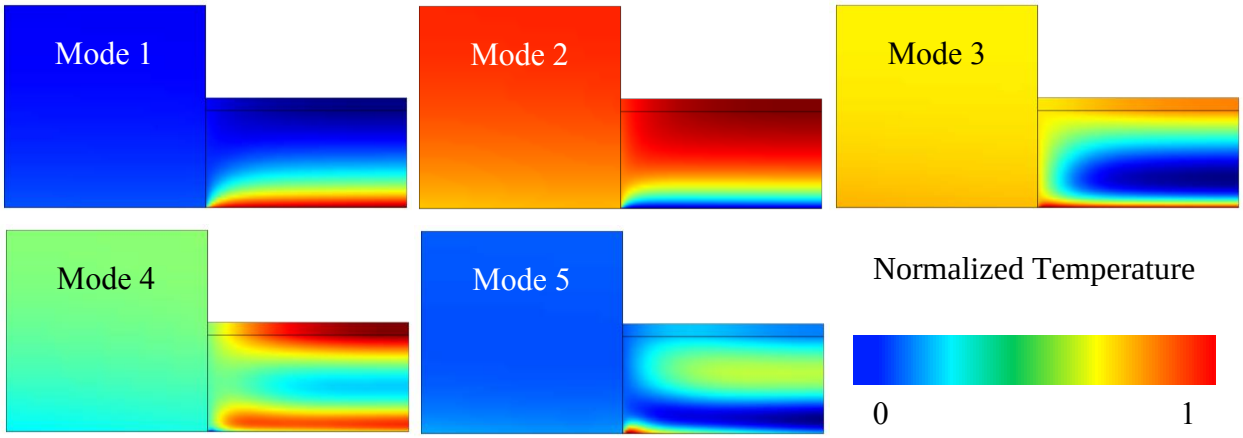

Figure 6.40: First 5 most prominent POD thermal modes

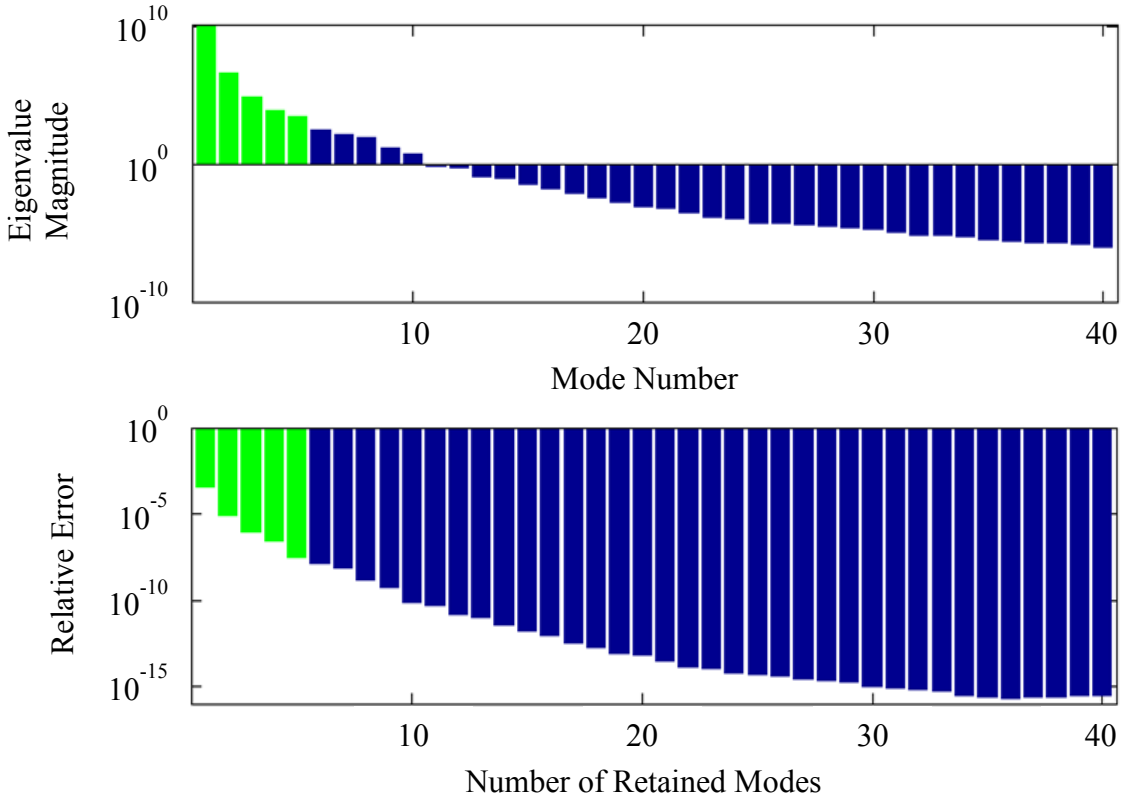

Figure 6.41: Relative POD eigenvalue magnitude and truncation error

6.3.4 Reduced-Order Model Accuracy

For each ROM type, the number n of training samples was varied by powers of 2 from $n = 2$ to $n = 1024$. Each of the resulting models was then tested using the same $k = 1000$ samples to evaluate each ROMs' accuracy. The root-mean-squared-error (RMSE) and normalized maximum error (Norm L_∞) of each ROM type are shown in Figure 6.42 with the most accurate of each type compared in Figure 6.43. For all ROM types, the higher order regression and polynomial functions resulted in the lowest errors when a sufficient number of training samples were provided. However if too few training samples were provided, the higher orders often resulted in higher errors than their lower order counterparts, especially for the least squares and SVD models. For $n > 200$, both the least-squares and SVD ROMs did not exhibit a reduction in error given further training samples. This was due to the limitation of their maximum cubic polynomial function order. The Kriging method produced two distinct groups of models. The first was when the 0^{th} order polynomial regression was used. This allowed Kriging models to be constructed using very few training samples and is akin to radial basis function type ROMs. However once $n \geq 8$, 1^{st} and then 2^{nd} order regression polynomials were shown to be superior. For all Kriging ROMs, the RSME continued to reduce as additional training samples were added until $n = 1024$, with the exception of the 0^{th} order regression and general exponential (expg) formulation which appeared to be especially sensitive to the pseudo-random LHS sampling pattern. This is evident by the uneven and erratic shape of the maximum RMSE line in Figure 6.42. Kriging was found to be the most accurate ROM type of those considered. For all ROM types, a steady decline in the normalized L_∞ was observed and all ROM types showed approximately the same order of normalized L_∞ for $n > 100$. Some minor noise was observed due to the random nature of the LHS

method, but the overall trend that more training samples resulted in lower measures of error was clear. For the largest training set size considered, the least-squares cubic model, 25 bases SVD model with cubic regression, and kriging model with a quadratic regression and spherical correlation were found to be the most accurate of their respective ROM types.

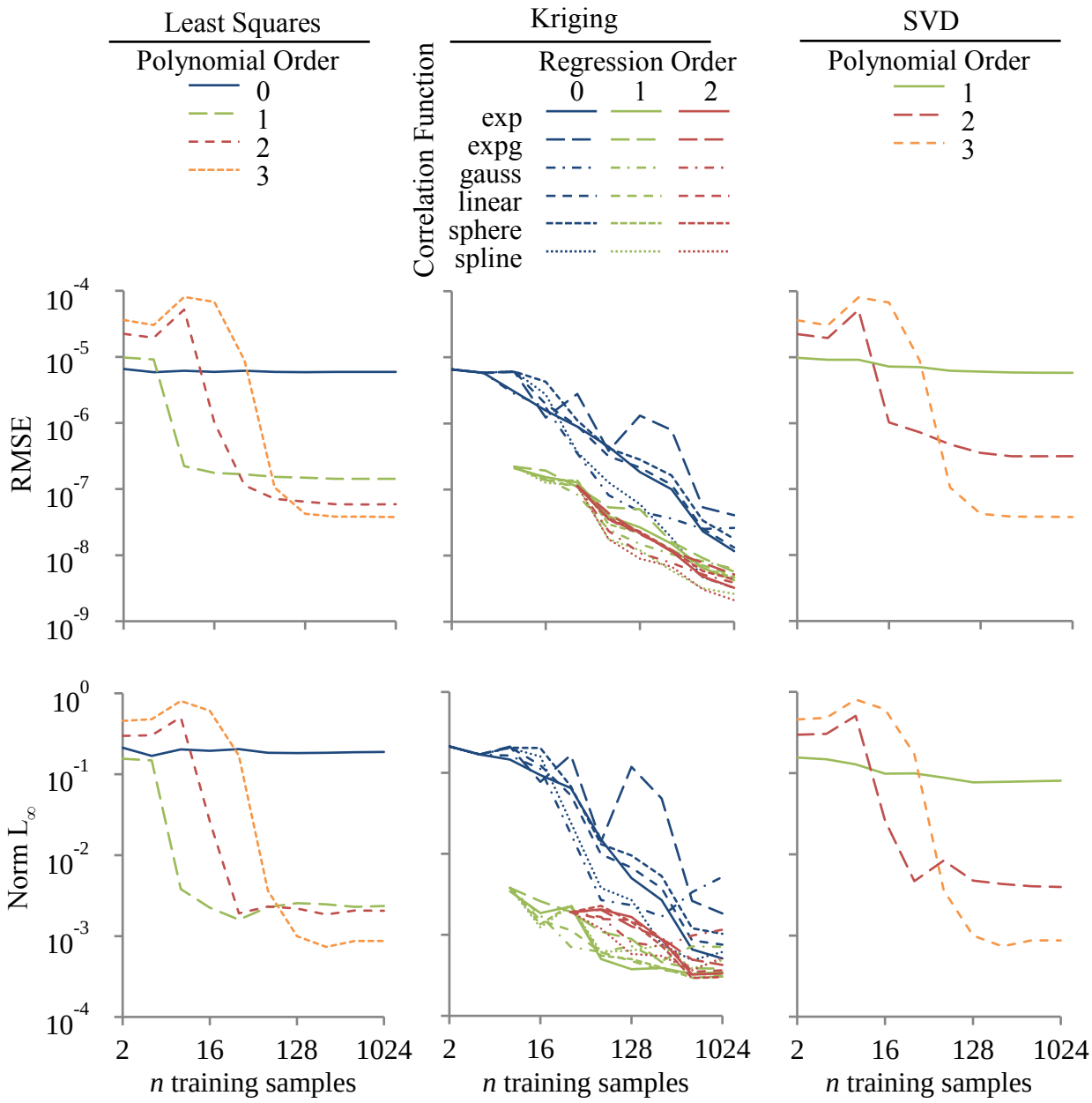

Figure 6.42: Error of each ROM type for a given training set sample size

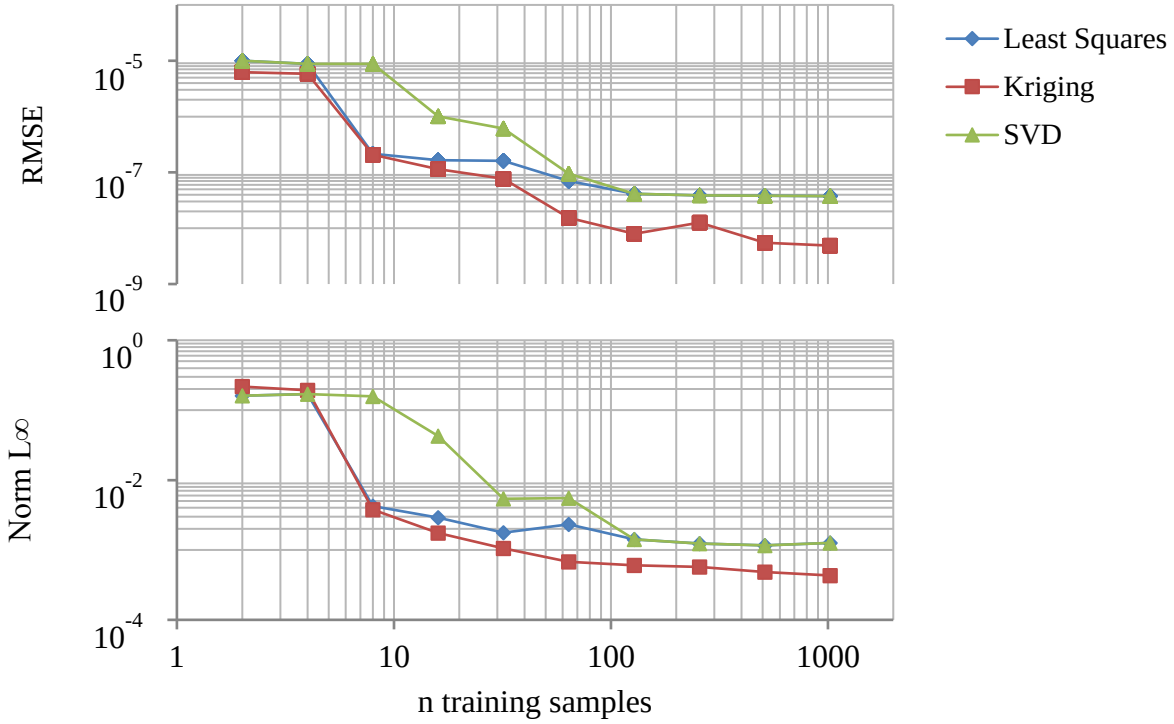

Figure 6.43: Effect of training sample size on the accuracy of ROMs generated from three different approaches

6.3.5 Reduced-Order Model Computational Efficiency

Also critical to evaluation of a ROM's utility is the computational efficiency of a ROM. To quantify computational efficiency, the amount of computer memory the ROM must occupy and the time required for the ROM to be executed were considered. For each of the ROM types and training sets, the memory consumption and execution time required to run the $k = 1000$ test samples was recorded and are shown in Figure 6.44. It can be seen that while the Kriging ROM was the most accurate, this accuracy came at the price of rapidly growing memory requirements and slower execution times than the least-squares and SVD ROMs. This agreed with intuition since

the method of Kriging is able to reproduce the entire training set and thus contains all of the information used to train the ROM. The least-squares and SVD approaches did not have the ability to reproduce the training set and thus retained only a fraction of the information used to train the ROMs which resulted in lower memory requirements for the computer.

In terms of processing speed, the least-squares and SVD ROMs were roughly two orders of magnitude faster than Kriging. The SVD ROM was also slightly faster than the least-squares ROM, however at these sub-millisecond scales, the specific implementation of the models and state of the computer's background programs may influence which of these two ROMs would be processed more quickly. To reduce random fluctuations in processing speed, each ROM was run 10 times, timed using the *tic* and *toc* functions of Matlab®, and the results averaged.

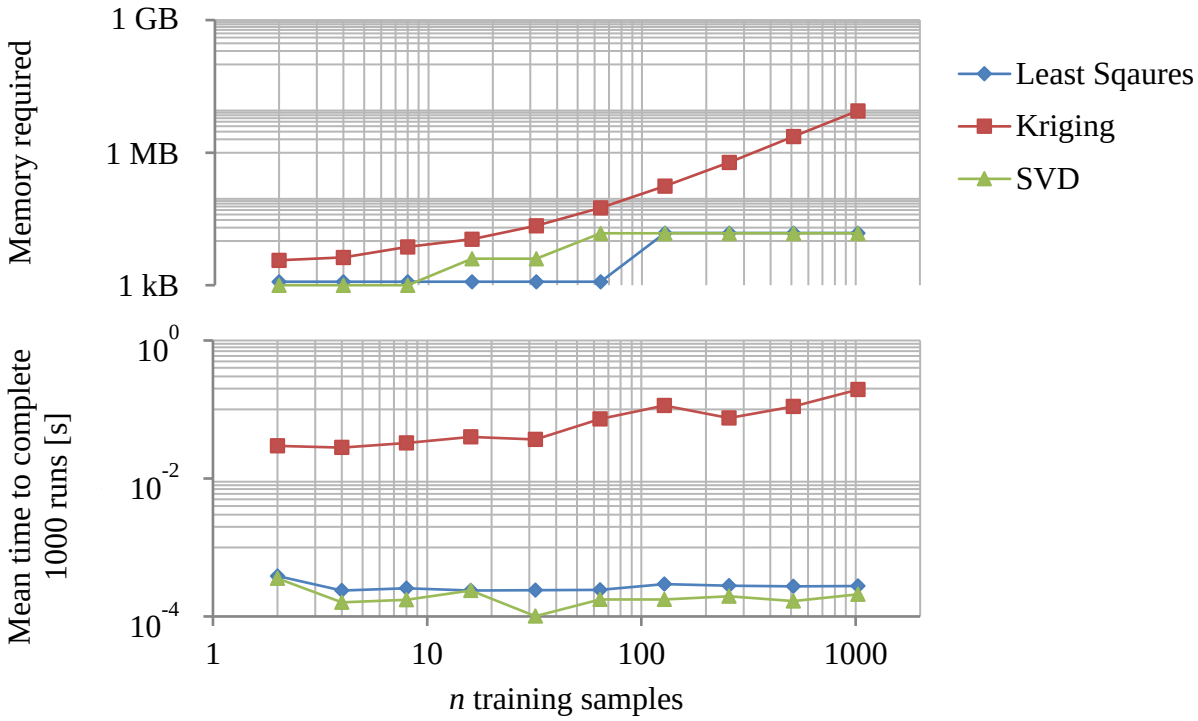

Figure 6.44: Effect of training sample size on the computational cost of ROMs generated from three different approaches

6.3.6 Comparison to Finite Element Analysis

As a check of ROM accuracy and efficiency, simulations of the generalized thermal problem with constant thermal properties and with each ROM approach were conducted. The sample structure was started at a uniform 1260 K similar to the structure temperature at the initiation of the terminal phase of the trajectory. A steady outward heat flux was then applied with the spatial distribution

$$\dot{q}_w = -20341.7\left[\exp\left(-100x + 4\right)/10 + 0.9\right] \tag{6.24}$$

to simulate a cooling boundary layer with a logarithmic thickness profile. Here x is the distance in meters from the ballast edge furthest from the TPS and $\dot{q}_w$ is the heat flux in Watts per square meter. This is not physical since the boundary layer imposing the heat flux would change with the change in the wall boundary conditions. However, the accuracy of the boundary layer heat flux is not the focus of this paper and a consistent heat flux profile allowed for direct comparison of the methods. The constant thermal properties were taken from the materials at the mean temperature distribution observed during the FEA simulation shown in Figure 6.45.

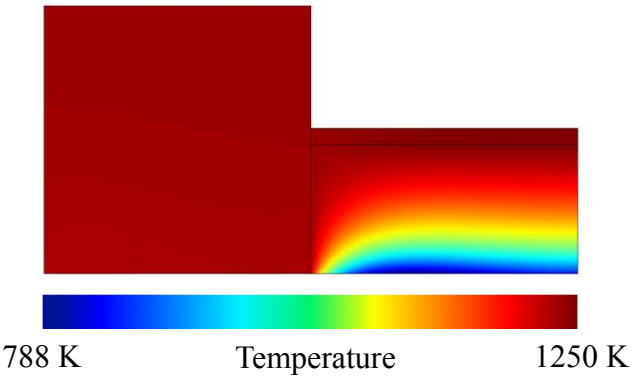

Figure 6.45: Mean temperature distribution

All thermal problems were integrated for 37.5 seconds, the duration of the terminal phase of the trajectory. The final temperature distributions for the FEA, 5-POD mode generalized system with constant thermal properties, and 5-POD mode generalized system with the SVD, least-squares fit, and Kriging ROMs varying the thermal properties can be seen in Figure 6.46. An overall improvement in the agreement between the FEA and 5-POD mode system solutions is evident when using the ROMs to model the thermal properties of the substructure. Processing times and final error measurements for each approach are shown in Table 6.5. As expected, Kriging was the slowest, increasing the total processing time for the simulation by a factor of 24. SVD and least-squares were much faster and slowed the simulation by a factor of 2.4. The SVD and least-squares approaches provided the lowest final RMSE of the temperature field. However, all of the approaches vastly improved the accuracy of the simulation compared to using no thermal property model. It is likely that the RMSE of about 2 K arose from generalization of the governing equations with the 5 thermal modes rather than the thermal property ROMs.

Table 6.5: Simulation performance of each ROM approach

Thermal Property ROM	Processing Time	RMSE
None	2.6 s	167.7 K
SVD	6.3 s	2.2 K
Least-Squares	6.3 s	2.2 K
Kriging	62.5 s	2.8 K

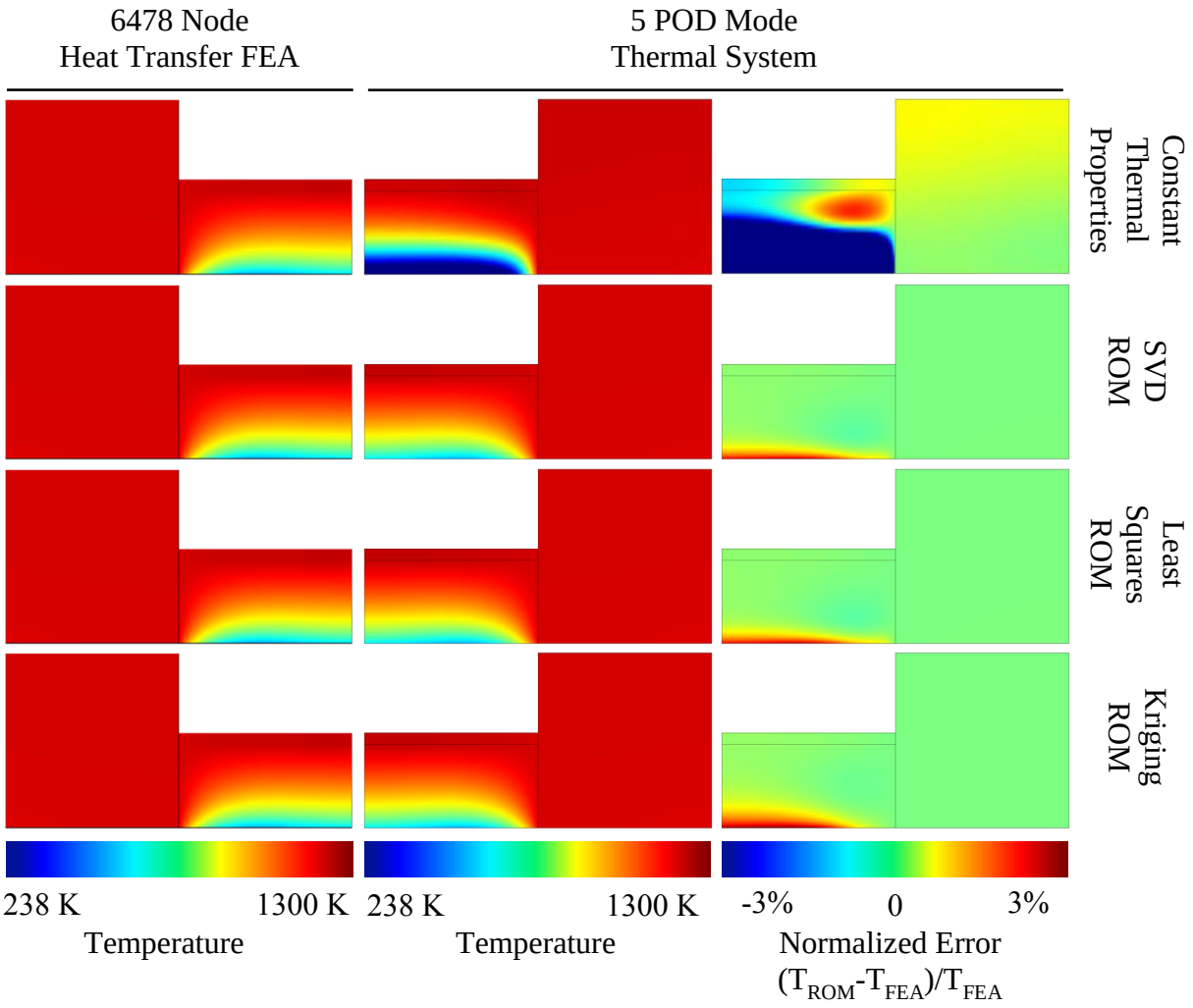

Figure 6.46: Significant qualitative improvement when using the thermal property ROMs with the 5 mode thermal system compared to with constant thermal properties

6.3.7 Variation of Singular Value Decomposition Reduced-Order Model Number of Thermal Modes

Since the SVD ROM approach is novel to this type of problem, the effect of varying the number of retained thermal modes was also studied. Using the methods previously described, SVD ROMs which considered the top 2, 5, and 8 POD thermal modes were trained and used to simulate the steady heat-flux case in the previous section. The temperature range of each simulation compared to the FEA solution is shown in Figure 6.47 and RMSE in Figure 6.48. It can be seen that using only 2 modes provided a reasonable range of temperatures for much of the simulation, but was unable to accurately express the initial temperature profile. Further modes first refined the initial portion of the solution when 5 modes were included, and later refined the later portion when 8 modes are included. A final RMSE as low as 0.4 K is shown in Figure 6.48 when 8 modes are included.

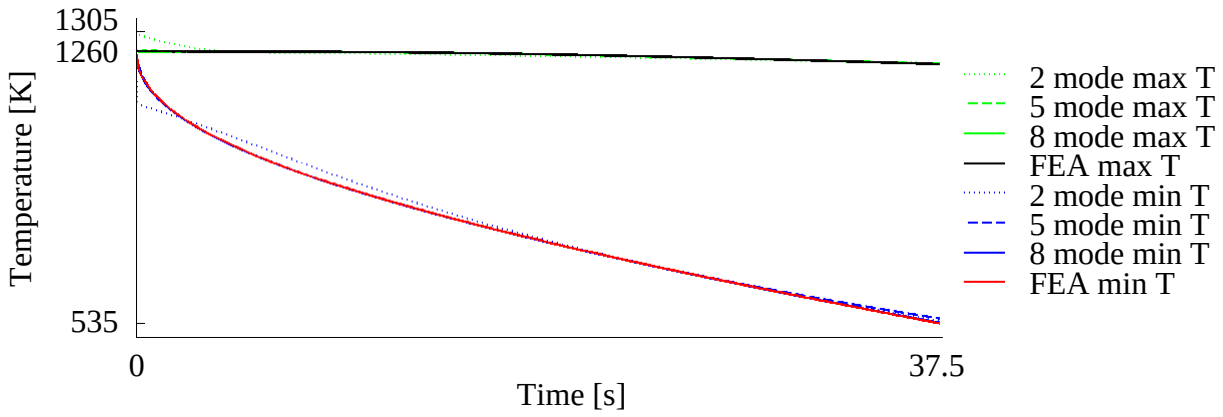

Figure 6.47: Temperature range of SVD ROM simulation converges on FEA solution as the number of retained thermal modes is increased

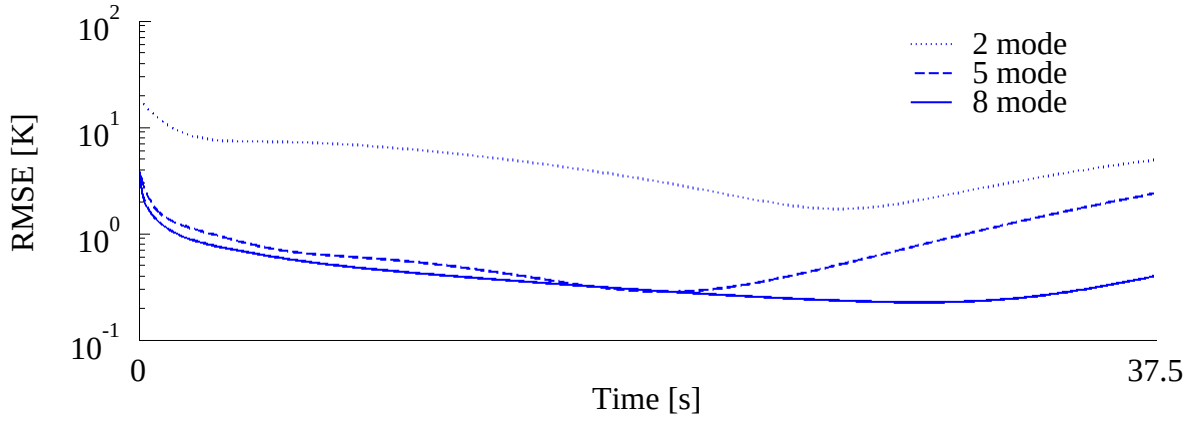

Figure 6.48: Convergence of SVD ROM to FEA solution with increasing number of retained thermal modes

6.3.8 Truncation of Singular Value Decomposition Bases

In some cases, it may be impractical to perform a full SVD on the snapshot matrix. This could be due to the matrix being too large because it contains too many degrees of freedom, snapshots, or both. In such a scenario, the Lanczos algorithm or some other method may be used to find only most important singular values and bases. A threshold value could be chosen by the engineer below which the singular values and bases would be neglected. This truncation of the SVD bases may degrade the accuracy of the final ROM, but so long as the most dominant bases are retained, this degradation would be minimal. Figure 6.49 shows the sorted magnitudes of the singular values of the 8 thermal mode snapshot matrix. It can be determined from the singular values that bases 1 through 9 dominate the solution space while higher bases are negligible. Therefore, neglecting these higher bases still produced a good SVD ROM. From Figure 6.50 it can be seen that this was the case as SVD ROMs generated with truncated bases continue to closely

match the temperature ranges of the FEA solution during simulation and have very small errors compared to retaining the full, 64 bases set.

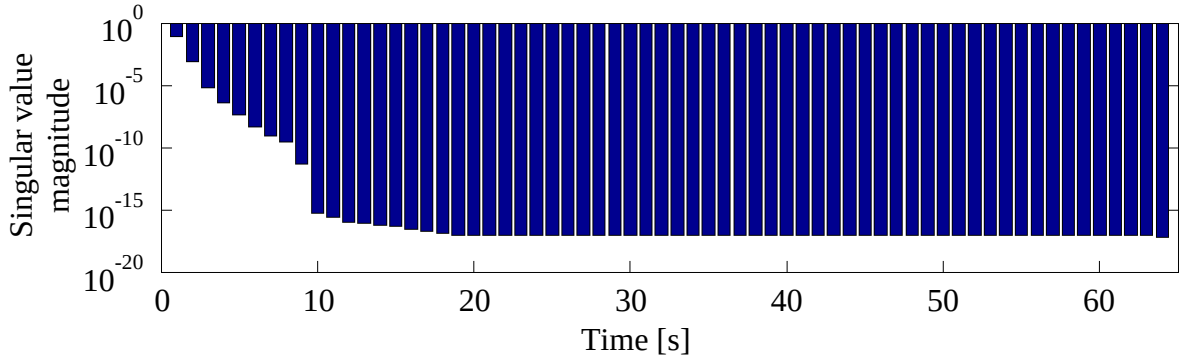

Figure 6.49: Sorted singular values of the 8 thermal mode snapshot matrix

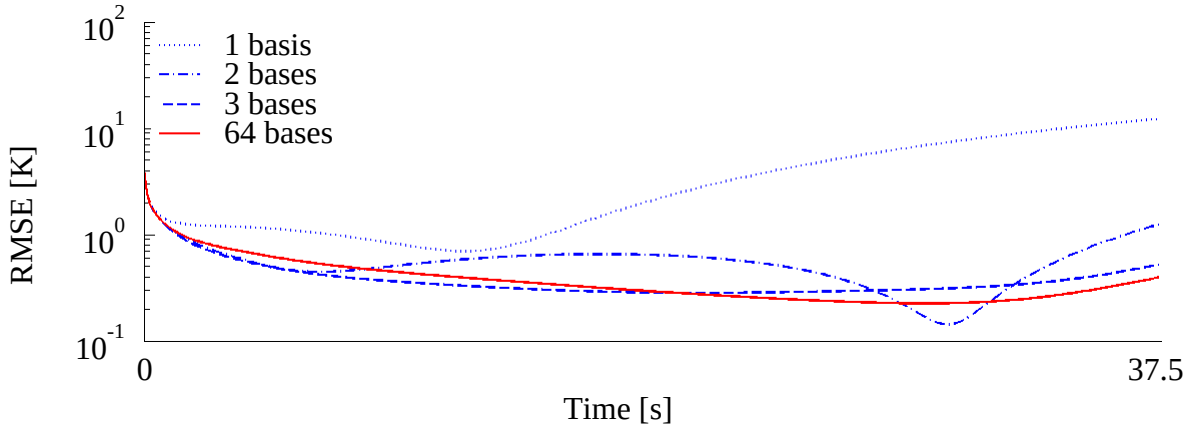

Figure 6.50: Low RMSE compared to FEA when as few as three SVD bases are retained

6.4 Rapid Simulation through Singular Value Decomposition

A reduced order model based on singular value decomposition and correlation is developed to capture the nonlinear dynamics of a hypersonic vehicle in flight. A set of training samples in state space form are collected using the complex step method. These samples are used to identify

a set of ordered bases that describe the variation of the state matrices and state rates. Surrogate functions are fit to the coefficients of these bases to approximate the training samples and predict the state matrices outside of the training set. The dynamics of the system may then be rapidly simulated, provided the training set sufficiently populates the state space. This approach is first applied to a spring-mass-damper system with variable nonlinearity and number of degrees of freedom to determine training sample size and surrogate function orders that produce stable and accurate time simulations. The IC3X vehicle is then considered to demonstrate the potential of this approach for rapid simulation of hypersonic flight.

6.4.1 Reduced-Order Model Training

The process of collecting state samples, training the SVD ROM, and determining if the model is complete is outlined in Figure 6.51. It begins with the definition of states and their respective limits. An LHS[139] of the states is considered and state space representations of the system under the sampled conditions are estimated using the complex-step method[192] described previously. The *s* samples are compiled into the sample matrix s and divided into two groups of *m* and *k* samples. The first *m*-samples for training the SVD ROM while the second is *k*-samples for testing the predictive accuracy of the trained ROM. The *m*-samples enter the ROM training function where the decomposition and surrogate fitting are carried out. The resulting ROMs are then evaluated for accuracy using normalized root mean square error (NRMSE) and maximum error (L_∞) metrics for the *k*-testing samples. If the most accurate SVD ROM presents an error below some user defined tolerance, the SVD ROM is completed and ready for use as a surrogate for the higher fidelity reference model. If the error tolerance is exceeded, then additional samples are selected using LHS and the training process is repeated.

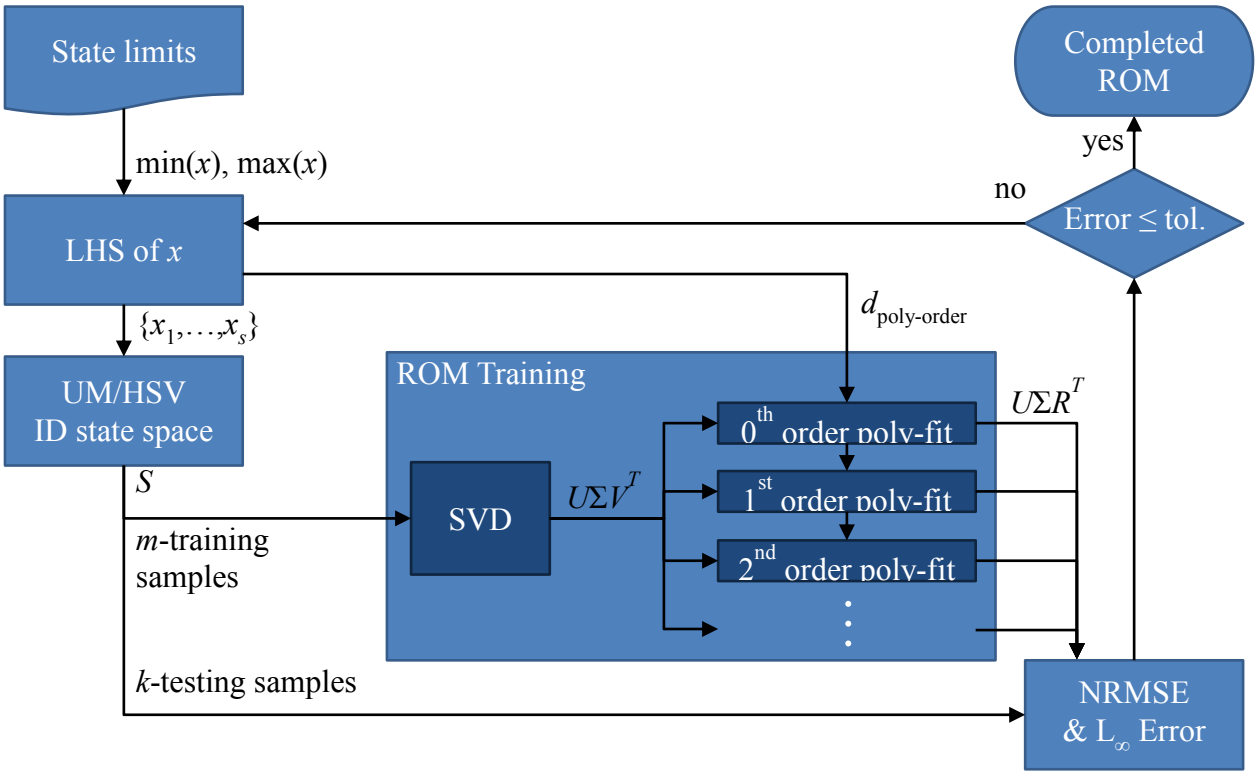

Figure 6.51: Outline of the SVD ROM training process

6.4.2 Nonlinear-Spring, Mass, Damper

A nonlinear-spring, mass, and damper system is shown in Figure 6.52. With this system, the number of degrees of freedom could be easily varied by chaining any number of masses together and the nature of the nonlinearity can be varied by choosing any of the stiffness, damping, and/or mass coefficients to be a function of displacement or time. For this study, the masses and damping coefficient were held constant while the stiffnesses were polynomial function of displacement ranging from 1st to 6th order. These coefficients are given in Table 6.6.

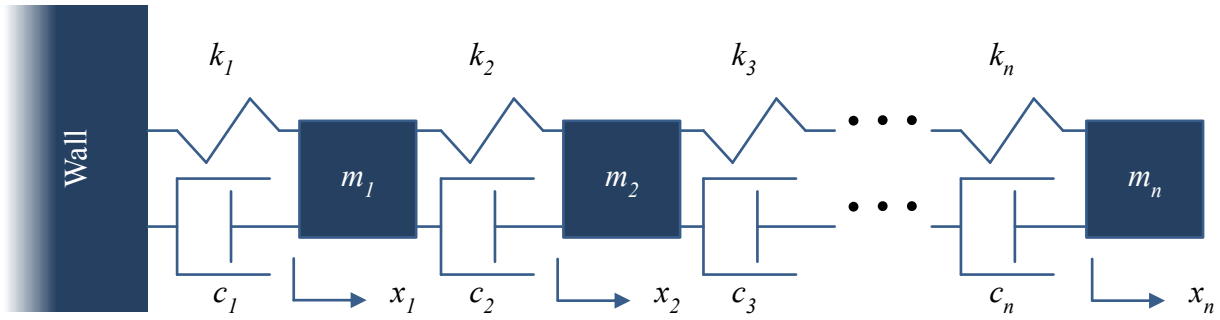

Figure 6.52: Nonlinear-spring, mass, damper system

Table 6.6: Nonlinear-spring, mass, damper coefficients (i = 1 ... n)

Symbol	Value
m_i	10.0
c_i	0.1
k_i	$(x_i\text{-}x_{i-1})^p$
x_0	0

n: total number of spring, mass, and damper groups in chain
i: index of spring, mass, and damper group in chain
p: order of spring stiffness polynomial

The state space representation of this system is given by

$$\begin{bmatrix} \dot{x}_1 \\ \dot{x}_2 \\ \vdots \\ \dot{x}_n \\ \ddot{x}_1 \\ \ddot{x}_2 \\ \vdots \\ \ddot{x}_n \end{bmatrix} = \begin{bmatrix} 0 & 0 & \cdots & 0 & 1 & 0 & \cdots & 0 \\ 0 & 0 & \cdots & 0 & 0 & 1 & \cdots & 0 \\ \vdots & \vdots & \ddots & \vdots & \vdots & \vdots & \ddots & \vdots \\ 0 & 0 & \cdots & 0 & 0 & 0 & \cdots & 1 \\ \frac{-k_1}{m_1} - \frac{k_2}{m_1} & \frac{k_2}{m_1} & \cdots & 0 & \frac{-c_1}{m_1} - \frac{c_2}{m_1} & \frac{c_2}{m_1} & \cdots & 0 \\ \frac{k_2}{m_2} & \frac{-k_2}{m_2} - \frac{k_3}{m_2} & \cdots & 0 & \frac{c_2}{m_2} & \frac{-c_2}{m_2} - \frac{c_3}{m_2} & \cdots & 0 \\ \vdots & \vdots & \ddots & \frac{k_n}{m_{n-1}} & \vdots & \vdots & \ddots & \frac{c_n}{m_{n-1}} \\ 0 & 0 & \frac{k_n}{m_n} & \frac{-k_n}{m_n} & 0 & 0 & \frac{c_n}{m_n} & \frac{-c_n}{m_n} \end{bmatrix} \begin{bmatrix} x_1 \\ x_2 \\ \vdots \\ x_n \\ \dot{x}_1 \\ \dot{x}_2 \\ \vdots \\ \dot{x}_n \end{bmatrix}, \quad (6.25)$$

and may be used to directly check the accuracy of the SVD ROM's estimates.

6.4.3 Reduced-Order Model Stability

To begin to understand the behavior and performance of the SVD ROM approach, the number of required samples to represent a system of given order and degrees of freedom was investigated using the nonlinear-spring, mass, and damper test case. The chain of masses was initially set to an equilibrium state with zero velocity and all masses at zero displacement. The n^{th} mass was then displaced by 1, released, and the system dynamics integrated forward in time using the MATLAB[193] ode45 solver.

During testing, it was found that if a state exceeded the range of the training set, causing the SVD ROM to extrapolate, the states would often diverge toward infinity. This instability would frequently prevent numerical integration of the system dynamics. Insufficient range of the training set is typically a symptom of too sparse of a sampling of the state space and was remedied by increasing the number of training samples. An example of this unstable system dynamics due to under-sampling is shown in Figure 6.53.

To determine the boundary of the SVD ROM stability, the training set size m was varied from 2 to 2^{14} by powers of 2 and the maximum number of stable degrees of freedom was determined for each case. This was carried out for systems whose spring constants were 2^{nd}, 4^{th}, and 6^{th} powers of the elongation of the springs. The results are shown in Figure 6.54.

It can be seen by fitting power-law curves to the results how the number of stable degrees of freedom depend on the training set size and system order. It is apparent that greater the number of degrees of freedom and the greater the order of the system, then the greater the number of

samples that will be needed to capture the behavior of that system for both the 2-step and 1-step SVD ROM approaches. The 1-step approach also requires more samples than the 2-step approach for a given number of degrees of freedom and system order. This is due to the fact that in the 1-step approach, there is no second multiplication by the state vector x after the SVD ROM is exercised. Thus the 1-step approach is only capable of modeling one order less than the 2-step approach. The efficiency of the SVD ROM as additional training samples were added can be considered as

$$\text{Efficiency} = m^{(-1/n)} \quad . \tag{6.26}$$

In this form, the fewer the number of training samples m required by the SVD ROM to capture the behavior of a system with n degrees of freedom, and therefore a sample space of n dimensions, then the closer the efficiency value approaches unity. From Figure 6.55 it can be seen that the efficiency of the training set tends to increase as the number of degrees of freedom increase. This means that for a system similar to the nonlinear-spring, mass, and damper chain posed in this work, where the dynamics of each state are similar, the training sample point density in the state space may be reduced as more degrees of freedom are considered. This is a typical feature of the LHS used in this work, as each additional sample strives to be far and equidistant from all previous samples in all dimensions to maximize the amount of useful information obtained.[168]

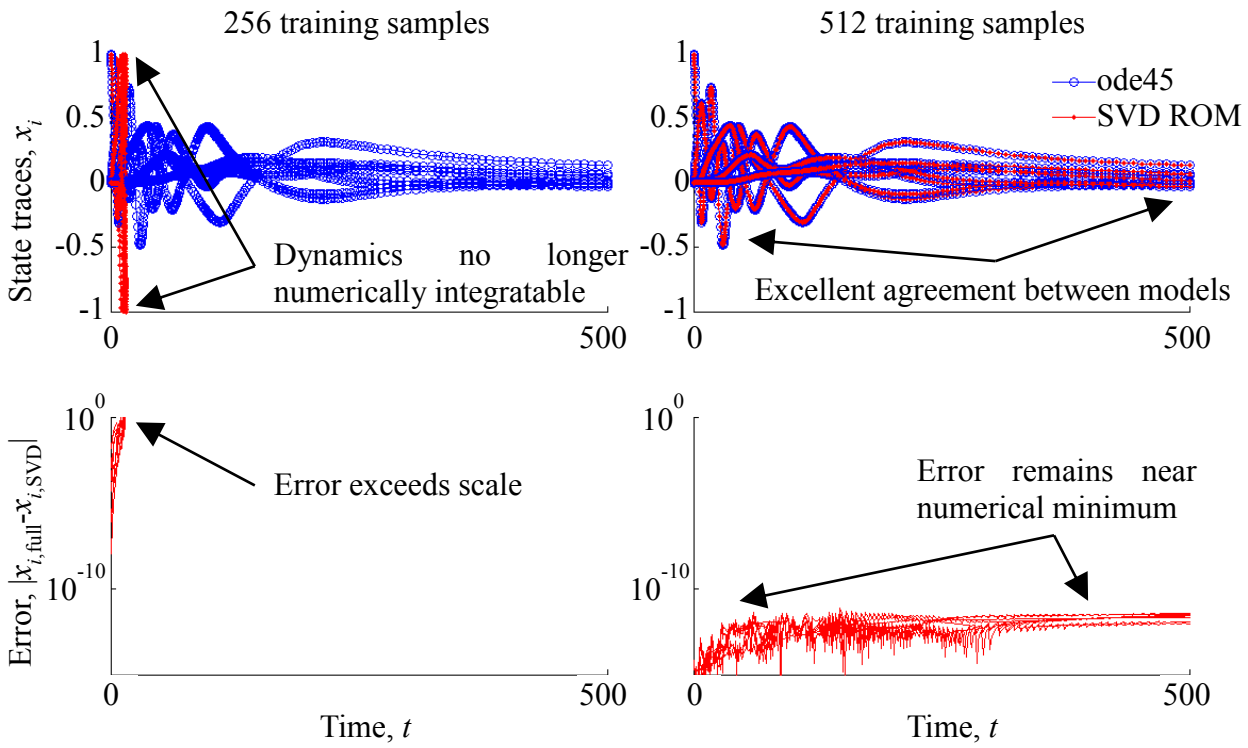

Figure 6.53: Example of SVD ROM instability due to under-sampled 4th order, 8 degree-of-freedom nonlinear-spring, mass, and damper case

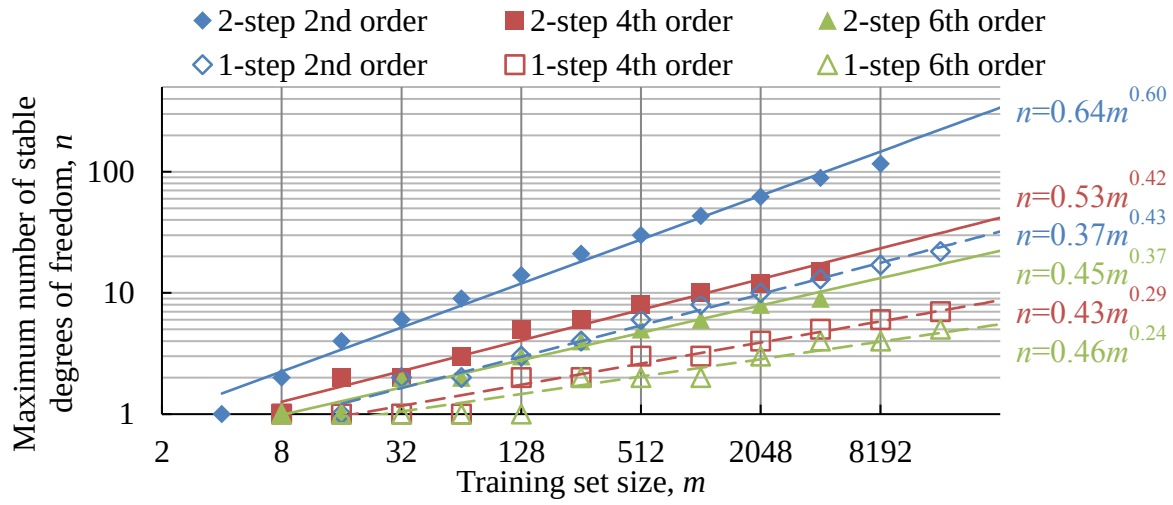

Figure 6.54: Stability boundary of the SVD ROM for various system orders

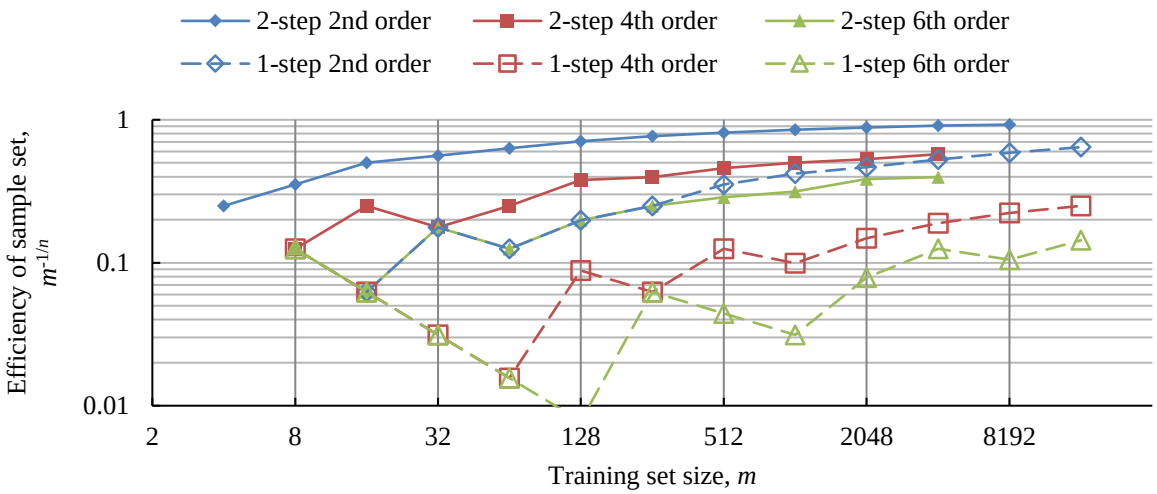

Figure 6.55: Increasing efficiency of training sample set with increasing number of degrees of freedom

6.4.4 Application to the IC3X Vehicle

To test the SVD ROM approach on a more realistic system, the IC3X vehicle dynamics were considered. In addition to the 12 rigid body states typical of 6-degree of freedom flight simulations and the 4 elastic states required to consider the 2 elastic degrees of freedom, the deflection angles of the 4 control fins were also included. The sampling ranges for each of these states for the experiments to follow are shown in Table 6.7. A training set of m=270,000 samples was collected and a 1-step, 4th order SVD ROM trained with 20 retained bases. This training set size was selected by solving the power-curve fit to the data shown in Figure 6.54 for the n=16 independent degrees of freedom and rounding up. A time simulation using the SVD ROM was then compared to the UM/HSV code for a 1 second top-hat pitch-up maneuver in which the fins were deflected 1° shown in **Error! Reference source not found.**. The resulting state traces throughout the 3-second maneuver are shown in Figure 6.57 with the individual longitudinal states

shown in Figure 6.58 and Figure 6.59 along with the normalized error of the SVD ROM according to

$$\text{Normalized error} = \frac{\left| x_{i,\text{HSV}} - x_{i,\text{SVD}} \right|}{\max\left(\left| x_{i,\text{HSV}} \right| \right)}, \tag{6.27}$$

where x_i is a column matrix containing the trace of the i^{th} state. For all longitudinal states, the SVD ROM solution matches very well with UM/HSV. A maximum error of 25.9% for the longitudinal bending rate $\dot{\eta}_2$ is shown during the initial deflection of the fins but recovers quickly to a mean error of 0.5% over the duration of the maneuver. Most profound is the difference in processing time. To consider this 3 second maneuver using a computer with an Intel Xeon E5-2650 2.0 GHz processor and 32 GB of memory, the UM/HSV code required 239.3 seconds while the SVD ROM required 17.2 seconds. This is nearly a 14 times increase in simulation speed.

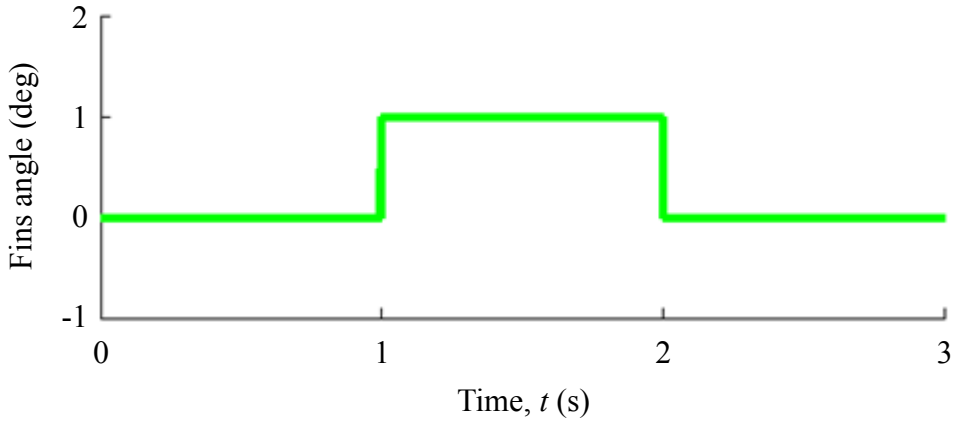

Figure 6.56: Fin deflection input signal

Table 6.7: State and input sample ranges for the IC3X vehicle SVD ROM training set

Description	Symbol	Min.	Max.
Body axial velocity (m/s)	u	1744	1770
Body lateral velocity (m/s)	v	-0.01	0.01
Body vertical velocity (m/s)	w	-40	24
Roll rate (°/s)	p	-0.6	0.6
Pitch rate (°/s)	q	-23	29
Yaw rate (°/s)	r	-0.6	0.6
Earth-body axial displacement (m)	x	0	5310
Earth-body lateral displacement (m)	y	-0.1	0.1
Earth-body vertical displacement (m)	z	-6	9
Earth-body roll angle (°)	ϕ	-0.6	0.6
Earth-body pitch angle (°)	θ	-1.2	12
Earth-body yaw angle (°)	ψ	-0.6	0.6
Lateral bend amplitude	η_1	-0.001	0.001
Longitudinal bend amplitude	η_2	-0.001	0.001
Lateral bend rate (1/s)	$\dot{\eta}_1$	-0.1	0.1
Longitudinal bend rate (1/s)	$\dot{\eta}_2$	-0.1	0.1
Fin 1 deflection (°)	δ_1	0	1
Fin 2 deflection (°)	δ_2	0	1
Fin 3 deflection (°)	δ_3	0	1
Fin 4 deflection (°)	δ_4	0	1

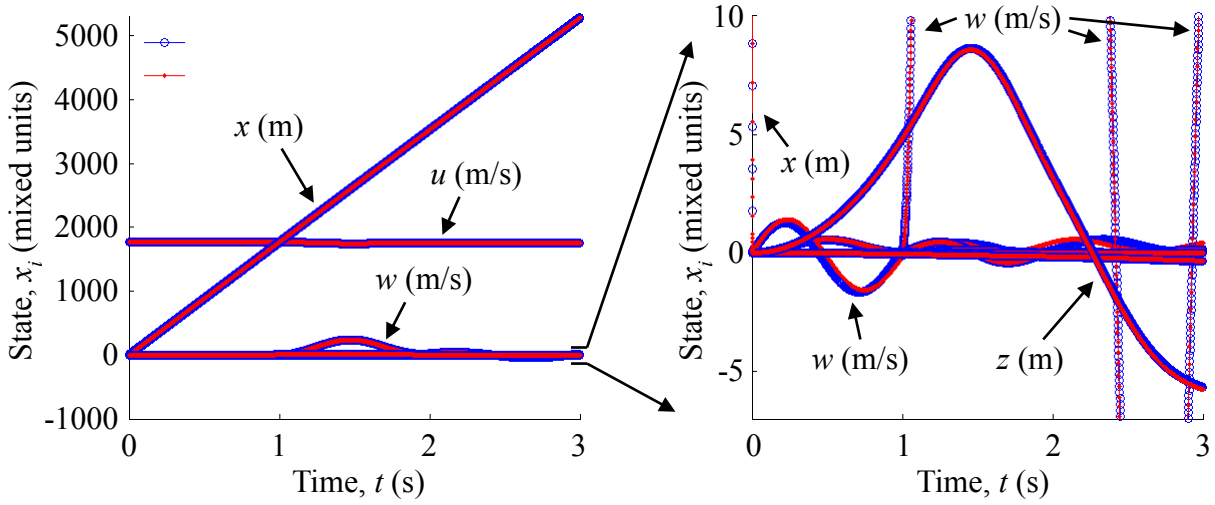

Figure 6.57: Comparison of UM/HSV and the 1-step, 4th-order SVD ROM with 20 retained bases during a 3-second, 1-degree pitch maneuver

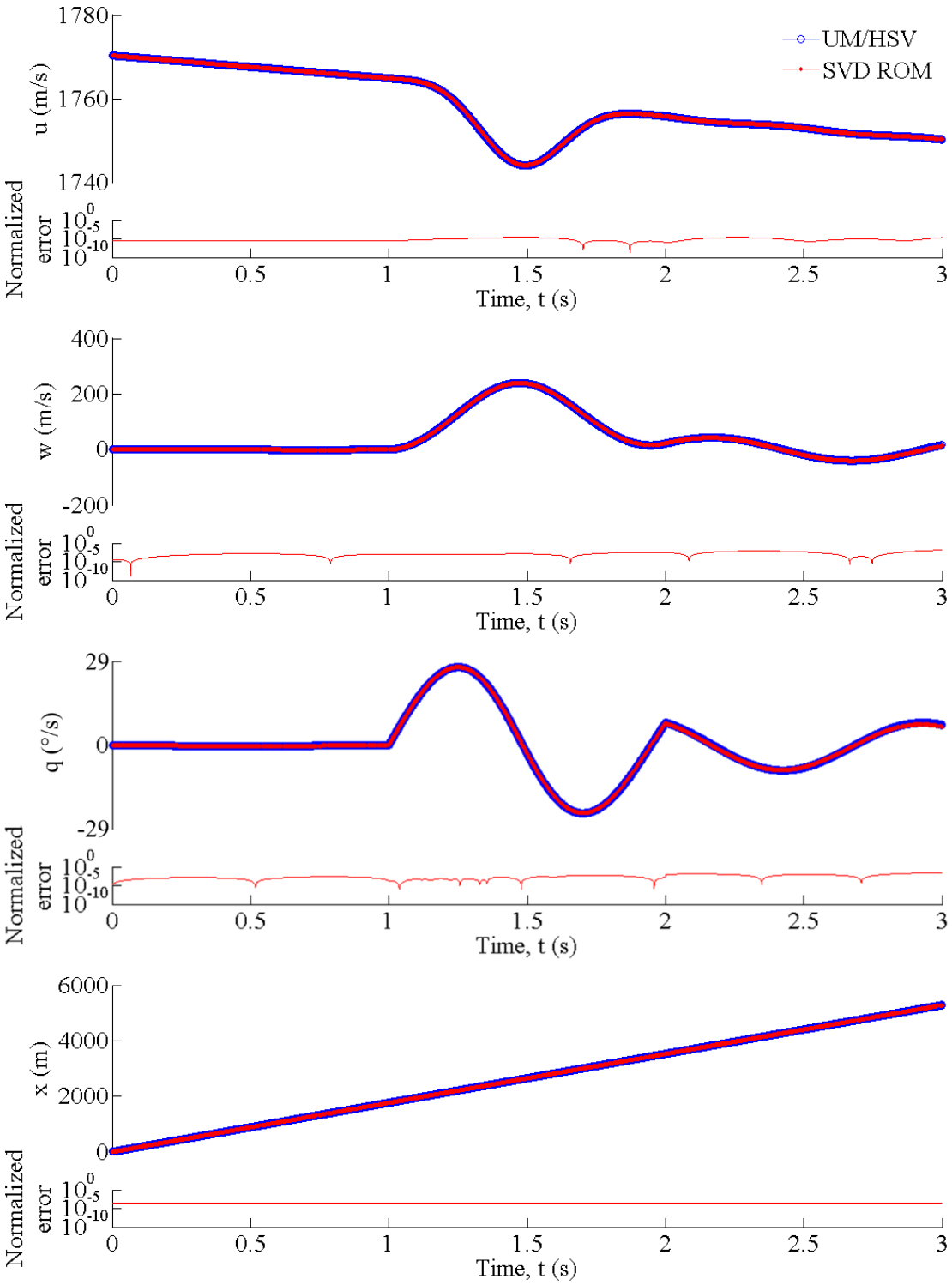

Figure 6.58: Comparison of first 4 longitudinal states from UM/HSV and 1-step, 4th-order SVD ROM with 20 retained bases

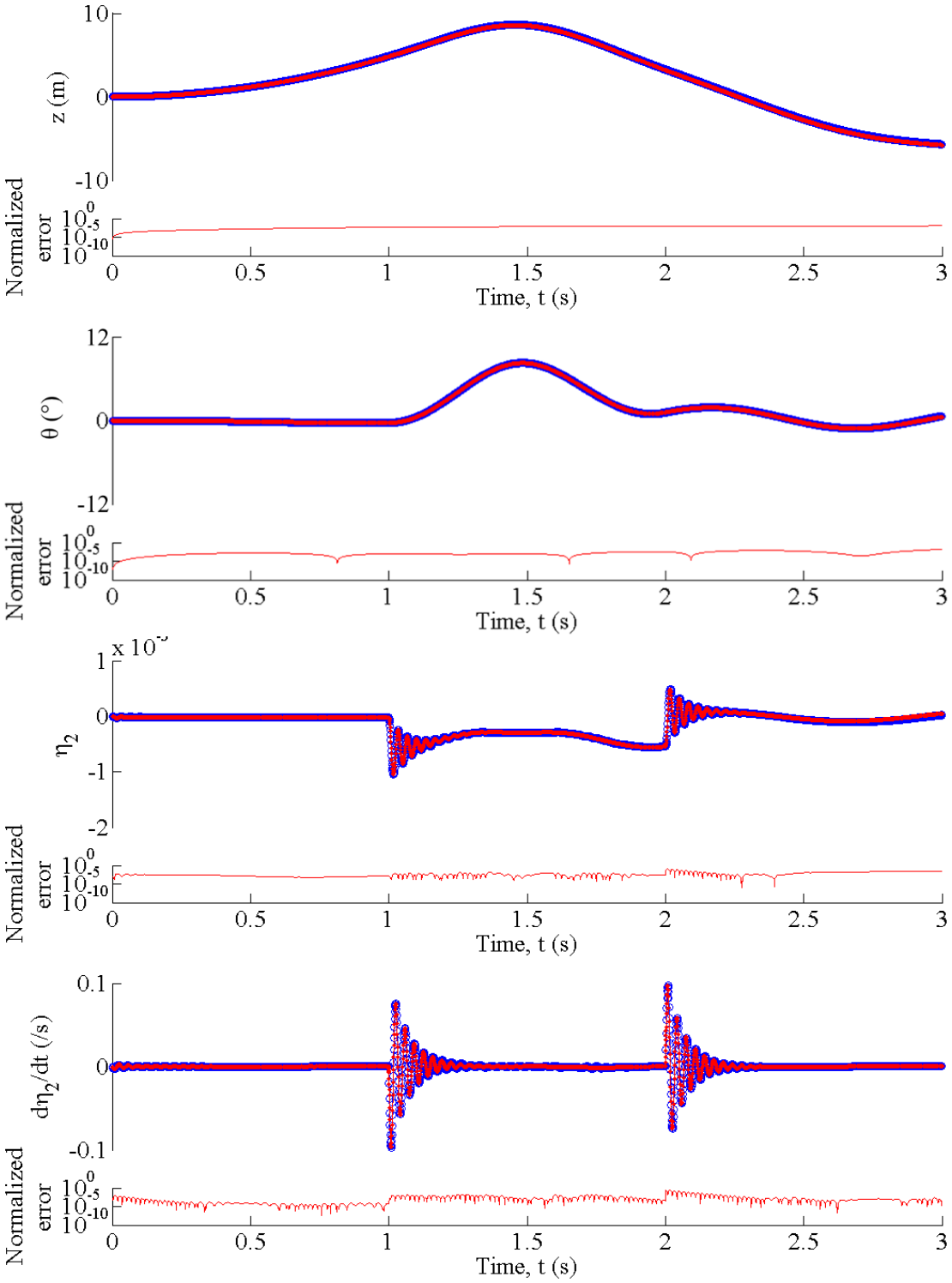

Figure 6.59: Comparison of last 4 longitudinal states from UM/HSV and 1-step, 4th-order SVD ROM with 20 retained bases

6.4.5 Singular Vector Truncation

As previously discussed, the singular values contained in Σ offer a means of ranking the relative importance of the singular vectors U in describing the singular space. In order to further decrease the processing time of the SVD ROM simulation, it may be possible to reduce the number of relevant singular vectors by truncating those corresponding to the lowest singular values. The number of dimensions in the singular space would then be reduced, simplifying the integration problem, while sacrificing as little accuracy as possible.[35] To determine the effect of truncation on the solution accuracy, the IC3X 1-step, 4th order SVD ROM was retrained while retaining the 1st through 20th most important singular vectors. The root-mean-squared error of all 16 states was then determined at the final time step for the 1-degree pitch-up maneuver and is shown in Figure 6.60. The processing time required to integrate the maneuver's equations of motion is shown in Figure 6.61.

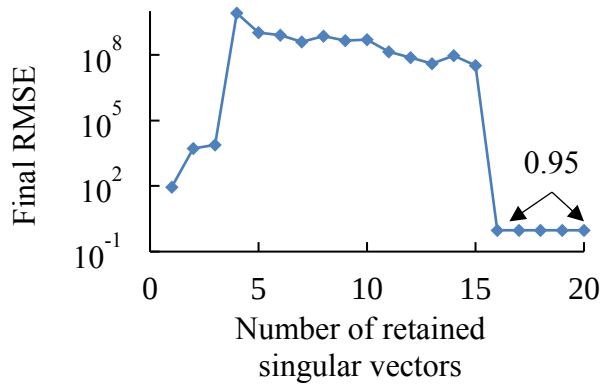

Figure 6.60: Error occurred due to truncation of the singular vectors

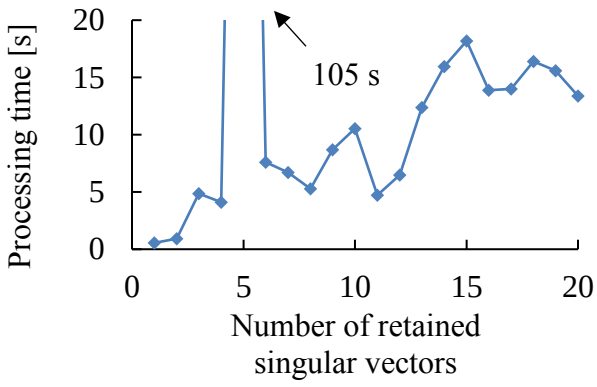

Figure 6.61: Processing time reduction due to truncation of the singular vectors

While retaining 1, 2, or 3 singular vectors appeared to provide a somewhat accurate solution using a small amount of processing time, this was largely due to the fact that the solution was numerically integratable, as shown in Figure 6.62. Retaining 4 to 15 vectors lead to solutions that increasingly matched the UM/HSV solution, but inevitably diverged and were unable to be integrated. The divergence of the SVD ROM estimated states from the UM/HSV solution was not unique to any single state, but rather would occur in all states simultaneously. This was a result of the SVD ROM expressing the states as combinations of singular vectors. As any one singular vector was forced to extrapolate because of a combination of states that was outside of the training set, then all state estimates would express divergent behavior similar to that observed in Figure 6.53. Retaining 16 or more vectors, matching the original number of degrees of freedom, resulted in accurate and stable solutions. Retaining more singular vectors typically required more processing time, but this trend was not closely followed as the ode45 solver attempted to refine the time steps near highly dynamic periods.

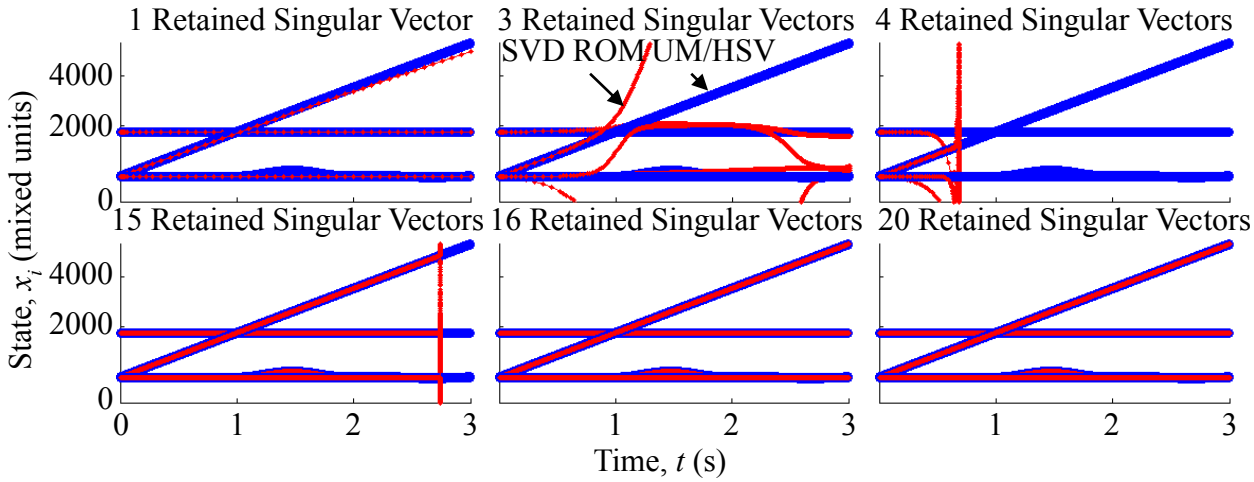

Figure 6.62: Comparison of the SVD ROM and UM/HSV solutions for a 3-second, 1-degree pitch maneuver using various numbers of retained singular vectors

6.4.6 Coefficient Matrix Compression

Another approach to reduce the processing time of the SVD ROM is to consider the structure of the matrix $U \Sigma R^T$ for the 1-step approach as shown in Figure 6.63 for the IC3X 1-step, 4th-order model. Not all terms of the state polynomial significantly affect the state rates. This results in a great number of columns of $U \Sigma R^T$ containing only zeros or very small values. Neglecting columns whose maximum values are below some tolerance and forming a more compact matrix could reduce the number of operations required to integrate the system. By simply removing the zero columns, the number of entries can be reduced by more than half, from 28,640 to 11,264.

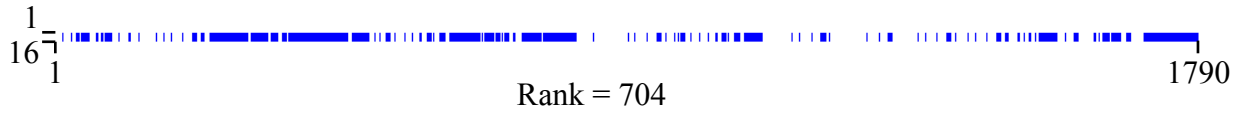

Figure 6.63: Non-zero entries of $U \Sigma R^T$ marked in blue for the IC3X, 1-step, 4th-order SVD ROM

Similar to the previous section, the RMSE at the end of the 3-second, 1-degree pitch-up maneuver was used to indicate the accuracy of the SVD ROM. A minimum magnitude tolerance varying from 10^{-10} to 10^{-5} was used to determine which columns of $U \Sigma R^T$ would be retained. The number of retained columns for a given tolerance, the RMSE after integration, and the processing time are shown in Figure 6.64. Using a low tolerance value (below 10^{-8}) reduced processing time by 22% without increasing error when removing all unnecessary zeros. Between 10^{-8} and $3 \cdot 10^{-7}$, non-zero containing columns were removed which caused the error to increase slightly, but between $3 \cdot 10^{-7}$ and 10^{-6} solution error curiously decreased below the uncompressed solution. This

could be due to removing coefficients that contained some numerical error from the SVD or fitting process, but merits further investigation before a conclusion is reached regarding its cause. Beyond 10^{-6} the accumulated error during integration grew beyond the sample set range and caused the SVD ROM to extrapolate, which caused the solution to not be numerically integratable, as previously shown for with the nonlinear-spring, mass, and damper case.

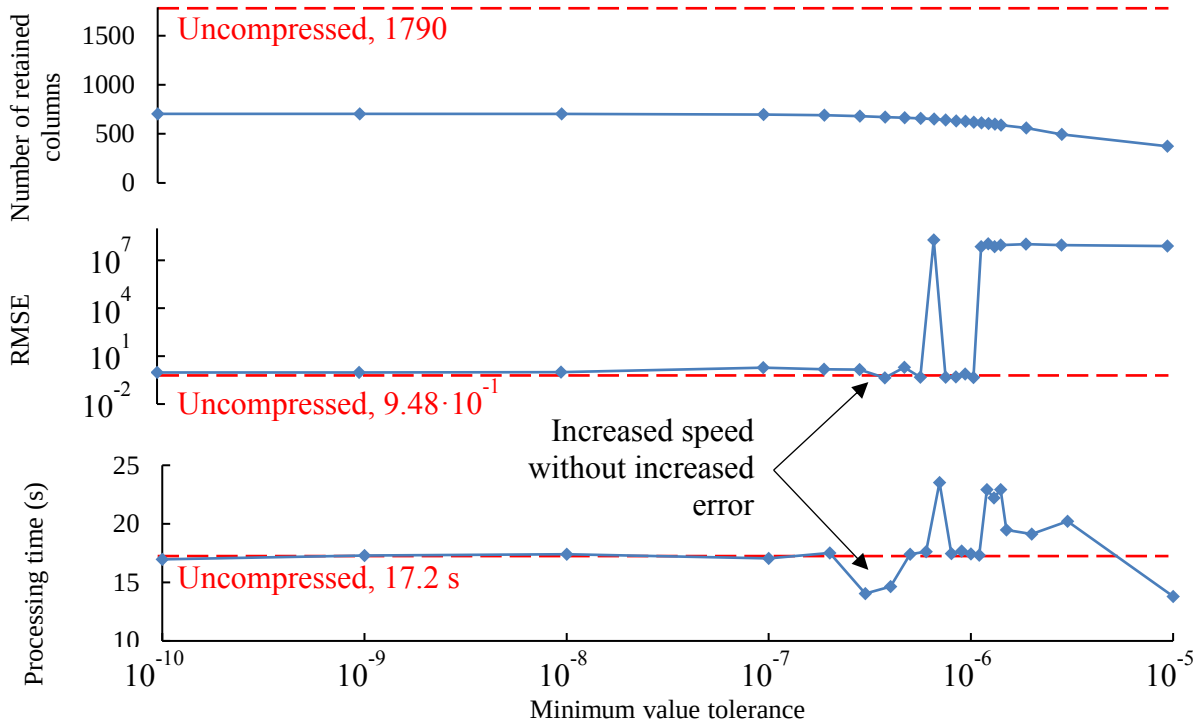

Figure 6.64: Performance of compressed SVD ROM

6.5 Aeroelastic Stability of High-Speed Cylindrical Vehicles

Different levels of structural modeling fidelity are evaluated against experimental results for the aeroelastic stability boundaries of an internally pressurized circular cylindrical shell. Finite element analysis is used to inform a modal approach taken to model the structural dynamics with

third-order piston theory used to model the external and internal surfaces' unsteady aerodynamic pressures. Results are used to drive model improvements of free-flight aero-thermo-elastic simulation in order to accurately predict aeroelastic instabilities in a representative supersonic vehicle. The stability of a finite-element model when inclined to the flow is also considered to inform future work where a cylindrical high-speed vehicle is required to perform maneuvers.

6.5.1 Finite Element Model

To numerically recreate the results found by Olson and Fung[126], a finite element model was created in the Dassault Abaqus FEM/CAE software[191] and is shown in Figure 6.65. The model consists of 20,145 nodes and 39,780 S3-type linear triangle elements. Loads are applied to the external and internal surfaces based on user-defined subroutines that estimate the surface pressures as described previously, using the displacement and displacement rate fields provided by Abaqus. The solution is integrated explicitly in increments no greater than 1 μs with nonlinear geometry considered. The shell and internal gas are assumed to be at an adiabatic temperature to the external surface flow according to the Eckert's reference temperature method[114] and are determined at the onset of each time simulation. The through-thickness temperature distribution is assumed uniform due to the high thermal conductivity of copper and thinness of the shell wall.

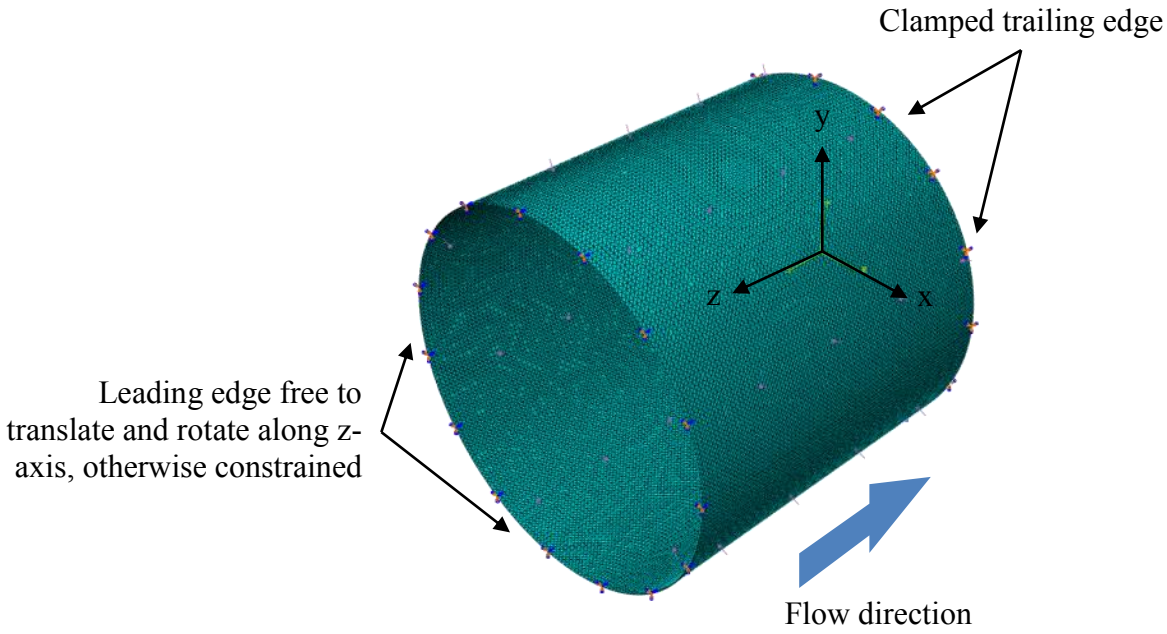

Figure 6.65: Finite element mesh of the cylinder test case

6.5.2 Cylinder Mode Shapes

Simulating the cylinder deformation with the UM/HSV code requires the mass-normalized mode shapes. These were determined using the Lanczos solver[194] included in the Abaqus FEM software for all modes up to 500 Hz for an unpressurized shell. A selection of mode shapes is shown in Figure 6.66. A grouping and pattern can be seen in Figure 6.67 when the mode shapes are organized by numbers of circumferential and longitudinal waves that lie within previously published results,[135] although differences in the boundary conditions prevented an exact match. The frequency limit was chosen to include all modes experimentally observed by Olson and Fung[126] to contribute to flutter, namely up to modes with 25 circumferential waves whose frequency was 299 Hz. Adding internal pressure causes the cylinder to inflate and increases the membrane stress, stiffening the structure. To account for this in the UM/HSV code, multiple sets

of mode shapes and frequencies were determined for 0, 1, 2, 3, 4, 5, 6, and 7 kPa of internal gauge pressure. The variation of the mode frequencies is shown in Figure 6.68.

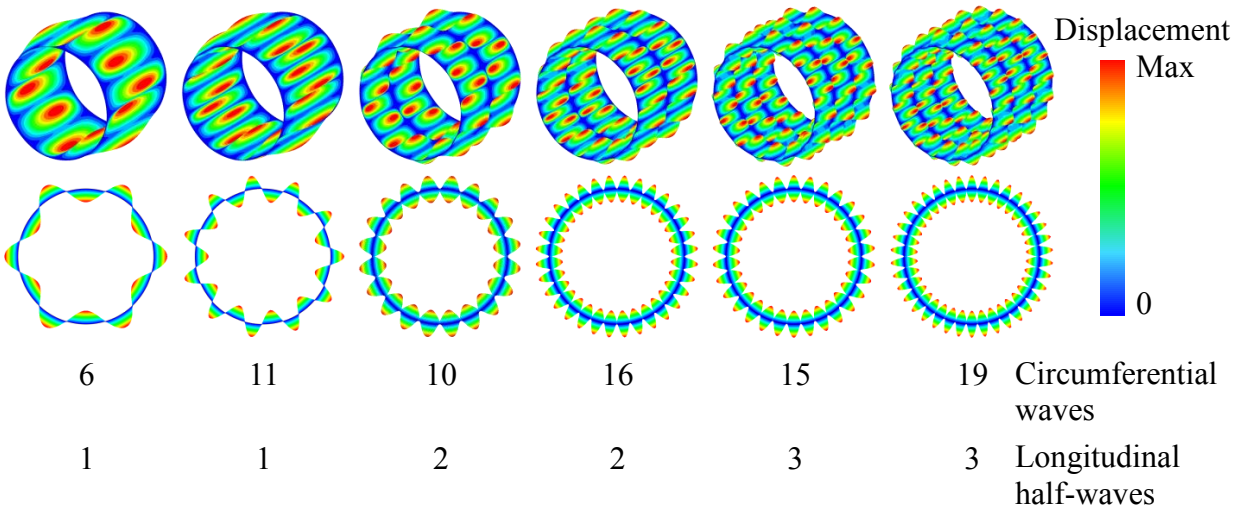

Figure 6.66: Sample unpressurized mode shapes

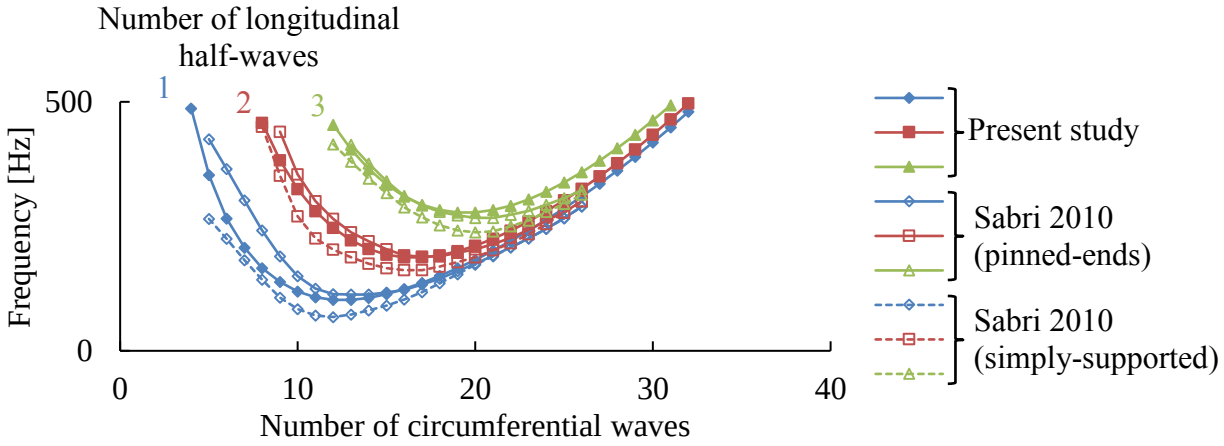

Figure 6.67: Unpressurized mode frequencies

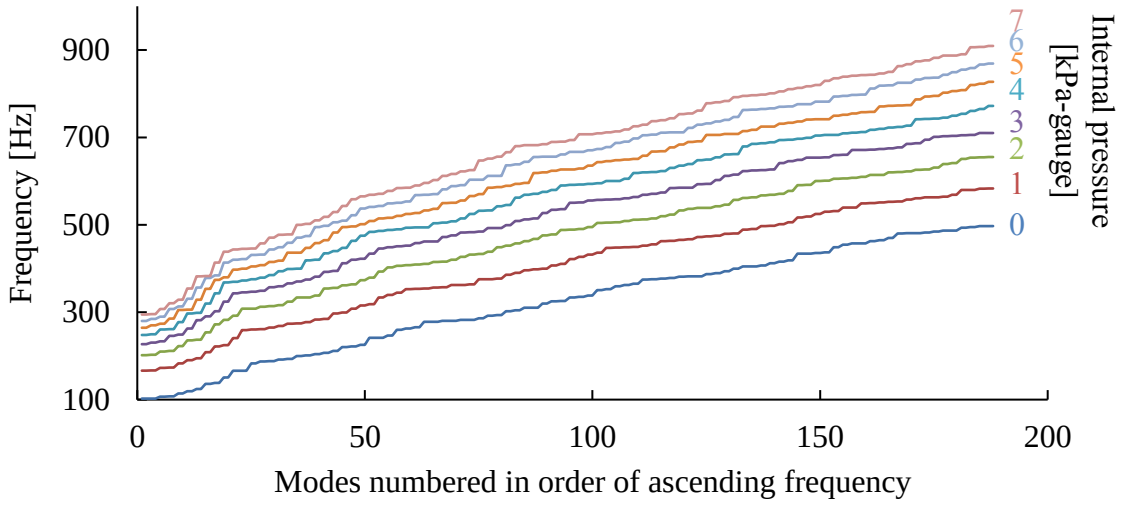

Figure 6.68: Variation of mode frequency due to internal pressure

6.5.3 Effect of Internal Pressure of Finite Element Model Flutter

Aeroelastic simulations were conducted for the FEM and UM/HSV models and used to determine the stability boundaries with various amounts of internal gauge pressure. The results are compared with published experimental,[126] analytical,[126,133] and numerical[135] results.

The onset of flutter was observed to be the limiting factor in stability when the model was exposed to flow aligned with its axis, 0° angle of attack. Snapshots of a simulation exhibiting flutter are shown in Figure 6.69 along with a trace of the radial displacement of a node midway along the upper surface. For each simulation, the cylinder was started in a relaxed state, meaning that a static solution was found which arose from the difference of internal and external pressures. A perturbation was induced at the start of each simulation by applying a 25 Pa impulse to the internal pressure. This pressure impulse would cause a maximum initial displacement of a maximum of 0.1 μm, about 0.1% the shell thickness. Cases that exhibited flutter all appeared to follow a similar evolution that started with large, low frequency waves that traveled axially from

the leading to trailing edge. Interference of these waves and their reflections from the boundaries would yield increasingly smaller waves, some of which traveled circumferentially. These small, circumferential waves would grow in amplitude until the end of the simulation.

Displacement traces at the surface location shown in Figure 6.69 were extracted from the FEA solutions. The traces are divided into 0.02-s long windows in which the maximum absolute displacements were determined. If the maximum displacement in each window grew over time for a given case, then that case was considered unstable. The window length was selected such that the lowest frequency natural mode determined in section during mode shape selection would complete at least one cycle per window. The boundary between stable and unstable pressure conditions was then converged upon for several internal pressure cases by varying the freestream static pressure for Mach 3 flow with a total temperature of 322 K. The results are shown in Figure 6.70.

Overall, the predicted flutter boundary from this study behaves more like the experimental results of Olson and Fung[126] than the analytical results of Olson and Fung,[126] Amabili,[133] or FEA results of Sabri and Lakis.[135] The destabilizing effect of moderate amounts of internal gauge pressure between 1 and 4 kPa is captured before recovering above 5 kPa. However, the FEA results under predict the experimental result for most cases.

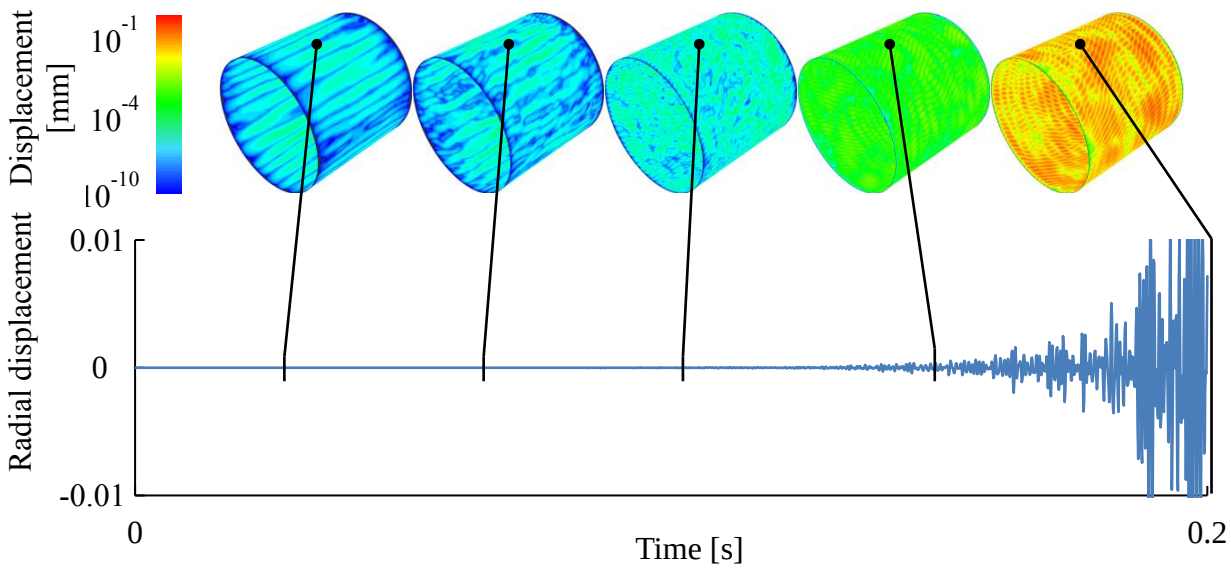

Figure 6.69: Sample snapshots and trace of displacement for a simulation exhibiting flutter, 4.8 kPa freestream pressure, 0.0 kPa-gauge internal pressure, 0° angle of attack, Mach 3 flow

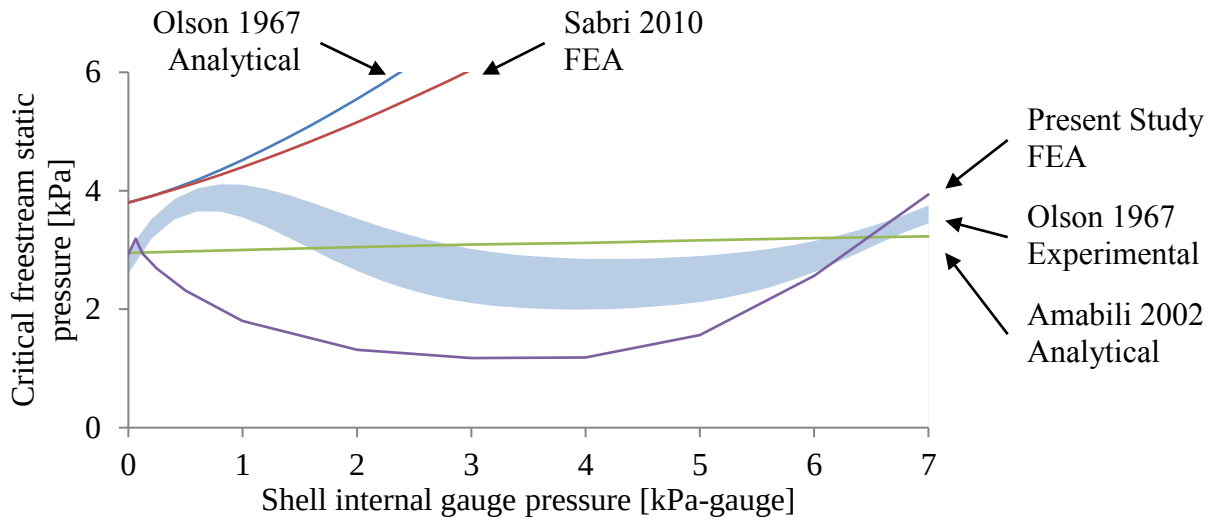

Figure 6.70: Experimental flutter boundary of the cylinder at Mach 3, 322 K total temperature, 0° angle of attack. Numerical flutter boundary predictions from present and previous studies[126,133,135] are included for comparison

From observations of the displacement field, the destabilization and re-stabilization behavior appeared to arise from two competing effects:

1. As the internal gauge pressure was increased, the shell was pushed outward, into the flow. Most of the shell expanded uniformly except near the leading and trailing edges where the boundary conditions restrained the cross section radius. An incline was created which resulted in a region of slightly higher pressure sufficient to initiate oscillations in the shell near the leading edge (Figure 6.71).
2. Increasing the internal pressure also induced a geometric stiffening of the structure by placing the shell in tension. If the pressure was sufficiently increased, then this stiffening overcame the previous destabilizing effect.

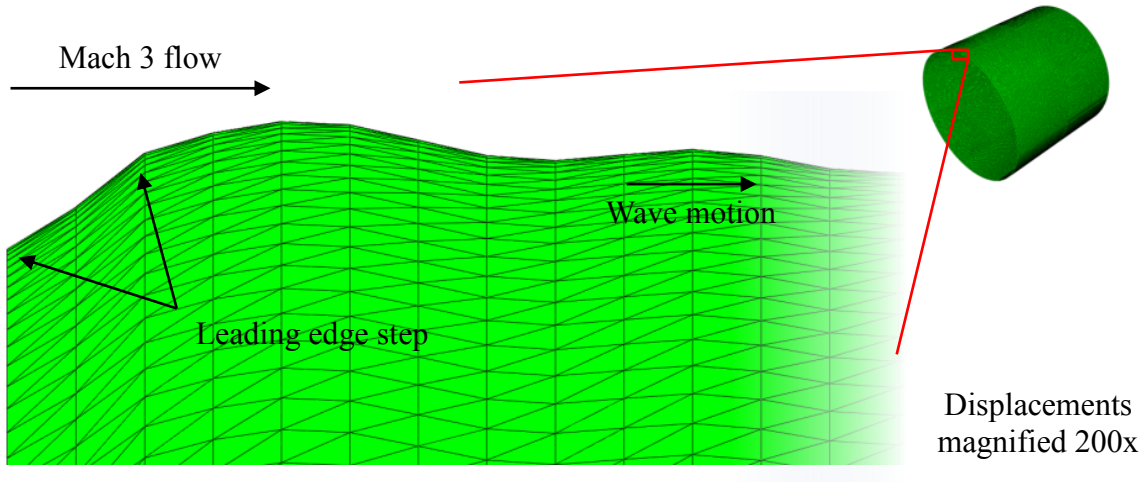

Figure 6.71: Example of the development of oscillations near leading edge incline due to internal pressurization

To better understand which features of the FEA were responsible for the destabilization and re-stabilization processes, four variations of the FEA were considered. These variations

consisted of all combinations on the use of a linear versus a nonlinear geometric model, and a steady versus unsteady internal pressure model. The flutter boundary for each model combination was determined as previously described and is shown in Figure 6.72.

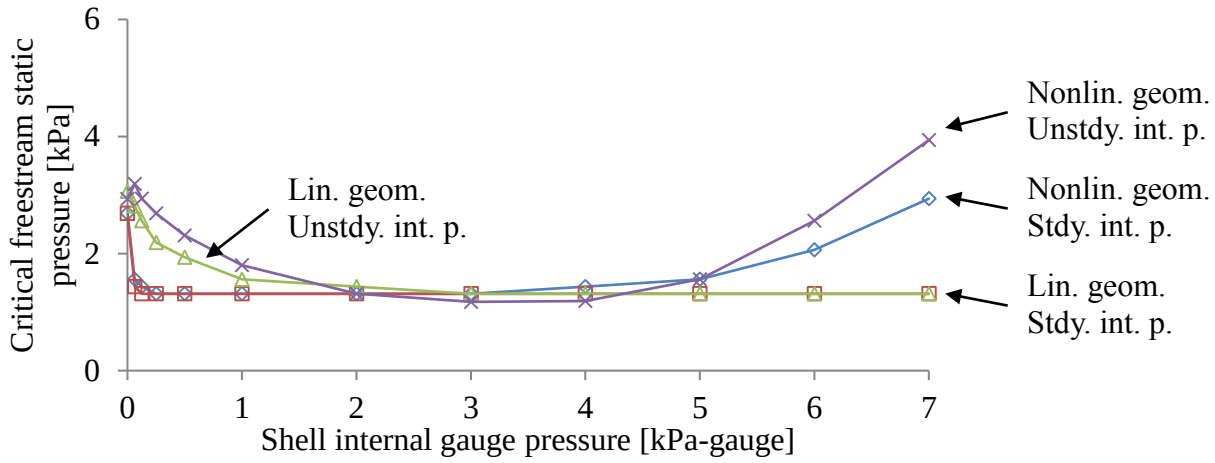

Figure 6.72: Comparison of FEA model combination effects on cylinder flutter boundary

Two key features can be seen. The first feature is that the slope of the initial destabilization appears to be driven by the aerodynamic damping of the internal pressure model. When the unsteady internal pressure model was used, the stability boundary gradually reduced from a critical freestream pressure of 3 to 4 kPa when the cylinder was unpressurized, down to a minimum of 1.3 kPa when the internal pressure was 3 kPa-gauge. When the steady internal pressure model was used, the boundary reduced sharply and settled to a minimum of 1.3 kPa with only 0.3 kPa-gauge internal pressure. The second feature is that the recovery of the stability boundary at high internal pressures appears to be due to geometric nonlinearity. Despite which internal pressure model was used, if geometric nonlinearity was considered during the FEA, then the inflation of the cylinder above 3 kPa-guage began to stiffen the cylinder and increased the critical freestream pressure.

6.5.4 Effects of Internal Pressure on the Flutter of the UM/HSV Model

With an FEA model which captured the destabilizing effects of moderate internal pressure with which to compare against, the cylinder model was constructed with the UM/HSV code. Aeroelastic simulations were conducted using the modes and frequencies determined previously. Snapshots of a simulation which exhibited flutter are shown in Figure 6.73. Despite simulating the same flow conditions as used in Figure 6.69, it can be seen from Figure 6.73 that the process of flutter onset is somewhat different when considered by the UM/HSV code. Little initial displacement is observed and the growth of the oscillations that do appear is more sudden than in the FEA case. The modal approach taken in this case also results in the appearance of much more ordered displacement patterns on the shell, despite the large number of mode shapes considered. Circumferentially travelling waves appear early, without an initial transient period.

The flutter boundary of the cylinder model in the UM/HSV code was converged upon using the same method as with the FEM. The resulting boundary is compared to previous results in Figure 6.74. The UM/HSV code was able to predict the correct magnitude of the flutter boundary for the unpressurized case but did not capture the destabilizing effect of internal pressure. Instead it predicted a monotonic increase in the flutter boundary similar to previous works[126,129,132,135] but shifted toward the experimental boundary. During early simulations, it was observed that the UM/HSV solution was unable to represent the outward inflation of the cylinder due to internal pressure since the free-vibration mode shape which would be used to represent this deformation was well outside of the 500 Hz limit imposed by the authors for the unpressurized case. To overcome this limitation, the mode set was enhanced by including the deformation of a static solution of the cylinder subjected to the steady component of the internal pressure considered for

each case. A modified Gram-Schmidt algorithm was used to orthogonalize the statically loaded shape against the free-vibration derived bases and was appended to the basis set.[36]

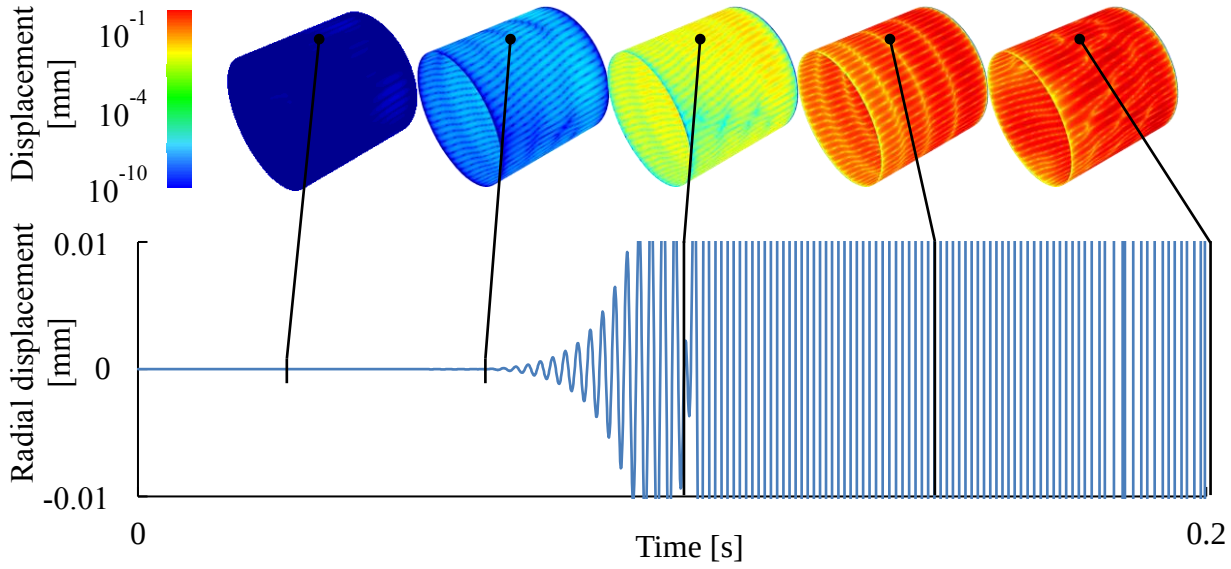

Figure 6.73: Sample snapshots and trace of displacement for a simulation exhibiting flutter as processed by the UM/HSV code, 4.8 kPa freestream pressure, 0.0 kPa-gauge internal pressure, 0° angle of attack, Mach 3 flow

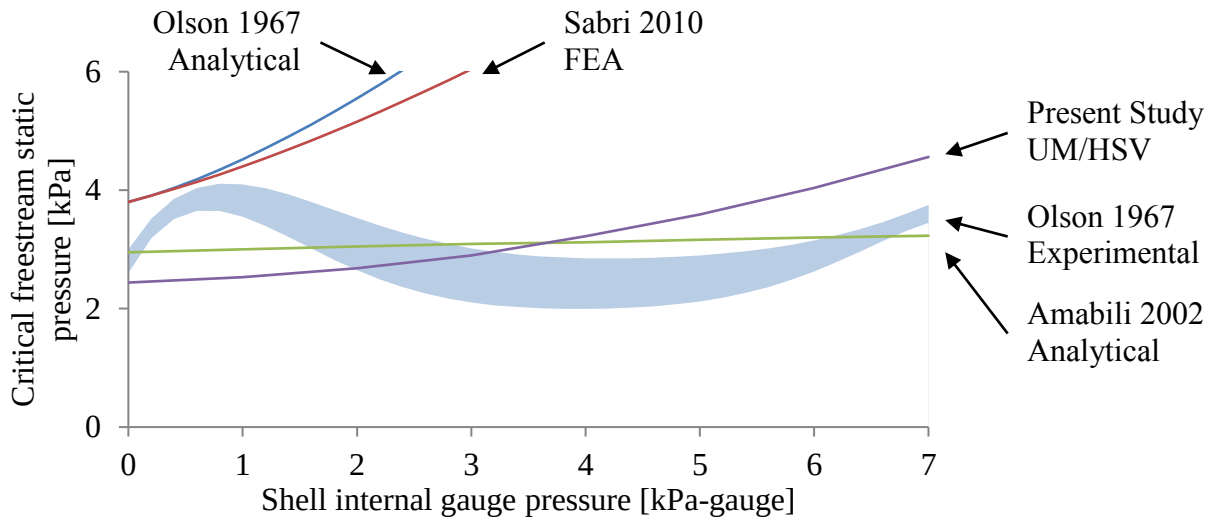

Figure 6.74: Comparison of Mach 3, 322 K total temperature flutter boundary for the UM/HSV model with previous analytical,[126,133] numerical,[135] and experimental results[126]

To confirm that a sufficient number of elastic modes were selected in the test case formulation to capture the onset of flutter, the number of retained elastic modes was varied from 2 to 188, ordered by frequency, for the unpressurized cylinder. The critical freestream pressures and indices of the critically stable modes were recorded and are shown in Figure 6.75. When fewer than 28 modes were retained, the critical freestream pressure was above 10 kPa and not converged upon. Between 28 and 128 retained modes, the critical freestream pressure and critical mode indices varied as additional modes were included, but for 160 modes or more, a critical pressure of 2.4 kPa and critical modes indices 113 and 114 were constant. Additional modes did not influence the stability boundary. Thus, it is not sufficient to include additional linear vibration modes to capture the destabilizing effect of internal pressure. Some other basis set or nonlinear formulation should be used if pressurized structures are to be considered in the UM/HSV framework.

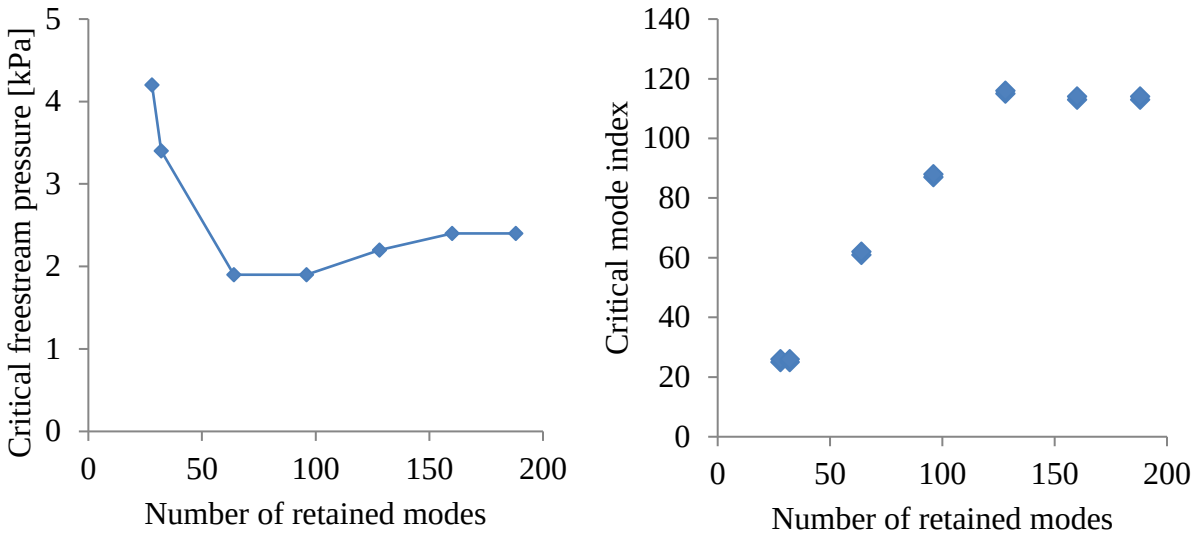

Figure 6.75: Convergence of number of retained elastic modes, 0.0 kPa-gauge internal pressure

6.5.5 Effects of Angle of Attack on Stability Boundary

As the eventual goal of this work is to improve the aeroelastic stability predictions of the UM/HSV code for a maneuvering high-speed vehicle, it was of interest to study the effect of the angle of attack on the stability of a cylindrical shell. To do this, the cylinder FEM was incrementally inclined at 1, 2, 4, 8, and 16° to the Mach 3 free stream flow. The limit of 16° was selected since, at this angle, the windward surface normal Mach number is approximately 0.8 for the undeformed cylinder. This approached the upper limit of the isentropic assumptions of the piston theory[24] aerodynamic model considered in this work, which does not permit surface normal flow to exceed Mach 1, but leaves a margin for unsteady motion.

Unlike with axial flow, instability of the cases with an angle of attack often resulted in the buckling of the cylinder shell on the windward side, similar to the case shown in Figure 6.76. Depending on the exact manner in which the shell buckled, the post-buckled shape either could be stable or could continue to exhibit low frequency oscillations on the sides of approximately 20 Hz.

The stability boundary was converged upon as described previously and is shown in Figure 6.77. Increased angles of attack lead to a decreased stability boundary as low as 0.42 kPa at 16°. This represented a 90% loss in the critical freestream flutter pressure when the cylinder was unpressurized. Increasing the internal pressure from 0.125 to 4 kPa-gauge tended to decrease the stability boundary at a 0 to 2° angle of attack, as was previously overserved. However, for angles of attack above 8°, increased internal pressure resulted in an increased stability boundary. While circumferentially traveling waves were dominant at 0° to 2°, above 8° traveling waves which initiated on the windward side and terminated on the leeward side, similar to those shown in Figure 6.78, were dominant.

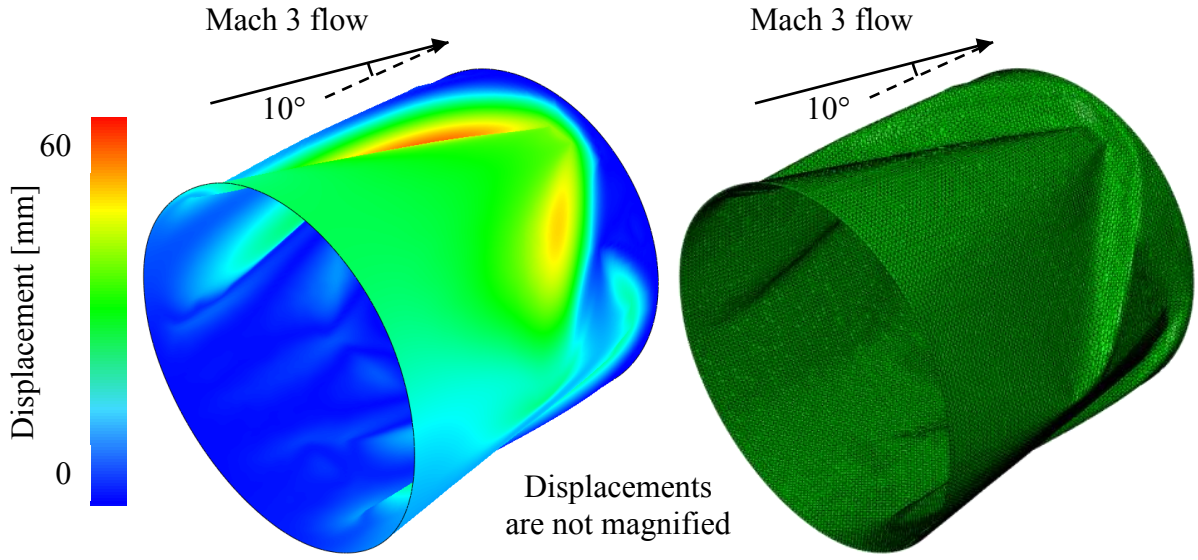

Figure 6.76: Example of buckled cylinder due to inclined flow, 0.69 kPa freestream pressure, 0 kPa-gauge internal pressure, Mach 3 flow, 10° angle of attack

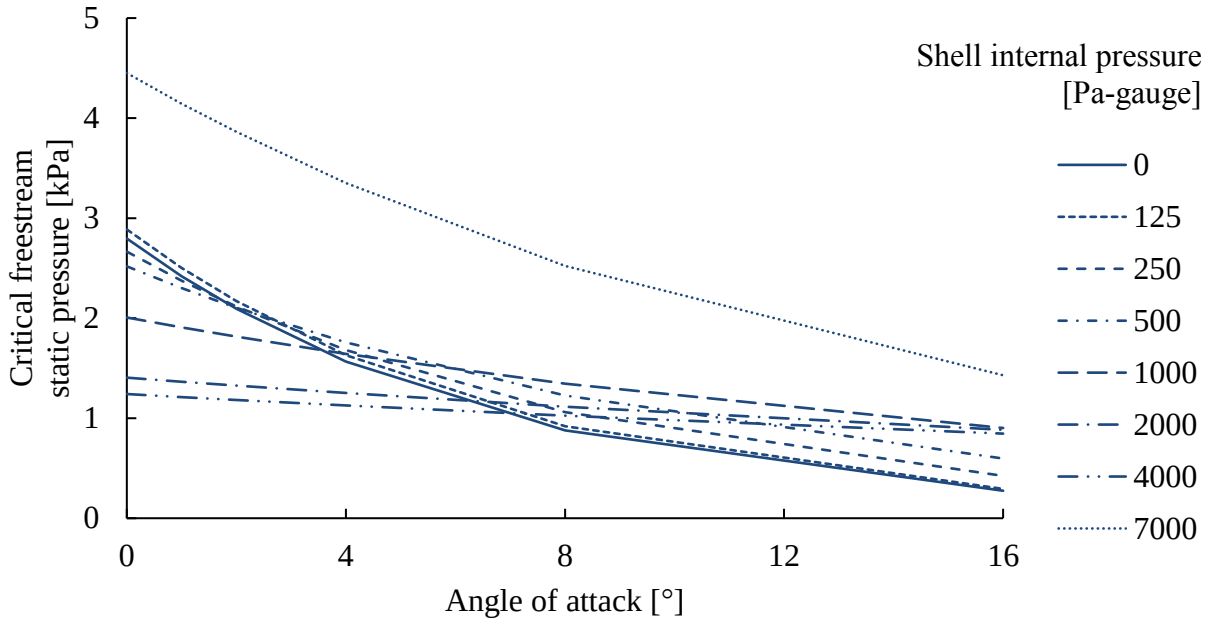

Figure 6.77: Stability boundary of the cylinder FEM at an angle of attack, Mach 3 flow

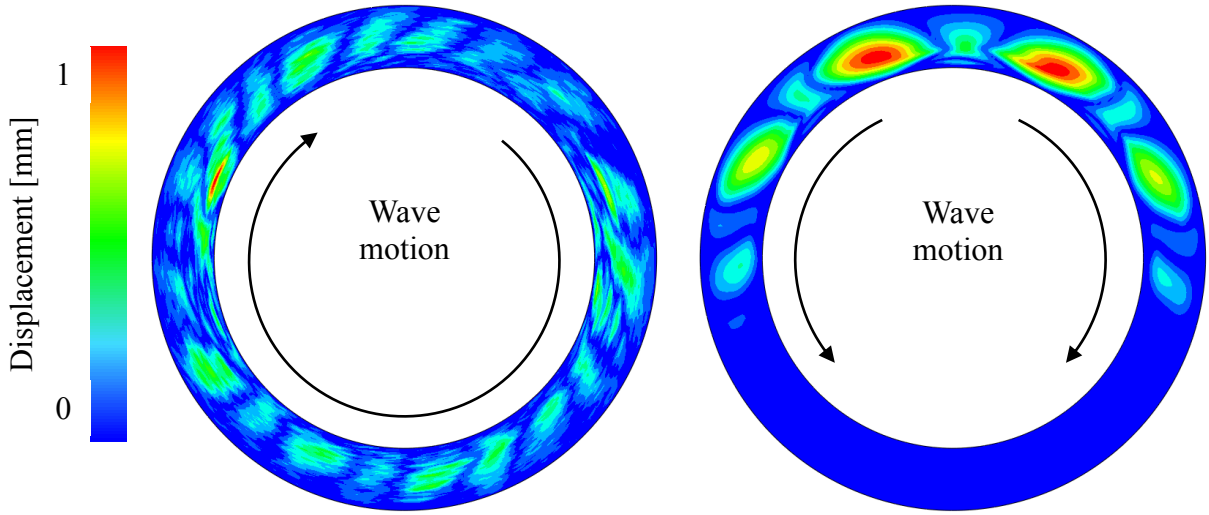

Figure 6.78: Comparison of circumferentially and windward to leeward traveling waves

CHAPTER VII

Concluding Remarks

To conclude the main body of this dissertation, a summary of each chapter is given followed by the key novel contributions to the field made by this research. Then the main conclusions of each study are reviewed. Finally, recommendations of future research areas are provided.

7.1 Summary

Hypersonic vehicles are exposed to a uniquely energetic flight environment that induces strong couplings between the fluid, structural, and thermal dynamics governing the vehicle performance. Disparity between the scaling terms of these disciplines limits physical testing to nearly full-scale models which exceed the capacity of most, if not all, ground testing facilities. Numerical simulation is possible, but full- or high-order models are prohibitively computationally expensive and lack sufficient robustness for exploratory design studies. Many fundamental models exist that can be useful during design, and are outlined in Chapter II, but their simplifying assumptions often limit their applicability. In this work, surrogate and reduced-order models are developed to distill the dominant underlying trends present in high-order training data, to provide numerically efficient models. These models are then coupled within the UM/HSV framework introduced in Chapter I and further described in Chapter IV, to perform 6-DOF, aerothermoelastic simulations of full vehicles over entire flight trajectories. The framework began as an

implementation of the partitioned solution approach[137] to vehicle simulation, but has grown to be a general tool for vehicle flight, trim, and stability analyses. The focus of this dissertation has been on the exploration of the interactions of previously developed ROMs for the UM/HSV framework, development and enhancement of thermodynamic models, and the reduction of coupled systems as a whole in order to accelerate simulation.

Enhancements to existing theory are covered in Chapter III, which include the introduction of material thermal property models for generalized heat transfer systems and a collection of system identification and linearization techniques. To capture the variation of material thermal properties due to changes in temperature, high-dimensional polynomials, the method of kriging, and a novel singular value decomposition and correlation based method. System identification techniques include a finite-difference approach that is up to 6^{th} order accurate, the complex step method[192] which introduces small imaginary numbers to the vehicle state vector to estimate the state space Jacobian matrices, and a direct method which leverages the ordinary differential equation format of the equations of motion for non-partitioned vehicle models. Combination of the singular value decomposition and correlation method with the complex step method was also considered for the rapid estimation of nonlinear state space representations of an aerothermoelastic hypersonic vehicle.

Chapter IV provides additional details to the implementation of the partitioned solution approach within the UM/HSV framework and outlines how the vehicle solution is divided on the model and physical levels. The use of a publish-subscribe code architecture is described, and permits the introduction, exchange, and reconfiguration of the physics model sets without compromising code stability. This code architecture also promotes modularity of the model functions that eases the future development since each module may be treated as a black box with

flexible inputs and outputs. The vehicle trim algorithm is described and uses state rate error minimization to determine steady-level, turn, climb, and other trim settings for control surfaces and propulsion systems. Time simulation is performed via a set of nested convergence loops which maintain partition interface, aeroelastic, and aerothermal error tolerances below user-defined maximums.

Two families of sample cases were considered by this dissertation and are presented in Chapter V. The first is based on the AFRL ISR Cruiser with the control surfaces replaced by the all-movable surfaces of Falkiewicz and Cesnik.[35,173,195] This vehicle model consisted of an aeroelastic main body whose elastic behavior was that of a pair of Euler-Bernoulli beams,[137] aerothermoelastic control surfaces based on the F-104 Starfighter wing planform and diamond supersonic airfoils,[36] and an approximately 2-D ramjet/scramjet flow path. The second family is based on the AFRL IC3X, which is a representative strike-type vehicle for reaching time sensitive surface targets. The entire vehicle is represented as an aerothermoelastic body whose elastic and thermal characteristics are derived from FEA. A small representative thermal FEM is derived from a region of the IC3X's windward side to perform rapid thermal studies and contains material thermal properties of the nose ballast, thermal protection system, and monocoque structure. A cylindrical shell model is also considered to represent a section of the mid-body for aeroelastic study.

A number of verification studies were performed and are described in Chapter VI. This began with comparing the partitioned solution approach to the traditional monolithic approach for an aeroelastic model set of the AFRL ISR Cruiser steady-level trim solution and a time simulation with prescribed command inputs. The aerothermoelastic lifting surfaces are used to exercise the finite difference state space identification method and a root locus plot is produced to determine

the aerothermoelastic stability boundary. Time simulations of the isolated all-movable surface are used to determine how the system damping ratios vary with Mach number, and reinforce the root locus' results. The thermal and elastic basis identification methods of Falkiewicz and Cesnik[35,36] are applied to the IC3X vehicle along a terminal flight trajectory that was determined by using the GPOPS-II[60] Gaussian pseudo-spectral optimization code to maximize final kinetic energy of the vehicle during an unpowered hypersonic dive from cruising altitude.

Enhancement of the IC3X thermal model was also considered in Chapter VI, where it was shown that the use of a thermal basis when material thermal properties that are function of temperature might lead to poor temperature solutions and tracking the evolution of the generalized thermal matrices was not intuitive. Three surrogate model techniques were applied to capture the variation of the thermal matrices. These were high-dimensional polynomials, kriging, and a singular value decomposition (SVD) based method that was shown to be superior. With the success of the SVD method at predicting the thermal matrix evolution, it was investigated whether the method would be able to quickly estimate state space matrices during integration of a system's equations of motion. Sample set of state spaces were collected using the complex-step[192] and direct methods to form two variations of the state space model. A sample nonlinear-spring, mass, and damper system was considered to characterize the training and numerical stability characteristics of the SVD method before being applied to the IC3X vehicle as a whole. Finally, time simulations of the IC3X vehicle revealed a potential aeroelastic instability during the high dynamic pressure terminal dive that was characteristic of cylindrical shell flutter. It was unclear if the modeling methods employed by the UM/HSV code were adequate to predict this type of instability. The experimental flutter results of Olson and Fung[126,127,130] were considered and numerically reproduced using nonlinear FEA. The resulting FEM was then used to determine an elastic basis

and the equations of motion for used by the UM/HSV code and comparison to the experimental results.

7.2 Key Novel Contributions

Through the studies described in this dissertation, several key contributions were made to the field of aerothermoelastics:

1. Development of a modular and computationally efficient publish-subscribe implementation of the UM/HSV framework for simulation, trim analyses, and system linearization for multiple-stage high speed vehicles;
2. Development and successful demonstration of an all-in-one nonlinear reduced order modeling method based on SVD for the rapid simulation of aero-servo-thermo-elastic vehicle simulation;
3. Showing the importance of accounting for material thermal property temperature dependence in the HSV aero-thermo-elastic simulation and development of a method to effectively and accurately estimate generalized properties for reduced-order heat transfer simulations;
4. Demonstration of the impact of aerodynamic heating on the loss of aeroelastic stability of a hypersonic lifting surface;
5. Providing physical insight into how internal pressurization may reduce the stability of cylindrical shells in supersonic flow and numerically quantifying the effects when the shell is placed at an angle of attack to the freestream flow.

7.3 Principal Conclusions

Along with the contributions described in the previous section, a number of principle conclusions have been made:

1. The publish-subscribe code architecture for the UM/HSV framework has been shown to be effective in considering both monolithic and partitioned model sets of aerothermoelastic hypersonic vehicles. The comparison of trim results between the two modeling approaches when applied to a representative vehicle showed a maximum error less than 5% when the vehicle was rigid. Differences remained small when flexibility was introduced, not exceeding 0.5° difference between the elevon deflection angles and 0.02 between the scramjet fuel equivalence ratios. Time simulation of the partitioned and monolithic approaches also showed good agreement, with a small RSME in pitch angle of 0.14° and rotation rate of 0.58°/s during an open-loop pitch up command. These differences were attributed to the interface torques that were required to rotate the elevons in the partitioned approach. The monolithic approach rotated the elevons by directly modifying the vehicle outer mold line mesh, and thus omitted these torques.
2. A reduced-order model approach based on SVD and correlation has been developed and used to simulate quickly the dynamics of nonlinear systems. Two examples were chosen to demonstrate the new method: a nonlinear-spring, mass, and damper system and a representative hypersonic vehicle. State space and state rate samples were determined using the complex-step method for each system given a set of training states selected using LHS. Bases vectors where determined using SVD and polynomial functions up to sixth order were fit as surrogates to the training samples expressed in the singular space. During integration of a system's equations of motion, the SVD ROM could either be used in a 2-

step approach to estimate the state matrices of a system at a given state, thus capturing nonlinear effects typically excluded from a state space representation, or in a 1-step approach to estimate directly the state rates. While the SVD ROM method performed well when interpolating within the range of the training set and provided well behaved, accurate solutions during integration of the equations of motion. It was observed that extrapolation often resulted in divergent solutions with state values that tended toward infinity. This divergent behavior would also result from a too sparsely sampled state space. A nonlinear-spring, mass, and damper test case was used to determine the number of samples required to accurately represent a given number of states and nonlinearity. The dynamics of up to 116 states were captured with as few as 8192 training samples. The SVD ROM method was then applied to the IC3X vehicle with training samples obtained from the UM/HSV code. A 3-second pitch-up maneuver was performed by deflecting the control fins by 1 degree for which the UM/HSV code required 239.3 seconds to simulate. Integration of the equations of motion using the SVD ROM required 17.2 seconds in the same computer, a nearly 14-fold speedup, with mean normalized error of approximately 0.5%. Truncation of the singular vectors for additional simulation acceleration was investigated but did not yield improvement without inducing the divergent extrapolation behavior previously discussed. Compression of the $U \Sigma R^T$ matrix by removing small, maximum-valued columns moderately improved simulation speed and reduced the processing time for the maneuver down to 13.5 seconds, nearly an 18-fold speedup, without significantly increasing the solution error.

3. Three reduced-order models were applied to the problem of modeling the thermal conductivity and capacity variation with respect to temperature for a sample substructure

of a hypersonic vehicle. The thermal problem was first reduced through projection of the thermal states into bases determined by proper orthogonal decomposition. A relative error of order 10^{-8} was determined when the POD bases were truncated to the top 5 most prominent thermal modes. A Latin hypercube sample distribution of the thermal mode coordinates was then used to determine a sample set of generalized thermal conductivity and capacity matrices for the substructure. Various numbers of these samples were then used to create least-squares fit polynomial, Kriging, and singular-value decomposition based ROMs. These ROMs were then compared in terms of error compared to FEA solutions and numerical efficiency. The SVD ROM was determined to be the superior approach. For relatively small training sample sizes of around 200, this ROM provided similar accuracy to the least-squares and Kriging methods. However, the SVD ROM also required up to approximately 600 times less memory than the Kriging ROM and was similar to the least-squares ROM. The SVD ROM was also capable of execution slightly faster than the least-squares ROM and roughly 100 times faster than the Kriging ROM. Integration of the 5-mode generalized thermal problem was then performed with constant thermal properties and thermal properties varied according to the SVD, least-squares, and Kriging ROMs. Generalized solutions were compared to a full-order FEA solution with empirical thermal properties. Significant qualitative improvements were evident lending to the importance and utility of a thermal conductivity and capacity ROM for thermal problems spanning wide temperature ranges. Finally, the effect of the number of retained thermal modes and number of retained SVD bases on the performance of the SVD ROM during simulation was considered. Including more thermal modes improved the quality of

the ROM solution, as expected. However, as few as three SVD bases provided excellent agreement with the FEA solution with a RMSE between 0.5 and 4.2 K.

4. A flutter margin analysis was conducted on a representative hypersonic lifting surface through system linearization and eigenvalue analysis of the resulting state space representations. The flutter Mach number was shown to decrease significantly as aeroheating causes a reduction in the lifting surface stiffness. Flutter margin loss of over 78% was observed, from a critical Mach number of 16.1 to 3.5, over a 100 second flight at 10-km altitude. This loss was despite initial geometric stiffening of the lifting surface due to structural temperature gradients. Results were verified by inspection of short duration aerothermoelastic time simulations.
5. A nonlinear FEM was constructed which was able to capture the destabilizing effects of moderate amounts of internal pressure and circumferentially traveling waves on the aeroelastic stability of a circular cylindrical shell exposed to axial flow at Mach 3, observed experimentally by Evensen, Olson, and Fung.[126,127,130] While not an exact match to experiment, the results where an improvement over previous modern FEA solutions. Two competing effects of internal pressurization were identified. The first was the destabilizing effect of shell inflation, which inclined the leading edge of shell and created a region of higher dynamic pressure that could initiate traveling waves. The second was the stabilizing effect of membrane stress that effectively stiffened the shell by placing the shell in tension. The shell was also placed at several angles of attack to a Mach 3 flow. Applying an angle of attack was shown to decrease the critical freestream pressure by as much as 90% at 16° and often lead to buckling of the shell. The post-buckled shells were then stable with minor oscillations until the end of each simulation. For angles of attack below 4°, moderate

amounts of internal pressurization from 0.25 to 4 kPa-gauge further decreased the critical freestream pressure. However, even small amounts of internal pressure as low as 0.13 kPa-gauge were shown to stabilize the shell when the angle of attack was greater than or equal to 8°.

7.4 Recommendations for Future Research

Although the development of thermal models and improvement of the heat flux models were considered in this thesis, an important source of heat flux was omitted. Gap heating is a localized heat flux that occurs when high enthalpy flow enters a confined seam or fissure on in a surface. Such seams can be gaps between regions of a thermal protect system or the joints of actuated components, such as fins, flaps or other control surfaces. Exposed bonding agents may be susceptible to a heightened thermal load and lead to failure of the thermal protection system. Articulated structures and related actuation systems may also be especially prone to failure due to high heat flux and temperatures. However, the approaches considered in this thesis seek to express the heat transfer problem and temperature field as the sum of mode shapes that span the entire domain of the structure. Highly localized heat fluxes would require a great number of these mode shapes in order to describe a relatively small portion of the structure, and therefore would become less effective at reducing the order of the thermal system.

The implementation of multiple model scales may mitigate the problem of generalizing a thermal system with gap heating, as well as pave the way for other types of localized analyses. This would be done by using a coarse generalization of the overall structure to provide boundary conditions for a much more focused and localized region. Specialized models for the local region could then provide higher-fidelity solutions of a region's behavior. While passing information

from the global-scale to the local-scale is easily implemented, the challenge of passing information from the local-scale back to the global-scale remains unsolved as the coarser global-scale generalization may not have the appropriate DOFs to receive the local solutions. A component mode synthesis approach appears to be the best course of investigation toward solving this problem. The introduction of multiple model scales could also be extended to consider the effects of localized damage, crack-propagation, detailed simulation of sensor outputs, as well as many other analyses.

The temperature dependence of thermal and mechanical material properties is also investigated in this thesis within the domain of single material phases. However, extreme temperatures are known to vary material phase, particularly when considering crystalline metals, alloys, and some ceramics, to reorder the microstructure and therefore global properties. In some cases, a change of phase results in a discontinuous change in material properties that is not often considered. This might be exploited for the purposes of increasing structural flexibility and overall vehicle agility during critical phases of a mission, or intentionally bringing structural materials to an annealing condition to mitigate the nucleation of micro-cracks, extending the service life of a multi-flight system.

A system-level effect of material phase change is the melting, ablation, or other shedding of material that results in a change of vehicle shape and has not been considered in this work. Accounting of these effects is particularly critical to stagnation regions such as a nose-tip or leading edge and can result in aero-thermal-structural instabilities in which the shape change due to heating leads to an increase in heat flux that results in further shape change. How to include these processes in the generalization techniques described in this thesis remains unseen.

It has been shown in other works[18,196] that the selection of an optimal basis for a given discipline may not be optimal when considering the coupling between disciplines. The use of over-defined thermal, elastic, and possibly aerodynamic bases within the UM/HSV framework may allow for the identification of bases that tend to participate in pairs or larger groups, and whose mutual projection could be considered as a more optimal coupled-mode than the individual uncoupled-modes. Use of these coupled modes could allow for further reduction of the number of DOFs in the coupled system, if the individual discipline solutions are not the focus of a given analysis, but instead the interactions between them.

The processing speed of the UM/HSV framework and implementation opens the possibility of many maneuver and trajectory optimization studies, while considering aerothermoelastic effects. A number of critical maneuvers were assumed in this work simply to occur without specific details on how these maneuvers should be executed. Such maneuvers include the pitch-over of the IC3X during transition from the cruise to the terminal phases, separation of a booster body after accelerating to a cruising condition, and ignition/re-ignition of a scramjet engine for either the AFRL cruiser or IC3X. Furthermore, optimization of the terminal phase of the IC3X was carried out using simplified EOMs based on rigid-body dynamics, upon which thermal and elastic models were developed. It would be an interesting exercise to use the now developed ROMs as the system dynamics for optimization of the same trajectories in order to determine the relative importance of each model. Various open- and closed-loop maneuver tests when considering various model combinations and fidelities would also provide insight into which disciplines should be emphasized and which can be further reduced for aerothermoelastic analyses of the types in the UM/HSV framework.

Finally, the development of vehicle configuration aware ROMs would greatly accelerate the preliminary to mid-stage design optimization of HSVs. It has been shown in literature that the vehicle configurations considered in this thesis may not be optimal.[51,197] Producing ROMs or surrogate models that have structural configuration inputs as well as flight dynamics, temperature, or elastic inputs could permit rapid trade studies and overall aerothermoelastic vehicle optimization studies to design either mission-tailored, or overall robust designs for multiple mission types.

Bibliography

[1] Anderson, J. D., *Modern Compressible Flow: With Historical Perspective*, New York, New York: The McGraw-Hill Companies, Inc., 1990.

[2] Anderson, J. D., *Hypersonic and High Temperature Gas Dynamics*, Reston, Virginia: American Institute of Aeronautics and Astronautics, 1989.

[3] Klock, R. J., and Cesnik, C. E. S., "Aerothermoelastic Reduced - Order Model of a Hypersonic Vehicle," *AIAA Atmospheric Flight Mechanics Conference*, Dallas, Texas: American Institute of Aeronautics and Astronautics, 2015.

[4] Collar, A. R., "The First Fifty Years of Aeroelasticity," *Aerospace*, vol. 2, 1978, pp. 12–20.

[5] Kennedy, G. P., *Vengeance Weapon 2: The V-2 Guided Missile*, Washington D.C.: Smithsonian Institution Press, 1983.

[6] Heppenheimer, T. A., *Facing the Heat Barrier: A History of Hypersonics*, Berkshire, United Kingdom: Express Publishing, 2006.

[7] Davies, M., *The Standard Handbook for Aeronautical and Astronautical Engineers*, New York, New York: The McGraw-Hill Companies, Inc., 2003.

[8] Launius, R. D., and Jenkins, D. R., *Coming Home : Reentry and Recovery from Space*, Washington D.C.: National Aeronautics and Space Administration, 2012.

[9] Bilstein, R. E., *Testing Aircraft, Exploring Space : An Illustrated History of NACA and NASA*, Baltimore, Maryland: Johns Hopkins University Press, 2003.

[10] McNamara, J. J., and Friedmann, P. P., "Aeroelastic and Aerothermoelastic Analysis in Hypersonic Flow: Past, Present, and Future," *AIAA Journal*, vol. 49, Jun. 2011, pp. 1089–1122.

[11] Chase, R. L., and Tang, M. H., "A History of the NASP Program from the Formation of the Joint Program Office to the Termination of the HySTP Scramjet Performance Demonstration Program," *International Aerospace Planes and Hypersonics Technologies, International Space Planes and Hypersonic Systems and Technologies Conferences*, Chattanooga, Tennessee: American Institute of Aeronautics and Astronautics, 1995.

[12] Peebles, C., *Eleven Seconds into the Unknown*, Reston, Virginia: American Institute of Aeronautics and Astronautics, 2011.

[13] McClinton, C. R., "X-43 - Scramjet Power Breaks the Hypersonic Barrier: Dryden Lectureship in Research for 2006," *44th AIAA Aerospace Sciences Meeting and Exhibit*, Reno, Nevada: American Institute of Aeronautics and Astronautics, 2006.

[14] Norris, G., "High-Speed Strike Weapon to Build on X-51 Flight," *Aviation Week & Space Technology* Available: http://aviationweek.com/awin/high-speed-strike-weapon-build-x-51-flight [retrieved 4 August 2014].

[15] Sampson, C., and VanNierop, D., "Boeing X-51A WaveRider Sets Record with Successful 4th Flight," *Boeing News* Available: http://boeing.mediaroom.com/2013-05-03-Boeing-X-51A-WaveRider-Sets-Record-with-Successful-4th-Flight [retrieved 4 August 2017].

[16] Rosenburg, Z., "Hypersonic X-51 Programme Ends In Success," *Flight International* Available: https://www.flightglobal.com/news/articles/hypersonic-x-51-programme-ends-in-success-385481/.

[17] Gogulapati, A., Brouwer, K. R., Wang, X. Q., Murthy, R., McNamara, J. J., and Mignolet, M. P., "Full and Reduced Order Aerothermoelastic Modeling of Built- Up Aerospace Panels in High-Speed Flows," *58th AIAA/ASCE/AHS/ASC Structures, Structural Dynamics, and Materials Conference*, Grapevine, Texas: American Institute of Aeronautics and Astronautics, 2017.

[18] Murthy, R., Wang, X. Q., Matney, A. K., and Mignolet, M. P., "A Construction of Thermal Basis Functions for Coupled Structural - Thermal Reduced Order Models," *58th AIAA/ASCE/AHS/ASC Structures, Structural Dynamics, and Materials Conference*, Grapevine, Texas: American Institute of Aeronautics and Astronautics, 2017.

[19] Culler, A. J., and McNamara, J. J., "Impact of Fluid-Thermal-Structural Coupling on Response Prediction of Hypersonic Skin Panels," *AIAA Journal*, vol. 49, Nov. 2011, pp. 2393–2406.

[20] Miller, B. A., and McNamara, J. J., "Loosely Coupled Time-Marching of Fluid-Thermal-Structural Interactions with Time-Accurate CFD," *56th AIAA/ASCE/AHS/ASC Structures, Structural Dynamics, and Materials Conference*, Kissimmee, Florida: American Institute of Aeronautics and Astronautics, 2015.

[21] Miller, B. A., Crowell, A. R., and McNamara, J. J., "Loosely Coupled Time-Marching of Fluid-Thermal-Structural Interactions," *54th AIAA/ASME/ASCE/AHS/ASC Structures, Structural Dynamics, and Materials Conference*, Boston, Massachusetts: American Institute of Aeronautics and Astronautics, 2013.

[22] Culler, A. J., and McNamara, J. J., "Studies on Fluid-Thermal-Structural Coupling for Aerothermoelasticity in Hypersonic Flow," *AIAA Journal*, vol. 48, Aug. 2010, pp. 1721–1738.

[23] Rogers, M., "Aerothermoelasticity," *Aero/Space Engineering*, vol. 17, 1958, pp. 34–43.

[24] Holt, A., and Garabed, Z., "Piston Theory - A New Aerodynamic Tool for the

Aeroelastician," *Journal of the Aeronautical Sciences*, vol. 23, 1956, pp. 1109–1118.

[25] Eckert, E. R. G., and Tewfik, O. E., "Use of Reference Enthalpy in Specifying the Laminar Heat-Transfer Distribution Around Blunt Bodies in Dissociated Air," *Journal of the Aerospace Sciences*, vol. 27, 1960, pp. 464–466.

[26] Miller, B. A., and McNamara, J. J., "Efficient Time-Marching of Fluid-Thermal-Structural Interactions," *55th AIAA/ASME/ASCE/AHS/ASC Structures, Structural Dynamics, and Materials Conference*, National Harbor, Maryland: American Institute of Aeronautics and Astronautics, 2014.

[27] Bolender, M. A., and Doman, D. B., "Nonlinear Longitudinal Dynamical Model of an Air-Breathing Hypersonic Vehicle," *Journal of Spacecraft and Rockets*, vol. 44, 2007, pp. 374–387.

[28] Chavez, F. R., and Schmidt, D. K., "Analytical Aeropropulsive/Aeroelastic Hypersonic-Vehicle Model with Dynamic Analysis," *Journal of Guidance, Control, and Dynamics*, vol. 17, 1994, pp. 1308–1319.

[29] Jaslow, H., "Aerodynamic Relationships Inherent in Newtonian Impact Theory," *AIAA Journal*, vol. 6, 1968, pp. 608–612.

[30] Pike, J., "Newtonian Aerodynamic Forces from Poisson's Equation," *AIAA Journal*, vol. 11, 1973, pp. 499–504.

[31] McNamara, J. J., Crowell, A. R., Friedmann, P. P., Glaz, B., and Gogulapati, A., "Approximate Modeling of Unsteady Aerodynamics for Hypersonic Aeroelasticity," *Journal of Aircraft*, vol. 47, 2010, pp. 1932–1945.

[32] Sachs, G., "The Effects of Pitching-moments on Phugoid and Height Modes in Supersonic Flight," *Journal of Aircraft*, vol. 9, Mar. 1972, pp. 252–254.

[33] Frendreis, S. G. V., Skujins, T., and Cesnik, C. E. S., "Six-Degree-of-Freedom Simulation of Hypersonic Vehicles," *AIAA Atmospheric Flight Mechanics Conference*, Chicago, Illinois: American Institute of Aeronautics and Astronautics, 2009.

[34] Falkiewicz, N. J., Frendreis, S. G. V., and Cesnik, C. E. S., "Effect of Control Surface-Fuselage Inertial Coupling on Hypersonic Vehicle Flight Dynamics," *AIAA Atmospheric Flight Mechanics Conference*, Portland, Oregon: American Institute of Aeronautics and Astronautics, 2011.

[35] Falkiewicz, N. J., and Cesnik, C. E. S., "Proper Orthogonal Decomposition for Reduced-Order Thermal Solution in Hypersonic Aerothermoelastic Simulations," *AIAA Journal*, vol. 49, 2011, pp. 994–1009.

[36] Falkiewicz, N. J., and Cesnik, C. E. S., "Enhanced Modal Solutions for Structural Dynamics in Aerothermoelastic Analysis," *Journal of Aircraft*, vol. 54, 2016, pp. 870–889.

[37] Falkiewicz, N. J., Cesnik, C. E. S., Crowell, A. R., and Mcnamara, J. J., "Reduced-Order Aerothermoelastic Framework for Hypersonic," *AIAA Journal*, vol. 49, 2011, pp. 1625–1646.

[38] Falkiewicz, N. J., Cesnik, C. E. S., Bolender, M. A., and Doman, D. B., "Thermoelastic Formulation of a Hypersonic Vehicle Control Surface for Control-Oriented Simulation," *AIAA Guidance, Navigation, and Control Conference*, Chicago, Illinois: American Institute of Aeronautics and Astronautics, 2009.

[39] Frendreis, S. G. V, and Cesnik, C. E. S., "3D Simulation of Flexible Hypersonic Vehicles," *AIAA Atmospheric Flight Mechanics Conference*, Toronto, Ontario: American Institute of Aeronautics and Astronautics, 2010.

[40] Dalle, D. J., Frendreis, S. G. V., Driscoll, J. F., and Cesnik, C. E. S., "Hypersonic Vehicle Flight Dynamics with Coupled Aerodynamic and Reduced-Order Propulsive Models," *AIAA Atmospheric Flight Mechanics Conference*, Toronto, Ontario: American Institute of Aeronautics and Astronautics, 2010.

[41] Dalle, D. J., Fotia, M. L., and Driscoll, J. F., "Reduced-Order Modeling of Two-Dimensional Supersonic Flows with Applications to Scramjet Inlets," *Journal of Propulsion and Power*, vol. 26, 2010, pp. 545–555.

[42] Torrez, S. M., Driscoll, J. F., Dalle, D. J., and Micka, D. J., "Scramjet Engine Model MASIV: Role of Mixing, Chemistry and Wave Interaction," *45th AIAA/ASME/SAE/ASEE Joint Propulsion Conference and Exhibit*, Denver, Colorado: American Institute of Aeronautics and Astronautics, 2009.

[43] Dalle, D. J., and Torrez, S. M., "Scramjet Propulsive Analysis," *User Manual for the Michigan / AFRL Scramjet In Vehicle Program*, Ann Arbor, Michigan: University of Michigan, 2013.

[44] Torrez, S. M., Driscoll, J. F., Dalle, D. J., and Fotia, M. L., "Preliminary Design Methodology for Hypersonic Engine Flowpaths," *16th AIAA/DLR/DGLR International Space Planes and Hypersonic Systems and Technologies Conference*, Bremen, Germany: American Institute of Aeronautics and Astronautics, 2009.

[45] Torrez, S. M., Dalle, D. J., and Driscoll, J. F., "Design of Dual-Mode Engine Flowpaths for Hypersonic Vehicles Using Reduced-Order Models," *17th AIAA International Space Planes and Hypersonic Systems and Technologies Conference*, San Francisco, California: American Institute of Aeronautics and Astronautics, 2011.

[46] Torrez, S. M., Driscoll, J. F., Ihme, M., and Fotia, M. L., "Reduced-Order Modeling of Turbulent Reacting Flows with Application to Ramjets and Scramjets," *Journal of Propulsion and Power*, vol. 27, Mar. 2011, pp. 371–382.

[47] Dalle, D. J., and Driscoll, J. F., "Continuous Differentiation of Complex Systems Applied to a Hypersonic Vehicle," *AIAA Atmospheric Flight Mechanics Conference*, Minneapolis, Minnesota: American Institute of Aeronautics and Astronautics, 2012.

[48] Dalle, D. J., Torrez, S. M., and Driscoll, J. F., "Turn Performance of an Air-Breathing Hypersonic Vehicle," *AIAA Atmospheric Flight Mechanics Conference*, Portland, Oregon: American Institute of Aeronautics and Astronautics, 2011.

[49] Torrez, S. M., Dalle, D. J., and Driscoll, J. F., "Multidisciplinary Optimization of the Fuel Consumption of a Dual Mode Scramjet-Ramjet," *47th AIAA/ASME/SAE/ASEE Joint Propulsion Conference and Exhibit*, San Diego, California: American Institute of Aeronautics and Astronautics, 2011.

[50] Dalle, D. J., and Driscoll, J. F., "Flight Mechanics of Ram-Scram Transition," *AIAA Atmospheric Flight Mechanics (AFM) Conference*, Boston, Massachusetts: American Institute of Aeronautics and Astronautics, 2013.

[51] Dalle, D. J., and Driscoll, J. F., "Design Optimization of a Scramjet Vehicle for Ascent Using Surrogate Optimization," *52nd Aerospace Sciences Meeting*, National Harbor, Maryland: American Institute of Aeronautics and Astronautics, 2014.

[52] Richardson, D. F., and Rogers, C. E., "Computer Program for Aerospace Trajectory Optimization for Operation on a Personal Computer," Edwards Air Force Base: Air Force Flight Test Center, 1995.

[53] Zhang, K., and Chen, W., "Reentry Vehicle Constrained Trajectory Optimization," *17th AIAA International Space Planes and Hypersonic Systems and Technologies Conference*, San Francisco, California: American Institute of Aeronautics and Astronautics, 2011.

[54] Mor, M., and Livne, E., "Multidisciplinary Design Optimization of Reentry Vehicles : Trajectory Optimization and Sensitivities," *47th AIAA/ASME/ASCE/AHS/ASC Structures, Structural Dynamics, and Materials Conference*, Newport, Rhode Island: American Institute of Aeronautics and Astronautics, 2006.

[55] Zhao, J., and Zhou, R., "Reentry Trajectory Optimization for Hypersonic Vehicle Satisfying Complex Constraints," *Chinese Journal of Aeronautics*, vol. 26, 2013, pp. 1544–1553.

[56] Rao, A. V., and Clarke, K. A., "Performance Optimization of a Maneuvering Re-Entry Vehicle Using a Legendre Pseudospectral Method," *AIAA Atmospheric Flight Mechanics Conference and Exhibit*, Monterey, California: American Institute of Aeronautics and Astronautics, 2002.

[57] Grant, M. J., and Mendeck, G. F., "Mars Science Laboratory Entry Optimization Using Particle Swarm Methodology," *AIAA Atmospheric Flight Mechanics Conference and Exhibit*, Hilton Head, South Carolina: American Institute of Aeronautics and Astronautics, 2007.

[58] Hargraves, C. R., Paris, S. W., and Vlases, W. G., "OTIS Past, Present and Future," *Proceedings of the Astrodynamics Conference*, Hilton Head Island, South Carolina: AIAA, 1992.

[59] Garg, D., Patterson, M. A., Francolin, C., Darby, C. L., Huntington, G. T., Hager, W. W.,

and Rao, A. V., "Direct Trajectory Optimization and Costate Estimation of Finite-Horizon and Infinite-Horizon Optimal Control Problems Using a Radau Pseudospectral Method," *Computational Optimization and Applications*, vol. 49, 2011, pp. 335–358.

[60] Rexius, S. L., Rexius, T., Jorris, T. R., and Rao, A. V., "Advances in Highly Constrained Multi-Phase Trajectory Generation using the General Pseudospectral Optimization Software (GPOPS)," *AIAA Guidance, Navigation, and Control (GNC) Conference*, Boston, Massachusetts: American Institute of Aeronautics and Astronautics, 2013.

[61] Richie, G., "The Common Aero Vehicle: Space Delivery System Of The Future," *Proceedings of the AIAA Space Technology Conference & Exposition*, Albuquerque, New Mexico: American Institute of Aeronautics and Astronautics, 1999.

[62] Downey, J. J., Carr, R. W., Bull, K. I., and Jorris, T. R., "Design of Experiments Using Response Surface Methods to Optimize Simulated Reentry Trajectories," *28th Aerodynamic Measurement Technology, Ground Testing, and Flight Testing Conference*, New Orleans, Louisiana: American Institute of Aeronautics and Astronautics, 2012.

[63] Washabaugh, K., Amsallem, D., Zahr, M., and Farhat, C., "Nonlinear Model Reduction for CFD Problems Using Local Reduced-Order Bases," *42nd AIAA Fluid Dynamics Conference and Exhibit*, New Orleans, Louisiana: American Institute of Aeronautics and Astronautics, 2012.

[64] Lai, K. L., Won, K. S., Koh, E. P. C., and Tsai, H. M., "Flutter Simulation and Prediction with CFD-based Reduced-Order Model," *AIAA/ASME/ASCE/AHS/ASC 47th Structures, Structural Dynamics, and Materials Conference*, Reno, Nevada: American Institute of Aeronautics and Astronautics, 2006.

[65] Danowsky, B. P., Thompson, P. M., Farhat, C., Lieu, T., Harris, C., and Lechniak, J., "A Complete Aeroservoelastic Model : Incorporation of Oscillation-Reduction-Control into a High-Order CFD/FEM Fighter Aircraft Model," *AIAA Atmospheric Flight Mechanics Conference*, Chicago, Illinois: American Institute of Aeronautics and Astronautics, 2009.

[66] Shore, C. P., "Reduction Method for Thermal Analysis of Complex Aerospace Structures," *NASA Technical Paper 2373*, Langley Research Center: National Aeronautics and Space Administration, 1985.

[67] Craig, R.-R., and Bampton, M. C. C., "Coupling of Substructures for Dynamics Analyses," *AIAA Journal*, vol. 6, 1968, p. 1313.

[68] Guyan, R. J., "Reduction of Stiffness and Mass Matrices," *AIAA Journal*, vol. 3, 1965, pp. 380–380.

[69] Petit, D., Hachette, R., and Veyret, D., "A Modal Identification Method to Reduce a High-Order Model: Application to Heat Conduction Modelling," *International Journal of Modelling & Simulation*, vol. 17, 1997, pp. 242–250.

[70] Liang, Y. C., Lee, H. P., Lim, S. P., Lin, W. Z., Lee, K. H., and Wu, C. G., "Proper

Orthogonal Decomposition and Its Applications - Part I: Theory," *Journal of Sound and Vibration*, vol. 252, 2002, pp. 527–544.

[71] Bialecki, R. A., Kassab, A. J., and Fic, A., "Reduction of the Dimensionality of Transient FEM Solution Using Proper Orthogonal Decomposition," *Proceedings of the 36th AIAA Thermophysics Conference*, Orlando, Florida: American Institute of Aeronautics and Astronautics, 2003.

[72] Białecki, R. A., Kassab, A. J., and Fic, A., "Proper Orthogonal Decomposition and Modal Analysis for Acceleration of Transient FEM Thermal Analysis," *International Journal for Numerical Methods in Engineering*, vol. 62, 2005, pp. 774–797.

[73] Fic, A., Białecki, R. A., and Kassab, A. J., "Solving Transient Nonlinear Heat Conduction Problems by Proper Orthogonal Decomposition and the Finite-Element Method," *Numerical Heat Transfer, Part B: Fundamentals*, vol. 48, 2005, pp. 103–124.

[74] Prasad, K. S. R. K., Krishna-Murty, A. V., and Mahabaliraja, "Iterative Type Rayleigh-Ritz Method for Natural Vibration Problems," *AIAA Journal*, vol. 8, 1970, pp. 1884–1886.

[75] Irons, B. M., "Eigenvalue Economizers in Vibration Problems," *Journal of the Royal Aeronautical Society*, vol. 63, 1963, pp. 526–528.

[76] Keane, A. J., and Nair, P. B., *Computational Approaches for Aerospace Design: The Pursuit of Excellence*, Hoboken, New Jersey: John Wiley & Sons, Inc., 2005.

[77] Ghosh, S., Jacobs, R. B., and Mavris, D. N., "Multi-Source Surrogate Modeling with Bayesian Hierarchical Regression," *17th AIAA Non-Deterministic Approaches Conference*, Kissimmee, Florida: American Institute of Aeronautics and Astronautics, 2017.

[78] Forrester, A. I. J., Sóbester, A., and Keane, A. J., "Multi-Fidelity Optimization via Surrogate Modelling," *Mathematical, Physical and Engineering Sciences*, London, England: The Royal Society Publishing, 2007.

[79] Forrester, A. I. J., and Keane, A. J., "Recent Advances in Surrogate-Based Optimization," *Progress in Aerospace Sciences*, vol. 45, 2009, pp. 50–79.

[80] Berci, M., Toropov, V., Hewson, R., and Gaskell, P., "Metamodelling Based on High and Low Fidelity Model Interaction for UAV Gust Performance Optimization," *50th AIAA/ASME/ASCE/AHS/ASC Structures, Structural Dynamics, and Materials Conference*, Palm Springs, California: American Institute of Aeronautics and Astronautics, 2009.

[81] Umakant, J., Sudhakar, K., Mujumdar, P. M., and Rao, C. R., "Customized Regression Model for Improving Low Fidelity Analysis Tool," *11th AIAA/ISSMO Multidisciplinary Analysis and Optimization Conference*, Portsmouth, Virginia: American Institute of Aeronautics and Astronautics, 2006.

[82] Eldred, M., Giunta, A., and Collis, S., "Second-Order Corrections for Surrogate-Based Optimization with Model Hierarchies," *10th AIAA/ISSMO Multidisciplinary Analysis and*

Optimization Conference, Albany, New York: American Institute of Aeronautics and Astronautics, 2004.

[83] Alexandrov, N. M., and Lewis, R. M., "An Overview of First-Order Model Management for Engineering Optimization," *Optimization and Engineering*, vol. 2, 2001, pp. 413–430.

[84] Vitali, R., Haftka, R. T., and Sankar, B. V., "Correction Response Surface Approximations for Stress Intensity Factors of a Composite Stiffened Plate," *39th AIAA/ASME/ASCE/AHS/ASC Structures, Structural Dynamics, and Materials Conference and Exhibit*, Long Beach, California: American Institute of Aeronautics and Astronautics, 1998.

[85] Kennedy, M. C., and O'Hagan, A., "Predicting the Output from a Complex Computer Code When Fast Approximations are Available," *Biometrika*, vol. 87, 2000, pp. 1–13.

[86] Polynkin, A., and Toropov, V., "Multiple Mid-Range and Global Metamodel Building Based on Linear Regression," *50th AIAA/ASME/ASCE/AHS/ASC Structures, Structural Dynamics, and Materials Conference*, Palm Springs, California: American Institute of Aeronautics and Astronautics, 2009.

[87] Mendez Ramos, E. D., Mishra, P., Edwards, S., and Mavris, D., "Response Surface Regressions for Low-Thrust Interplanetary Mission Design," *AIAA SPACE 2016*, Long Beach, California: American Institute of Aeronautics and Astronautics, 2016.

[88] MacKenzie, D., "Cost Estimating Relationship Regression Variance Study," *AIAA Space 2003 Conference & Exposition*, Long Beach, California: American Institute of Aeronautics and Astronautics, 2003.

[89] Crowley, D., Robertson, B., Douglas, R., Mavris, D. N., and Hellman, B., "Aerodynamic Surrogate Modeling of Variable Geometry," *50th AIAA Aerospace Sciences Meeting including the New Horizons Forum and Aerospace Exposition*, Nashville, Tennessee: American Institute of Aeronautics and Astronautics, 2012.

[90] Gano, S. E., Kim, H., and Brown, D. E., "Comparison of Three Surrogate Modeling Techniques: Datascape, Kriging, and Second Order Regression," *11th AIAA/ISSMO Multidisciplinary Analysis and Optimization Conference*, Portsmouth, Virginia: American Institute of Aeronautics and Astronautics, 2006.

[91] Rendall, T. C. S., and Allen, C. B., "Multidimensional Aircraft Data Interpolation Using Radial Basis Functions," *25th AIAA Applied Aerodynamics Conference*, Miami, Florida: American Institute of Aeronautics and Astronautics, 2007.

[92] Fang, H., and Horstemeyer, M. F., "Metamodeling with Radial Basis Functions," *46th AIAA/ASME/ASCE/AHS/ASC Structures, Structural Dynamics and Materials Conference*, Austin, Texas: American Institute of Aeronautics and Astronautics, 2005.

[93] Mackman, T. J., and Allen, C. B., "Adaptive Sampling for CFD Data Interpolation Using Radial Basis Functions," *27th AIAA Applied Aerodynamics Conference*, San Antonio,

Texas: American Institute of Aeronautics and Astronautics, 2009.

[94] Mullur, A. A., and Messac, A., "Extended Radial Basis Functions: More Flexible and Effective Metamodeling," *10th AIAA/ISSMO Multidisciplinary Analysis and Optimization Conference*, Albany, New York: American Institute of Aeronautics and Astronautics, 2004.

[95] Apte, A. P., and Wang, B. P., "Topology Optimization Using Hyper Radial Basis Function Network," *AIAA Journal*, vol. 46, Sep. 2008, pp. 2211–2218.

[96] Yamazaki, W., "Efficient Robust Design Optimization by Variable Fidelity Kriging Model," *53rd AIAA/ASME/ASCE/AHS/ASC Structures, Structural Dynamics and Materials Conference, Structures, Structural Dynamics, and Materials and Co-located Conferences*, Honolulu, Hawaii: American Institute of Aeronautics and Astronautics, 2012.

[97] Jeong, S., Murayama, M., and Yamamoto, K., "Efficient Optimization Design Method Using Kriging Model," *Journal of Aircraft*, vol. 42, 2005, pp. 413–420.

[98] Toal, D. J., Bressloff, N. W., and Keane, A. J., "Kriging Hyperparameter Tuning Strategies," *AIAA Journal*, vol. 46, 2008, pp. 1240–1252.

[99] Martin, J. D., "Using Kriging Models to Perform Sensitivity Analysis," *52nd AIAA/ASME/ASCE/AHS/ASC Structures, Structural Dynamics and Materials Conference*, Denver, Colorado: American Institute of Aeronautics and Astronautics, 2011.

[100] Lee, T. H., and Jung, J. J., "Maxmin Eigenvalue Sampling of Kriging Model," *10th AIAA/ISSMO Multidisciplinary Analysis and Optimization Conference*, Albany, New York: American Institute of Aeronautics and Astronautics, 2004.

[101] Martin, J. D., "Robust Kriging Models," *51st AIAA/ASME/ASCE/AHS/ASC Structures, Structural Dynamics, and Materials Conference*, Orlando, Florida: American Institute of Aeronautics and Astronautics, 2010.

[102] Voitcu, O., and Wong, Y. S., "Neural Network Approach for Nonlinear Aeroelastic Analysis," *Journal of Guidance, Control, and Dynamics*, vol. 26, Jan. 2003, pp. 99–105.

[103] Jaw, L. C., "Neural Network Modeling of Engine Tip Clearance," *33rd Joint Propulsion Conference and Exhibit*, Seattle, Washington: American Institute of Aeronautics and Astronautics, 1997.

[104] Liu, W., and Batill, S., "Gradient-Enhanced Neural Network Response Surface Approximations," *8th Symposium on Multidisciplinary Analysis and Optimization*, Long Beach, California: American Institute of Aeronautics and Astronautics, 2000.

[105] Pitt, D. M., and Haudrich, D. P., "Artificial Neural Network for Multiple Aeroelastic Analysis," *45th AIAA/ASME/ASCE/AHS/ASC Structures, Structural Dynamics and Materials Conference*, Palm Springs, California: American Institute of Aeronautics and Astronautics, 2004.

[106] Villarreal, J. A., Lea, R. N., and Savely, R. T., "Fuzzy Logic and Neural Network Technologies," *30th Aerospace Sciences Meeting and Exhibit*, Houston, Texas: American Institute of Aeronautics and Astronautics, 1992.

[107] Koziel, S., and Leifsson, L., "Knowledge-Based Airfoil Shape Optimization Using Space Mapping," *30th AIAA Applied Aerodynamics Conference*, New Orleans, Louisiana: American Institute of Aeronautics and Astronautics, 2012.

[108] Robinson, T. D., Eldred, M. S., Willcox, K. E., and Haimes, R., "Surrogate-Based Optimization Using Multifidelity Models with Variable Parameterization and Corrected Space Mapping," *AIAA Journal*, vol. 46, Nov. 2008, pp. 2814–2822.

[109] Koziel, S., and Leifsson, L. T., "Wing Shape Optimization Using Local Response Surface Approximations, Space Mapping and Physics-Based Surrogates," *52nd Aerospace Sciences Meeting*, National Harbor, Maryland: American Institute of Aeronautics and Astronautics, 2014.

[110] Redhe, M., and Nilsson, L., "Using Space Mapping and Surrogate Models to Optimize Vehicle Crashworthiness Design," *9th AIAA/ISSMO Symposium on Multidisciplinary Analysis and Optimization*, Atlanta, Georgia: American Institute of Aeronautics and Astronautics, 2002.

[111] McMasters, R. L., Zhou, Z., Dowding, K. J., Somerton, C., and Beck, J. V., "Exact Solution for Nonlinear Thermal Diffusion and Its Use for Verification," *Journal of Thermophysics and Heat Transfer*, vol. 16, 2002, pp. 366–372.

[112] Carnes, B. R., and Copps, K. D., "Thermal Contact Algorithms in SIERRA Mechanics," *Technical Report SAND2008-2607*, Albuquerque, New Mexico: Sandia National Laboratories, 2008.

[113] Matney, A. K., and Mignolet, M. P., "Thermal Reduced Order Model Adaptation to Aero-Thermo-Structural Interactions," *Proceedings of the 55th AIAA/ASME/ASCE/AHS/ASC Structures, Structural Dynamics, and Materials Conference*, National Harbor, Maryland: AIAA 2014-0493, 2014.

[114] Eckert, E. R. G., "Survey of Boundary Layer Heat Transfer at High Velocities and High Temperatures," *Wright Air Development Center*, Fort Belvoir, Virginia: Defense Technical Information Center, 1960.

[115] Camarda, C. J., Haftka, R. T., and Riley, M. F., "An Evaluation of Higher-Order Modal Methods for Calculating Transient Structural Response," *Computers and Structures*, vol. 27, 1987, pp. 89–101.

[116] Camarda, C. J., "Development of Advanced Modal Methods for Calculating Transient Thermal and Structural Response," *Technical Memorandum 104102*, Langley Research Center: National Aeronautics and Space Administration, 1991.

[117] Balakrishnan, N., Hou, G., and Camarda, C., "Nonlinear Transient Thermal Analysis by the

Force-Derivative Method," *40th Structures, Structural Dynamics, and Materials Conference and Exhibit*, Saint Louis, Minnesota: American Institute of Aeronautics and Astronautics, 1999.

[118] Theis, J., Takarics, B., Pfifer, H., Balas, G. J., and Werner, H., "Modal Matching for LPV Model Reduction of Aeroservoelastic Vehicles," *AIAA Atmospheric Flight Mechanics Conference*, Kissimmee, Florida: American Institute of Aeronautics and Astronautics, 2015.

[119] Hjartarson, A., Seiler, P. J., and Balas, G. J., "LPV Aeroservoelastic Control Using the LPVTools Toolbox," *AIAA Atmospheric Flight Mechanics Conference*, Boston, Massachusetts: American Institute of Aeronautics and Astronautics, 2013.

[120] Poussot-Vassal, C., and Roos, C., "Flexible Aircraft Reduced-Order LPV Model Generation from a Set of Large-Scale LTI Models," *American Control Conference*, San Francisco, California: Institute of Electrical and Electronics Engineers, 2011.

[121] Adegas, F. D., Sønderby, I. B., Hansen, M. H., and Stoustrup, J., "Reduced-Order LPV Model of Flexible Wind Turbines from High Fidelity Aeroelastic Codes," *IEEE International Conference on Control Applications*, Hyderabad, India: Institute of Electrical and Electronics Engineers, 2013.

[122] Wang, Y., Song, H., Pant, K., Brenner, M. J., and Suh, P. M., "Model Order Reduction of Aeroservoelastic Model of Flexible Aircraft," *57th AIAA/ASCE/AHS/ASC Structures, Structural Dynamics, and Materials Conference*, San Diego, California: American Institute of Aeronautics and Astronautics, 2016.

[123] Carlson, H. A., and Verberg, R., "A Flight Simulator for Agile Fighter Aircraft and Nonlinear Aerodynamics," *53rd AIAA Aerospace Sciences Meeting*, Kissimmee, Florida: American Institute of Aeronautics and Astronautics, 2015.

[124] Morton, S. A., McDaniel, D. R., Sears, D. R., Tillman, B., and Tuckey, T. R., "Kestrel: A Fixed Wing Virtual Aircraft Product of the CREATE Program," *47th AIAA Aerospace Sciences Meeting including The New Horizons Forum and Aerospace Exposition*, Orlando, Florida: American Institute of Aeronautics and Astronautics, 2009.

[125] Morton, S. A., and Meakin, R. E., "HPCMP CREATE-AV Kestrel Architecture, Capabilities, and Long Term Plan for Fixed-Wing Aircraft Simulations," *54th AIAA Aerospace Sciences Meeting*, San Diego, California: American Institute of Aeronautics and Astronautics, 2016, pp. 1–17.

[126] Olson, M. D., and Fung, Y. C., "Comparing Theory and Experiment for the Supersonic Flutter of Circular Cylindrical Shells," *AIAA Journal*, vol. 5, 1967, pp. 1849–1856.

[127] Evensen, D. A., and Olson, M. D., "Circumferentially Traveling Wave Flutter of a Circular Cylindrical Shell," *AIAA Journal*, vol. 6, 1968, pp. 1522–1527.

[128] Barr, G. W., and Stearman, R. O., "Influence of a Supersonic Flowfield on the Elastic

Stability of Cylindrical Shells," *AIAA Journal*, vol. 8, 1970, pp. 993–1000.

[129] Bismarck-nasr, M. N., "Finite Element Method Applied to the Supersonic Flutter of Circular Cylindrical Shells," *International Journal for Numerical Methods in Engineering*, vol. 10, 1976, pp. 423–435.

[130] Evensen, D. A., and Olson, M. D., "Nonlinear Flutter of a Circular Cylindrical shell in Supersonic Flow," *NASA TN D-426*, Washington D.C.: National Aeronautics and Space Administration, 1967.

[131] Barr, G. W., and Stearman, R. O., "Aeroelastic Stability Characteristics of Cylindrical Shells Considering Imperfections and Edge Constraint," *AIAA Journal*, vol. 7, 1969, pp. 912–919.

[132] Amabili, M., and Pellicano, F., "Nonlinear Supersonic Flutter of Circular Cylindrical Shells," *AIAA Journal*, vol. 39, 2001, pp. 564–573.

[133] Amabili, M., and Pellicano, F., "Multimode Approach to Nonlinear Supersonic Flutter of Imperfect Circular Cylindrical Shells," *Journal of Applied Mechanics*, vol. 69, 2002, pp. 117–129.

[134] Bismarck-nasr, M. N., "Finite Elements in Aeroelasticity of Plates and Shells," *Applied Mechanics Review*, vol. 49, 1996, pp. 17–24.

[135] Sabri, F., and Lakis, A. A., "Finite Element Method Applied to Supersonic Flutter of Circular Cylindrical Shells," *AIAA Journal*, vol. 48, 2010, pp. 73–81.

[136] Falkiewicz, N. J., Cesnik, C. E. S., Crowell, A. R., and McNamara, J. J., "Reduced-Order Aerothermoelastic Framework for Hypersonic Vehicle Control Simulation," *AIAA Journal*, vol. 49, 2011, pp. 1625–1646.

[137] Frendreis, S. G. V, Falkiewicz, N. J., and Cesnik, C. E. S., "Partitioned Solution Based Stability Analysis of Hypersonic Vehicles," *AIAA Atmospheric Flight Mechanics Conference*, Toronto, Ontario: American Institute of Aeronautics and Astronautics, 2010.

[138] Williams, C. K. I., "Prediction with Gaussian Processes: From Linear Regression to Linear Prediction and Beyond," *Learning in Graphical Models*, Dordrecht: Springer Netherlands, 1998, pp. 599–621.

[139] Sacks, J., Welch, W. J., Mitchell, T. J., and Wynn, H. P., "Design and Analysis of Computer Experiments," *Statistical Science*, vol. 4, 1989, pp. 409–423.

[140] Martin, J. D., "Robust Kriging Models," *51st AIAA/ASME/ASCE/AHS/ASC Structures, Structural Dynamics, and Materials Conference*, Orlando, Florida: American Institute of Aeronautics and Astronautics, 2010.

[141] Lophaven, S. N., Søndergaard, J., and Nielsen, H. B., *DACE A Matlab Kriging Toolbox*, Kgs. Lyngby, Denmark: 2002.

[142] Hartley, T. T., Brandis, R., and Mossayebi, F., "Exact and Approximate Solutions the Oblique Shock Equations for Real-Time Applications," *Contractor Report 187173*, Lewis Research Center: National Aeronautics and Space Administration, 1991.

[143] Hayes, W. D., "On Hypersonic Simlitude," *Quarterly of Applied Mathematics*, vol. 5, 1947, pp. 105–106.

[144] Lighthill, M. J., "Oscillating Airfoil at High Mach Number," *Journal of the Aeronautical Science*, vol. 20, 1953, pp. 402–406.

[145] Saarlas, M., "Reference Temperature Method for Computing Displacement Thickness," *AIAA Journal*, vol. 2, 1964, pp. 2056–2057.

[146] Blasius, P. R. H., "Das Aehnlichkeitsgesetz bei Reibungsvorgangen in Flüssigkeiten (Similarity Conditions of Friction Processes in Fluids)," *Forschungsheft*, vol. 131, 1913, pp. 1–41.

[147] Guard, F. L., "Flat Plate Turbulent Heat Transfer at Hypervelocities," *Journal of Spacecraft and Rockets*, vol. 3, 1966, pp. 1549–1551.

[148] Crabtree, L. F., Dommett, R. L., and Woodley, J. G., "Estimation of Heat Transfer to Flat Plates , Cones and Blunt Bodies," *Aeronautical Research Council Reports and Memoranda*, 1970, pp. 1–59.

[149] Administration, N. A. and S., "U.S. Standard Atmosphere, 1976," *NASA-TM-X-74335*, Washington: Nat, 1976.

[150] Fay, J. A., and Riddell, F. R., "Theory of Stagnation Point Heat Transfer in Dissociated Air," *Journal of the Aeronautical Sciences*, vol. 25, 1958.

[151] Zuppardi, G., and Verde, G., "Improved Fay–Riddell Procedure to Compute the Stagnation Point Heat Flux," *Journal of Spacecraft and Rockets*, vol. 35, 1998, pp. 2–4.

[152] Mcbride, B. J., Zehe, M. J., and Gordon, S., "NASA Glenn Coefficients for Calculating Thermodynamic Properties of Individual Species," *NASA TP-2002-211556*, Glenn Research Center: National Aeronautics and Space Administration, 2002.

[153] Fay, J. A., and Nelson, H., "Theory of Stagnation-Point Heat Transfer in a Partially Ionized Diatomic Gas," vol. 1, 1963, pp. 2741–2751.

[154] Crowell, A. R., Mcnamara, J. J., Kecskemety, K. M., and Goerig, T. W., "A Reduced Order Aerothermodynamic Modeling Framework for Hypersonic Aerothermoelasticity," *51st AIAA/ASME/ASCE/AHS/ASC Structures, Structural Dynamics, and Materials Conference*, Orlando, Florida: American Institute of Aeronautics and Astronautics, 2010.

[155] Crowell, A. R., and McNamara, J. J., "Model Reduction of Computational Aerothermodynamics for Hypersonic Aerothermoelasticity," *AIAA Journal*, vol. 50, 2012, pp. 74–84.

[156] Gunzburger, M., and Peterson, J., "Reduced-Order Modeling of Complex Systems with Multiple System Parameters," *Large-Scale Scientific Computing*, vol. 3743, 2006, pp. 15–27.

[157] Hughes, T. J. R., "Unconditionally Stable Algorithms for Nonlinear Heat Conduction," *Computer Methods in Applied Mechanics and Engineering*, vol. 10, 1977, pp. 135–139.

[158] Ritter, M., Cesnik, C. E. S., and Kruger, W. R., "An Enhanced Modal Approach for Large Deformation Modeling of Wing-Like Structures," *56th AIAA/ASCE/AHS/ASC Structures, Structural Dynamics, and Materials Conference*, Kissimmee, Florida: American Institute of Aeronautics and Astronautics, 2015.

[159] Allen, M. S., Kuether, R. J., and Deaner, B., "A Numerical Continuation Method to Compute Nonlinear Normal Modes Using Modal Reduction," *53rd AIAA/ASME/ASCE/AHS/ASC Structures, Structural Dynamics and Materials Conference*, Honolulu, Hawaii: American Institute of Aeronautics and Astronautics, 2012.

[160] Kuether, R. J., and Allen, M. S., "Nonlinear Modal Substructuring of Systems with Geometric Nonlinearities," *54th AIAA/ASME/ASCE/AHS/ASC Structures, Structural Dynamics, and Materials Conference*, Boston, Massachusetts: American Institute of Aeronautics and Astronautics, 2013.

[161] Craig, R. R., and Kurdila, A. J., *Fundamentals of Structural Dynamics*, Hoboken, New Jersey: John Wiley & Sons, Inc., 2006.

[162] Anon., "MSC Nastran Basic Dynamic Analysis User's Guide," *Version 68* Available: https://simcompanion.mscsoftware.com/infocenter/index?page=content&cat=MSC__MD_NASTRAN_DOCUMENTATION&channel=DOCUMENTATION [retrieved 4 August 2017].

[163] Torrez, S. M., Driscoll, J. F., Ihme, M., and Fotia, M. L., "Reduced Order Modeling of Turbulent Reacting Flows with Application to Scramjets," *Journal of Propulsion and Power*, vol. 27, 2011, pp. 371–382.

[164] Torrez, S. M., Dalle, D. J., and Driscoll, J. F., "New Method for Computing Performance of Choked Reacting Flows and Ram-to-Sram Transition," *Journal of Propulsion and Power*, vol. 29, 2013, pp. 433–445.

[165] Dalle, D. J., Torrez, S. M., and Driscoll, J. F., "Rapids Analysis of Scramjet and Linear Plug Nozzles," *Journal of Propulsion and Power*, vol. 28, 2012, pp. 545–555.

[166] Lillian, C. S., Mcdaniel, D. R., and Morton, S. A., "An Efficient Method of Computing Maneuvering Aircraft Surface Loads Using CFD, Proper Orthogonal Decomposition, and System Identification," *49th AIAA Aerospace Sciences Meeting*, Orlando, Florida: American Institute of Aeronautics and Astronautics, 2011.

[167] Eglajs, V., and Audze, P., "New Approach to the Design of Multifactor Experiments," *Problems of Dynamics and Strengths*, vol. 35, 1977, pp. 104–107.

[168] Manteufel, R. D., "Evaluating the Convergence of Latin Hypercube Sampling," *41st Structures, Structural Dynamics, and Materials Conference and Exhibit*, Atlanta, Georgia: American Institute of Aeronautics and Astronautics, 2000.

[169] Martins, J. R. R. A., and Hwang, J. T., "Review and Unification of Methods for Computing Derivatives of Multidisciplinary Computational Models," *AIAA Journal*, vol. 51, 2013, pp. 2582–2599.

[170] Lagarias, J. C., Reeds, J. A., Wright, M. H., and Wright, P. E., "Convergence Properties of the Nelder-Mead Simplex Method in Low Dimensions," *SIAM Journal of Optimization*, vol. 9, 1998, pp. 112–147.

[171] Anon., "fminsearch," *MathWorks Documentation* Available: http://www.mathworks.com/help/matlab/ref/fminsearch.html [retrieved 8 December 2014].

[172] Dormand, J. R., and Prince, P. J., "A Family of Embedded Runge-Kutta Formulae," *Journal of Computational Applied Mathematics*, vol. 6, 1980, pp. 19–26.

[173] Falkiewicz, N. J., Frendreis, S. G. V., and Cesnik, C. E. S., "Effect of Control Surface-Fuselage Inertial Coupling on Hypersonic Vehicle Flight Dynamics," *AIAA Atmospheric Flight Mechanics Conference*, Portland, Oregon: American Institute of Aeronautics and Astronautics, 2011.

[174] Ko, W. L., Shideler, J. L., and Fields, R. A., "Buckling Behavior of Rene 41 Tubular Panels for a Hypersonic Aircraft Wing," *Technical Memorandum 86798*, Dryden Flight Research Facility: National Aeronautics and Space Administration, 1986.

[175] Anon., "Flexible Min-K®," *Material Data Sheet*, Raleigh, North Carolina: Morgan Advanced Materials, 2013.

[176] Pasiliao, C. L., Sytsma, M. J., Neergaard, L. J., Witeof, Z. D., and James.W., T., "Preliminary Aerothermal Structural Simulation," *14th AIAA Aviation Technology, Integration, and Operations Conference*, Atlanta, Georgia: American Institute of Aeronautics and Astronautics, 2014.

[177] Witeof, Z. D., and Neergaard, L. J., "Initial Concept 3.0 Finite Element Model Definition," *Report AFRL-RWWV-TN-2014-0013*, Eglin Air Force Base: Air Force Research Laboratory, 2014.

[178] Anon., "Acusil(R) II Thermal Protection System," *Excelis* Available: https://d2cy52pj4xpl74.cloudfront.net/file/502ca1c8-267c-48e8-a770-e085a4083154/503a237a-5fb3-4a2a-8ac5-5d6f50576be8/503a237a-5fb3-4a2a-8ac5-5d6f50576be8.pdf?version=1 [retrieved 2 August 2017].

[179] Ohlhorst, C. W., Vaughn, W. L., Ransone, P. O., and Tsou, H., "Thermal Conductivity Database of Various Structural Carbon-Carbon Composite Materials," *Technical Memorandum 4787*, Langley Research Center: National Aeronautics and Space Administration, 1997.

[180] Rehmer, B., Beckmann, J., Finn, M., and Glaubitz, S., "Determination of Elastic Moduli of C/C-Composite at Temperatures up to 1900C," *Report 2004-157bg*, Berlin, Germany: Federal Institute for Materials Research and Testing, 2004.

[181] Fitzer, E., and Manocha, L. M., *Carbon Reinforcements and carbon/carbon composites*, New York, New York: Springer-Verlag Berlin Heidelberg, 1998.

[182] Anon., "Young Modulus of Elasticity for Metals and Alloys," *The Engineering Toolbox* Available: http://www.engineeringtoolbox.com/young-modulus-d_773.html [retrieved 25 April 2016].

[183] Anon., "Metals - Specific Heats," *The Engineering Toolbox* Available: http://www.engineeringtoolbox.com/specific-heat-metals-d_152.html [retrieved 7 April 2015].

[184] Allegheny Technologies Incorporated, "ATI Ti-6Al-4V, Grade 5, Technical Data Sheet," *UNS R56400*, Pittsburg, Pennsylvania: Allegheny Technologies Incorporated, 2012.

[185] Schmidt, F. F., and Ogden, H. R., "The Engineering Properties of Tungsten and Tungsten Alloys," *AD 425547*, Columbus, Ohio: Defense Technical Information Center, 1963.

[186] Anon., "Young Modulus of Elasticity for Metals and Alloys," *The Engineering Toolbox* Available: http://www.engineeringtoolbox.com/young-modulus-d_773.html [retrieved 25 April 2016].

[187] White, G. K., and Collocott, S. J., "Heat Capacity of Reference Materials: Cu and W," *Journal of Physics, Chemistry, and Reference Data*, vol. 13, 1984, pp. 1251–1257.

[188] Zettl, D., Dreyer, E. R., Grier, B. J., McNamara, J. J., and Pasiliao, C. L., "Rapid Steady-State Pressure Prediction for Ultra High-Speed Vehicles," *15th Dynamics Specialists Conference*, San Diego, California: American Institute of Aeronautics and Astronautics, 2014.

[189] Rexius, S. L., Rexius, T. E., Jorris, T. R., and Afb, E., "Advances in Highly Constrained Multi-Phase Trajectory Generation using the General Pseudospectral Optimization Software GPOPS," *Proceedings of the AIAA Guidance, Navigation, and Control (GNC) Conference*, Boston, Massachusetts: American Institute of Aeronautics and Astronautics, 2013.

[190] Swiler, L. P., Slepoy, R., and Giunta, A. A., "Evaluation of Sampling Methods in Constructing Response Surface Approximations," *47th AIAA/ASME/ASCE/AHS/ASC Structures, Structural Dynamics, and Materials Conference, Structures, Structural Dynamics, and Materials and Co-located Conferences*, Newport, Rhode Island: American Institute of Aeronautics and Astronautics, 2006.

[191] Anon., "Abaqus FEM/CAE v6.13," *Dassault Systemes Simulia Corporation* Available: http://dsk.ippt.pan.pl/docs/abaqus/v6.13/index.html [retrieved 4 August 2017].

[192] Martins, J. R. R. A., Kroo, I. M., and Alonso, J. J., "An Automated Method for Sensitivity Analysis Using Complex Variables," *38th Aerospace Sciences Meeting and Exhibit*, Stanford, California: American Institute of Aeronautics and Astronautics, 2000.

[193] Anon., "MATLAB Documentation," *MathWorks* Available: https://www.mathworks.com/help/ [retrieved 21 October 2016].

[194] Ojalvo, I. U., and Newman, M., "Vibration Modes of Large Structures by an Automatic Matrix-Reduction Method," *AIAA Journal*, vol. 8, 1970, pp. 1234–1239.

[195] Falkiewicz, N. J., and Cesnik, C. E. S., "Enhanced Modal Solutions for Structural Dynamics in Aerothermoelastic Analysis," *Journal of Aircraft*, vol. 54, 2017, pp. 870–889.

[196] Murthy, R., Wang, X., Matney, A., and Mignolet, M. P., "Optimum Thermal Modes for Coupled Structural-Thermal Reduced Order Models," *57th AIAA/ASCE/AHS/ASC Structures, Structural Dynamics, and Materials Conference*, San Diego, California: American Institute of Aeronautics and Astronautics, 2016.

[197] Witeof, Z. D., Neergaard, L. J., Vanderwyst, A. S., Shelton, A. B., Martin, C. L., and Pasiliao, C. L., "Dynamic Fluid-Thermal-Structural Interaction Effects in Preliminary Design of High Speed Vehicles," *15th Dynamics Specialists Conference*, San Diego, California: American Institute of Aeronautics and Astronautics, 2016.